

**Experimental and Finite Element Study of the Behaviour of
Structural Members to Combined Tension and Torsion
Loadings**

Nuri M. Zarroug

Ph.D

2003

**Experimental and Finite Element Study of the Behaviour
of Structural Members to Combined Tension and
Torsion Loadings**

By

Nuri M. Zarroug B.Sc.Eng. M.Sc

This thesis is submitted to Dublin City University as the fulfilment of the
requirement for the award of the degree of

Doctor of Philosophy

Supervisor. Professor M.S J. Hashmi, Ph.D. D Sc

**School of Mechanical and Manufacturing Engineering
Dublin City University**

June 2003

DECLARATION

I hereby certify that this material presented in this thesis is entirely my own work, except where specific references have been made to the works of others, and no part of this work has been submitted in support of an application for another degree or qualification to this or any other establishment

Signed _____ Date _____

Nuri M Zarroug

ID 98971336

Acknowledgements

I would like to express my sincere gratitude to Prof M S J Hashmi for his guidance and supervision throughout the course of this project

I would like also to thank Dr AbdulGani Olabi, Dr Dermot barbazon and Dr Brian MacDonald for their help and assistance

Thanks to Mr Chris Crouch, Jim, Martin and all the members of the mechanical workshop

Last by no means least, special thanks to my parents, family and friends for their kindness and encouragement

ABSTRACT

Experimental and finite element study of the behaviour of structural members to combined tension and torsion loadings

By

Nuri M. Zarroug B.Sc.Eng. M.Sc

This research work is concerned with the determination of elastic-plastic deformation behaviour of structural members to combined tension-torsion loadings. Three aspects of the work were examined. In the first, an adaptive control system is developed for performing combined tension and torsion tests on solid and thin-walled tubular specimens by using systems supplied by National Instruments to control the axial and torsion loads on the specimen through data acquisition boards. The LabView software in conjunction with data acquisition board, servo-controllers and servomotors form the adaptive control system for the torque-tension machine. The second aspect was to carry out experimental investigations, where solid steel rods (structural steel) were subjected to non-proportional combined tension-torsion loading paths. In these loading paths, initial elastic tension followed by torsion, holding corresponding axial displacement constant and initial elastic torsion followed by tension, keeping the corresponding angle of twist constant, were examined. The experimental programme also considered the non-proportional combined tension-torsion loading of thin walled steel tubes. It has been observed experimentally that, when the rod is initially subjected to an axial load keeping the corresponding axial displacement constant and then followed by subsequently application of the torque the rod behaves as if its axial load carrying capacity decreases without affecting its torque carrying ability. Similarly when the rod is initially subjected to a torque, keeping its corresponding angle of twist constant, and then followed by subsequently application of the axial load the rod behaves as if its torque carrying capacity is reduced without affecting its axial load carrying ability.

The third aspect was devoted to the finite element analysis. The finite element analysis package ANSYS (version 5.7) was used for the analysis of the combined tension-torsion loadings of the steel rods. The geometry of the steel rod was supplied

to the Ansys package and meshed. The preconditioning conjugate gradient (PCG) and the sparse direct solver were used to solve all the combination of loads. Experimental results obtained were compared with computed values from the finite element analysis and are presented. Reasonably good agreement is obtained between the experimental and computed stresses and displacements. This work has direct bearing on the relaxation of tightening torques or axial loads as experienced by critical engineering components, such as couplings, bolted joints, rotating shafts, and steel structures that are subjected to similar types of combined loadings. It is also hoped that the information generated in this research work will guide the designer towards the use of more realistic materials and achieve better design.

NOMENCLATURE

Symbol	
f	Force
l	Element characteristic length
t	Time
v	Element volume
x	Velocity of specific node
B	Strain displacement matrix
C	Global damping matrix
D	Stress-strain matrix
E	Young's modulus
E_T	Tangent modulus
F	Axial load
F	Normalised axial load (F/F_Y)
F_Y	Yield load
H	Displacement interpolation matrix
I	Identity matrix
K	Global stiffness matrix
M	Global mass matrix
R	Load vector
T	Torque
T	Normalised torque (T/T_Y)
T_Y	Yield torque

U	Virtual displacement
\bar{U}	Displacement in global X direction
U	Nodal point velocity
U	Nodal point accelerations
\bar{V}	Displacement in global Y direction
\bar{W}	Displacement in global Z direction
Y	Yield stress in tension

Greek

σ	Axial stress
σ_y	Yield stress
τ	Shear stress
ϵ	Axial strain

LIST OF FIGURES

Figure No	Description	Page No
1 1	The method of approach used in the present study	8
3 1	Tension-torsion experimental set up	25
3 2	Schematic diagram of the machine (front view)	27
3 3	Schematic diagram of the machine (side view)	28
3 4	The schematic diagram of a moog brushless drive system	31
3 5	Schematic diagram of a moog brushless servomotor	33
3 6	The characteristic curve of motor-1	34
3 7	The characteristic curve of motor-2	36
3 8	The flow chart of the operation principle of the controllers	38
3 9	Various connections of the controller and the power supply unit	39
3 10	Circuit diagram among the controllers and the motors	42
3 11	The output characteristic curve of the angle measuring transducer	46
3 12	The RDP Module 600 amplifier	48
3 13	The front panel for constant load test	51
3 14	The block diagram for constant load test	51
3 15	The front panel for constant axial displacement test	52
3 16	The block diagram for constant axial displacement test	52
3 17	The front panel for constant angular twist test	53
3 18	The block diagram for constant angular twist test	53
3 19	The front panel for constant torque test	54
3 20	The block diagram for constant torque test	54
3 21	Block diagram of device1 AT-AO-6	57
3 22	AT-AO-6 DAQ device1	58
3 23	Block diagram of device2 AT-MIO-16E-10	59
3 24	At-MIO-16E DAQ device2	60
3 25	Axial load calibration curve	62
3 26	Torque load cell calibration curve	64
3 27	LVDT calibration curve	66
3 28	Angle of twist calibration curve	67
3 29	Geometry of the specimen	69
3 30	The assembly drawing of the thin-walled tube	70
3 31	Specially designed head to fit with the thin-walled tube	71
3 32	Different types of strain gauges used	73
4 1	Axial stress versus axial strain	82
4 2	Uniaxial tensile load versus axial strain	83
4 3	Torque versus shear strain curve	84
4 4	Normalised axial load versus normalised torque curves (constant axial displacement)	86
4 5	Normalised shear strain versus normalised axial load and torque curves (F=YL)	88
4 6	Normalised shear strain versus normalised axial load and torque curves (F=75%YL)	89

4 7	Normalised shear strain versus normalised axial load and torque curves (F=50%YL)	90
4 8	Normalised shear strain versus normalised axial load and torque curves (F=25%YL)	91
4 9	Normalised shear strain versus normalised axial strain (constant load)	93
4 10	Normalised axial load versus normalised torque (constant angle of twist)	94
4 11	Normalised axial stress versus normalised shear stress (constant angle of twist)	95
4 12	Normalised axial strain versus normalised torque and load curves (T=YT)	97
4 13	Normalised axial strain versus normalised torque and load curves (T=90%YT)	98
4 14	Normalised axial strain versus normalised torque and load curves (T=50%YT)	99
4 15	Normalised axial strain versus normalised torque and load curves (T=25%YT)	100
4 16	Normalised axial strain versus normalised shear strain (constant torque)	101
4 17	Axial stress versus shear stress (constant axial displacement)	103
4 18	Axial stress versus shear stress (constant angle of twist)	104
4 19	Comparison of experimentally obtained yield stresses with those of Mises' and Tresca's	106
4 20	The uniaxial tensile load versus the axial strain curve of the thin-walled tube	108
4 21	The torque versus the shear strain curve of the thin-walled tube	109
4 22	Normalised torque versus normalised axial load curve for the tube (angle of twist constant)	110
4 23	Axial stress versus shear stress (constant angle of twist)	111
4 24	Normalised torque versus normalised axial load (axial displacement constant)	113
4 25	Comparison of thin-walled tube's result with the solid rod (constant angle of twist)	114
4 26	Comparison of thin-walled tube's result with the solid rod (constant axial displacement)	116
5 1	Finite element model (solid rod)	131
5 2	Material model used for the solid rod	132
5 3	Finite element model (thin-walled tube)	133
5 4	Material model used for the tube	134
5 5	The basic steps of a non-linear elasto-plastic analysis	135
5 6	Axial stress versus shear stress (angle of twist constant)	138
5 7	Deformation of the rod after applying axial load (constant angle of twist) (T=25%YT)	139
5 8	Deformation of the rod after applying axial load (constant angle of twist) (T=50%YT)	140
5 9	Deformation of the rod after applying axial load (constant angle of twist) (T=75%YT)	141

5 10	Deformation of the rod after applying axial load (constant angle of twist) (T=100%YT)	142
5 11	Axial strain versus shear strain for solid rod (constant torque)	144
5 12	Axial stress versus shear stress for solid rod (constant torque)	145
5 13	Deformation of the rod after applying axial load (constant torque) (T=29%YT)	146
5 14	Deformation of the rod after applying axial load (constant torque) (T=57%YT)	147
5 15	Deformation of the rod after applying axial load (constant torque) (T=75%YT)	148
5 16	Deformation of the rod after applying axial load (constant torque) (T=92%YT)	149
5 17	Axial stress versus shear stress for the solid rod (axial displacement constant)	150
5 18	Deformation of the rod after applying torque (constant axial displacement) (F=25%YL)	152
5 19	Deformation of the rod after applying torque (constant axial displacement) (F=50%YL)	153
5 20	Deformation of the rod after applying torque (constant axial displacement) (F=75%YL)	154
5 21	Deformation of the rod after applying torque (constant axial displacement) (F=100%YL)	155
5 22	Shear strain versus axial strain for the solid rod (constant load)	156
5 23	Axial stress versus shear stress for the solid rod (constant load)	157
5 24	Deformation of the rod after applying torque (constant load) (F=25%YL)	158
5 25	Deformation of the rod after applying torque (constant load) (F=50%YL)	159
5 26	Deformation of the rod after applying torque (constant load) (F=75%YL)	160
5 27	Deformation of the rod after applying torque (constant load) (F=90%YL)	161
5 28	Axial stress versus shear stress for the tube (constant angle of twist)	163
5 29	Deformation of the tube after applying axial load (constant angle of twist) (T=25%YT)	164
5 30	Deformation of the tube after applying axial load (constant angle of twist) (T=50%YT)	165
5 31	Deformation of the tube after applying axial load (constant angle of twist) (T=75%YT)	166
5 32	Axial stress versus shear stress for the tube (axial displacement constant)	168
5 33	Deformation of the tube after applying torque (axial displacement constant) (F=25%YL)	169

5 34	Deformation of the tube after applying torque (axial displacement constant) (F=50%YL)	170
5 35	Deformation of the tube after applying torque (axial displacement constant) (F=75%YL)	171
5 36	Deformation of the tube after applying torque (axial displacement constant) (F=100%YL)	172
6 1	Comparison of experimental and FEA results of the solid rod (axial displacement constant)	174
6 2	Comparison of experimental and FEA results of the solid rod (constant load)	176
6 3	Comparison of experimental and FEA results of the solid rod (constant angle of twist)	177
6 4	Comparison of experimental and FEA results of The solid rod (constant torque)	180
6 5	Comparison of experimental and FEA results of the Tube(axial displacement constant)	181
6 6	Comparison of experimental and FEA results of the Tube(constant angle of twist)	182

LIST OF PLATES

Plate-3 1	Torque-Tension machine	76
Plate-3 2	Positioning of the LVDT	77
Plate-3 3	The RDP Module 600 Amplifier	78
Plate-3 4	The two identical “Mood T161-003” Brushless motor controllers	79
Plate 4 1-	fracture mode of the solid rod specimen	117
Plate 4 2-	Fracture mode of the tube specimen	117

LIST OF TABLES

Table-3 1	The specifications of the torque-tension machine	26
Table-3 2	The assigned channels for each transducer	55
Table-3 3	Chemical composition of the steel solid rod	68
Table-3 4	Chemical composition of the thin-walled tube	68
Table-4 1	Mechanical properties of the solid rod	85
Table-4 2	Mechanical properties of thin-walled tube	107
Table-5 1	Material data used for material model (solid rod)	131
Table-5 2	Summary of the theories involved in a material with bi-linear isotropic hardening behaviour	132
Table-5 3	Material data used for material model (thin-walled tube)	134

CONTENTS

DECLARATION	1
ACKNOWLEDGEMENTS	ii
ABSTRACT	iii
NOMENCLATURE	v
LIST OF FIGURES, PLATES AND TABLES	vii

CHAPTER ONE INTRODUCTION

1 1	Justification for the work	1
1 2	Finite element analysis	3
1 3	Aims of the study	4
1 4	Method of approach	5
1 5	Over view of thesis	6

CHAPTER TWO LITERATURE REVIEW

2 1	Introduction	9
2 2	Historical Back ground of combined loading in the elsto-plastic region	9
2 3	Finite Element Simulation Studies	21

CHAPTER THREE EXPERIMENTAL SET UP

3 1	Introduction	24
3 2	torque-tension machine	25
3 2 1	Main components of the machine	26
3 2 2	Ball screw	26
3 2 3	Guid Rod	26
3 2 4	Cross-Head	26
3 2 5	Shafts	26
3 2 6	Specimen Holding Devices	27
3 2 7	Drive System	27
3 2 8	Control System	30
3 2 9	Connection	31
3 2 10	Data Acquisition system	33
3 2 11	Modular amplifier	36
3 3	Labview Programme	37
3 4	Calibration of the test machine	41

3 4 1	Calibration of the axial load cell	41
3 4 2	Calibration of the torque load cell	42
3 4 3	Calibration of the LVDT	42
3 4 4	Calibration of the angular position transducer	43
3 5	Specimen selection and instrumentation	44
3 5 1	Test material and specimen design	44
3 5 2	Specimen instrumentation	45
3 5 3	Strain gauge attachment	45
3 6	Experimental programme of combined loading	46
3 6 1	Tension followed by torsion	46
3 6 2	Torsion followed by tension	47

CHAPTER FOUR ANALYSIS OF EXPERIMENTAL RESULTS AND DISCUSSION

4 1	Introduction	80
4 2	Preliminary tests	81
4 2 1	Uni-axial Tensile Test	81
4 2 2	Pure Torsion Test	81
4 3	Combined loading of solid rod	82
4 3 1	Torsion followed by tension	82
4 3 2	Tension followed by torsion	84
4 3 3	Determination of yield points	86
4 4	Combined loading of thin-walled tube	87
4 4 1	Torsion followed by tension	87
4 4 2	Tension followed by torsion	89

CHAPTER FIVE FINITE ELEMENT ANALYSIS

5 1	Introduction	117
5 2	The finite element method	118
5 2 1	General theory	118
5 2 2	Solution methodology	124
5 3	The finite element analysis package Ansys	126
5 3 1	Solution procedures	126
5 3 2	Large Strain Theory	127
5 3 3	Elasto-plastic behaviour	127
5 3 4	Material model	130
5 4	Modelling	130
5 4 1	Solid steel Rod	130
5 4 2	Thin-wall tube	133
5 5	Boundary conditions, loading and solution	134

5 6	Results and Analysis	136
5 6 1	Tension followed by torsion, Solid Rod	136
5 6 2	Torsion followed by tension, Solid Rod	137
5 6 3	Torsion followed by tension, Tube	139
5 6 4	Tension followed by torsion, Tube	139

CHAPTER SIX VERIFICATION OF FINITE ELEMENT RESULTS

6 1	Introduction	173
6 2	Verification of Finite element prediction	173
6 2 1	Tension followed by torsion, Solid Rod	173
6 2 2	Torsion followed by tension, Solid Rod	175
6 2 3	Tension followed by torsion, Tube	178
6 2 4	Torsion followed by tension, Tube	178

CHAPTER SEVEN CONCLUSION AND FURTHER WORK

7 1	Introduction	183
7 2	General conclusion	183
7 2 1	Experimental Investigation	183
7 2 2	Finite Element Analysis	184
7 2 3	Comparison of Experimental results with FEA results	185
7 3	Thesis contribution	185
7 4	Recommendation for further work	185

References	187
Appendix	
Publications	

CHAPTER ONE

INTRODUCTION

1.1 JUSTIFICATION FOR THE WORK

Many mechanical and structural components are subjected to variable loads. The stress analysis of such components often turns out to be very complicated when ever plastic strains and deformations occur. If the plastic strains are very large, as in many metal forming processes, the elastic component of strain is considered negligible and the material is assumed to be perfectly plastic. On the other hand where the elastic and plastic components of strain are of the same order, the problems are elasto-plastic. These types of problems are of paramount importance to structural engineers and designers. In many engineering applications, such as aerospace, automotive and missile, economical and environmental concerns have driven the need for lighter but safe structures [1]. With more attention having been made on the weight saving in these applications, large factors of safety can no longer be used by designers and the design must be done on the basis of minimum weight, which invariably means designing into the plastic range to obtain maximum load to weight ratios.

In the design of load carrying parts, it is a general rule to make sure that yielding does not occur under service loading as usually structural elements are designed so that material does not yield under the expected loading conditions. The magnitude of the stress, which causes the material to yield under uniaxial or combined loading, can be predicted by various theoretical yield criteria. For structures composed of members carrying loads in the elastic-plastic range, deformation is more difficult to calculate than elastic deformations because relationships between the stresses and strains are non-linear and are dependent on the loading history. The stress distribution in most structural members loaded into the elastic-plastic range is difficult to determine because the shape of the elastic-plastic interface is itself related

to the stress distribution and is therefore unknown until the complete solution has been found. For a solid circular rod carrying combinations of axial load and torque, this restriction is removed since the shape of the interface must be annular to preserve axial symmetry. If a circular bar is subjected to combined axial load and torsion, yielding does not occur until the combined stress state reaches a critical value, that is, equivalent yield of that particular material reaching the yield locus, if axial load and /or torque is further applied, plastic flow starts in the material. The linear elastic torsion theory stipulates that the maximum shear stress occurs at the outer fibre of the material [2]. There are limited experimental works regarding the biaxial (combined) loading of solid rod, which have been subjected to combined torque and tension loads within the plastic region to observe the elastic-plastic response of the material. For simplicity, in most existing research works, thin-walled tubes have been used to conduct these types of investigations.

The demands for assurance of quality and reliability in engineering structures or components have steadily increased over the past two decades. All manufacturing bodies are trying to cut raw material costs, improve designs and enhance manufacturability. Since almost all manufacturing involves some form of component assembly, one logical place to tackle the problem is in the items and methods used to hold these components together. The task of holding all the components together is usually achieved by using fastening bolts. They are by far the most commonly used system for achieving safety, reliability and maintainability. The bolted joints are fundamental elements in most mechanical equipment. It is frequently the most highly stressed element in a structure and the bolt itself is likely to be the component of smallest cross-section. The information on tightening bolted joints is important to the design engineer, in order to ensure the reliability of the joint and a minimum clamp load which is necessary to provide adequate in-service durability. Therefore designers are drawn more and more towards tightening processes which minimise clamp load variation in order to obtain the benefits of more predictable service. The designs of bolted joints and techniques used to tighten them have received increased attention by the Automotive, Aerospace and Petro-Chemical industries. Considerable investigations are still being carried out into bolted joints, especially into the quality of the tightening involved and into the bolt itself [3]. During the fastening process, a

fastener is subjected to torsion as well as axial stress. Subsequently, when the joint is subjected to an external load, the fastener is subjected to additional axial load due to the external load. It is expected that the plastic yielding of the fastener would occur at the combined yield load. Accordingly, this research programme has been undertaken to carry out detailed experimental investigations to know how the external tensile load affects the magnitude of the initially applied torque or how the application of torque affects the initially applied axial load or pre-load in a bolt in the elastic-plastic range. A circular rod has been used as a specimen for this investigation to avoid the complex relationships between the tightening torque, friction coefficient and pre-load in the bolt. During the tightening process other stress components arise due to the effects of the helix angle and the geometry of the thread, the effect of these stresses are not considered in this study because of the simple design of the test specimen.

In this research programme, the specimen is subjected to various complex non-proportional biaxial loading paths. In these loading paths, elastic torsion followed by application of tension, holding the angle of twist or the torque constant and elastic tension followed by application of torsion, holding the axial displacement or axial load constant, until failure of the specimen was examined.

1.2 FINITE ELEMENT ANALYSIS

Finite element analysis (FEA) is a computer based numerical technique for calculating the strength and behaviour of engineering structures [4]. It can be used to calculate stresses, deflections, vibration, buckling behaviour and many other phenomena. With the advances in computer technology and CAD systems, complex problems can be modelled with relative ease and several alternative configurations can be tested on a computer before the first prototype is built. In the finite element method of analysis, a structure (or rather, the mode) is mathematically divided into a set of connected blocks, or elements which can have various shapes. The material properties (such as young's Modulus and Poisson's ratio in linear elastic and isotropic problems) and the governing relationships are considered over these

elements and expressed in terms of strain and stress at element corners. The behaviour of an individual element can be described with a relatively simple set of equations. Just as the set of elements would be joined together to build the whole structure, the equations describing the behaviours of the individual elements are joined into an extremely large set of equations. Solution of these equations gives the behaviour of whole structure under the set of boundary conditions. With the replacement of analog with digital computers and the development of the first commercial finite element analysis codes in the early 1960's, linear static analysis was available to the analysts who could justify the expense. The finite element method was introduced to the plasticity problems in the late 1960's when an elastic-plastic constitutive equation was incorporated in the standard solution routine that had been used in the solution of elasticity problems. The large increase in computer speed and the power and more availability of finite element software, made these commercial finite element packages available for analysts and engineers. The number and variety of packages available appears to be increasing rapidly with different strengths and weaknesses. Abaqus, Marc, Ansys, Sap and MSC/Nastran are some of such finite element analysis packages.

In this research work the commercial finite element package ANSYS [5] (version 5.7) was used for the analysis of the combined tension-torsion loadings of the steel rod and thin-walled tubes. The geometry of the rod and tube were modelled to be consistent with the specimen used in the experiments. The loading method used in the finite element analysis was identical to that used in the experiments. The analysis was carried out in two steps. In the first step, an initial axial load or initial torque was applied to the model. The second step consists of applying the torque beyond the yield torque or applying the axial load beyond the yield load. The preconditioning conjugate gradient solver (PCG) and the sparse direct solver were used to solve all the combination of loads.

1.3 AIMS OF THE STUDY

In this research work, the main objectives can be summarised in four sections as follows.

- The first section is to develop an adaptive control system to perform combined tension and torsion tests by using systems supplied by National Instruments to control the axial and torsion loads on the specimen through data acquisition boards. The LabView software in conjunction with data acquisition board, servo-controllers and servo-motors form the adaptive control system for the torque-tension machine.
- The second section is to carry out a detailed experimental investigation using a servo-controlled instrumented torque-tension machine to determine the elastic-plastic deformation behaviour of structural steel rods under combined tension and torsion loadings under different controlled and boundary conditions.
- The third is to use the finite element analysis package ANSYS (version 5.7) for the analysis of the combined tension and torsion loadings of the steel rods and tubes.
- The fourth one is to compare the experimental results obtained during the combined loading with the results from the finite element analysis. To achieve the above mentioned objectives, the following method of approach has been adopted.

1.4 METHOD OF APPROACH

The method of approach adopted in this research work, as schematically shown in figure 1, has been divided into four sections. The first section was concerned with the development and application of an adaptive control system for performing combined tension and torsion tests by using systems supplied by National Instruments. The LabView software is used to control the axial and torsion loads on the specimen through data acquisition boards.

The second was devoted to the experimental investigations, where mild steel rods were subjected to different combined loading modes using a purpose built torque-tension machine. Four different modes of loading the rods were considered.

- (i) Initial torque, within the elastic range, was applied and then, holding its corresponding angle of twist, constant an axial load was gradually applied beyond the uniaxial yield load
- (ii) Procedure (i) was repeated except the initial torque applied maintained constant rather than the angle of twist
- (iii) Initial axial load within the elastic range was applied and then, holding its corresponding axial displacement constant, torque was gradually applied beyond the yield torque
- (iv) Procedure (iii) was repeated except the initial axial load maintained constant rather than axial displacement

The experimental programme also considered the combined tension-torsion loading of thin-walled tubes. The third was wholly devoted to the finite element analysis (FEA), where the finite element analysis package ANSYS (version 5.7) was used to simulate the deformation behaviour of the mild steel rods. The geometry of the rod was modelled to be consistent with the specimen used in the experiments. The loading method used in the finite element analysis (FEA) was identical to that used in the experiments. The preconditioned conjugate gradient solver (PCG) and the sparse direct solver were used to solve all the combination of loads. The fourth is to compare the experimental results with the computed values from the finite element analysis results.

1.5 OVERVIEW OF THESIS

This thesis is divided into seven chapters. Chapter one gives an introduction to and a description of the problem under consideration together with the justification for undertaking the present investigation. Chapter two gives a review of the relevant literature while chapter three contains the details of the experimental set up, where the technical details of the torque-tension machine, transducers, amplifier and LabVIEW programme are presented. Chapter four contains the analysis of the experimental results and discussions. Chapter five gives the theoretical outline of the numerical methods used to solve the problem and also contains the analysis of the finite element simulation results and discussions. Chapter six is devoted to the

verification of the finite element simulation results against experimental results
Chapter seven draws general conclusions from the present research, highlights the contribution arising from this research and pin-points areas of research which may further contribute to this field of study, this is followed by a list of references, appendix and list of publications

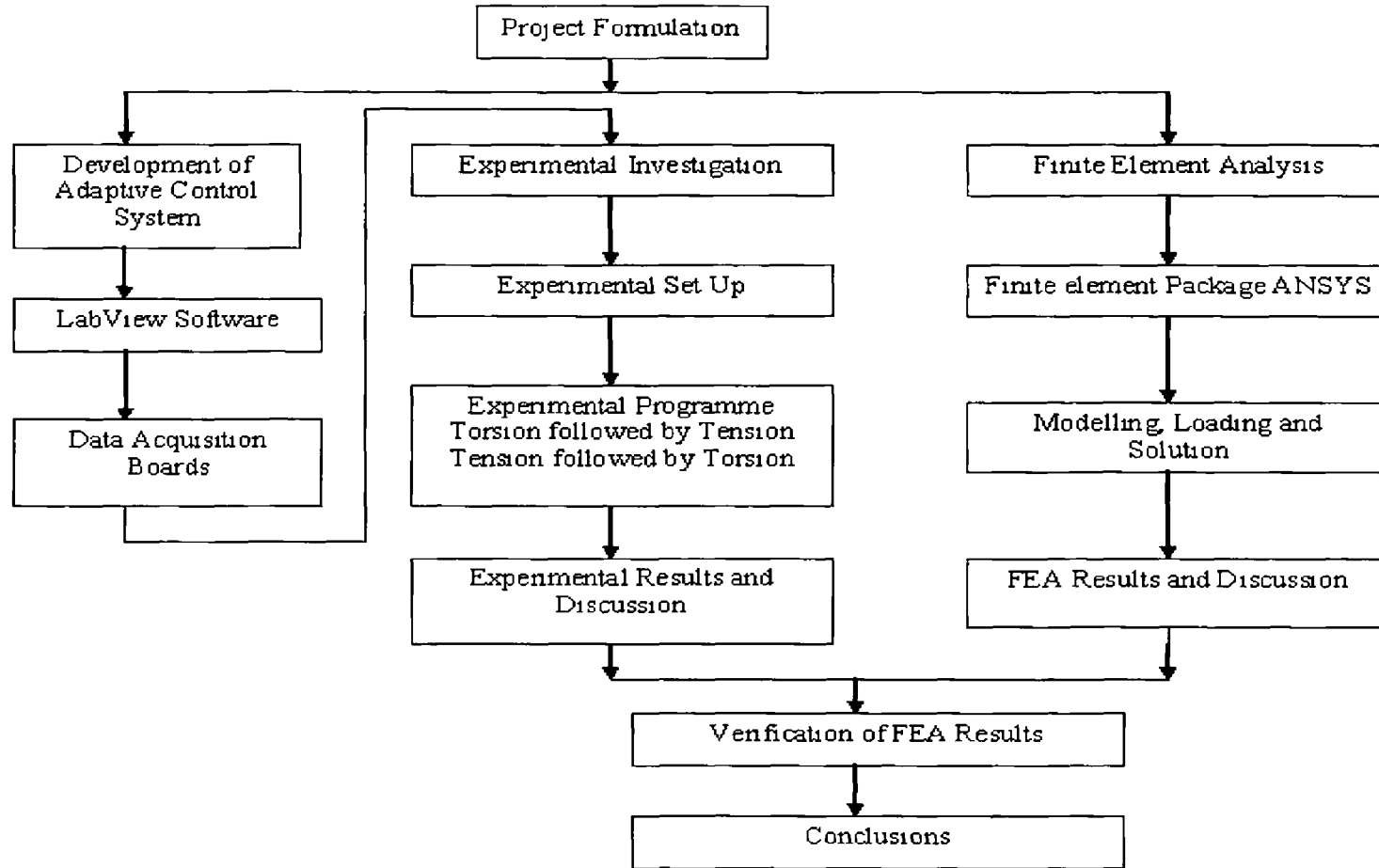


Figure 1.1 The method of approach used in the present study

CHAPTER TWO

LITERATURE REVIEW

2.1 INTRODUCTION

The experimental investigations of material behaviour under combined stresses have attracted much attention in recent years, since uni-axial experiments have been found to be inadequate for revealing the material behaviour under complex loading conditions. There are very few experimental studies regarding the combined loading of a solid rod, which has been subjected to combined torque and tension, as most of existing research works concerning the elastic-plastic response of materials have been conducted using thin-walled tubes for simplicity of analysis since the area under consideration is minimal and subsequently the stress variation is negligible, as the linear elastic torsion theory stipulates that the maximum shear stress occurs at the outer fiber of the material. Most of these experimental investigations in the elastic-plastic or in the fully plastic region were conducted either to verify different analytical and numerical solutions of the elastic-plastic or plastic stress-strain relationships or to verify the various yield criteria, suggested by various researchers. This chapter gives a review of the previous research works on the combined loading.

2.2 Historical back ground of combined loading in the elastic-plastic region

A study of the conditions under which the materials begin to deform plastically have been the subjected of many investigations conducted chiefly in the last few decades. Most investigators performed experiments on thin-walled tubes by combination of tension, torsion and internal pressure. Investigations have also been carried out with the tension and torsion of a solid cylinder subjected to pressure on its lateral surface. Among the investigators who have studied these conditions Nadai, [6] who outlined tests on various materials such as, ductile metals, rock materials, marble and sand

stone under combined stress. Also tests on iron, copper, nickel, aluminium, mild steel, glass and brass were reported in reference [6].

Lode [7] carried out the most detailed experimental investigations under combined stresses in the elastic-plastic range as mentioned by Mendelson [1]. This research tested thin-walled tubes of steel, copper, and nickel under various combinations of longitudinal tension and internal pressure loads in an effort to determine the influence of the intermediate principal stress on yielding. Lode devised a very sensitive method of differentiating between Tresca and Von Mises criteria, and used a parameter called "Lode's stress parameter" to account for the influence of the intermediate stress in the Von Mises criteria. The experimental results favoured Von Mises yield criterion. Lode also carried out the same type of experiments, as mentioned by Hill [8], to investigate the validity of the Levy-Mises stress-strain relations.

Guest carried out tests with thin tubes of steel, iron, and copper according to [8]. These were subjected either to pure axial tension, to axial tension simultaneously with internal hydraulic pressure, or to a twisting moment and a tensile force. For these tests Guest concluded that the condition of yielding of the metals he had investigated was expressed by a linear equation connecting $\sigma_1 - \sigma_2$ and $\sigma_1 + \sigma_3$ ($\sigma_1 > \sigma_2 > \sigma_3$) where σ_1 , σ_2 and σ_3 are principal stresses.

Experimental investigations have been carried out by Hohenemser [9] to verify the validity of the Reuss stress-strain equations. In the report a cylindrical tube was twisted to obtain an approximately uniform distribution of stress at the point of yielding and then holding the angle of twist constant, the tube was extended longitudinally. A pre-strained mild steel thin tube specimen was used to secure a sharp yield point and reduce the rate of hardening to a value small compared with the elastic modulus.

To verify different yield criteria, Taylor and Quinney [10] performed experiments in which copper, mild steel, and aluminium thin-walled tubes were loaded in tension in

to the plastic range, then partially unloaded and twisted until some further plastic flow occurred. The axial load was held constant while the torque was increased, so that stress ratio were not constant. The torque twist or torque extension diagrams were extrapolated back to zero twist or zero extension to establish approximately, but fairly accurately, the torque at which plastic flow recommenced. The degree of anisotropy was kept within the allowable limits by observations of the change in internal volume of the tubes during pure tension. Although the report ignored the possibility of an elastic increment of strain during plastic flow and concluded that the deviation from the Von-Mises yield criterion was real.

Morrison and Shepherd [11] used thin-tubes of 5 percent steel and 11 percent silicon-aluminum alloy. The thin tubes were subjected to tension and torsion to follow a complex path of stress to compare the experimentally found strain path with those calculated by Prandtl-Reuss and Hencky stress-strain relations. The elastic and plastic strains were of comparable magnitude. The tension was applied as first step, holding the tensile stress constant, applied torsion, followed by further tension and torsion to obtain various strain paths. The length and twist were measured and found to be in substantial agreement with the prediction of the Reuss equations.

Hill and Siebel [12] strained steel bars of circular cross section in combined bending and twisting, to investigate the rapidity of approach to the plastic-rigid yield point values. The ratio of bending and twisting was kept constant in each test. In the study the experimental results were compared with the calculated yield point of the bar and obtained upper and lower solutions. The results show that the plastic-rigid yield points may be used in design calculations.

A theoretical and experimental investigation was carried out by Meguid et al [13, 14] under combined tension and torsion loading for elastic-perfectly plastic and work hardening materials. In reference [14] the behaviour of a circular bar of elastic-viscoplastic material subjected to either proportional or non-proportional straining in tension and torsion was investigated. Closed form solutions were obtained for the

stresses, load, and torque corresponding to fully plastic conditions, for quasi-static straining and for a range of finite effective strain rates

Naghdi and Rowley [15] carried on their tests with ten tabular 24S-T4 aluminium alloy specimen. These were subjected to combined tension and torsion with variable loading paths. Tension was applied alone then followed by torsion and permitted the determination of the initial shear modulus when twisted began. The experimental results were discussed in the light of incremental strain (flow) theories of plasticity.

Prager and Hodges [16] and Gaydon [17] determined explicit expressions for the stress distribution and deformation of solid circular bars subjected to combined tension and torsion in the elastic-plastic range. The analysis was restricted to material with Poisson's ratio ($\nu = 0.5$) in both cases, i.e. they did not take the effect of elastic compressibility.

Gaydon considered various combinations of twist and extension. The Reuss equations were used throughout and these were integrated, for different cases, to give the shear stress and tension in the plastic range.

Sved and Brooks [18] investigated the behaviour of a round bar subjected to axial loading and torque in the elasto-plastic range, elastic compressibility of the material was taken into account, and the von-Mises yield condition was used, together with the Reuss stress-strain relationships.

A method for the analysis of a round bar subjected to combined axial load and torque in the elasto-plastic range was presented by Brooks [19]. Ramberg-Osgood curves were used to describe the material behaviour and the analysis was based on the Prandtl-Reuss incremental stress-strain laws and the von-Mises yield criterion. The elastic compressibility was taken into consideration, which was shown to be negligible for all practical purposes.

Experimental investigations have been carried out by Ali and Hashmi [20] to determine the elastic-plastic response of a circular rod subjected to combined torque and tension. Specimens were initially loaded either by torque or by axial load within the elastic range of the material, then either the tensile load or torque was gradually applied beyond the elastic range, holding different parameters such as angle of twist or torque or the axial displacement or tension constant. The results showed that the initially applied torque or tension started to decrease when the combined stress reached the uni-axial yield stress of the material.

Tsangarakis et al [21] loaded Alumina fiber-reinforced aluminium composite in combined tension-torsion. The tests were conducted in a MTS servohydraulic machine. The experimental results indicated that the super-imposition of a 0.0025 shear strain reduced the tensile strain to failure by 67 percent. Similarly, superposition of a 0.0007 tensile strain reduced the shear strain to failure by 81 percent. It was inferred that applying the torque first and then the axial load or the axial load first and then the torque, had no significant effect on the failure envelope.

Rees [22] examined the flow and fracture behaviour of particulate reinforced 2124 aluminium from combining torsion with either tension or compression. Incremental loadings were applied along both radial and stepped paths. The results of all tests show that the yield locus for the material obeys a von Mises description. The observed flow behaviour is compared with that predicted from the Prandtl-Reuss incremental plasticity theory.

Maguid [23] subjected thin-walled tubular specimens of annealed medium carbon steel (En8) to combined tension-torsion at room temperature using a closed-loop servo-controlled, electrohydraulic biaxial testing machine. Bilinear deformation paths of twist at a constant rate followed by extension at different rates were investigated to evaluate the plastic flow of the material under abruptly changing deformation paths and strain-rates. The experimental results indicated that there exist appreciable differences between the von-Mises equivalent stress versus equivalent

plastic strain curves for the different bilinear paths investigated. These differences were attributed to the strain-rate sensitivity of the material investigated.

The kinematics and stress analyses of the tension-torsion test of a thin-walled tube at finite strain were discussed by McMeeking [24]. The relationships between increments of tension and torque and increments of extension and twist for an elastic-plastic material at finite plastic strain were formulated for the most common constitutive assumptions. Also the validity of the Prandtl-Reuss equations for different ranges of plastic strains were evaluated.

Spring back of rectangular bars under combined torsion and tension was investigated by Narayanaswamy and Samanta [25]. The tension-torsion experiments were of two types. First the bars were initially pulled at different level of axial strains in the plastic region, then were twisted for different angles of twist. Load and torque were removed simultaneously at the end, and both spring back and twist back were measured. The other type of experiment, the specimen twisted and then pulled. It was concluded that the angular spring back was analytically predictable and twist followed by pull produced smaller spring back than that produced deformation in the reverse order.

The strain hardening of copper and steel under combined tension and torsion was investigated by Schmidt, as mentioned by Hill [8], who simultaneously twisted and pulled permanently hollow thick-walled cylinders in the tension-torque machine. The ratio of the shearing and the axial normal stress was maintained at constant value during the permanent distortion of the specimens. Schmidt concluded that a strain hardening function $\tau_{oct} = f(\gamma_{oct})$ expresses the behaviour of a ductile metal under increasing value of the stress.

Correa et al [26] carried out experimental investigations on Cu-Zn brass samples. The experiments were performed in a MTS servo-hydraulic testing machine. The

tests were conducted at room temperature. Three sequences of strain paths were performed: tension-torsion, torsion-tension and tension-torsion-tension. Monotonic tension and torsion experiments were also conducted. The results were observed in terms of effective stress-effective strain and strain hardening rate-effective strain curves. The influence of strain path changes on the flow behaviour of Cu-Zn brass has been analyzed. The results were compared with the results obtained for low carbon steel in reference [27].

Wei Jiang [28,29] investigated the elastic-plastic response of thin-walled tubes subjected to combined axial and torsional loads. The kinematic hardening model was used and exact closed-form solutions were obtained for linear loading path. The stress-strain relationships with the corresponding movements of the yield centre were discussed for both monotonic and variable loadings. The response of the tube under non-proportional loading was shown to be path-dependent. Similar work carried out by Jiang and Wu [30] as mentioned above, where thin-walled tubes subjected to combined axial load and internal pressure instead of torsional load.

Non-proportional torsion-tension and biaxial compressive experimental results were presented on tantalum, tantalum alloy with 2.5% tungsten, and AerMet100 steel by Khan and Liang [31]. The torsional test was performed first with free-end condition after certain deformation, torque was kept constant and axial tension was applied, then axial load was kept constant and torsional deformation was continued. These test results formed a comprehensive set of data to show the material behaviours at complex strain and strain-rate deformation.

To investigate yield surfaces and stress-strain relationships, Daneshi and Hawkyard [32] used a tension-torsion machine in which aluminium and Copper specimens were pulled and twisted while being immersed in liquid nitrogen. The test materials were especially treated to approach conditions of isotropy and homogeneity. Stress-strain curves in simple tension and pure shear were obtained at $T=292\text{K}$ and $T=78\text{K}$. The

report concluded that at 78K the initial yield surface obeys the von-Mises yield criterion

A few relevant works regarding experimental investigations under combined tension and torsional loading have been carried out to obtain the initial and the subsequent yield loci for different materials under different loading conditions. The experimental investigations to obtain the initial yield locus were carried out by Meguid et al [33]. Thin tubular specimens of annealed mild steel (En8) were tested under combined torque and tension. They obtained almost the whole positive quadrant of the initial yield locus from a single run without unloading or reloading (neutral loading).

Phillips et al [34-38] carried out the first experiments on pure aluminium. They subjected the specimens of aluminium 1100-0 to pre-stressing in tension, in torsion, and in combined tension and torsion. They observed that the subsequent yield surfaces were convex and that cross effect was weak. Translation of the subsequent yield surface in the direction of pre-stressing was observed and the yield surface changes its size in the direction of the pre-stressing and becomes smaller when moved away from the origin and larger when directed towards the origin.

Naghdi et al [39] investigated the subsequent yield surface by carrying out tension-torsion tests using tubular specimens of 24S-T-4 aluminium alloy. The shapes of the subsequent yield surfaces were determined in the first and fourth quadrant of the axial stress and shear stress plane. It is observed that the initial as well as subsequent yield surfaces were convex. Bauschinger effect and a lack of cross effect were also observed.

Tension-torsion tests were carried out by Mair and Pugh [40] on thin-walled copper tubes. The specimens were pre-strained in tension, partially unloaded, and then strained in torsion. Yield was defined by the Lode extrapolation technique. The yield surfaces were consistent with isotropic hardening accompanied by relatively slight distortion.

Moreton et al [41] conducted experimental investigations where thin-walled tubular specimens were subjected to combination of internal pressure, axial load and torsion to investigate the yield surface behaviour of the steels

The initial and subsequent yield surfaces of annealed AISI type 304 stainless steel have been experimentally determined by Han and Yeh [42] in the axial-torsional stress space. Three loading paths were studied: Pure axial path, a pure torsional path and a proportional axial-torsional path. Each path included loading, unloading, reloading and the cyclically steady state.

Experimental investigations by Daneshi and Hawkyard [43] are made into yield criteria and stress-strain relationships for aluminium and copper at room temperature and 78K by tension-torsion testing of tubular specimens. Initial and subsequent yield surfaces are determined after prestrain in tension and torsion. The laws of normality and convexity and the possibility of the existence of corners on the yield surfaces are considered. The experimental results verified the Mises yield criterion.

Phillips and Lu [44] reported the results of two tension-torsion experiments with an MTC computer controlled servo-hydraulic testing machine on pure aluminium specimens. The first of these experiments was with the loading being controlled while the second experiment was with the strain being controlled. For the load controlled experiment they obtained an initial and four subsequent yield surfaces, the development of the plastic strains, and by carefully monitoring the simultaneous increases in strain they were able to judge the manner in which the yield surface moved during the motion of the stress point on the stress path. They concluded that the loading surface may also depend on the amount of plastic strain developed during loading. For the strain-controlled experiment they obtained continued stress relaxation at the end of each segment of the strain path and they observed that while the path is located within the loading surface, plastic strains were obtained mostly near the loading surface.

The plastic deformation of thin-walled tubes of aluminium alloy 5056 were examined in detail by Ohashi and others [45] for various proportional combined loadings of axial force and torque, as a first stage of investigating the plastic behaviour of isotropic aluminium alloy. The experimental results showed that the third invariant of stress deviator affects considerably the plastic deformation of the material.

As investigations for obtaining detailed information about the plastic behaviour of real materials, precise measurements of plastic deformation of thin-walled tubular specimens of initially-isotropic mild steel was performed by Ohashi and Tokuda [46] under combined loading of torsion and axial force having trajectories consisting of two straight lines at a constant rate of the effective strain.

Ikegami and Nitsui [47] experimentally investigated the plastic deformation of stainless steel at room temperature by subjecting thin-walled tubular specimens to combined axial load and torsion. The stress-strain curves after plastic prestraining are obtained by subsequent loading along the stress path with corners.

Nitsui et al [48] investigated the plastic behaviour of S25C mild steel at room temperature. The combined loading tests were carried out with the thin-walled tubular specimens by applying the axial and torsional loads. The initial yield condition of the material obeyed Tresca's law.

Khan and Wang [49] presented experimental data from combined tension-torsion loading of thin-walled tubes of annealed polycrystalline copper subjected to loading, partial unloading, and then loading in a different direction. Special attention is focused on the direction of the plastic strain increment, experimental values of which are compared with predicted values from the Ziegler and Mroz kinematic hardening models, and endochronic theory. The main objective of their study is to investigate

the effect of finite deformation on subsequent infinitesimal deformation due to 180° and 90° changes in loading paths in the tension-torsion loading space. From the comparison, the Mroz model is shown to predict the direction of the plastic strain increment closest to the experimental results.

Khan and Parikh [50] subjected thin-walled tubes of annealed polycrystalline copper to combined tension-torsion, of various non-proportionate loading, unloading and reverse loading paths using a dead weight type tension-torsion machine. The experimental results were compared with predicted values from classical incremental theory of plasticity in terms of true stress and true strain and a recently developed incremental theory of plasticity by Bell in terms of nominal stress and nominal strain. These experimental results reveal that the plastic strain produced by the various proportionate and non-proportionate loading, unloading and reverse loading paths are in better agreement with Bell's incremental theory of plasticity as compared to classical incremental theory.

Krempel and Bordonaro [51] subjected tabular specimen of commercial Nylon 66 to non-proportional loading in strain control at room temperature. All tests were performed in a servo-hydraulic, computer controlled, MTS axial-torsion mechanical testing machine. One specimen was first loaded to a certain axial strain which was subsequently held constant while the tube was twisted. For the other specimen torsional strain was applied first followed by axial loading. They observed that the stresses at the same strain point were found to be path dependent. The stress corresponding to the strain that is kept constant drops as the other axis is being loaded. There is considerable interaction between axial and shear behaviour. The stress drop can be a "plasticity effect" or regular relaxation.

One of the main applications of this type of combined loading, where solid rods are subjected to combined torque and tension, is in the development of fasteners. As it is well known that during the tightening process a fastener is subjected to both torsional and axial stress applied simultaneously. Subsequently, when the assembly or the joint

is subjected to external load, the fastener is subjected to additional axial stress or axial and bending stress. Most of theoretical and experimental investigations within this area have been conducted for the purpose of improving the performance and reliability of the fasteners and their joints. Experimental investigations of the behaviour of bolted joints (i.e. solid bars) in the elastic and plastic region have been carried out by Maruyama and Nakagawa [52]. The direct tension test of the bolt under uniaxial load firstly was carried out, then the bolted joint was tightened in elastic or plastic region and the axial load was applied to that tightened joint after screwing the joint to a material testing machine. In other similar test, the bolt was tightened at first to a certain torque and then the torque in the threaded portion was reduced to zero, this done by untightening the bolt by a few degrees. Then the axial load was applied to that pre-tightened bolted joint. The results showed that the threaded part torque has a little influence on the axial tension-elongation curve, and the curve under external loading approached rapidly the curve of the single bolt regardless of whether or not the torsional stresses were eliminated by joint spring back or backward rotation before the external load was applied. It was also found that when bolts were tightened into the plastic region, the joint can withstand higher working loads.

The factors affecting the torque-tension relationships of fasteners during the tightening process were investigated by Gardiner [53]. This relationship is governed by both direct and indirect parameters. The direct parameters consist of tangible items, such as fastener strength level, surface finishes, hardness of the components, lubrication, class of thread fit and resiliency of the clamped assembly. The indirect parameters which affect this relationship are not related to assembly materials, but to assembly methods. The fasteners were tightened using zinc plated and cadmium plated nuts and found that the torque needed to reach a similar load was almost twice as much for the zinc plated hardware than for the cadmium plated one.

Hariri [54] carried out experimental investigations to determine the response of fasteners to combined torque and axial load. The bolts were initially pre-torqued in the elastic range by an electronic hand torque wrench and then external tensile loads

were applied holding angle of twist constant. The uniaxial tensile load was applied by a hydraulic cylinder. The results showed that the torque started decreasing when the combined stresses in the bolt reached the yield stress in tension.

The behaviour of bolted joints tightened in to the plastic region has been investigated by Tsuji and Maruyama [55,56]. A new estimation method for the interaction curve of the threaded portion is proposed based on the flow theory [55]. They developed a combined load testing machine in order to apply the tensile and torsional combined load on the threaded portion of the bolt, and the interaction curves of the threaded portion are obtained experimentally. In their conclusion, it is shown that the new method is superior to the traditional one considering only the local yield condition.

The static and dynamic strength of bolted joint tightening the bolts to their yield points was investigated by Chapman et al [57]. A series of bolts were tightened to their torque-tension yield points with the SPS joint control system, and then external tensile load was applied until the bolts failed. They found that all bolts behaved elastically when external loads were applied to the joints even when the fasteners were tightened to their torque-tension yield points. Dynamic test results showed that fatigue strength increased with the preload and high fatigue bolts gave an improvement over standard fasteners at all preloads.

2.3 Finite Element Simulation Studies

During the last two decades considerable advances have been made in the application techniques to analyse basic structural elements as well as highly sophisticated structures in various fields of engineering. Among these numerical procedures, the finite element methods are the most frequently used today. Finite element analysis (FEA) of structures plays an increasingly important role in engineering practice. In general, finite element analysis is a powerful tool in predicting the loads and deformation of structural members. The extensive application of the finite element

method analysis has now become possible by using relevant software packages for numerical simulation

A number of simulation works concerned with analysis of different engineering applications have been reported. The effect of cross section variation on formability of prestrained samples has been investigated using finite element analysis simulations of a standard sheet tensile test by Menezes et al [58]. The finite element code was used to simulate the uniaxial tensile test in reloading of sheet samples with different pre-strained values using a modified Swift law that describes the material behaviour after prestrain history. The simulations presented in this investigation are in good agreement with experimental evidence which attest the good behaviour of the modified Swift law developed, and also the good performance of the finite element code used.

Tsukahara and Lung [59] showed that the finite element method (FEM) can be used to simulate the localisation phenomenon of Portier-Luders behaviour in an uniaxial tensile test. To simulate this phenomenon, the finite element code Abaqus version 5.6 has been used.

Dumoulin et al [60] determined the equivalent stress-equivalent strain relationship, using a tensile test on copper specimen. Image analysis and a conventional extensometer are used for strain measurements. Then this equivalent stress-equivalent strain is used in a finite element code to simulate the same tensile test. This simulation validates the image analysis measurement all the more since the strain levels simulated are identical to the experimental ones, until the onset of transversal necking.

Pietrzyk [61] reviewed applications of the rigid-plastic finite element approach to the simulation of metal forming processes involving large plastic deformation. The analysis of the rigid plastic finite element approach was the objective of this work. It

recapitulates the research on the finite element modelling of large plastic deformation problems

The elasto-plastic finite element simulations of the plastic deformation behaviour of copper samples during torsional deformation have been carried out by Kim [62] using the commercial finite element code, Abaqus. In another study by Kim [63] and Kim et al [64], the results of the elasto-plastic finite element analysis of the plastic deformation behaviour of bulk nano-structured materials during torsion straining process have been presented. The simulated geometry (thickness distribution) of the workpiece is compared with previous experimental data obtained using copper specimens with different number of rotations.

Savaidis et al [65,66] performed an elastic-plastic finite element analysis for a notched shaft subjected to multi-axial non-proportional synchronic tension/torsion loading. The elastic-plastic material property is described by the von Mises yield criterion and the kinematic hardening rule of Prager/Ziegler. The finite element code Abaqus is used to solve the boundary value problem. They also considered combined tension/torsion loading in reference [66].

A three dimensional model of a twisted cord embedded in rubber matrix was investigated by Pıdapartı et al [67] to estimate the interface stresses. Finite element analysis was performed on the models under axial and combined axial and lateral loading using the finite element analysis package ANSYS. The deformations and maximum interface stresses were obtained from the finite element analysis. The results obtained from the present analysis were validated with existing solutions in the literature.

CHAPTER THREE

EXPERIMENTAL SET UP

3.1 INTRODUCTION

Mathematical theories of plasticity have received considerable development in the past few decades with major analytical contributions from many well known workers. However, the quantity of suitably accurate experimental work, carried out to examine the validity of the theories appear to be quite limited and adequate evaluation had not been always possible. As the theories have increased in sophistication the accuracy with which the experiments must be performed has also increased. The application and measurement of stresses and strains must be determined to a high degree of accuracy.

Previous workers, utilizing hydraulic and mechanical systems, have used various methods of applying torque and axial load. The straining mechanisms can be categorised as providing direct control of either strain or load (or torque) and the manner in which the experiment is conducted is determined by this. As part of this research work an instrumented mechanical torque-tension machine was used to enable the application of the combined torque and tension loading under controlled conditions.

The machine is controlled from a remote personal computer using Labview software and data acquisition devices. Four transducers were used to measure the axial load, the axial displacement, the torque and the angle of twist. The measured units were then amplified with a modular amplifier and fed to the Lab view for control and display. A closed loop is created with Lab view, as the programme takes action according to the signals from the transducers. These inputs from the transducers were recorded as a database for analysis. The tension-torsion experimental set up is shown in figure 3.1.

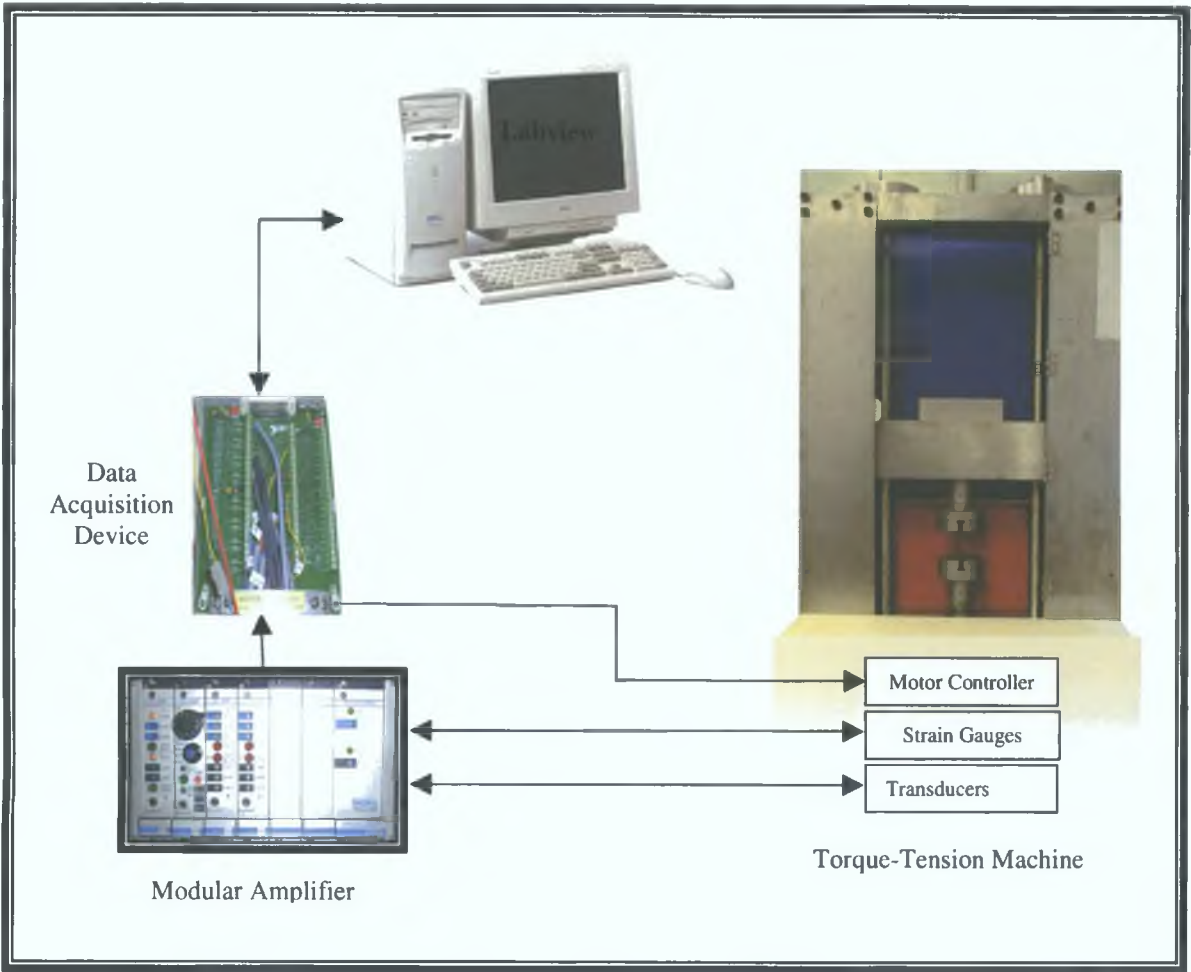


Figure 3.1 Tension- torsion experimental set up

3.2 TORQUE-TENSION MACHINE

The servo-controlled instrumented torque-tension machine is capable of applying combined loads (i.e., torque and tension) under controlled conditions. The machine was designed to carry a maximum tensile load of 100 kN and a torque of 200 Nm. The stiffness of the machine is approximately 41.5 kN/mm. The overall length, width, and height of the machine are 0.48m, 1.00m, and 1.96m respectively. The main features of the machine are as follows. It can apply either simultaneous or individual loading (torque and/or tension) according to a specific load programme. It facilitates the time variations of the control and the resulting deformation parameters using the appropriate load cells and control elements. The machine is controllable with either analogue or digital (from a P.C.). It is capable of maintaining different strain rates for both types of loading. Figures 3.2 and 3.3 show the details of the machine. The specifications of the machine are shown in table 3.1 in detail.

Table- 3.1 The specifications of the torque-tension machine

	Axis 1 (For tension)	Axis 2 (For torque)
Capacity		
Force rating	100kN up to 48mm/min	200Nm up to 30 ⁰ /sec
Load range(using analogue command)	3kN to 100kN	2Nm to 200Nm
Cross-head speed range	0.56mm to 48mm/min	
Drive shaft's rotational speed range		0.15 ⁰ to 30 ⁰ /sec
Cross - head alignment	0.5mm throughout full travel (no load condition)	
Cross-head travel	460cm	
Testing space	420cm	

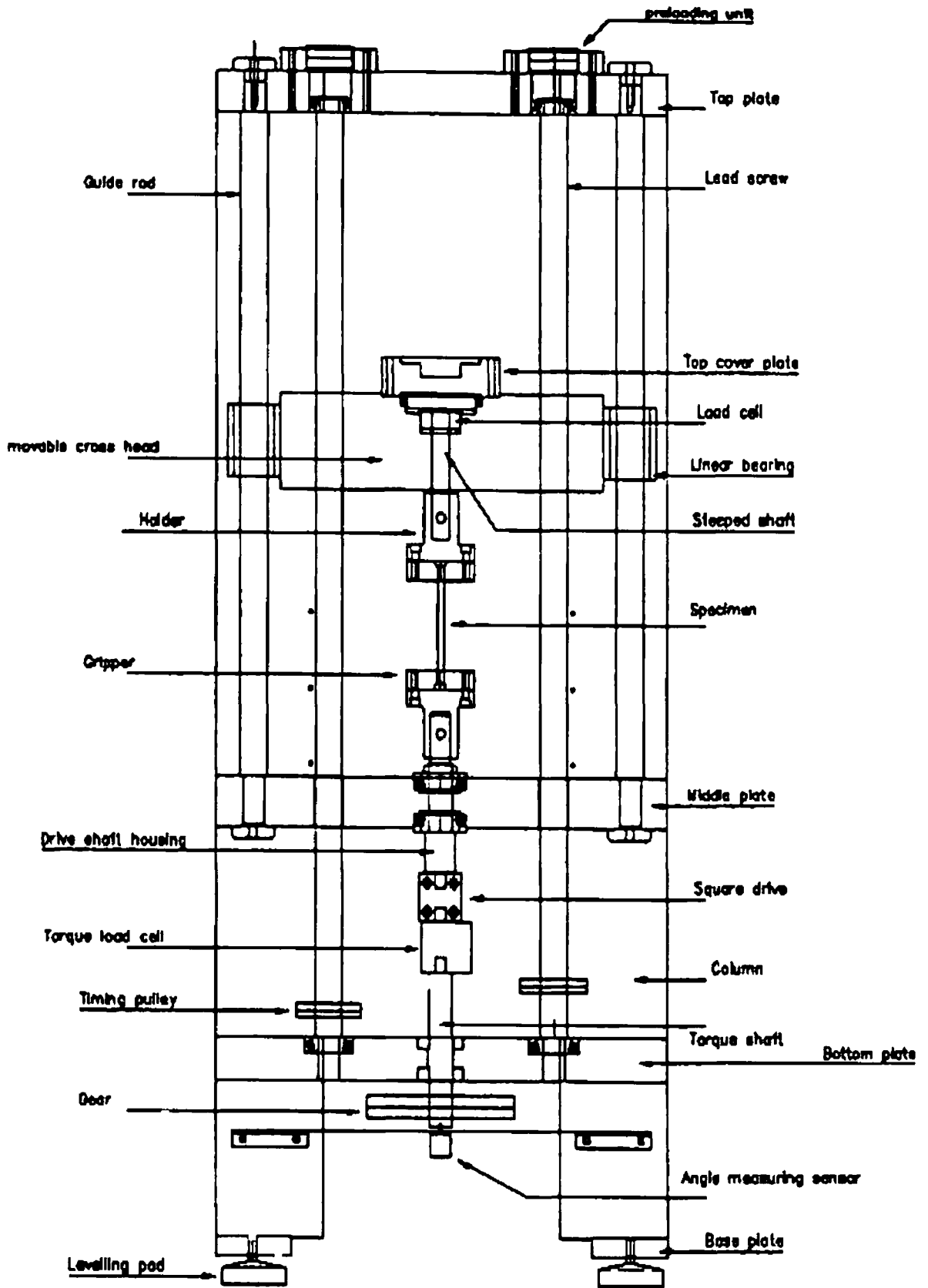


Figure 3 2 Schematic diagram of the machine (Front view)

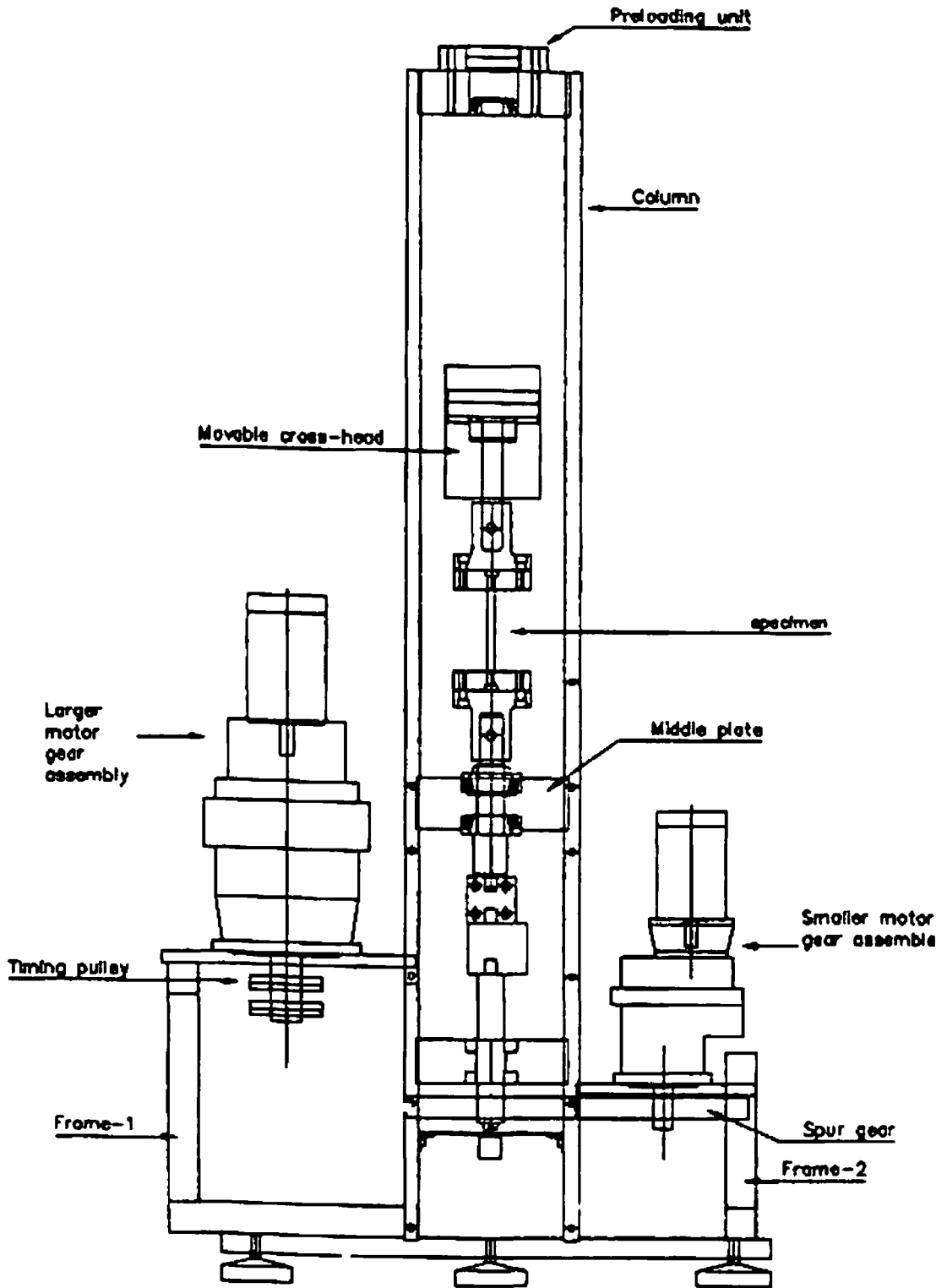


Figure 3 3 Schematic diagram of the machine (Side view)

3 2 1 MAIN COMPONENTS OF THE MACHINE

3.2.2 Ball Screw

Two induction hardened ball screws were used to drive the cross-head and apply the necessary axial load to the specimen. The long nut of each ball screw was in to the cross-head so that it attains a linear vertical motion when ever the ball screws rotate. These screws experience only compressive forces.

3.2.3 Guide Rod

Two steel shafts were chosen as guide rods. When torque is applied to the test specimen through the torque-tension shaft, the cross-head, and hence the ball screws, also experience the same torque from the resulting twisting moment. Thus the guide rods were used to prevent the ball screws from experiencing the bending forces which develop due to this twisting moment.

3 2.4 Cross-Head

The cross-head was used to apply the axial load to the specimen. It can attain linear vertical motion by the pair of ball screws.

3.2 5 Shafts

1 Three steel shafts were used in the machine for various purposes. These are as follows:

2 Stepped shaft, this shaft was used to carry the tensile as well as torsion load applied to the specimen.

3 Torque-tension shaft, this shaft transmits the torque and the axial load applied to the specimen.

Torsion shaft, this shaft is able to rotate freely about its vertical axis and helps to transmit torque from the lower portion of the machine to the upper portions.

3 2 6 Specimen Holding Devices

Two steel holders to fix the specimen in the machine, and to transmit the necessary loads. These have been designed to withstand combined torque and tensile loads applied simultaneously.

i) Gripper

Two steel grippers were used to hold the machine head of the specimens.

ii) Square Drive

A steel block of square cross-section connects the top of the torque load cell to the bottom of the torque-tension shaft. The drive experiences only the torque applied to the specimen and does not transmit any axial forces from the drive system to the mechanism.

iii) Pre-Load Unit

These pre-loading units were designed to apply a necessary pre-load to the top roller bearings fitted at both ends of the ball screws.

3 2 7 Drive System

The torque-tension machine is operated by two separate drive systems. Two "Moog" brushless servo motors of different torque capacity and two "Carl Bockwoldt" helical gear of different speed ratio. Drive system-1 provides the necessary axial load, while drive system-2 provides the necessary torque applied to the specimen. Figure 3.4 shows the schematic diagram of a Moog brushless drive system.

i) Drive System-1

Drive system-1 used to apply the axial load, which consists the following parts

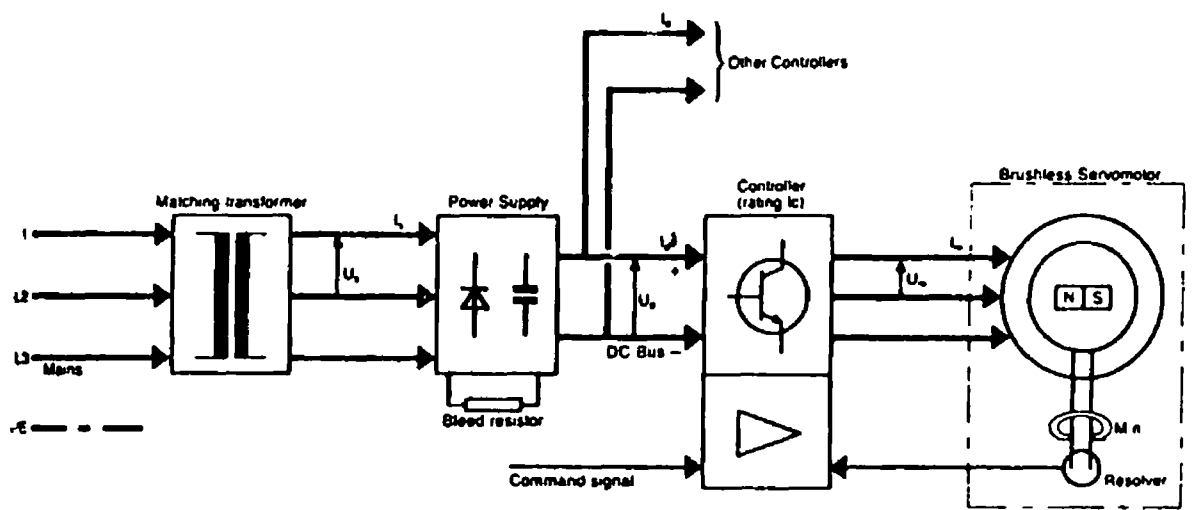


Figure 3 4 The schematic diagram of a Moog brushless drive system

Motor-1

This is a Moog D315-L15 type brushless Ac servo- motor. Figure 3.5 shows the schematic diagram of a Moog brushless servo motor. The motor has a continuous stall torque capacity of 8.1 Nm and nominal speed of 3000 rpm. The characteristic curve of this motor is shown in figure 3.6. The motor supplies the necessary torque, which is converted into the required axial force via the gear box, timing pulleys, timing belt, ball screws and cross-head.

Gear Box-1

Is a "Carl Bockweldt" three stage, CB59-NF80 type, helical gear box. Its gear ratio is 295.8 and the gear box has a maximum permissible output torque at rated power of 1200 Nm. Its maximum permissible input speed is 4000 rpm. The motor and gearbox are assembled together to form the MGA unit-1.

Timing Pulleys and Belts

The timing pulleys are made of stainless steel with steel flanges. The number of teeth of each pulley is 40. Two pulleys were keyed to the shaft of gear box-1, and one pulley to each ball screw. Figures 3.2 and 3.3 show the positions of the pulleys in gear box-1 and in the ball screws. A polyurethane "Bando" type timing belt is mated around one of the pulleys on the gear box output shaft to one of the pulleys on the ball screws. These belts are capable of transmitting approximately 30 kW with an efficiency of 98% with no slip or back lash. These belts are oil resistance, their speed can be increased up to 80 m/s and the number of teeth on each is 121. Each belt was fitted over one pair of pulleys.

11) Drive System-2

Drive system-2 provides the necessary torque applied to the specimen, it consists of the following parts:

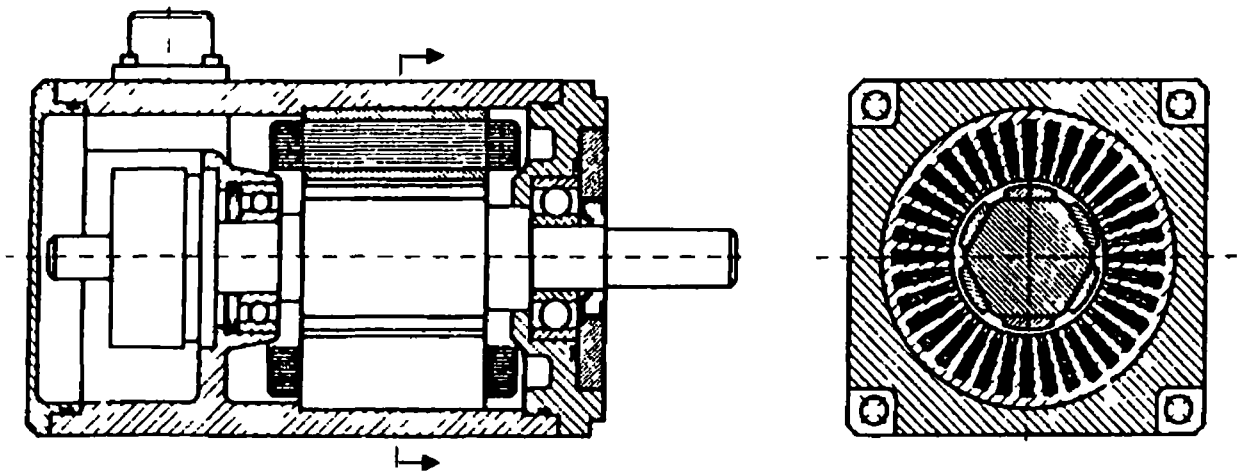


Figure 3 5 Schematic diagram of a Moog brushless servomotor

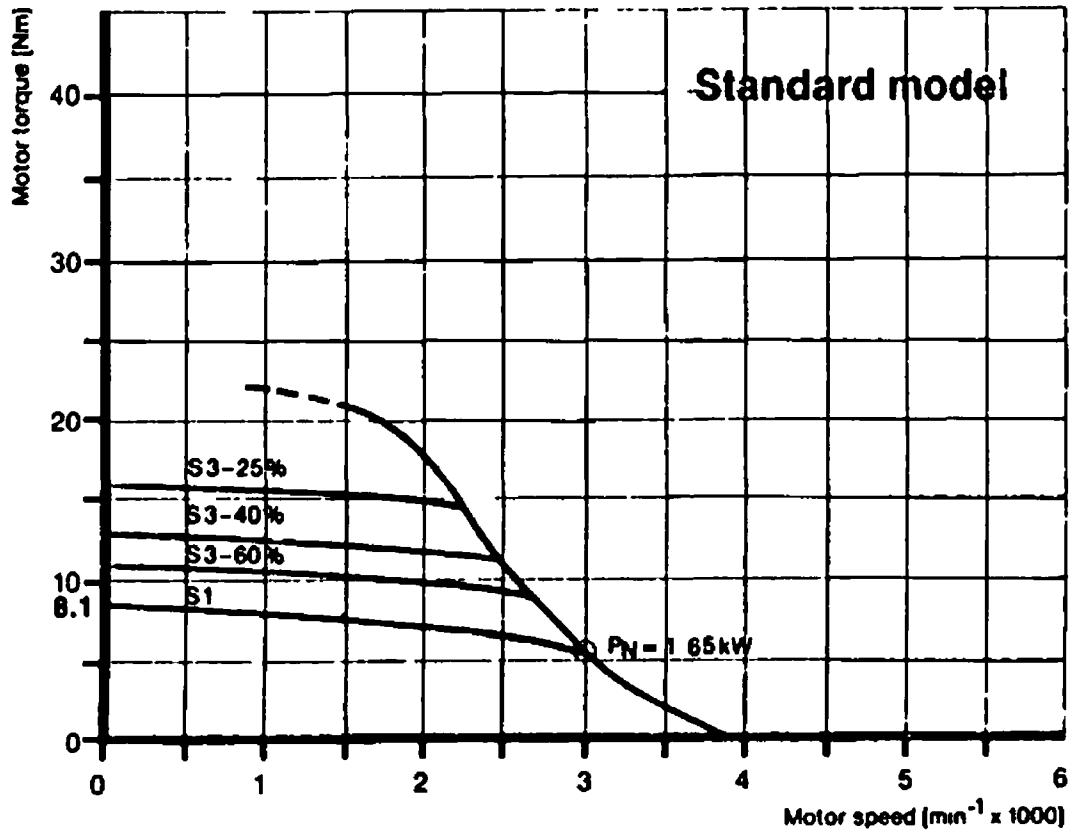


Figure 3 6 The characteristic curve of motor-1

Motor-2

A “Moog ” brushless AC servo- motor of types “D413-L10 “. This motor was assembled with gear box-2 to form the MGA unit-2. The continuous stall torque capacity of the motor is 2.7Nm and nominal speed of 4900rpm. Its continuous stall current capacity is 6.7amp. The motor’s characteristic curve (torque Vs speed) is shown in figure 3.7. This motor applies torque to the specimen through gear box-2.

Gear Box-2

This is a “Carl Bock Woldt” three stage, helical gearbox of type “CB29-NF-63 “. It was assembled with motor-2 to form the MGA unit-2. Torque from motor-2 is amplified by this gear box and is transmitted to the specimen via a pair of spur gears and a number of auxiliary parts. Its gear ratio is 150.7 and has maximum permissible output torque at rated power of 300Nm and input speed of 4000rpm.

Spur Gear

A pair of case of hardened steel spur gears of MOD3.0 and PCD 282 mm was used to transmit torque from the gear box to the torsion shaft of the machine. Their maximum power carrying capacity is 62kW at 1000rpm. One spur gear was keyed to the output shaft of the gearbox and the other to the end of the torsion shaft. Torque from the MGA unit-2 is transmitted to the torsion shaft via this pair of gears, and from there to the square drive and then to the torque-tension shaft, and eventually to the specimen through holder and grippers.

3.2.8 Control System

Two identical “Moog T161-003 “ brushless motor controllers together with power supply, were used to control the load and torque motors. Controller-1 operates the larger motor-gear assembly and controls the different levels of axial load and linear

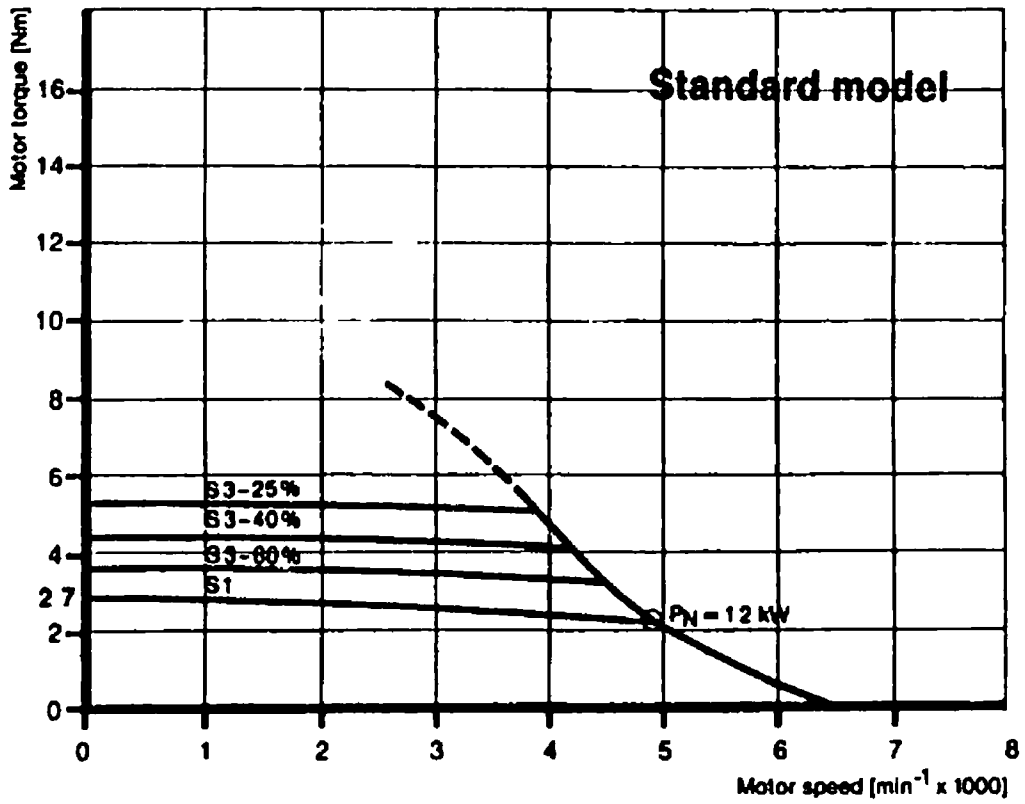


Figure 3 7 The characteristic curve of motor-2

movement of the cross-head. The controller-2 drives the smaller motor-gear assembly and controls different levels of torque and rotational speed assigned to the specimen. These controllers are controlled by a 16 bit-microprocessor, and provide full velocity servo loop closure with subordinate motor current control. Figure 3.8 shows the flow chart of the operating principal of these controllers. Power connector $\mu 6$, shown in figure 3.9, supplies power to the motors. Pin 4, 5, 6 and 7 are used. The I/O connector $\mu 5$ facilitates the reading of various I/O parameters of the motors. The input signals ($\pm 10v$) of the controllers is supplied to pin 19. At the front of the controllers, there are three status LED's to diagnose whether different system and input limits are satisfactory. Port X6 can be used to control various input/output command signals by means of a digital link from a computer. Axes enable input voltage of each controller is 15VDC

i) Controller-1

Controller-1 was used to control motor-1. Different levels of output torque from motor-1 are eventually converted to axial load via gear box-1. Rotational speed of the motor is converted to linear vertical motion of the cross-head. Control torque rotational speed of motor-1, by controller-1 means control of axial load, applied to the specimen, and the vertical linear movement of the cross-head. Clockwise rotation of the motor causes the cross-head to move in an upward direction and counter clockwise rotation causes it to move in downward direction.

ii) Controller-2

It is used to control motor-2 and hence MGA unit-2. Different levels of output torque from motor-2 are eventually transmitted to the specimen, as pure torque, via its corresponding gear box. Thus control of torque and velocity of motor-2 means the control of torque and rotational speed transmitted to the specimen. The control of clockwise and counter clockwise rotation of motor-2 means the control of counterclockwise and clockwise rotation of the specimen respectively.

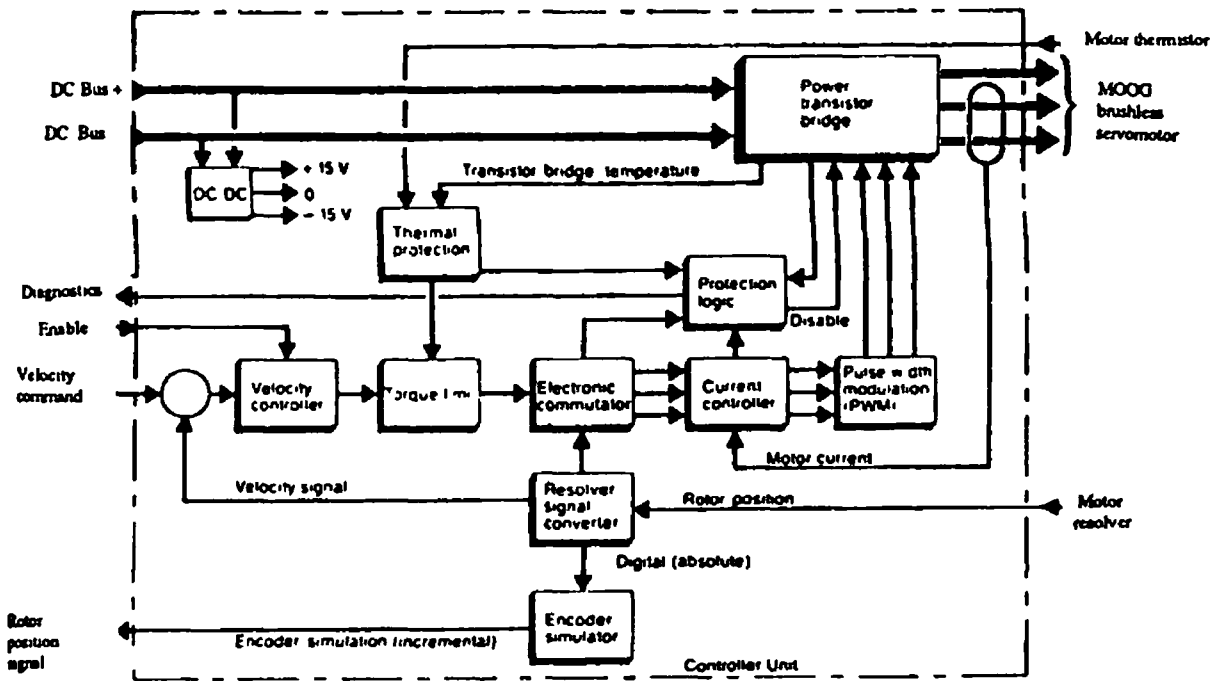


Figure 3 8 The flow chart of the operation principle of the controllers

iii) Interface Connector

At the front panel of each controller there is a connector (X6) which is used for interfacing the controllers with a personal computer. The controllers were manufactured to interface with a computer via an RS232 serial link.

iv) Power Supply Unit

One Moog motor-controller power supply unit type (160-003) is used to supply the main power to both controllers and both motors. This single-phase power supply unit has a continuous power supply capacity of 1.5kW. Nominal input voltage is 230VAC, 44-66Hz. It can supply power up to six controllers and it has an integrated bleed resistor to dissipate excess motor energy during motor regeneration and therefore avoids an unacceptable increase in the DC voltage. At the back panel, there are several input/output connectors including AC power connector (X3), external bleed resistor connector (X4), power supply signal and I/O connector (X5), serial interface connector (X6), DC bus connector (X7) and fan connector (X9). In the low voltage power and status connector 'X5, there are a number centralized power supplies such as +15VDC-2A line, -15VDC-2A line, +5VDC-7.5A line, etc. to supply power to other external devices if necessary. The +15VDC-2A line (pin9) was utilized to power the hardware of the motors. The 5VDC line (pin8) was used for digital input signals.

3.2.9 Connections

The following additional connections, besides the built in connections in each device, were made to the power supply for both motors and controllers.

i) Power Supply

The main 220VAC input is fed into the power supply via its back plane connector (X3). Various outputs from the back plane connector (X5) were set up for the

following purposes The +5VDC output from pin 8 and digital ground connection from pin 12 are used as a signal digital input signals to select different modes of operation of the motors, such as, run or hold mode, forward or reverse mode, etc From each of these pins, four parallel lines were drawn, two for each controller, and connected to four “ two way “ switches to supply either 5 or zero voltage to pin 3 and pm 6 of each X μ 7 connector The +15VDC from pin 9 was used to make the motor’s hardware “ enable “ by two ‘one way ‘ ON/OFF switches Enabling of the motors means shafts are able to turn freely with or without load, i e , commissioning of the Motor An analogue ground connection from pin 11 was used as the negative terminals of the four external power supply units A circuit diagram, including the power supply, controllers and motors, is shown in figure 3 10

n) Controllers

The two controllers have the same connections with the motors and power supply unit “ 160-003 “Power connector X μ 4 of each controller was connected with the “ 8 pole power mating connector “ of the motor Connections were made as follows

Pin No	Input reference	Wire colour
4	PE	Green/Yellow
5	W	Brown
6	V	Blue
7	U	Black

A resolver connector X μ 6 of each controller was connected with the “12 pole signal mating connector “of the motors

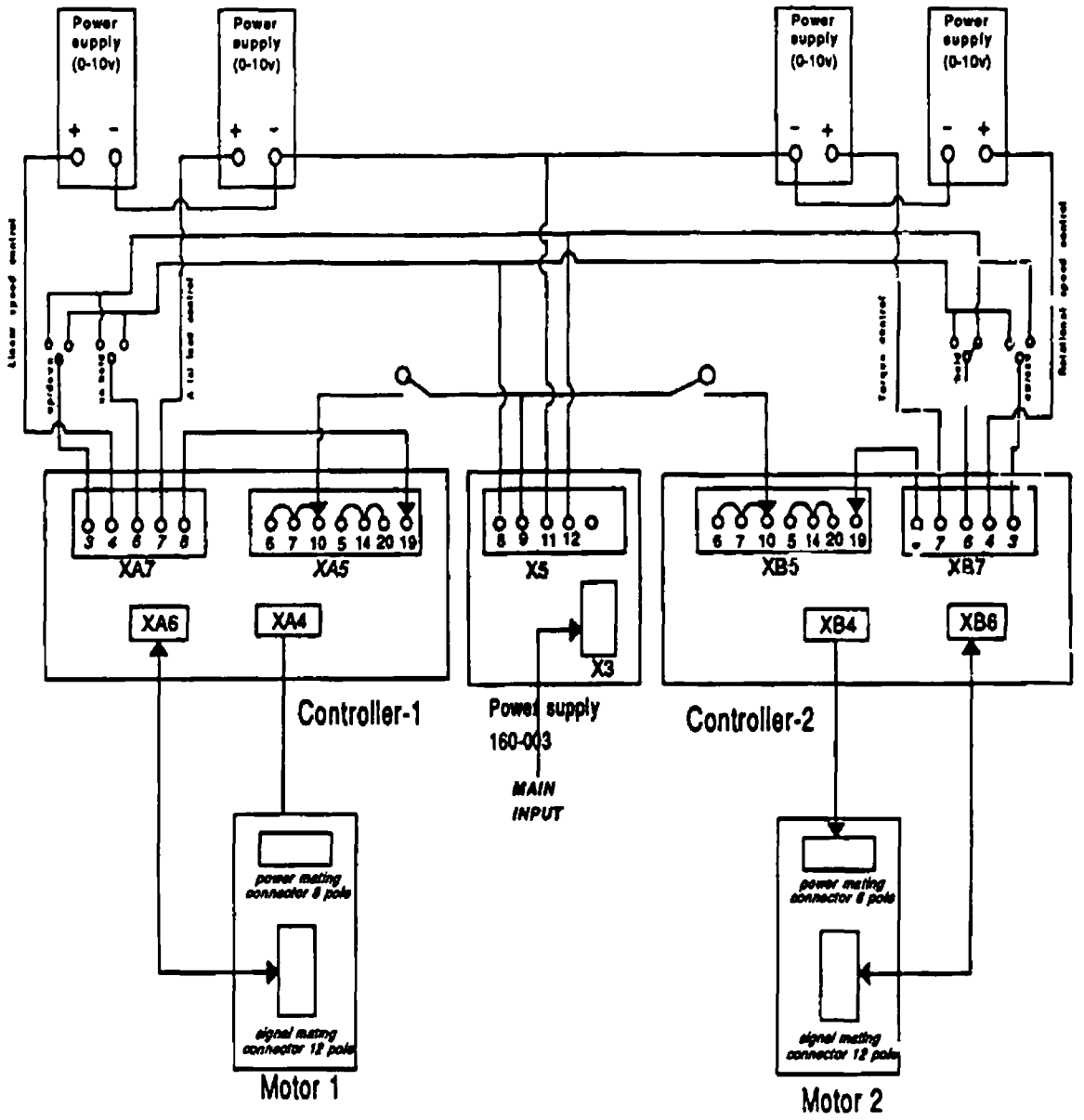


Figure 3 10 Circuit diagram among the controllers and the motors

3.2.10 DATA ACQUISITION SYSTEM

For the present set up, a number of external sensors were attached in the vicinity of the specimen. The outputs from these transducers are read by common "RDP" amplifier Module 600. The devices used for data acquisition from the machine are as follows:

i) Axial Load Cell

A donut shaped, 133.5 kN capacity, compression type load cell used to measure the applied axial load. This load cell has bonded foil type strain gauges, its maximum excitation voltage is 10.0 VDC and full scale non-linearity is $\pm 0.5\%$. The output for full scale deflection for a 10 VDC excitation is 28.945 mV, response of this load cell is 0.21681 mV/kN.

Connection

The four coloured cables of the load cell represent the following connection:

RED	(+) Excitation
BLACK	(-) Excitation
GREEN	(-) Output
White	(+) Output

ii) Torque Load Cell

To measure the torque applied to the specimen a "Norbar" rotary type torque transducer of 500 Nm capacity was used. It is a strain gauged torsion bar made from heat-treated alloy. It has a full bridge arrangement for maximum signal output and temperature stability. It can measure both static and dynamic loads and can operate in both directions, i.e., clockwise and counter clockwise directions. The maximum

bridge excitation voltage of this load cell is 10V and has been calibrated up to 200Nm. Its output for a full scale deflection is 8.17mv, i.e., 0.0408mv/Nm torque applied. The top of the load cell is connected to the bottom gripper shaft and the bottom of the load cell is connected to the torsion shaft. It has a centre shaft which rotates with the torsion shaft and the outside housing measures the torque of the shaft.

Connection

Various pins of the load cell were connected with the amplifier as follows

Pin no.	Connection to
F	Excitation +ve
D	Excitation -ve
A	Signal (+)
B	Signal (-)

iii) Angular Position Transducer

The angular position transducer is used to measure the resulting angle of twist of the specimen. It is a D.C/D.C angular position transducer. It is basically a transformer in which the output is governed by the angular position of the input shaft in relation to the transducer body. The output is electrically isolated from the input. The output reading is 33mv/degree rotation of its shaft for a 10VDC input. This transducer can rotate 360 degrees mechanical angle continuously. Its effective electrical angle is 300 degrees, and the residual voltage is maximum at zero degree arc and its value is 50mv, i.e., output voltage is linear from 50mv up to 995mv. The transducer shaft is screwed in to a small hole on the end of the torsion shaft and experiences the same

angle of twist as the torsion shaft. The output is determined by the position of the shaft inside the transducer. As the shaft turns the position is read in binary and outputted in volts. Figure 3.11 shows the characteristic curve of the angle measuring transducer. The residual voltage is maximum at zero degree arc and its value is 50mv, i.e., output voltage is linear from 50mv up to 995mv ($33\text{mv/deg} \times 300\text{ deg} + 50\text{mv} = 995\text{mv}$). Output increases for clockwise rotation of the shaft. The maximum non-linearity is $\pm 0.5\%$ of full scale.

Connection

Pin colour	Connection
RED	Excitation (+ve)
BLCK	Excitation (-ve)
BROWN	Signal (+)
BLUE	Signal (-)

iii) Linear Variable Displacement Transducer (LVDT)

The linear velocity displacement transducer of 26mm stroke length capacity was used to measure the total deformation of the specimen along the axial direction. The LVDT is positioned on the frame of the tension-torque machine, before conducting the test, to measure the movement of the cross-head as the load increases or decreases.

3.2.11 Modular Amplifier

The RDP Module 600 is an Eurocard based system and provides conditioning for a number of different transducers types including strain gauge transducer, LVDT, strain gauge, voltage and current inputs and linearisation for RDP non-contact inductive sensors. The front panel controls include fine gain, zero and excitation with

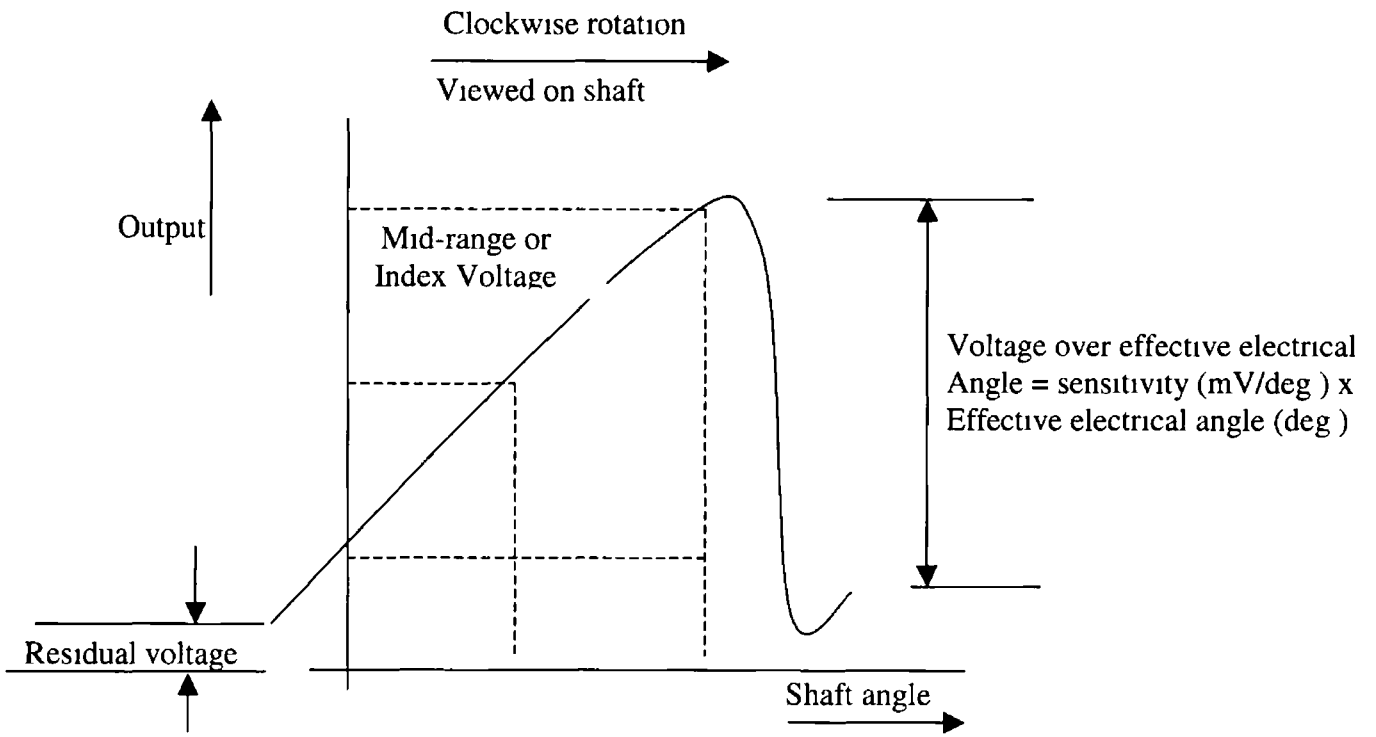


Figure 3 11 The output characteristic curve of the angle measuring transducer

a push button for shunt calibration. The modular system includes a housing, powersupply and transducer conditioning modules. The modular amplifier is shown in figure 3.12.

i) Module 611

The RDP 611 strain gauge signal conditioning amplifier module is part of the modular 600 system. It is designed for use with strain gauge and DC type transducers. The module has dual channels and provides the excitation for the bridge as well as precision amplification, and also provides a shunt calibration facility. The torque and load cell were excited and the output signal from the transducers were conditioned and amplified in this module before they were sent to Labview.

ii) Module 621

The RDP 621 LVDT amplifier is a dual channel amplifier for the use with LVDT and inductive type displacement transducers. It provides the excitation to the transducer and conditions the return signal. The amplifier has outputs of both voltage and 4-20mA, a broad range of adjustments ensures that the voltage and 4-20mA outputs may be calibrated over all or just parts of the transducer range.

iii) Module 628

The RDP 628 strain gauge signal-conditioning amplifier provides precision amplification and calibration of strain gauges outputs. The RDP module 628 is part of the modular 600 system and the module is designed to work with quarter, half and full bridge gauges and features gauge factor selection and switchable micro-strain ranges, and is calibrated for use with gauges of known gauge factor.

iv) Module 631

The RDP 631 module provides power to the modular 600 system busses enabling the amplifier to pick up their power at the appropriate positions. The a.c supply to the module 631 is via a standard a.c lead, which plugs into the back of the modular 600 system housing.

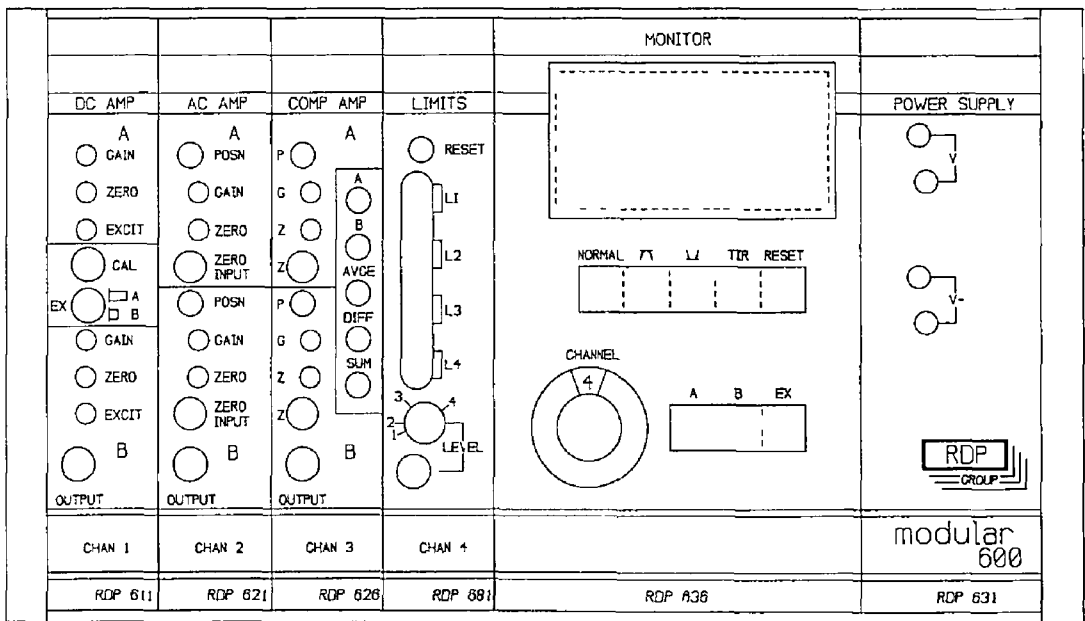


Figure 3 12 Typical Modular 600 System

3.3 LABVIEW PROGRAMME

LabView by National Instruments [69] is an advanced general purpose programming tool for data acquisition, analysis and instrument control. LabView (an acronym standing for laboratory virtual instrumentation and engineering work bench) is a graphical programming environment. It is designed for communication with hardware such as IEEE 488 (GPIB), PXI, RS232, and plug-in data acquisition cards. A program in LabView is called a VI (virtual instrument) and consists of two windows, the front panel and the block diagram. The front panel is the graphical user interface (GUI) of the virtual instrument. It contains control items such as knobs, buttons, slides and switches as well as graphical outputs that have the appearance of an actual instrument. This interface collects user input and displays programme output. The block diagram is the graphical representation of the programme code, which contains the graphical source code of the virtual instrument. In the block diagram the virtual instrument is programmed to control and perform functions on the input and present the output which created on the front panel. LabView has three palette sets, tools palette, control palette, and functions palette. The tools palette contains tools to edit and debug the front panel and the block diagram objects. The control palette contains the front panel control and indicator objects, which used to create the user interface. The functions palette contains the objects used to programme the virtual instrument and to build the source code.

The programme developed in this work was built to independently control the speed and direction of the two servo-motors. The program also acquired data from the transducers (axial load cell, torque load cell, angular position transducer, and LVDT). One of the two servo motors was used for the movement of the cross-head up and down to apply the axial load to the specimen while the other motor was used to apply torque to the specimen. These transducers produced milli-volt readings, which were amplified with a modular amplifier and were recorded in the LabView programme which was executed in a closed loop. From the front panel of the virtual instrument, the machine is operated and the signals from the transducers are recorded.

and used to control the further execution of the programme. Four different virtual instruments were built for the four different modes of loading the specimen,

- i) Keeping the axial load constant, while increasing torque
- ii) Keeping the axial displacement constant, while increasing torque
- iii) Keeping the angle of twist constant, while increasing axial load
- iv) Keeping the torque constant, while increasing axial load

The front panel and block diagram for each loading path are shown in figures 3.13, through 3.20 respectively.

The general format for all of these programmes is similar. In this format each of these programmes are split into two sections, the first section is concerned with the machine set up before starting the test. It has a variable voltage knob for each motor to adjust the position of the grippers to insert and remove the specimen, and an on/off switch to run the motor and a reset switch to reset the voltage to the motor after each execution of the programme. The second section is designed to control the machine for the four different tests indicated above. It has digital indicators to show the output from the transducers and controls to set the constant parameters as per the four programmes listed above such as axial load, torque, axial displacement and angle of twist. A while loop is used to enclose all the objects in the block diagram. The while loop executed until the test was complete after which the programme was stopped. A sequence structure with two elements was placed inside the while loop. The first element was used to control the machine and the second element of the sequence was used to send the data flow to the Microsoft Excel file. In the first element of the sequence structure, a case structure was entered. A case structure has two or more sub diagrams or cases, one of which executes when the structure executes. This depends on the value of an integer, Boolean, String or enum value wired to the external side of the selection terminal or selector. For this case, the Boolean switch was used for switching between machine set up and test programme, which are

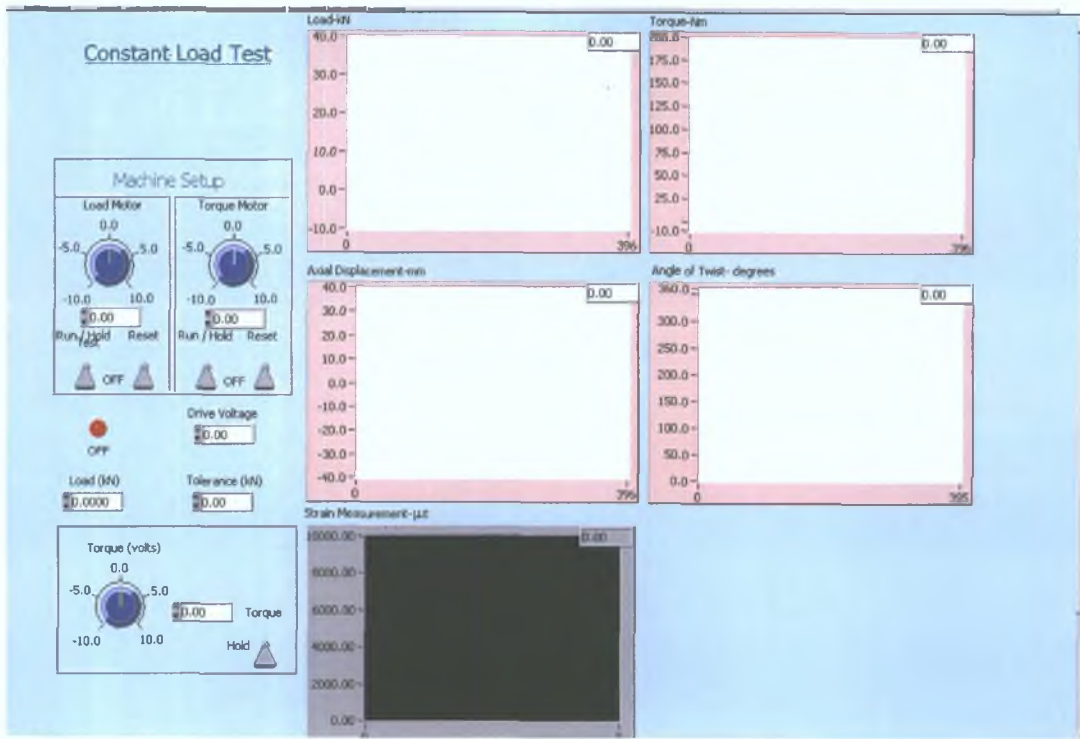
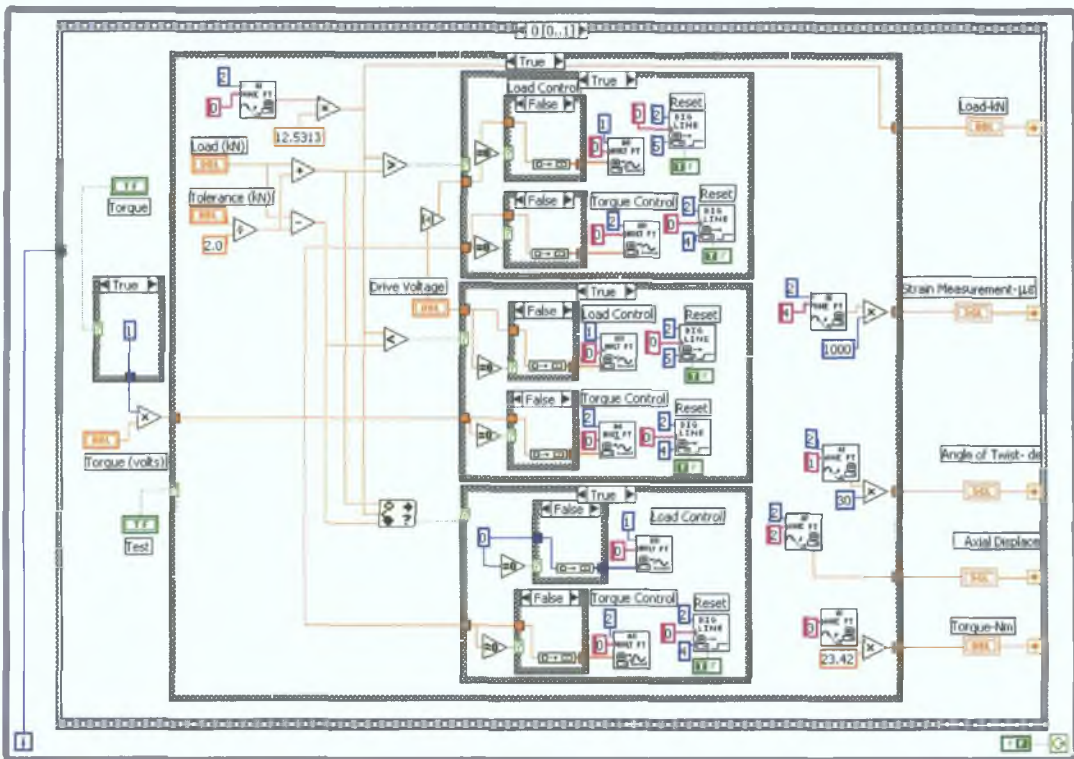


Figure 3.13 The front panel for constant axial load test



C

Figure 3.14 The block diagram for constant axial load test

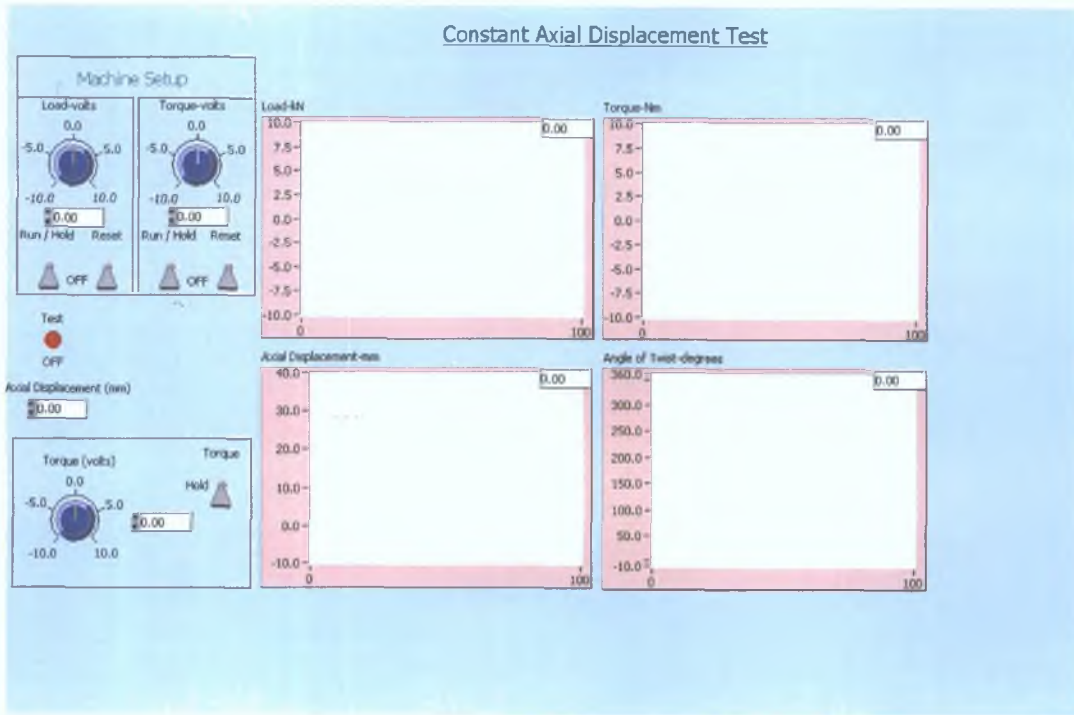


Figure 3.15 The front panel for constant axial displacement test

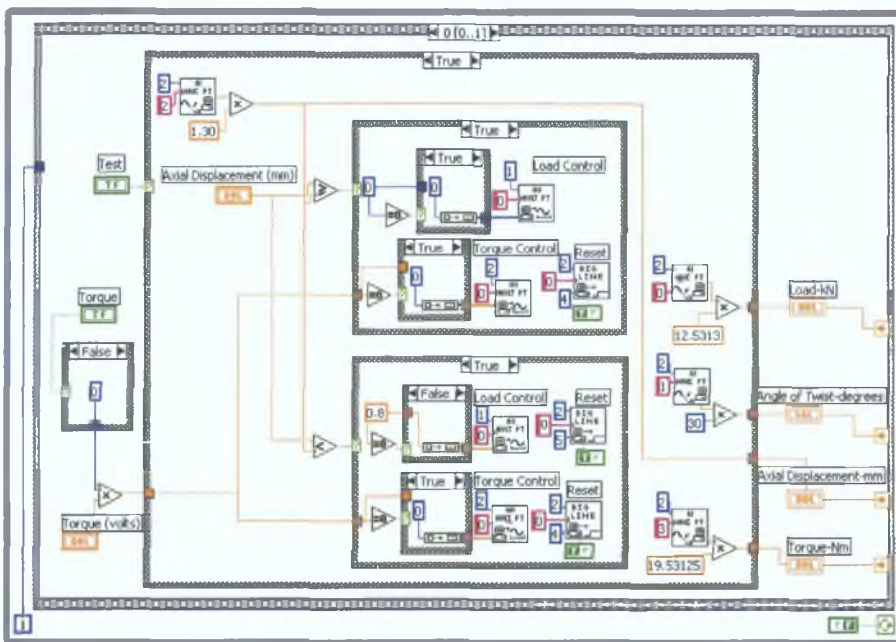


Figure 3.16 The block diagram for constant axial displacement

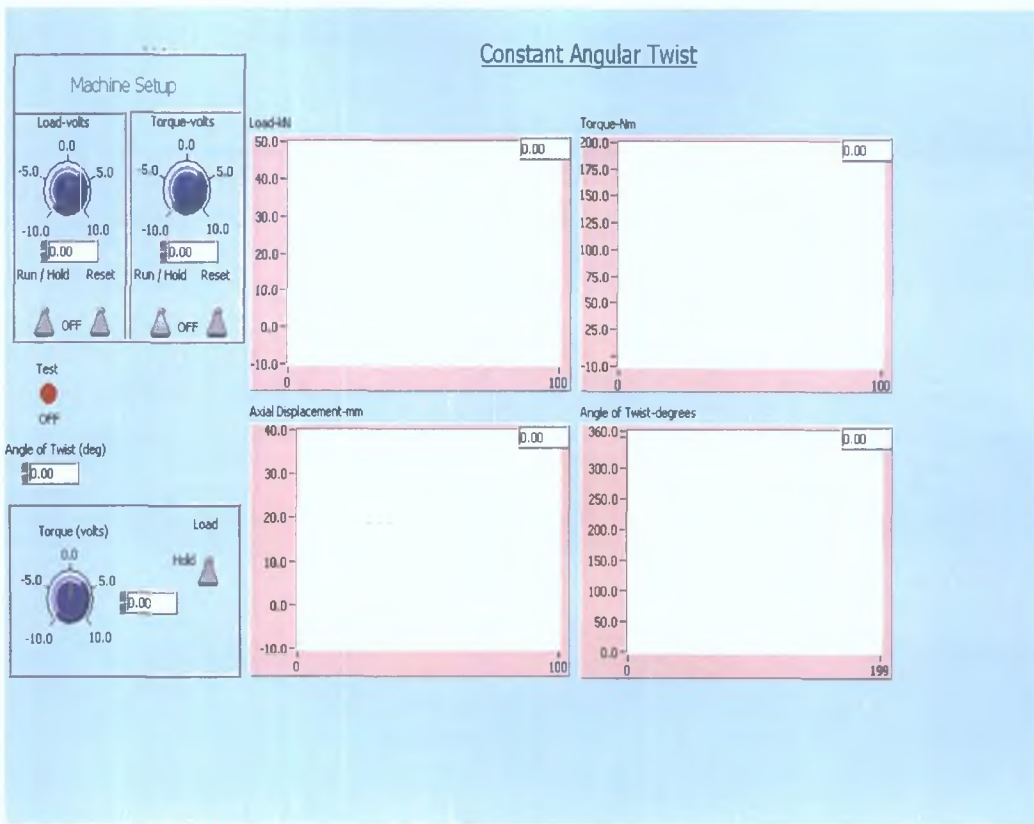


Figure 3.17 The front panel for constant angle of twist test

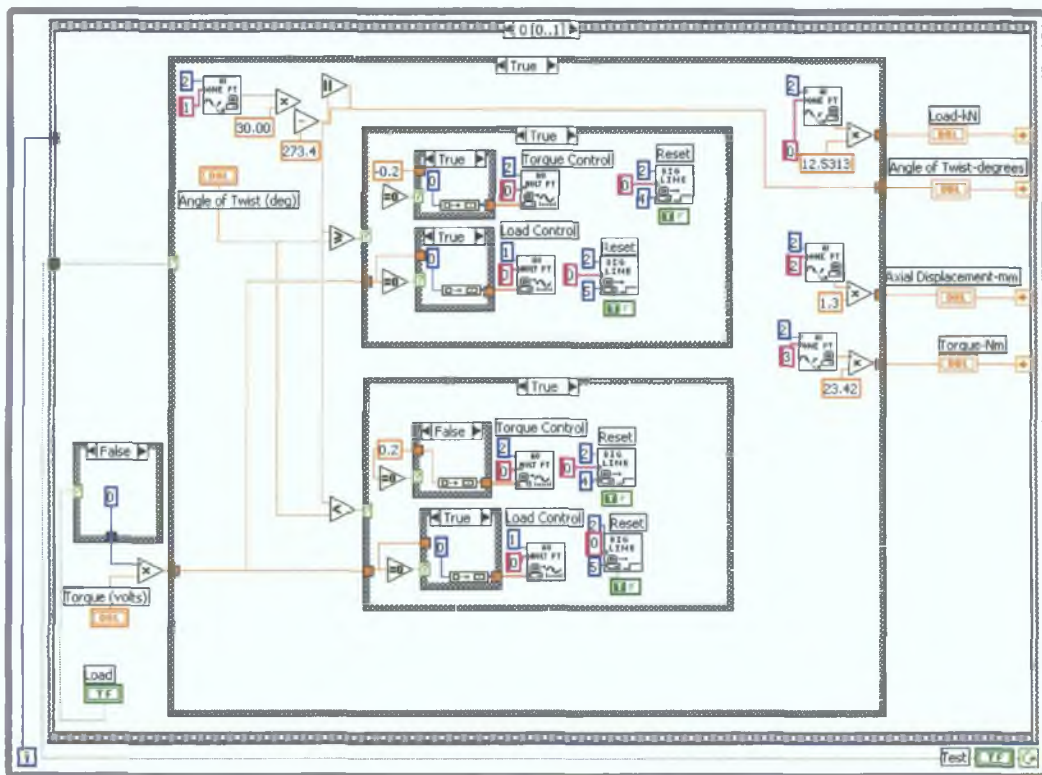


Figure 3.18 The block diagram for constant angle of twist test

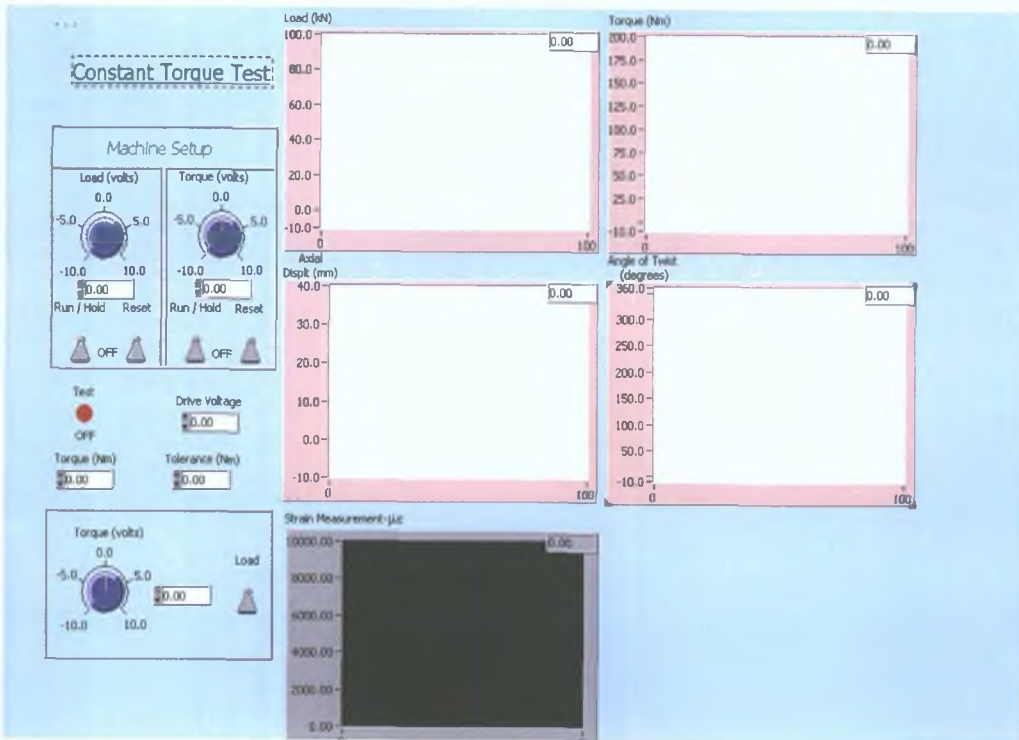


Figure 3.19 The front panel for constant torque test

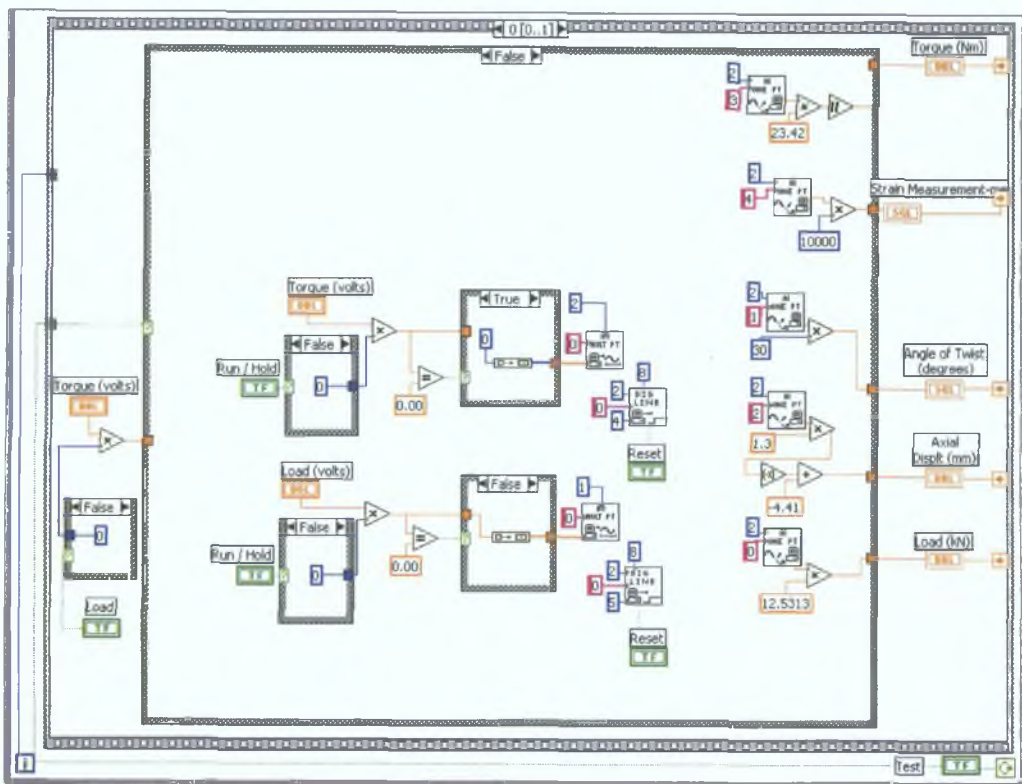


Figure 3.20 The block diagram for constant torque test

separately built in the two cases. If the test switch is on in the front panel, the control flows to the test programme, or otherwise to the machine set up. The objects necessary for operating the machine were placed in the machine set up frame, such as instrument input/output VI, data acquisition operations, file input/output VI, and arithmetic operations.

The motor is operated by two supplied voltages, one voltage to enable the motor axis and the second one to supply the voltage to run the motor at a specified speed or torque. Two case structures are used for each motor. First case structure becomes 0 or 1 depending on the position of the switch. The analogue output data acquisition VI sends the voltage to the respective motor through the data acquisition device.

Analogue input VI's are placed in the frame to read the input signals from the transducers. Each transducer is assigned a channel and all uses device2. The signal input is scaled by a factor, this factor is the gradient of the curve for each transducer during calibration. All the transducer readings are shown in the front panel in graphical form and all the data received is recorded in a Microsoft Excel file. The assigned channels for each transducer are shown in table 3.2.

Table- 3.2 the assigned channels for each transducer

Transducer	Channel number	Gradient
Axial load	0	12.5313
Axial displacement	2	1.71
Torque	3	23.42
Angle of twist	1	30
Strain	4	Depends on the scaling factor of the modular amplifier

3.2.3 DAQ Device

Two data acquisition devices AT-AO-6 and AT-MIO-16E were used to send the voltage signals to the servo motor controllers from analogue and digital output channels on the devices. Device1 is used for load motor and device2 for torque motor.

i) Device-1

The AT-AO-6 is a high performance analogue output and digital I/O board for the PC. It is a version with six analogue output channels and has six double-buffered, multiplying 12-bit DAC's uni-polar and bi-polar voltage output. Its voltage output ranges from $0 - \pm 10V$. The AT-AO-6 is designed for applications such as automation of machine and process control, instrumentation and electronic test signal generation. It is interfaced to the national instrument RTSI bus. With this bus, National instruments AT series boards can send timing signals to each other and can send signals from the on board counter/ timers to another board, or another board can send control signals to the AT-AO-6. The block diagram and I/O connector pin assignment of the board is shown in figures 3.21 and 3.22.

ii) Device-2

The AT-MIO-16E is a high-performance multi function analogue, digital and timing I/O boards for the PC AT and compatible computers. It features 12-bit and 16-bit ADC's with 16 and 64 analogue inputs, 12 DAC's with voltage outputs, 8 and 32 lines of TTL-compatible digital I/O and two 24-bit counter/timers for timing I/O. The board is easily configured and calibrated using software as the board has no DIP switches, jumpers or potentiometers. The AT-MIOE board is completely software configurable due to the DAQ-PnP features. Two types of configuration was performed on the board, bus-related configuration and data acquisition- related configuration includes setting the base I/O address, DMA channels, and interrupt channel. Data acquisition-related configuration includes such setting as analogue input polarity and range, analogue output reference source, and other settings. The board has two input polarities, unipolar and bi polar, the uni-polar input range of (0-10V) and a bipolar input range of (-5Vto+5V). The analogue output channels were configured for bipolar output as the motors should be run in either direction. The block diagram and I/O connector pin assignment of the board is shown in figures 3.23 and 3.24.

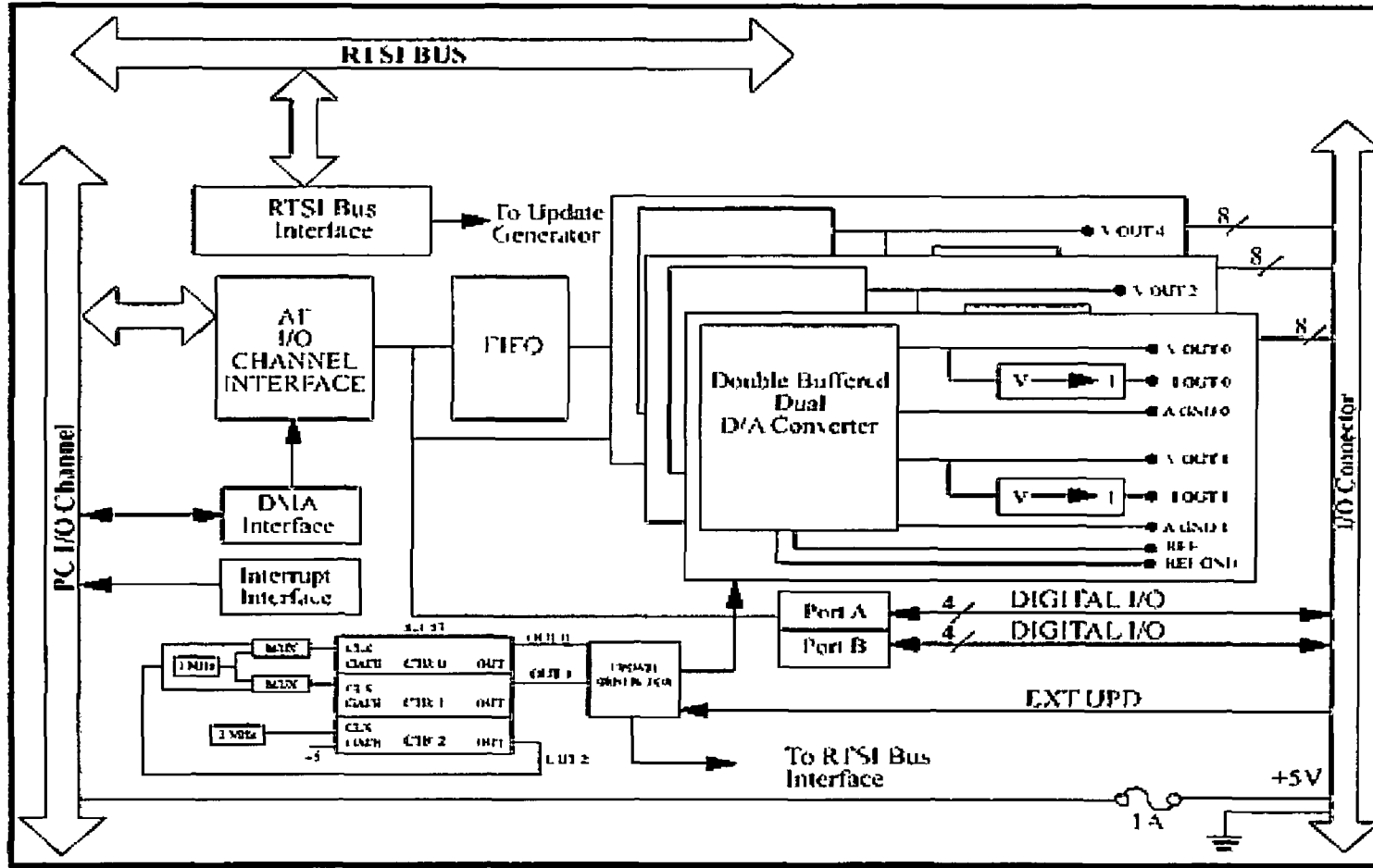


Figure 3 21 Block Diagram of Device 1 AT-AO-6

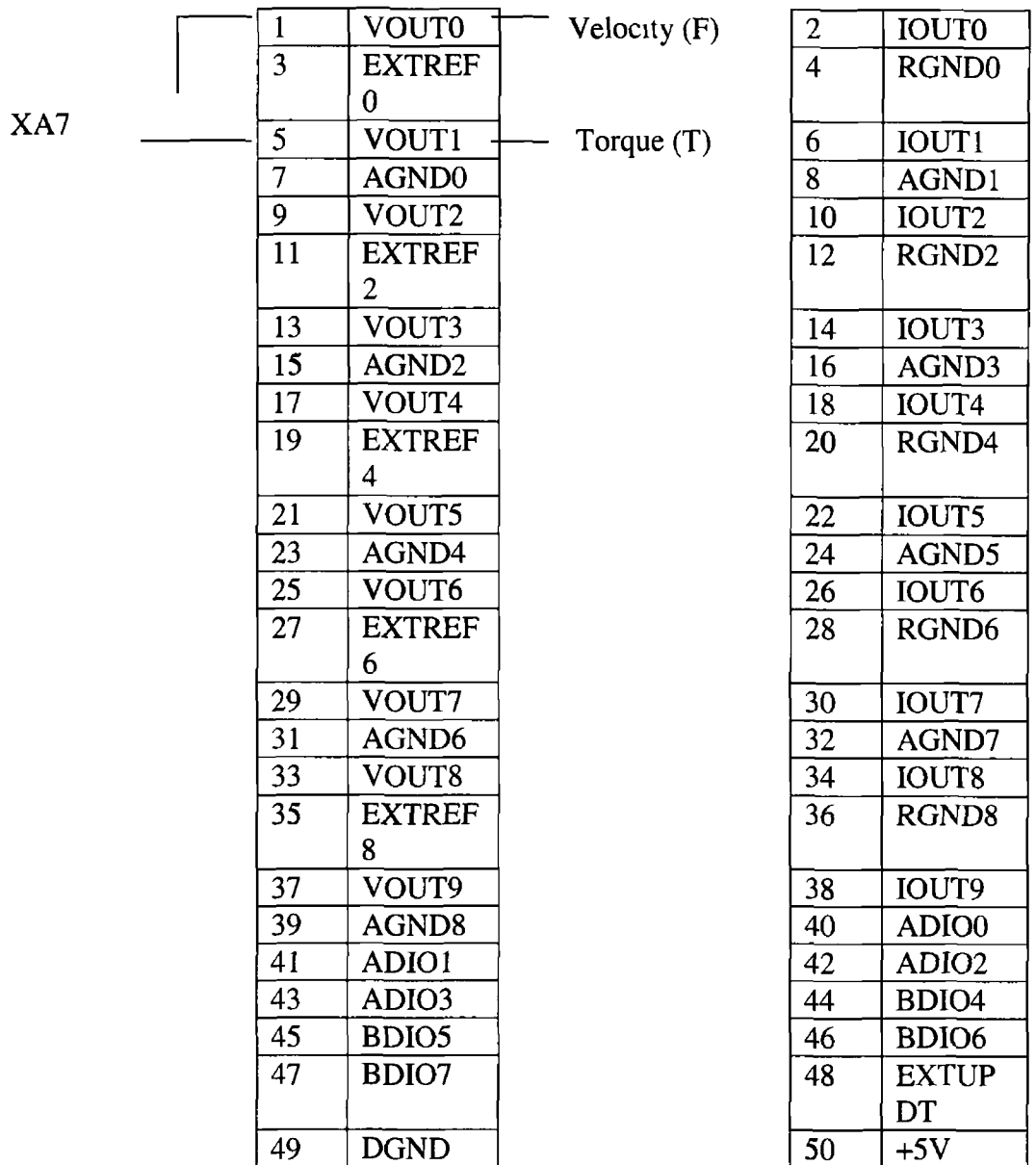


Figure 3 22 AT-AO-6 DAQ device 1

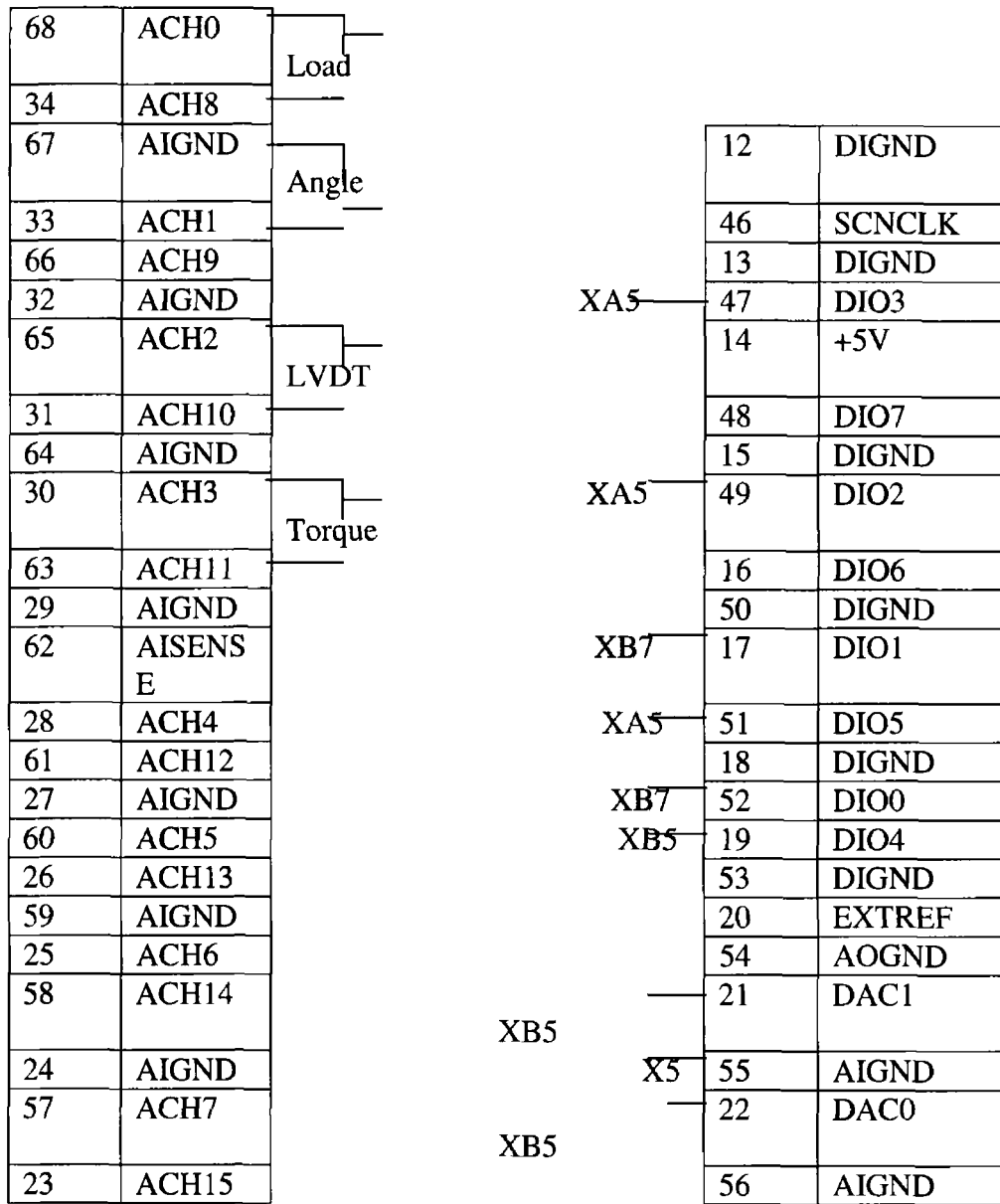


Figure 3 24 AT-MIO-16E DAQ Device 2

3.4 CALBRATION OF THE TEST MACHINE

All the transducers on the testing machine were calibrated. The axial load cell was calibrated using the Instron machine, the torque load cell was calibrated using a crane electronic digital torque wrench. The LVDT was calibrated using Instron machine, while the angular transducer was calibrated using 360 marking around the bottom gripper of the machine. The positions of the transducers are shown in figure 3.2

3.4.1 Calibration of the Axial Load Cell

This calibration was carried out by removing the axial load cell from the testing machine, then the load cell was placed in the Instron machine and then place the heads that will give an applied load on the diameter of the load cell. Calibration was set up in the labview to read the signals coming in to the analogue input channel assigned to force which is channel 0. On the front panel of the programme the input data was represented on a graph and a digital indicator gave precise readings. The amplifier module 3 band on the RDP modular 600 was removed from the amplifier to change the input range to the amplifier. This was accomplished by turning on the appropriate gain switches. The input signals was zeroed against the zero axis on the graph by adjusting the zero screw on the amplifier on the appropriate channel. Increasing loads of 5 kN were applied to the load cell on the Instron machine, the precise load applied and the input voltage from the digital indicator on the front panel was recorded for each load. These recorded values were entered into the Microsoft Excel and the data graphed to find the slope of the best fit line. The calibration curve is shown in figure 3.25 which shows a linear relationship between the load and voltage. The inverse of this slope gave the scaling factor load is 12.53kN/V

3.4.2 Calibration of the Torque Load Cell

This calibration was carried out to find the relationship between the applied torque from the torque bar and the output voltage from the transducer on the front panel

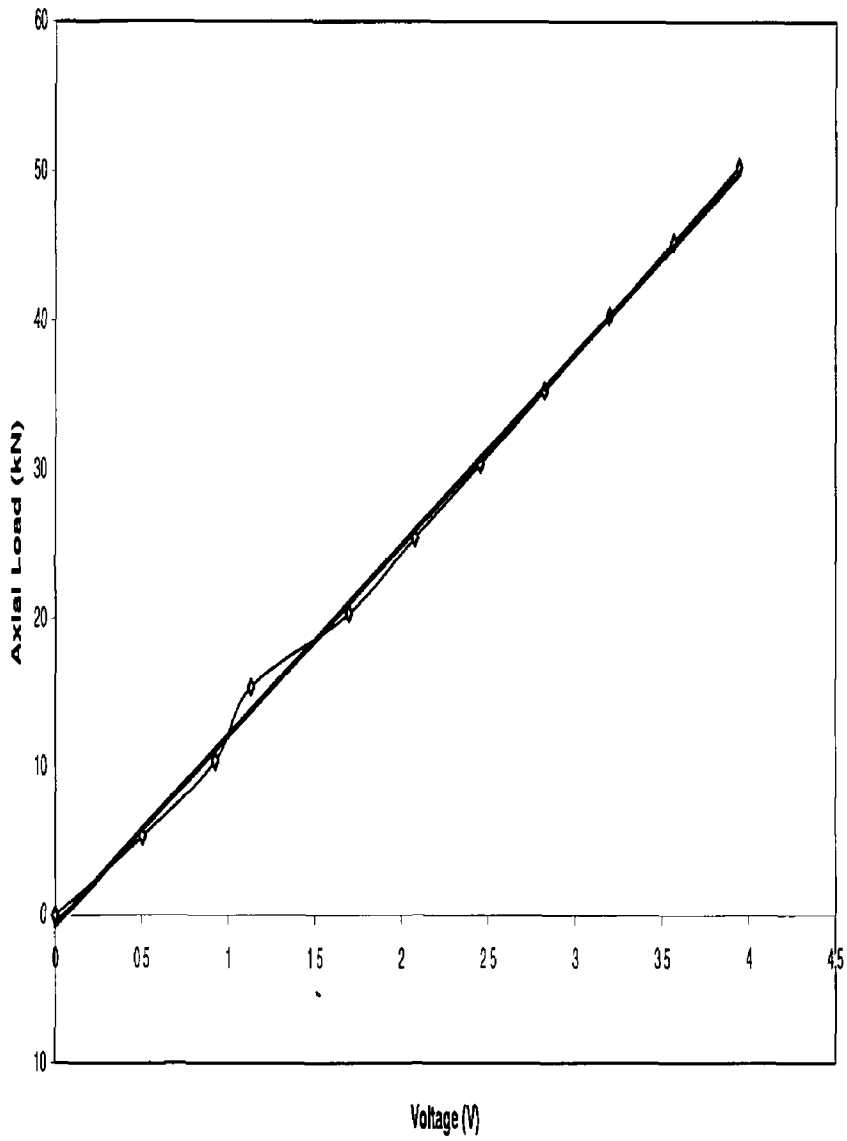


Figure 3.25 Axial load calibration curve

The bottom gripper was removed from the torque-tension machine and replaced with a plate attachment, and then the digital torque wrench was screwed to the plate until a light fit was achieved. The Labview program 'calibration' was set up to read the signal coming in to the analogue input channel assigned to torque which is channel 3. The input data on the front panel of the program was represented on a graph and a digital indicator gave precise readings. On the RDP modular 600 amplifier module 4 board was removed from the amplifier to change the input range to the amplifier, this was accomplished by turning on the appropriate gain switches. The input signal was zeroed against the zero axis on the graph by adjusting the zero screw on the amplifier on the appropriate channel. Increasing torque of 10Nm was applied to the torque-tension shaft on the machine using the torque velocity voltage control. The torque applied from the torque bar and the output voltage from the transducer on the front panel was recorded for each torque. These recorded values were entered in to Microsoft Excel and the data graphed to find the slope of the best fit line. Figure 3.26 shows the calibration curve. The inverse of this slope gave a scaling factor for torque is 23.42Nm/V.

3.4.3 Calibration of the LVDT

This calibration was carried out to find the relationship between the precise axial displacement and the input voltage from the digital indicator on the front panel. At first the LVDT was placed in the Instron machine set up with the flat heads, the labview program 'calibration' was set up to read the signals coming in to the analogue input channel assigned to LVDT which is channel 2. The input data on the front panel of the program was represented on a graph and a digital indicator gave precise readings. To change the input range to the amplifier, the RDP modular 600 amplifier module 1 board was removed from the amplifier, this was accomplished by turning on the appropriate gain switches. The input signal was zeroed against the zero axis on the graph by adjusting the zero screw on the amplifier on the appropriate channel. Increasing axial displacement of 2 and then 1mm were applied to the LVDT on the Instron machine using the plug depth gauge. The axial displacement and the input voltage from the digital indicator on the front panel was recorded for each

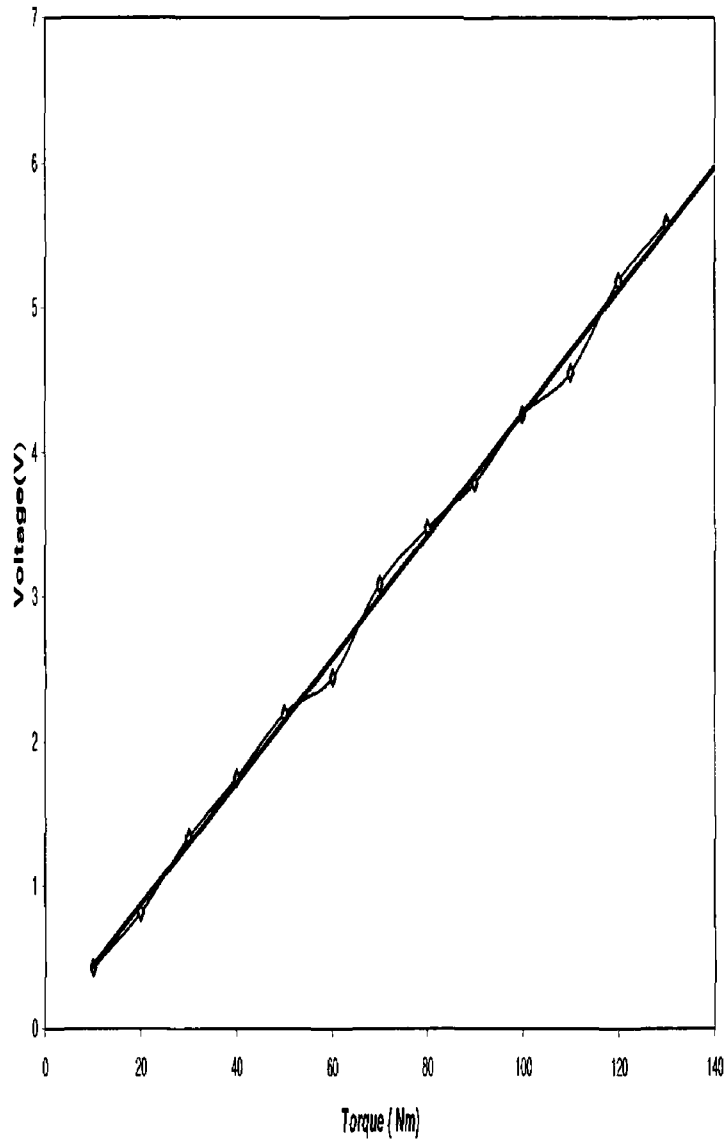


Figure 3 26 Torque load cell calibration curve

displacement. These recorded values were entered in to Microsoft Excel and the data graphed to find the best fit line. Figure 3 27 shows the calibration curve. The inverse of this slope gave the scaling factor for the LVDT is 1.71mm/V.

3 4 4 Calibration of the Angular Position Transducer

This calibration was carried out to find the relationship between the analogue command (0-10V) applied to the front panel of the Labview program and the resulting angle. 360 degree markings were placed around the bottom gripper shaft and an indicator was created using a hole in the shaft. The labview program 'calibration' was set up to read the signals coming in to the analogue input channel assigned to the angle of twist which is channel 1. The input data on the front panel of the program was represented on a graph and a digital indicator gave precise readings. The board was removed from the amplifier (RDP modular 600) to change the input range to the amplifier, this was accomplished by turning on the appropriate gain. The input signal was zeroed against the zero axis on the graph by adjusting the 'zero screw' on the amplifier on the appropriate channel. Torque velocity voltage was applied from the front panel of the Labview program to rotate the bottom gripper clockwise, using the run/hold switch on the front panel, the angle was recorded against the input voltages read on the graph for each angle. These recorded values were entered in to Microsoft Excel. Figure 3 28 shows the calibration curve when the shaft rotated in a clockwise direction. The inverse of this slope gave the scaling factor for the angle of twist as 30 deg/V.

3 5 SPECIMEN SELECTION AND INSTRUMENTATION

3.5.1 Test Materials and Specimen Design

The material used for the specimen was structural steel (BS970). The chemical composition (in percentage) of the steel was as given in table 3 3 as supplied.

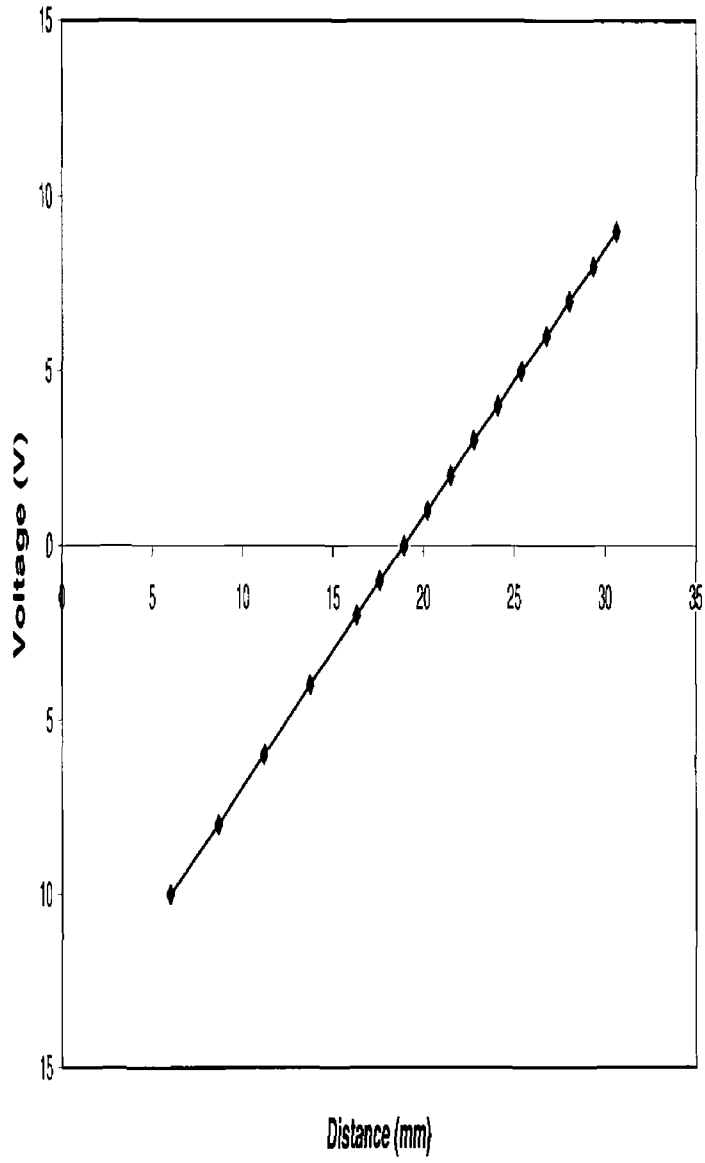


Figure 3.27 LVDT calibration curve

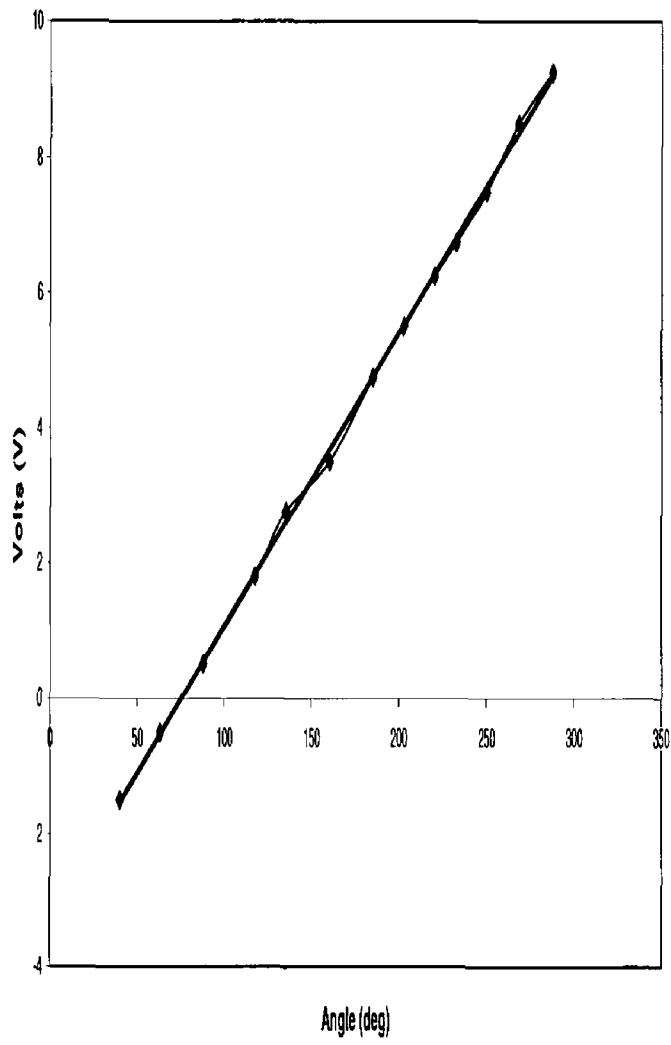


Figure 3.28 Angle of twist calibration curve

Table 3 3 Chemical composition of the steel solid rod

Component	C	Mn	P	Si	S
Weight %	0.36-0.44	0.60-0.90	0.05	0.10-0.40	0.05

A solid bar was used as the test specimen to avoid the complex relationships among the tightening torque, friction coefficient and pre-load, which results in case of a bolt. Except for the two extended end heads, the specimen had a circular cross-section throughout. Details of the specimen are shown in figure 3 29. The specimen was designed according to ASTM standardised form (ASTM E8) for a ductile-metal tension-test specimen. To apply the tensile load and torque, either simultaneously or individually, the ends of the specimen were designed in such way that when the torque was applied, the straight faces prevented the specimen from rotation, and when the tensile loads were applied, the 7.8mm deep heads held the specimen in the slots of the grippers.

In the present experimental investigations thin-walled tubes were also tested under combined tension-torsion loading. The specimens were cold finished seamless pressure tubes (BS3602 part1, CFS 360), and with 6.8mm outside diameter, 5mm inside diameter and 60mm in length. The chemical composition of the tube (in percentage) was as given in table 3 4. Details of the thin-walled tube specimen are shown in figure 3 30. The specially designed head to fit with the thin-walled tube is shown in figure 3 31.

Table 3 4 Chemical composition of the thin-walled tube

Component	C	Si	Mn	S	P
Weight %	0.17	0.35	0.40-0.80	0.045	0.045

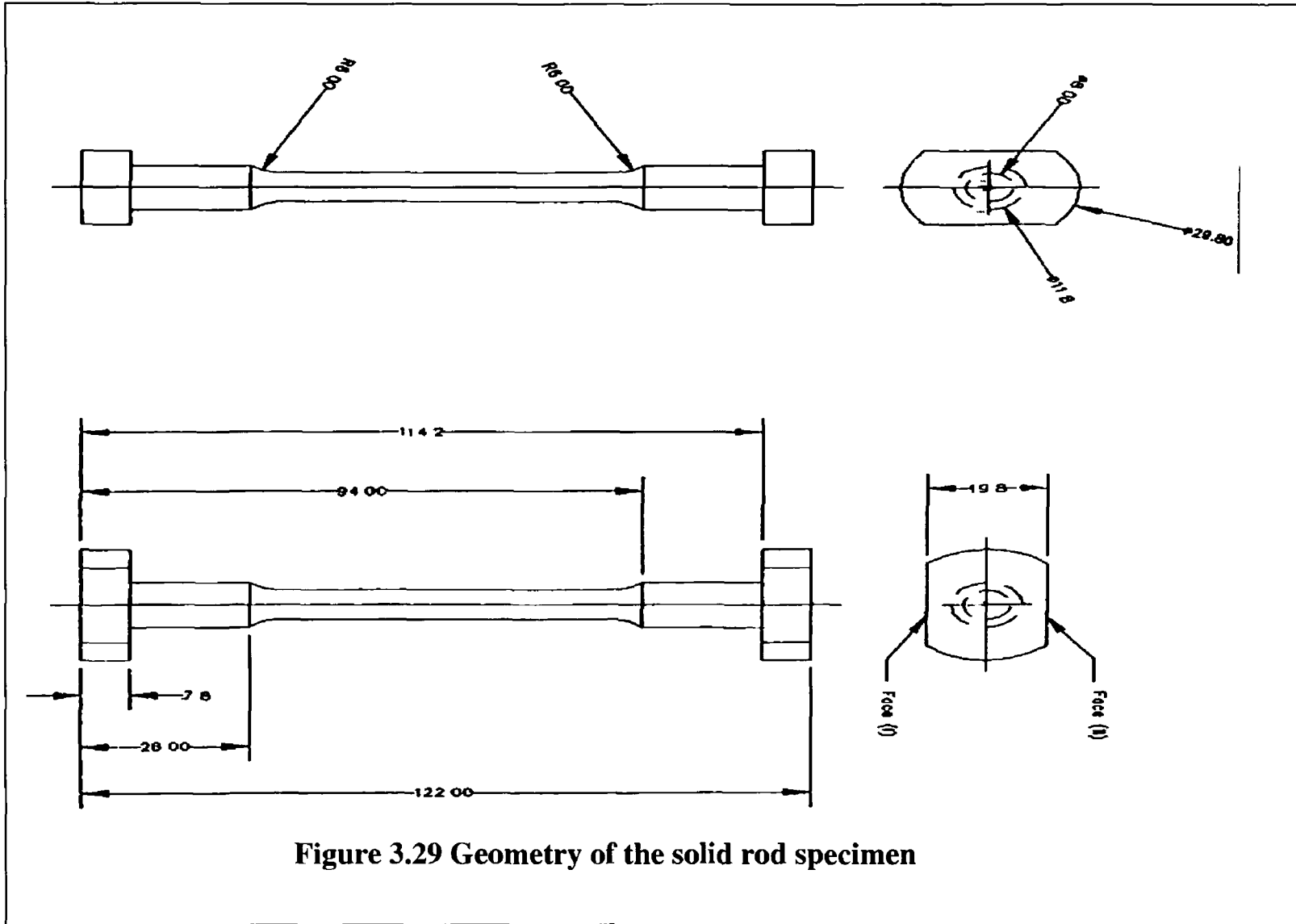


Figure 3.29 Geometry of the solid rod specimen

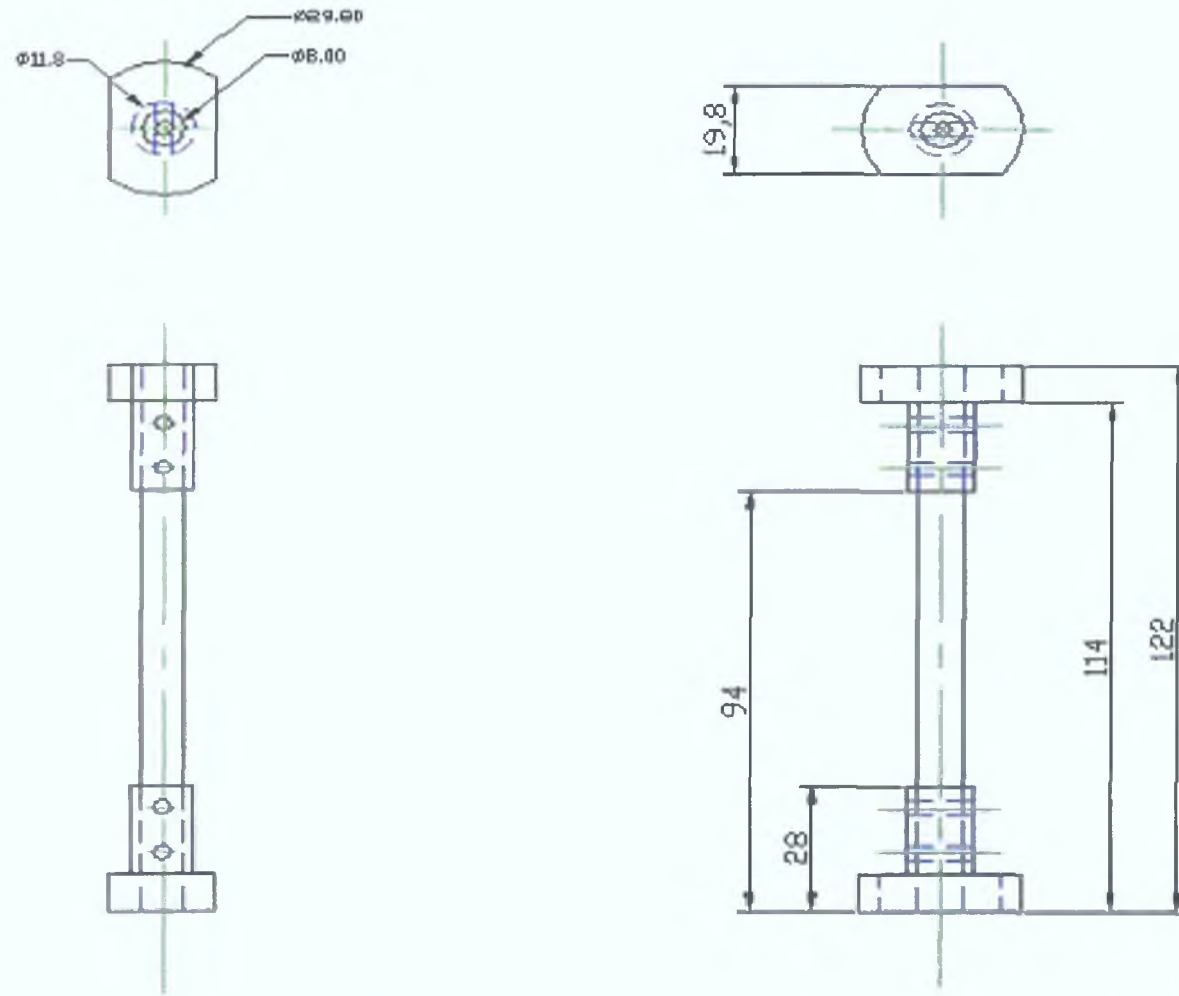


FIGURE-3.30 The assembly drawing of the thin-walled tube

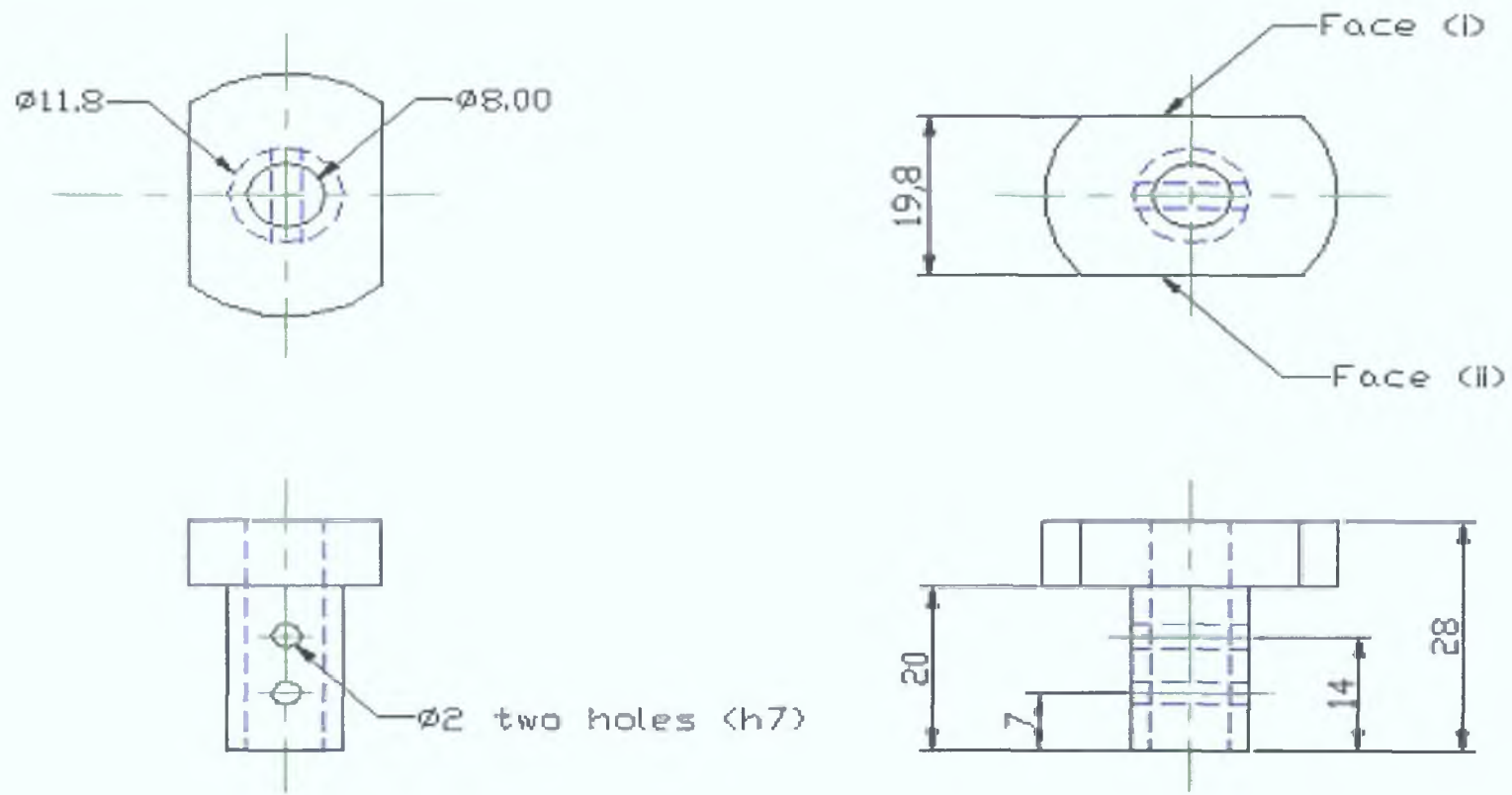


FIGURE- 3.31 Specially designed head to fit with the thin-walled tube

3.5.2 Specimen Instrumentation

In the present experimental investigations, three types of strain gauges were used to measure the axial and shear strains of the loaded specimen. All these gauges were purchased from the 'Measurements Group UK Ltd'. The strain gauge, type CER-06-250UN-350, was used to measure the axial strain during the uni-axial loading of the specimen. Types EA-06-125TM-120 and CEA-06-UV-350 were used during combined loadings. The details of these three different types of strain gauges are shown in figure 3.32.

3.5.3 Strain Gauge Attachment

The strain gauges are attached to the specimen to obtain the strain information of the specimen under different loading. The strain gauges are balanced properly for resistance and the output voltage is supplied to the modular amplifier for further amplification and then to the Labview system. In order to obtain the best results from strain gauges, it is important to prepare the gauge and the surface of the specimen to which the gauge is to be attached. To prepare the surface of the specimen, an area larger than the installation was smoothed with a fine grade emery paper to provide a sound bonding surface. Then the area was degreased with a solvent cleaner. Finally the surface of the specimen was neutralised with a 'M-prep Neutraliser-5'. Lint free cloth was used for this operation. After preparing the specimen surface, a short length of adhesive tape was placed over the entire length of the gauge tabs. Then the back of the gauge and the specimen surface were coated with a thin layer of '270schnellklebstoff' adhesive. The strain gauge was placed in its desired location and reasonable pressure was applied over the whole length of the gauge for approximately one minute. Then the connecting wires were soldered to each strain gauge element.

3.6 EXPERIMENTAL PROGRAMME

The experimental programmes were performed on an instrumented mechanical torque-tension machine at normal environmental conditions (room temperature).



Strain gauge type CEA-06-250-UN-350



Strain gauge type CEA-06-2UV-350



Strain gauge type EA-06-125TM-120

Figure 3 32 Different types of strain gauges used

Number of preliminary tests, such as, uni-axial tensile tests and pure torsion tests were carried out to determine the characteristics (uni-axial yield load and yield torque) of the material investigated. The axial load is measured by the axial load cell, and the axial displacement is measured by the linear velocity displacement transducer. The torque and the angle of twist are measured by the torque load cell and the angle measuring device. The signals from the transducers are fed to the modular amplifier where they are amplified and then fed to Labview. The signals from the amplifier, in volts, are scaled and shown in digital indicators on the front panel and stored in Microsoft Excel files for further analysis. Four different types of non-proportional combined tension-torsion loading paths are carried out as mentioned above.

3.6.1 TENSION FOLLOWED BY TORSION

Axial Displacement Held Constant

In this load test, the specimen was subjected to initially applied tensile load, and then its corresponding axial displacement was kept constant. This was achieved by setting the load motor hold mode to keep the axial displacement constant, then the torque motor was enabled to apply the torque gradually at constant strain rate till the specimen fails. The same procedure of the above test was repeated for different levels of initial axial load for solid steel rod and thin-walled specimens.

Axial Load Held Constant

An EA-06-125-TM-120 type axial strain gauge is attached with the specimen to measure the axial strain. Then the specimen was subjected to an initial axial load within the elastic range, maintaining the axial load constant through out the test. This was achieved by enabling the load motor to run till the present axial load was reached, then the torque motor was enabled to apply the torque gradually till the specimen failed. During the application of the initial axial load, the specimen was extended at quasi-statically at a nominally constant axial strain rate of $8.33 \times 10^{-4} \text{ s}^{-1}$.

This test was repeated for different levels of initial axial load, and for the solid steel rod specimens only. The effect of the strain rate is negligible.

3.6.2 TORSION FOLLOWED BY TENSION

Angle of Twist Held Constant

In this type of loading path, the specimen was subjected to an initial torque within the elastic range of the material, and then the corresponding angle of twist was held constant throughout the test. While keeping the angle of twist constant, an axial load was gradually applied until failure of the specimen. To achieve this, the torque motor was switched to 'hold' mode, and the load motor was enabled to apply the axial load. The load motor was kept running until failure of the specimen. The same procedure was repeated for different levels of initial torque (i.e., with different values of angle of twist). This test was carried out for both the solid steel rod and thin-walled tube steel specimens.

Torque Maintained Constant

Before this test was carried out a "CEA-06-062UV-350" type shear strain gauge was attached to the specimen. After set up, the specimen was subjected to an initial torque within the elastic range of the material. The applied initial torque, rather than the angle of twist, was maintained constant throughout the test and the axial load was then applied gradually till the specimen failed. During the application of the axial load the specimen was extended at the same strain rate as previously, whereas during the torque application the specimen was twisted at a shear strain rate of $1.34 \times 10^{-3} \text{ s}^{-1}$. The same test procedure was repeated for different levels of initial torque.



Plate 3.1 Torque-tension machine



Plate 3.2 Positioning of the LVDT

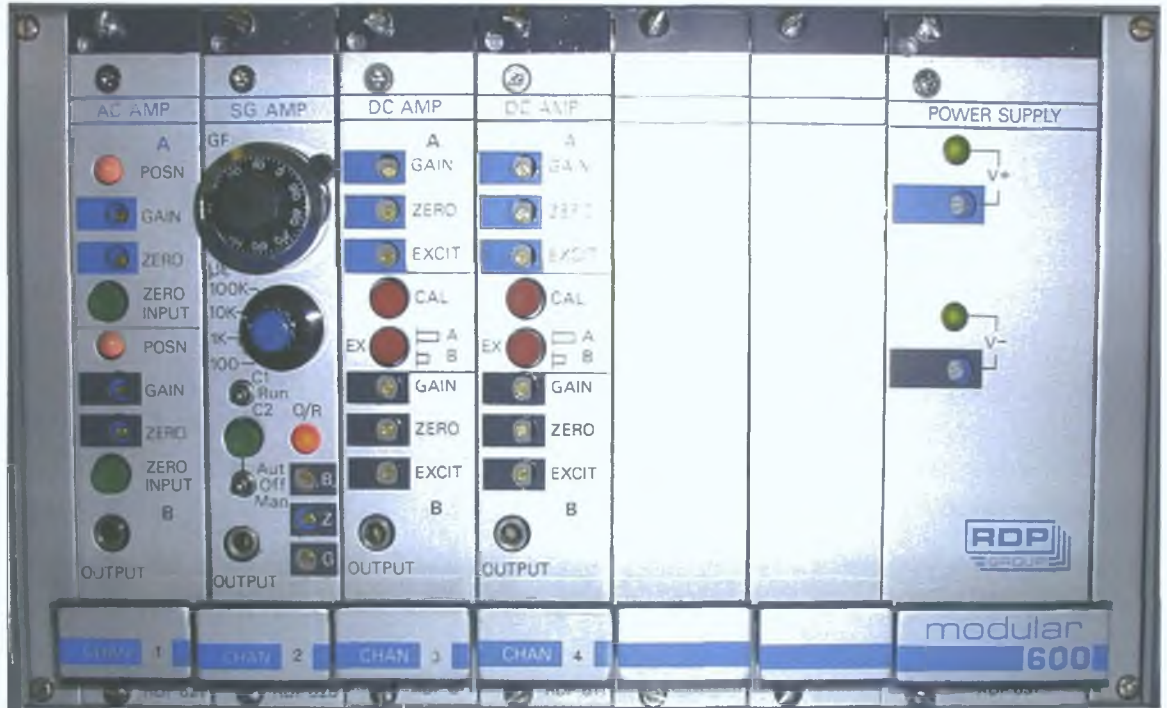


Plate 3.3 The RDP module 600 Amplifier



Plate 3.4 The two identical "Moog T161-003" brushless motor controllers

CHAPTER FOUR

ANALYSIS OF EXPERIMENTAL RESULTS AND DISCUSSION

4.1 INTRODUCTION

This chapter details the analysis and discussion of the experimental results carried out according to the experimental programme mentioned in section 3.5 of chapter three. Two tension tests and two pure torsion tests were carried out on virgin specimens under the same loading conditions to determine the characteristics (i.e. uni-axial yield load and yield torque) of the material investigated. After the determination of the yield axial load and yield torque, various combinations of these loads were used for the combined load tests. Combined tension-torsion tests are carried out at normal room temperature in a number of different loading path details which are given below. Four different types of loading paths were investigated as follows:

- Initial axial load of known level, within the elastic range was applied to the specimen and subsequent application of a torque, maintaining the axial load constant throughout the test, until the failure of specimen.
- Initial torque of known level, within the elastic range was applied to the specimen, and then, the axial load was gradually increased until the failure of the specimen. The torque was maintained constant while the axial load increased.
- The specimen was subjected to an initial extension and subsequent application of torsion, maintaining the initial extension constant throughout the experiment.

- The specimen was subjected to a twist of an initial angle and subsequent application of axial load, maintaining the initial angle of twist constant until the failure of the specimen

During the tensile loading the specimen was extended quasi-statically at a nominally constant axial strain rate, while during the torque loading the specimen was twisted at a constant shear strain rate. The experimental investigations were conducted on structural steel, as it is the most commonly used material in the engineering industries.

4.2 Preliminary Tests

4.2.1 Uni-Axial Tensile Tests

The uni-axial tensile tests were carried out on two separate specimens to determine the necessary mechanical properties of the mild steel (En8). The yield strength of the specimen was measured at 0.2% offset. The average axial yield load was equal to 30.5 kN. Figure 4.1 shows the Uni-axial tensile load versus axial strain curve. The axial stress versus axial strain curve is depicted in figure 4.2, and the yield stress calculated for the corresponding yield load was 607 N/mm² (MPa). The modulus of elasticity was calculated from the slope of the straight line from the origin to the proportional limit of the stress-strain diagram. The average value of the modulus of elasticity was 210 GPa.

4.2.2 Pure Torsion Tests

Two pure torsion tests were carried out on two separate specimens. In torsion test, unlike the tension test where the stress is uniformly distributed across the section of the specimen, there is a stress gradient across the cross-section and hence at the end of elastic range yielding commences at the outer fibers first while the core is still elastic. With continued application of torque in to the plastic range, more and more of the cross-section yields until the entire cross-section becomes plastic. Figure 4.3 shows the torque-shear strain diagram for the steel specimen. The yield torque was measured at the proportional limit whose value was equal to 36.2 Nm and its

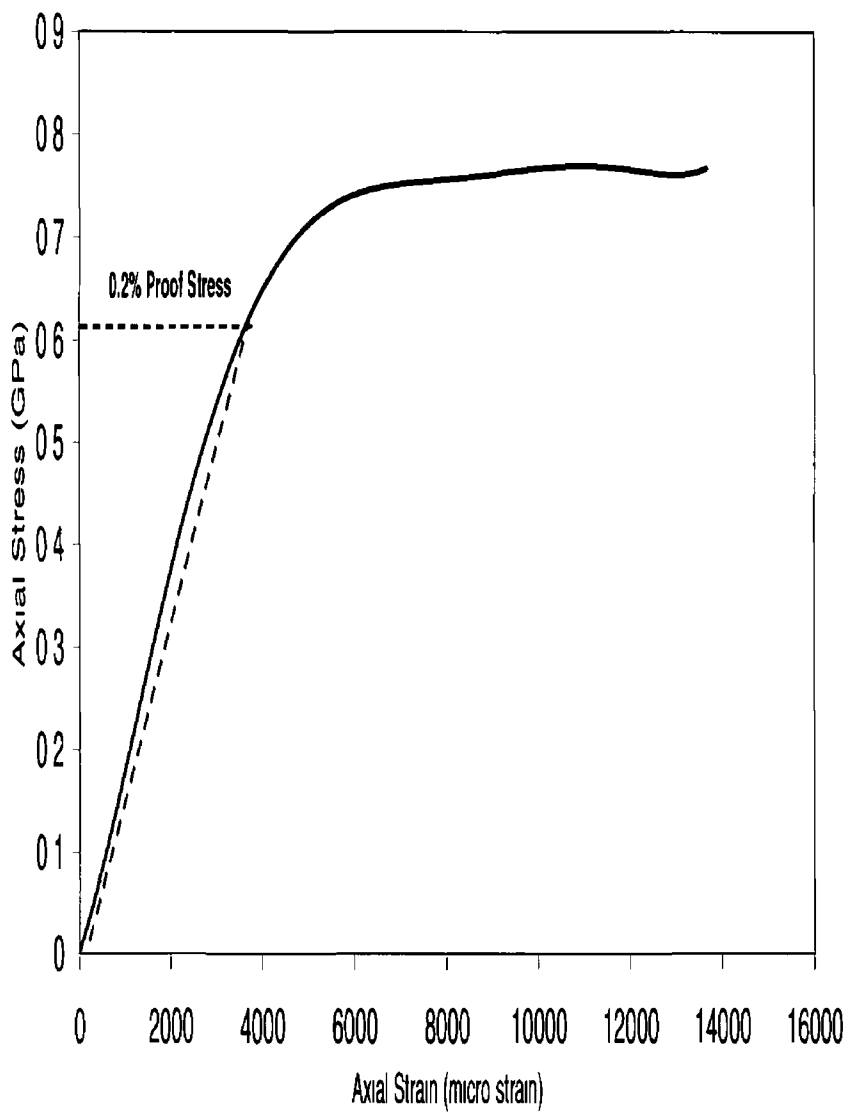


Figure 4.1 Axial stress versus axial strain

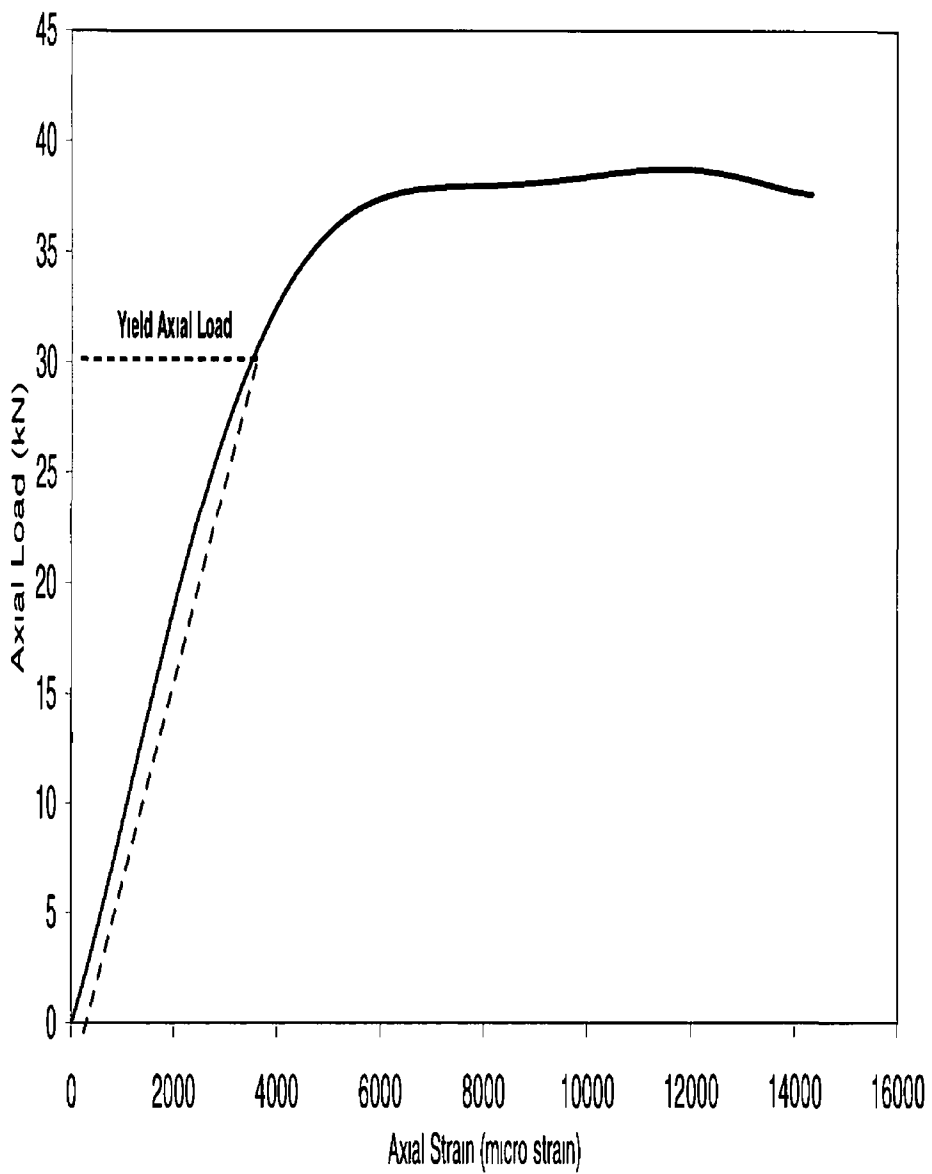


Figure 4.2 Uniaxial tensile load versus axial strain

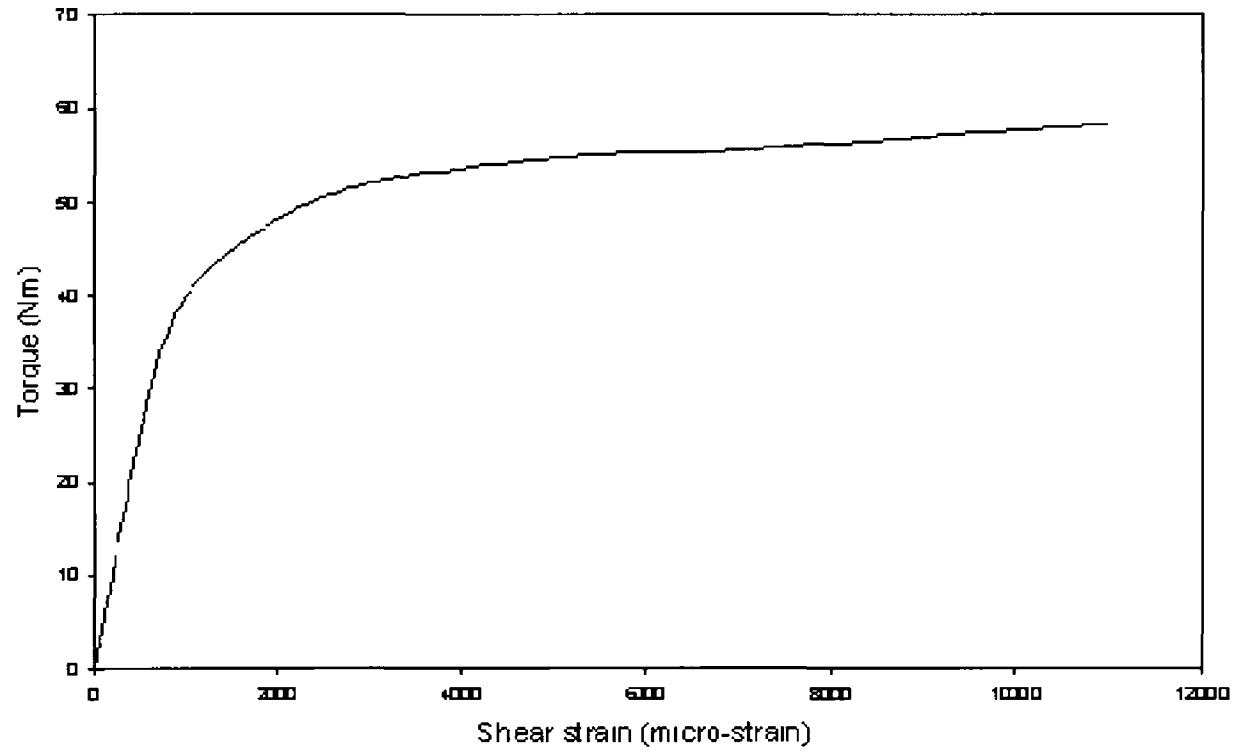


Figure 4.3 Torque versus shear strain curve

corresponding yield shear stress was equal to 360MPa. The mechanical properties of the steel investigated are given in table 4.1

Table 4.1 Mechanical properties of the steel

Modulus of elasticity (GPa)	Modulus of rigidity (GPa)	Tensile yield load (kN)	Yield torque (Nm)	Tensile yield stress (MPa)	Shear yield stress (MPa)
210	80	30.5	36.2	607	360

4.3 COMBINED LOADING OF SOLID ROD

4.3.1 TENSION FOLLOWED BY TORSION

Axial Displacement Held Constant

In the first type of loading, the specimen was subjected to an initial axial load within the elastic range and then, keeping its corresponding axial displacement constant, the torque was applied gradually at a nominal constant twist rate till the specimen failed. This procedure was repeated for four different initial normalised axial loads, F (F/F_Y) equal to 1.0, 0.75, 0.50 and 0.25.

For this type of loading the variation in the normalized axial load F with the subsequently applied normalized torque T , for different levels of initially applied loads, is depicted in figure 4.4. It is observed from this figure that as the torque is increased gradually, the initially applied axial load remains constant for a certain level of torque. It then decreases marginally until the combined axial load and torque produces von Mises yield condition. It is seen from the figure when the rod is subjected to a higher initial axial load and then torque is applied, the axial load starts to decrease at a greater rate at the initial stage of loading and tends to drop rapidly after about 1.2 times the yield torque. On comparison of the four different initial axial load cases, when the initial axial load is smaller, the subsequent torque holding

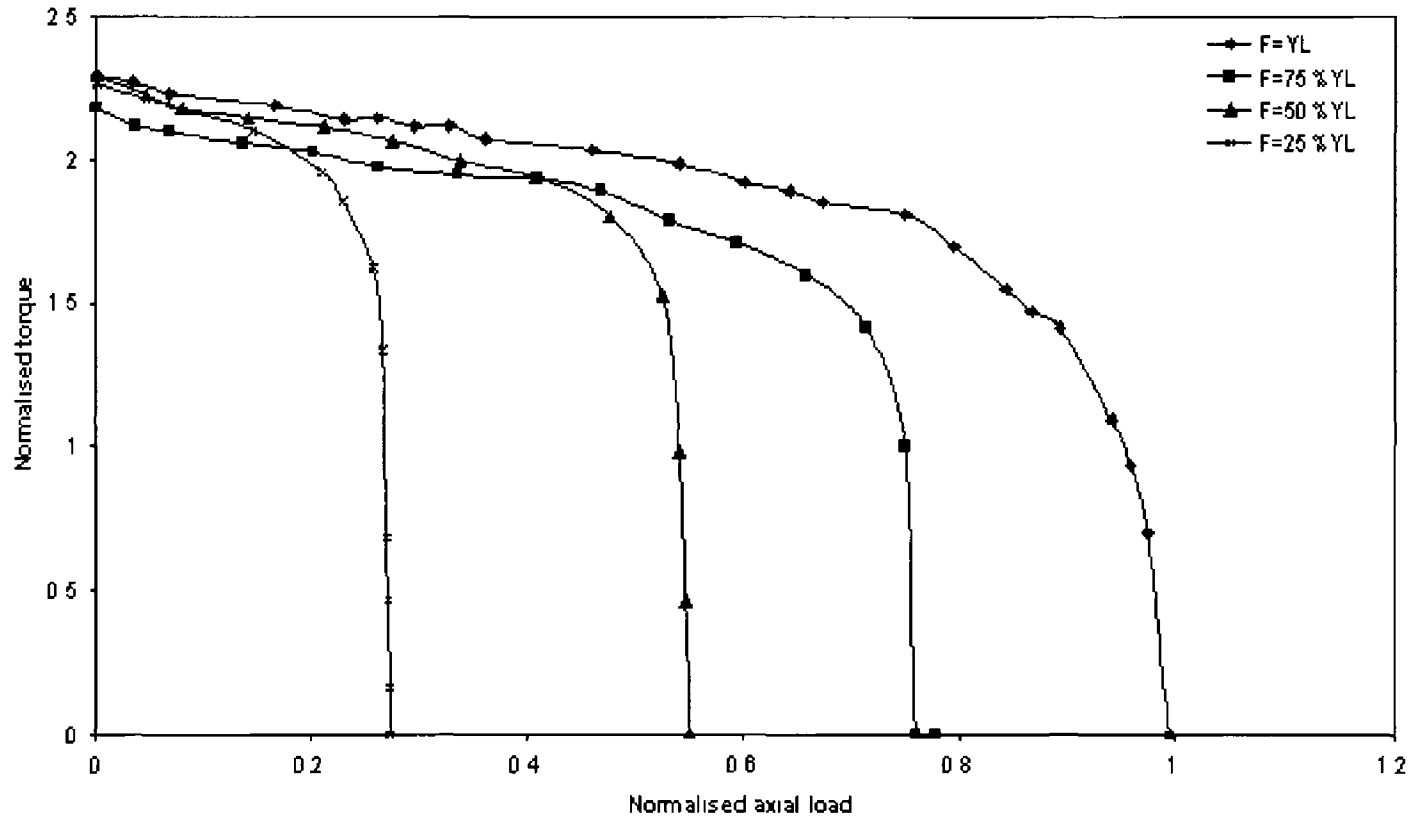


Figure 4 4 Normalised axial load versus normalised torque (constant axial displacement)

capacity of the rod is extended up to 1.3 times the yield torque after which yielding occurs rapidly. The rod sustains larger torque because of the non-linear, inelastic behaviour across the cross section in shear. This increases the torque carrying behaviour of the rod. From the yield criteria for combined loading according to von Mises, the material starts yielding at lower torque when the initially applied axial load is increased. This follows the yield criteria $\sigma^2 + 3\tau^2 = Y^2$, where σ is the axial stress, τ is the shear stress and Y is the axial yield stress. After reaching the yield plateau the combined stresses in the rod follow the yield plateau as shown in figure 4.4. The normalized torque exceeds unity due to the strain hardening property of the material.

Figures 4.5-4.8 are plotted as normalised shear strain versus normalised axial load and torque curves for different initially applied axial loads corresponding to 1.0, 0.75, 0.5 and 0.25 of the yield axial load. These figures show the variation of initially applied normalised axial load and subsequently applied torque with the shear strain. It is revealed from these curves that for the subsequent twisting of the rod, the increase in the shear stress due to the increase in the torque is developed faster than the decrease in the axial load and the corresponding axial stress. It can be seen also from these figures that even the material yields due to the combined loading well before the applied torque reaches its yield torque, all the torque curves behave almost the same. When the yielding starts, the axial load carrying ability is reduced, with the increasing torque, without affecting its torque carrying ability, the initially applied axial load decreases continuously with the subsequent applied torque, in the beginning rapidly and then slowly but nearly at a constant rate, because of the combined loading the yielding commences in the outer layer first and with subsequently applied torque the plastic zone starts to spread on the core of the rod with more reduction in its ability to sustain the initially applied axial load.

Axial Load Maintained Constant

In this loading case, the rod is subjected to an initial axial load within the elastic range of the material followed by the application of the torque, keeping the axial load constant. This procedure was repeated for four different levels of initial axial load corresponding to 1.0, 0.75, 0.50 and 0.25 of the yield axial load. To observe the effect

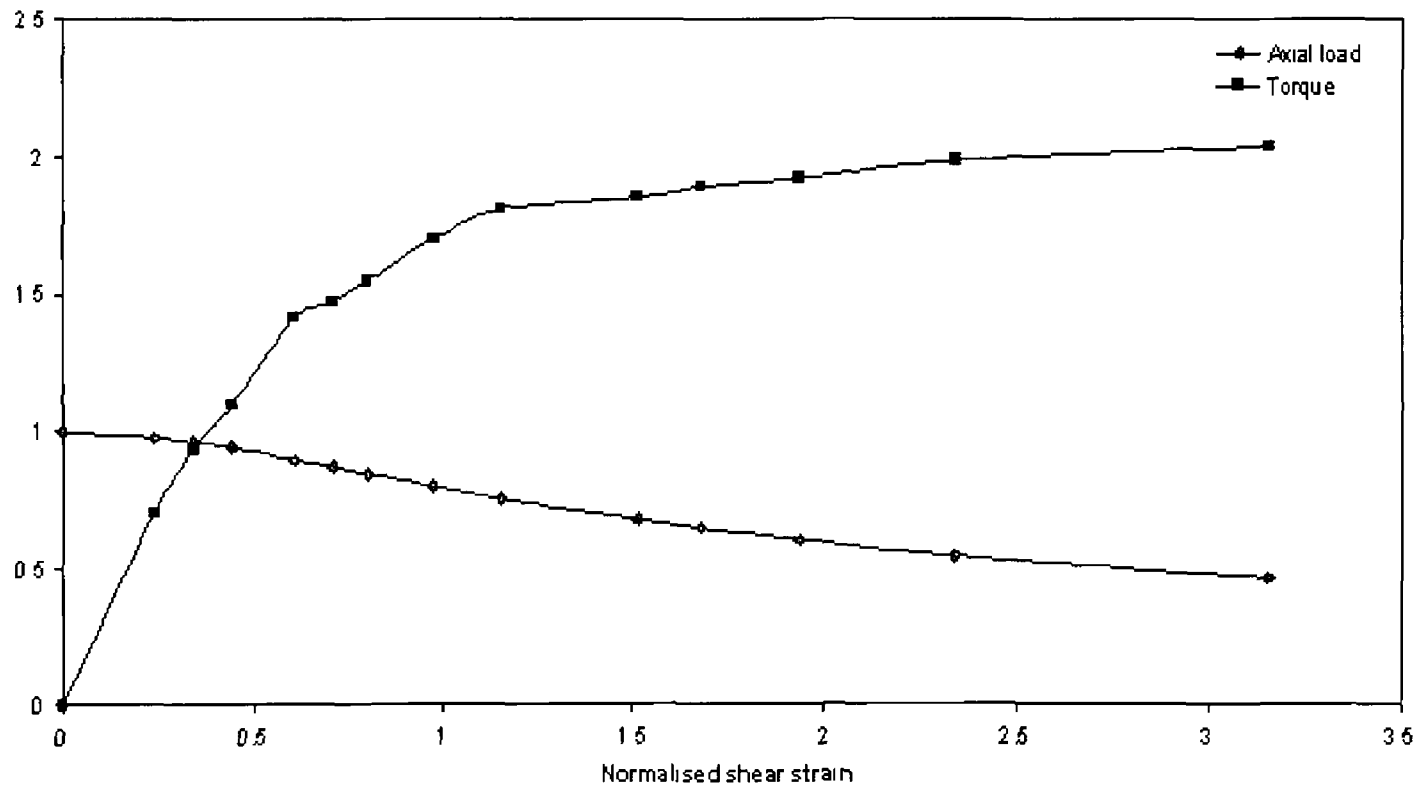


Figure 4 5 Normalised shear strain versus normalised axial load and torque curve (F=YL)

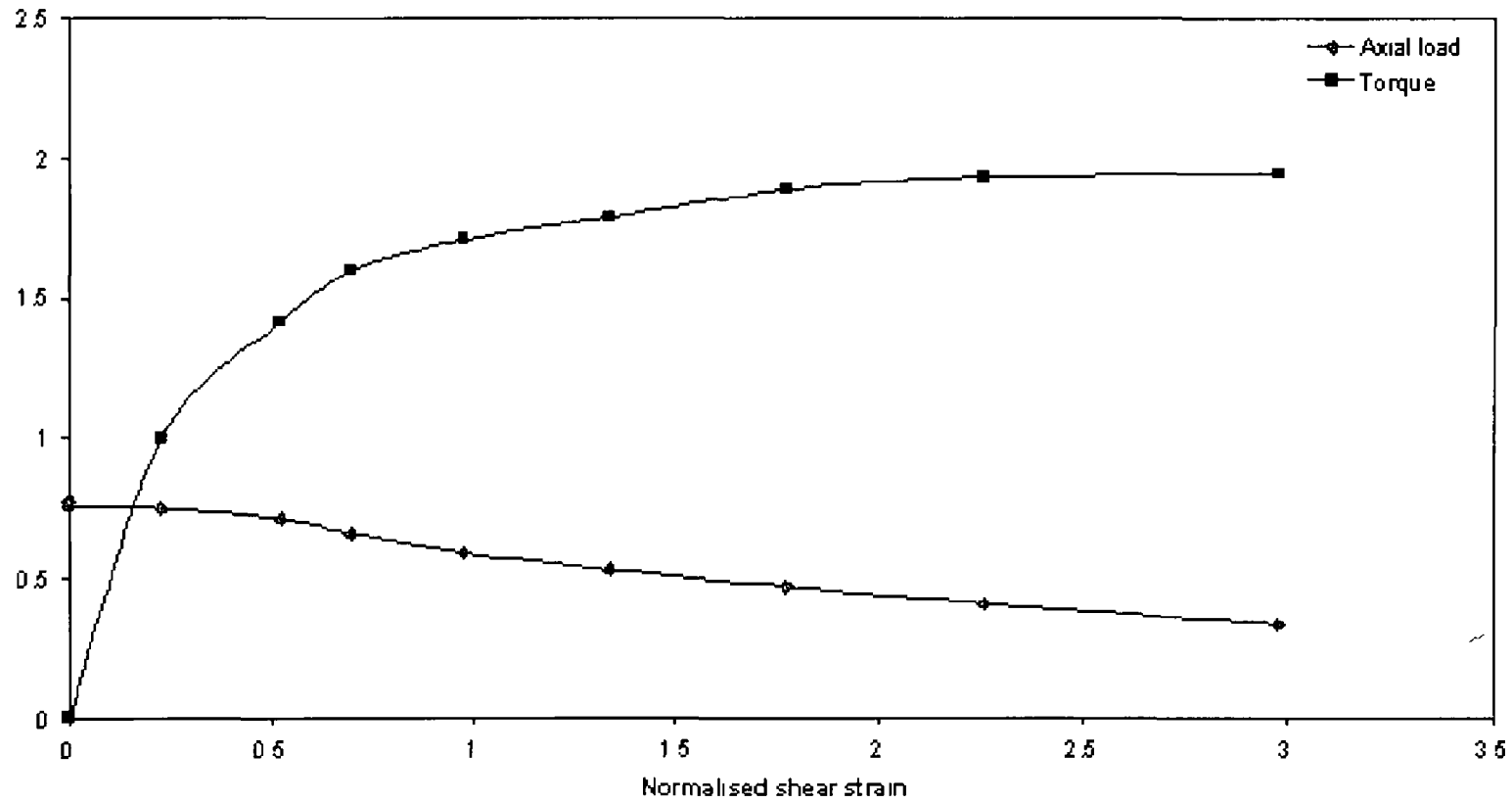


Figure 4.6 Normalised shear strain versus normalised axial load and torque curves (F=75% YL)

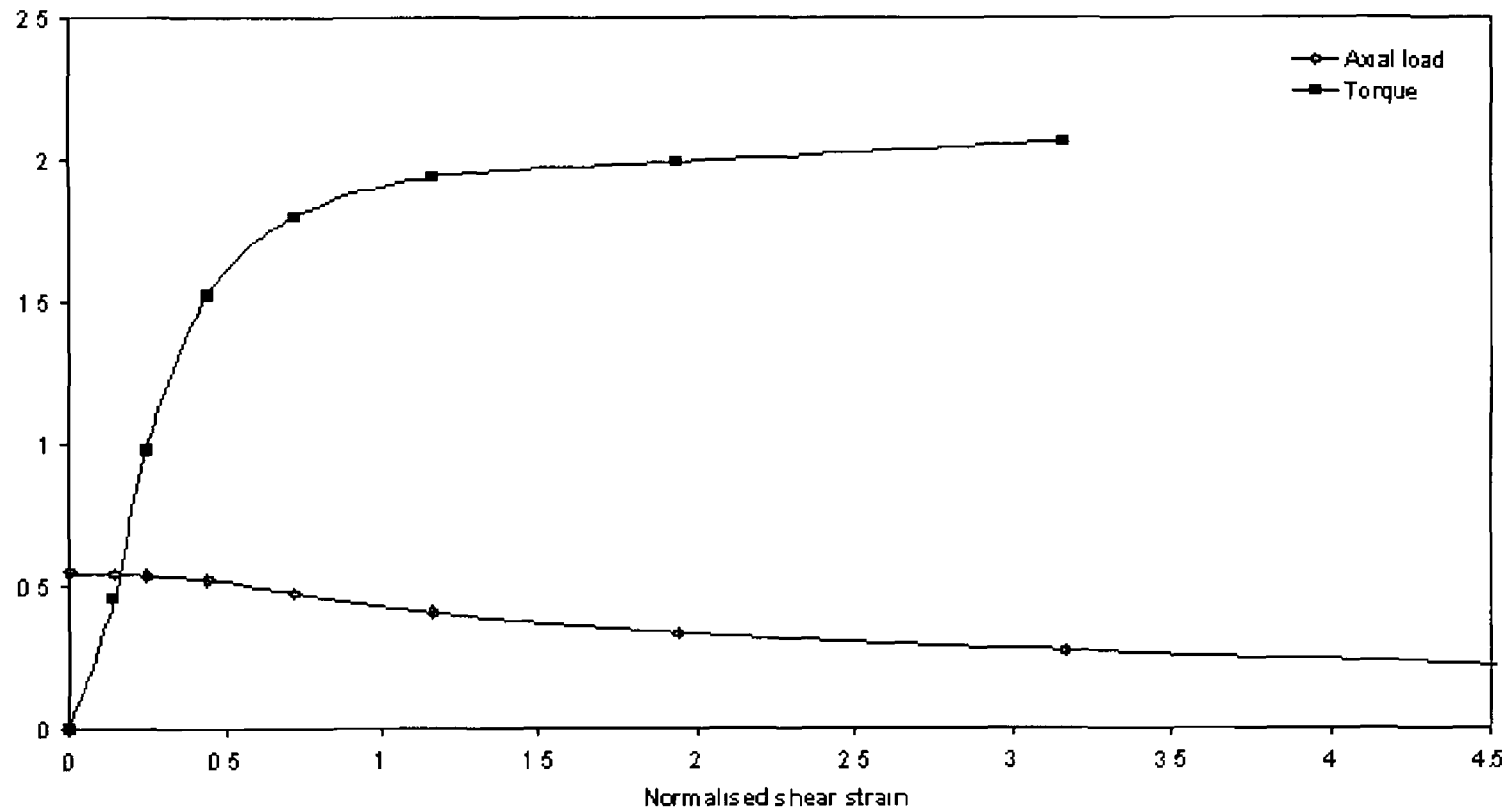


Figure 4 7 Normalised shear strain versus normalised axial load and torque curves (F=50% YL)

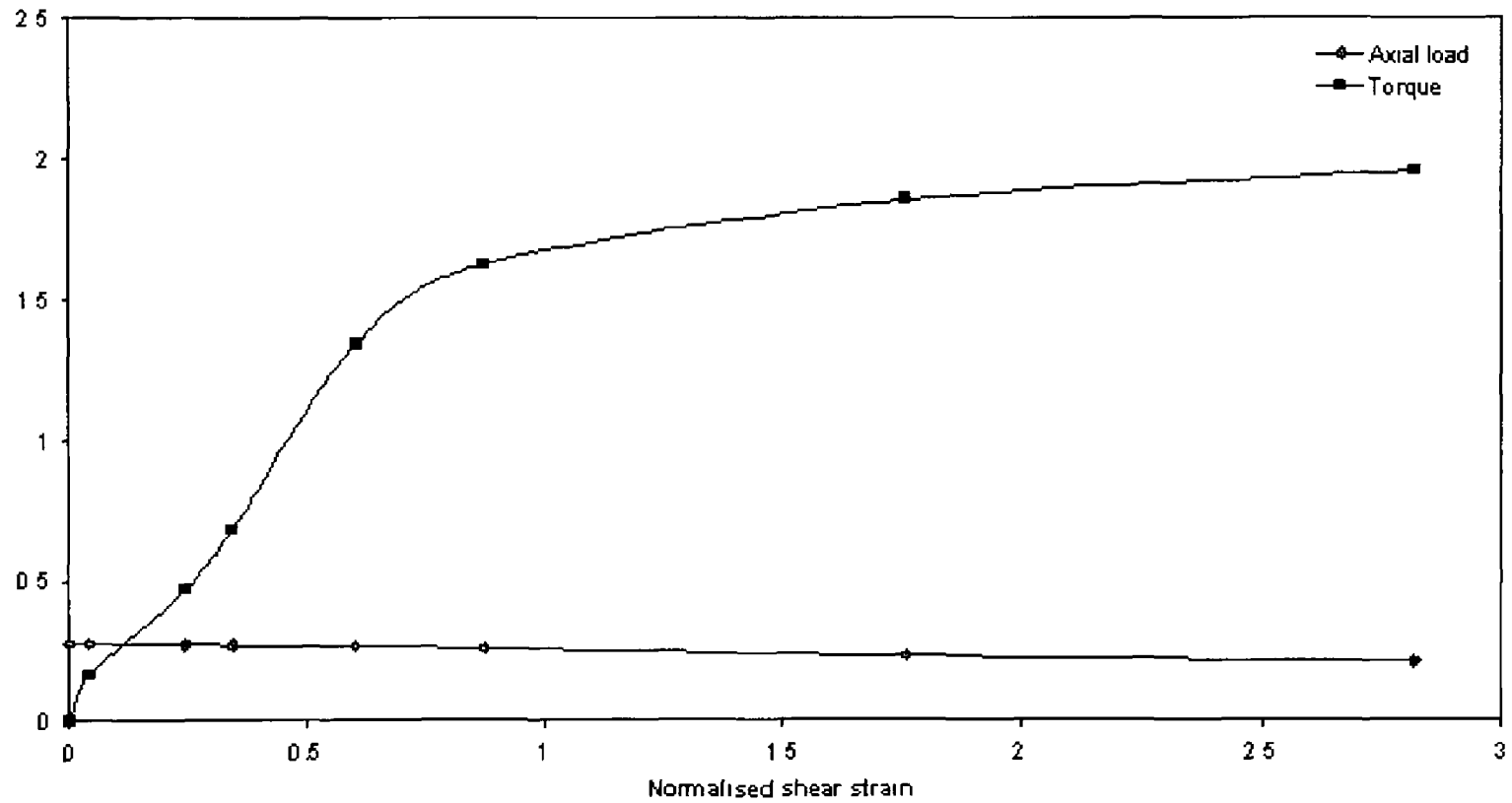


Figure 4.8 Normalised shear strain versus normalised axial load and torque curves (F = 25% YL)

of the initially applied axial load on the strength of the solid rod with the subsequently applied torque, the test results are plotted in terms of normalised axial strain versus normalised shear strain as shown in figure 4.9. The results show that as the torque is gradually increased, the shear strain as well as the axial strain increased to maintain the initially applied axial load constant. The figure also reveals that the rate of increase in the axial strain is significantly higher for the higher initial axial load compared to that for lower initial axial load, for a given increase in the shear strain and hence shear stress.

4.3.2 TORSION FOLLOWED BY TENSION

Angle of Twist Held Constant

In this type of loading, the rod was subjected to an initial torque within the elastic range and then, holding its corresponding angle of twist constant, the axial load was gradually applied till the failure of the rod. This procedure was repeated for four different initial normalised torques, T (T/T_y) equal to 1.0, 0.75, 0.5 and 0.25.

The variation of the initially applied normalised torque with the subsequent application of the normalised axial load is depicted in figure 4.10. The figure shows that the initially applied torque remains constant until the applied axial load reaches a value which when combined with the torque causes the material to yield. Thereafter for any increase in the axial load, the torque reduces rapidly till the axial load reaches a maximum of about 1.05 times the yield axial load. At this stage any attempt to increase the axial load causes the onset of plastic instability and necking. The axial load decreases rapidly at a constant torque until the rod fails resembling brittle fracture. The results plotted in terms of normalised shear stress and axial stress give a clearer indication of when plastic yielding commences under combined tension and torsion loadings. These results shown in figure 4.11 indicate that the rod subjected to higher initial torque followed by increasing axial load, yields plastically at an earlier stage than the rod subjected to a lower initial torque. This is due to the fact that the combined stress level meets the von Mises yield plateau at an early stage and takes a diversion due to strain hardening of the material until necking starts. The combined stress in the rod with the lower initial torque meets the yield plateau drawn using

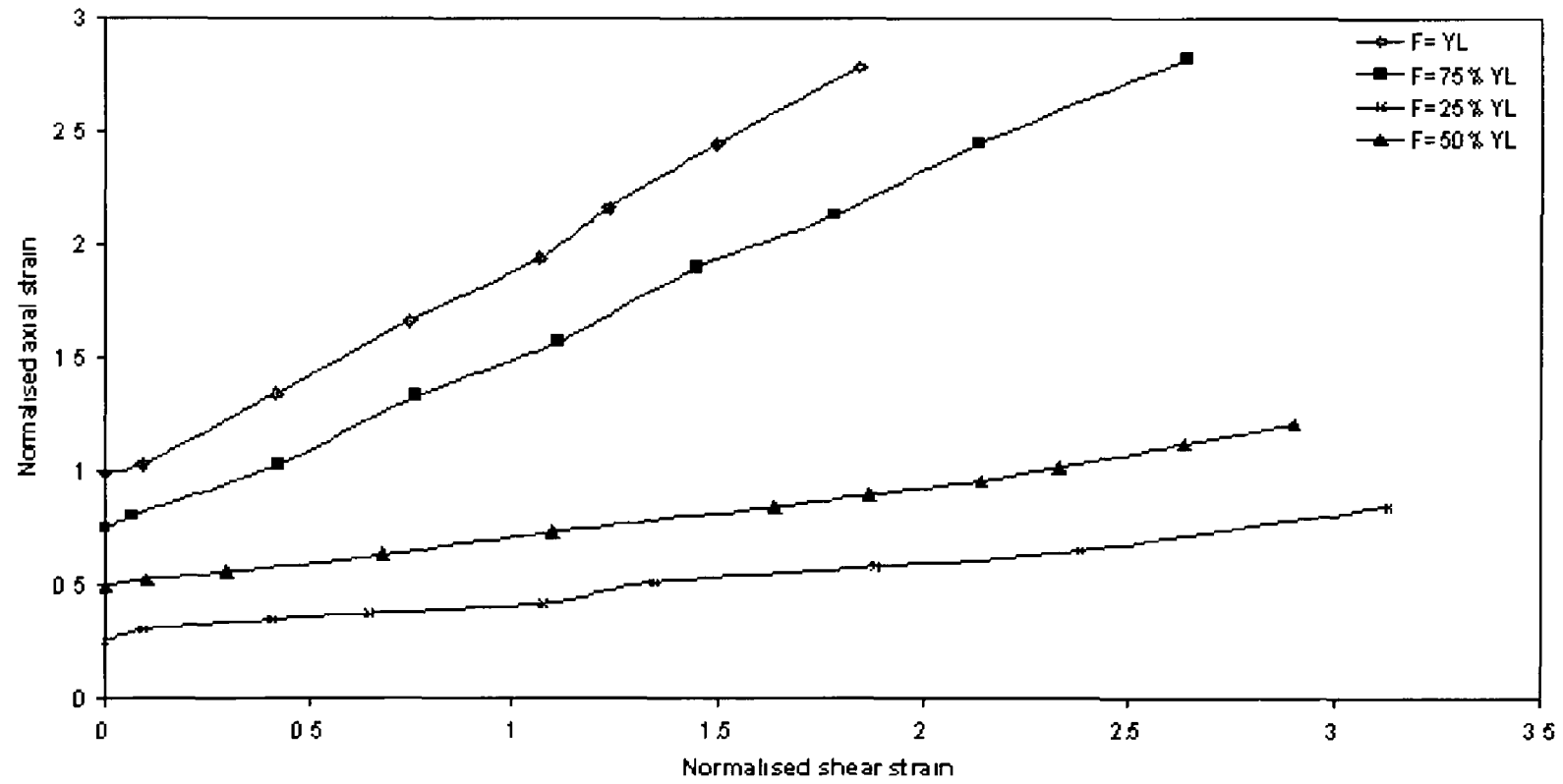


Figure 4.9 Normalised shear strain versus normalised axial strain (constant load)

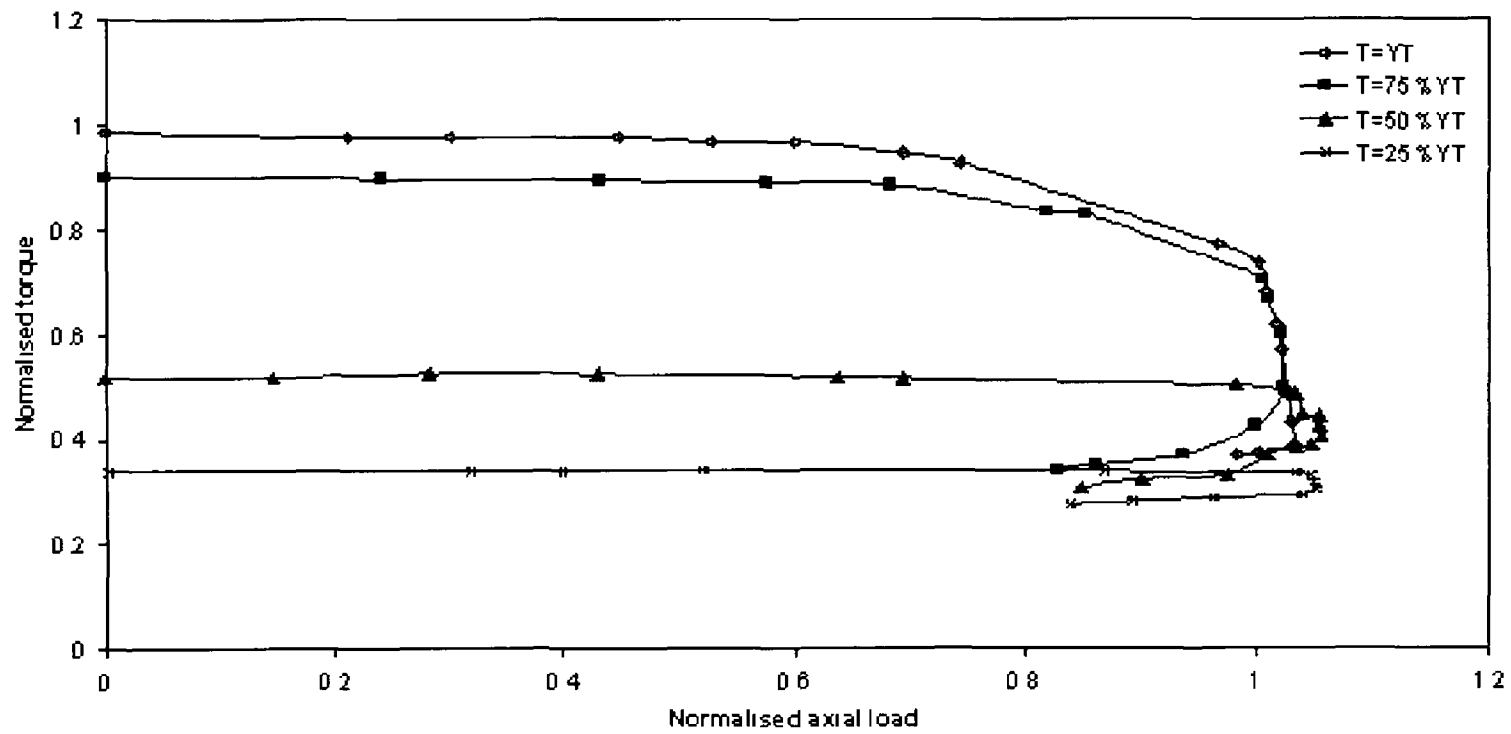


Figure 4 10 Normalised Axial load versus normalised torque (constant angle of twist)

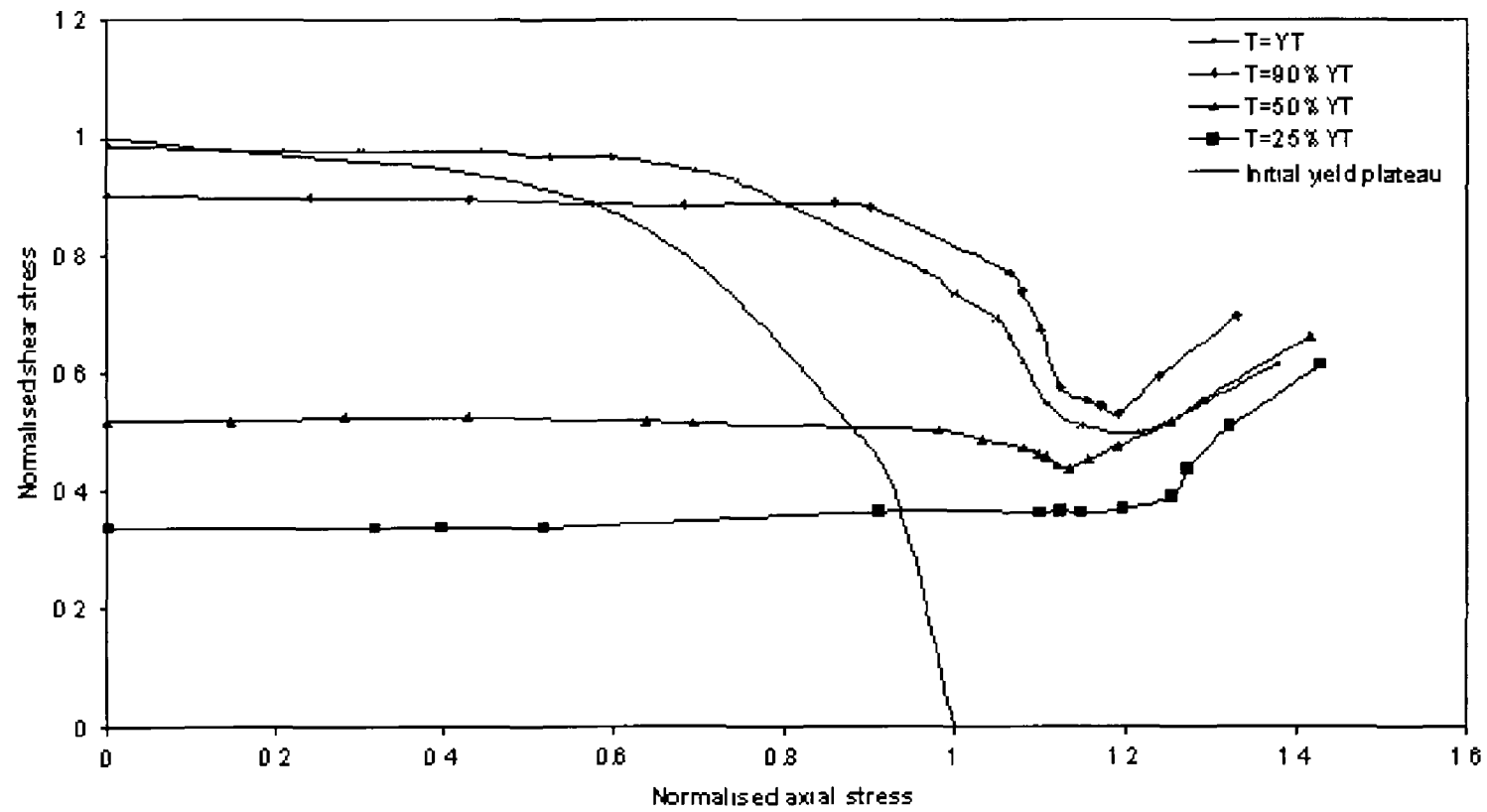


Figure 4.11 Normalised axial stress versus normalised shear stress (constant angle of twist)

maximum stresses just prior to the onset of necking. The combined stress levels in all the cases do not follow the yield plateau drawn with the values of initial yield stresses in tension and torsion due to the strain hardening behaviour of the material.

Normalised axial strain versus normalised torque and axial load curves are plotted as depicted in figures 4.12-4.15 for different levels of initial torques corresponding to 1.0, 0.90, 0.50 and 0.25 percent of the yield torque. These figures show that the initially applied torque carrying ability is reduced at a slower rate than the rate of the increase in axial load due to subsequently applied axial load. It can be seen from these figures that the rods have yielded due to combined loading, well before the subsequently applied load reaches its yield load, all the axial load curves follow the profile of uniaxial tensile load curve. When the yielding starts, the torque carrying ability is reduced, with the increasing subsequently applied axial load, without affecting its axial load carrying ability. From these figures it is also shown that, when the material yields due to combined loading, at the beginning the initially applied torque decreases at a faster rate with the increase in the axial load. As the axial load reaches about the uni-axial tensile strength, the torque decreases much slowly. This is due to when the axial load becomes equal to its ultimate load, necking starts, and after that the axial load begins to decrease and as the decrease in axial load no longer satisfies the yield criteria, the torque stops decreasing and becomes nearly constant.

Torque Maintained Constant

In this loading path, the specimen was subjected to an initial torque within the elastic range of the material and then the initial torque was maintained constant, and subsequently an increasing axial load was applied. The same procedure was repeated for four different initial torques, $T = 1.0, 0.75, 0.5$ and 0.25 . The normalised axial strain and shear strains are plotted as shown in figure 4.16. The figure shows that with increasing axial strain, due to the increase in the axial load, the shear strain increases to maintain the initially applied torque. This increase in shear strain is much higher for higher initially applied torque values. As the axial load and hence the axial strain increases, the outer layers of the specimen begin to yield and to maintain the torque constant the shear strain increases. Furthermore, initially the engineering shear strain remains constant for a given torque. But as the axial load and hence the axial

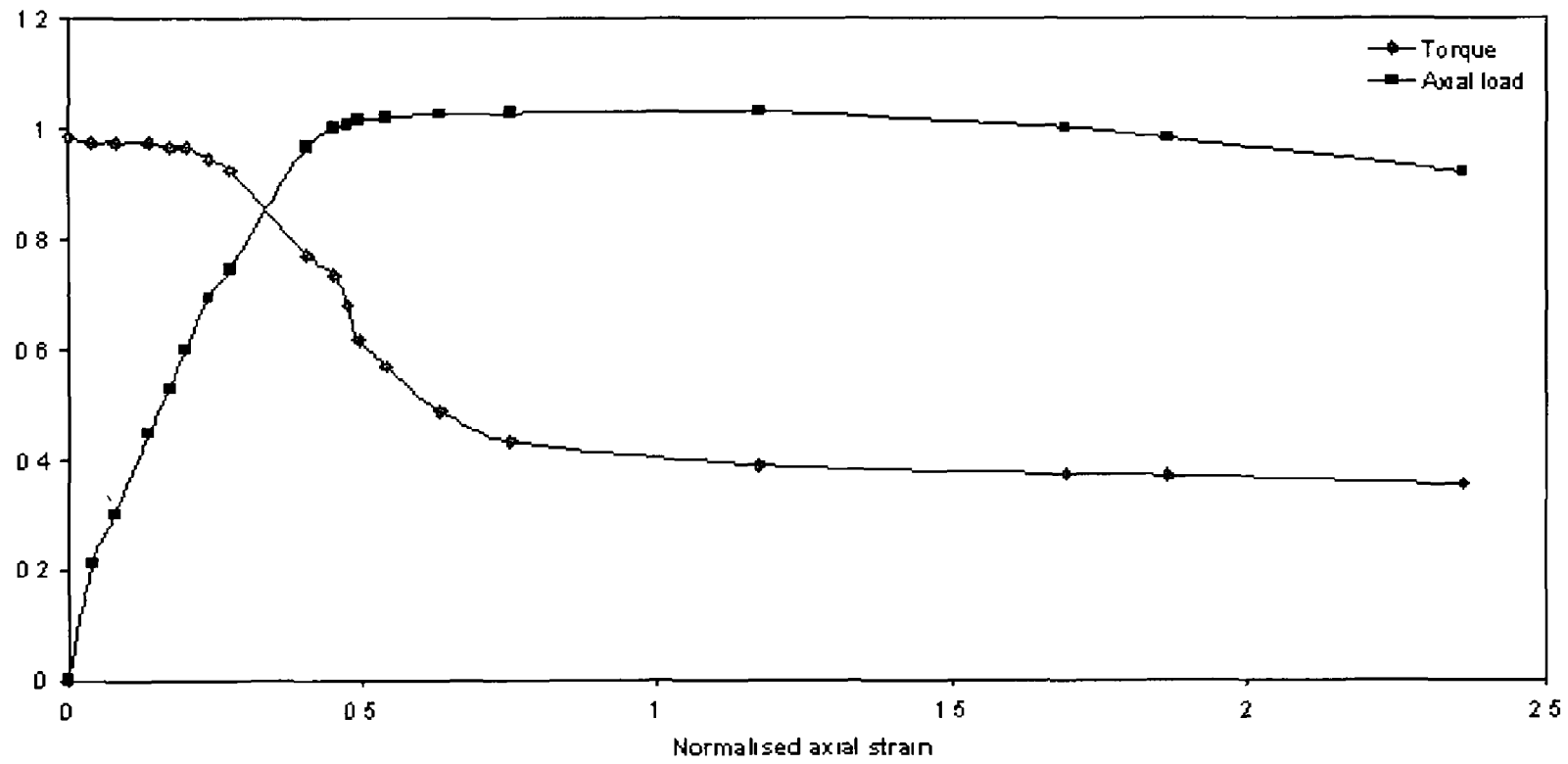


Figure 4.12 Normalised axial strain versus normalised torque and load curve ($T=YT$)

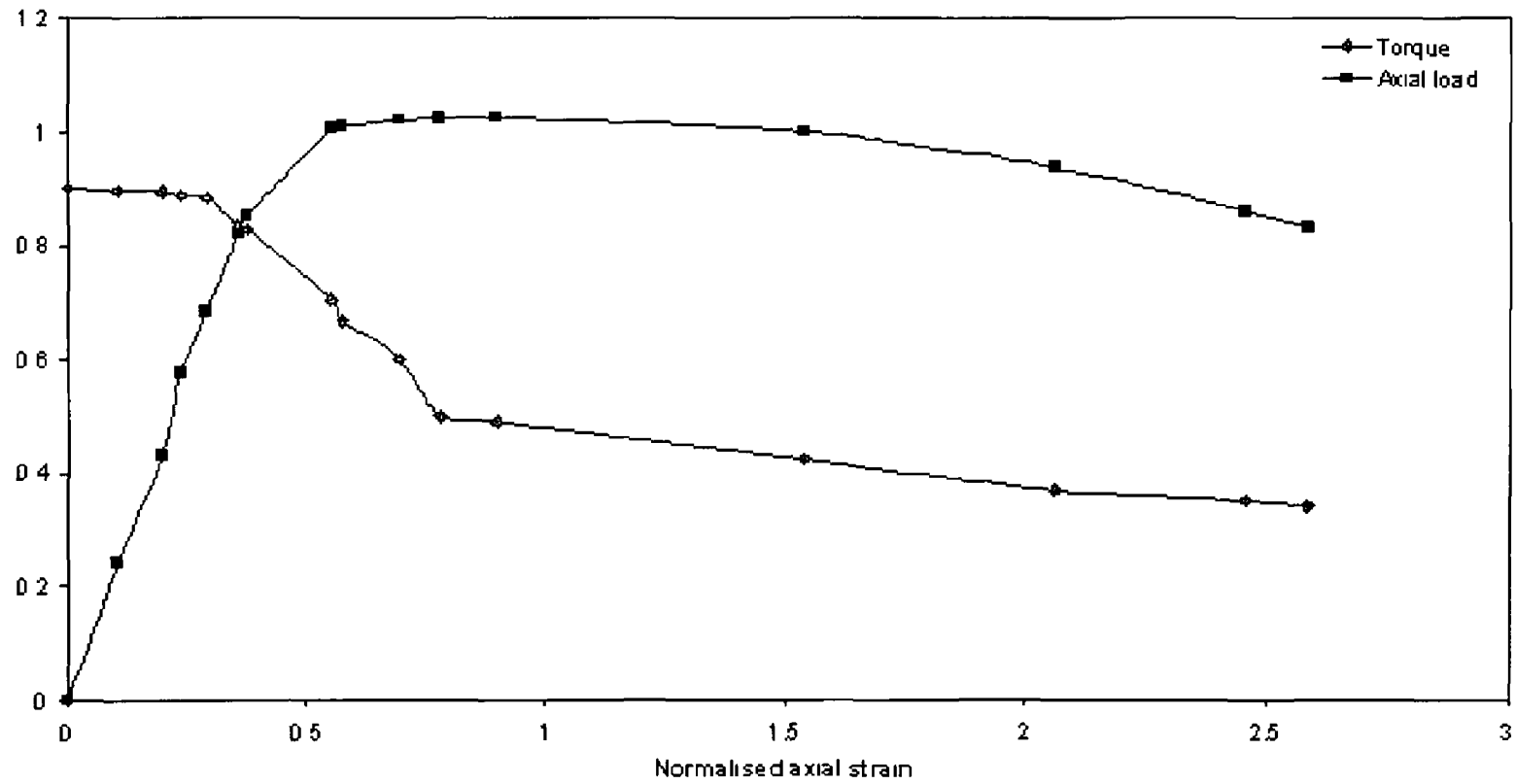


Figure 4 13 Normalised axial strain versus normalised torque and load curve (T=90% YT)

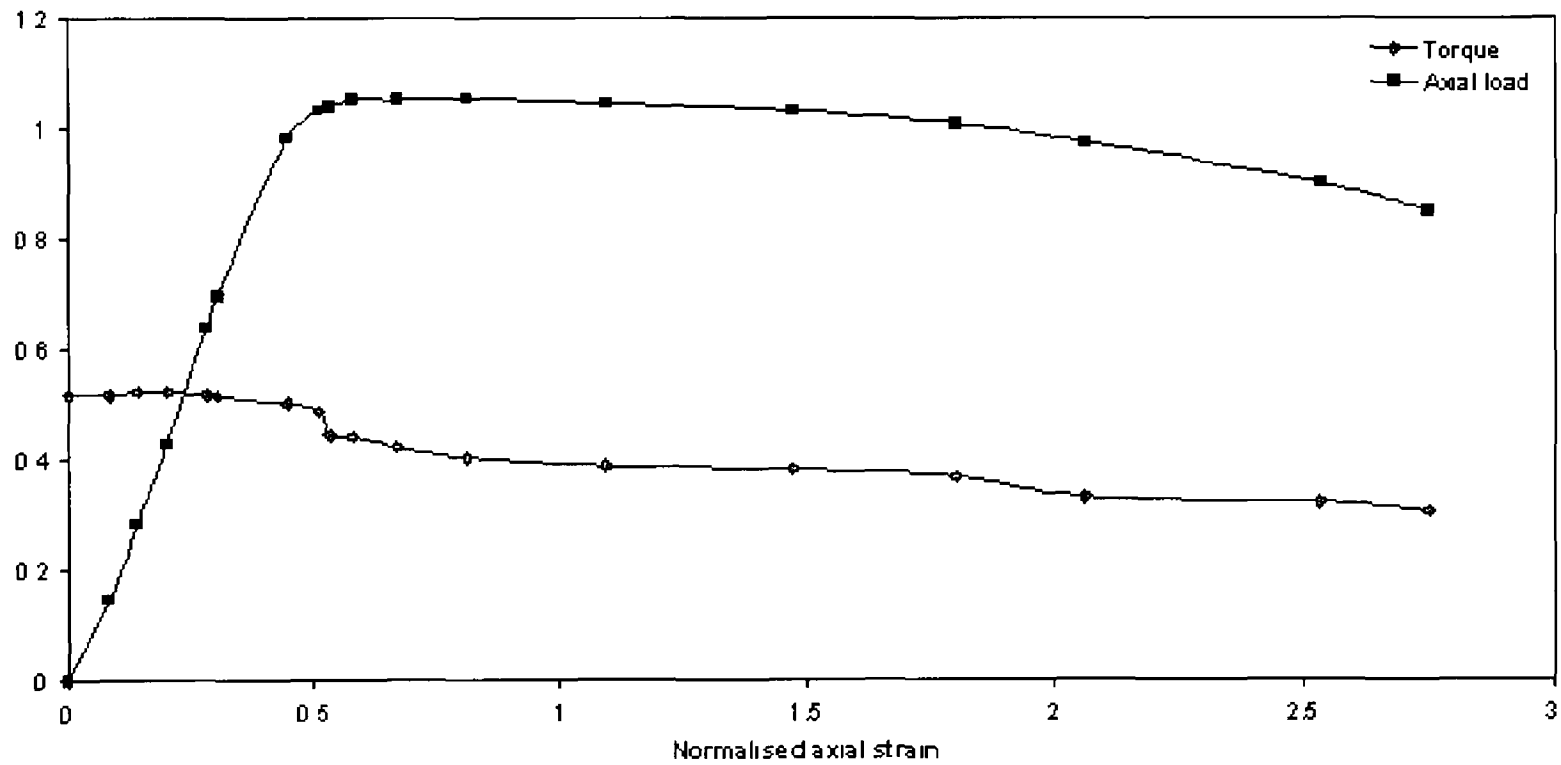


Figure 4.14 Normalised axial strain versus normalised torque and load curve (T = 50% YT)

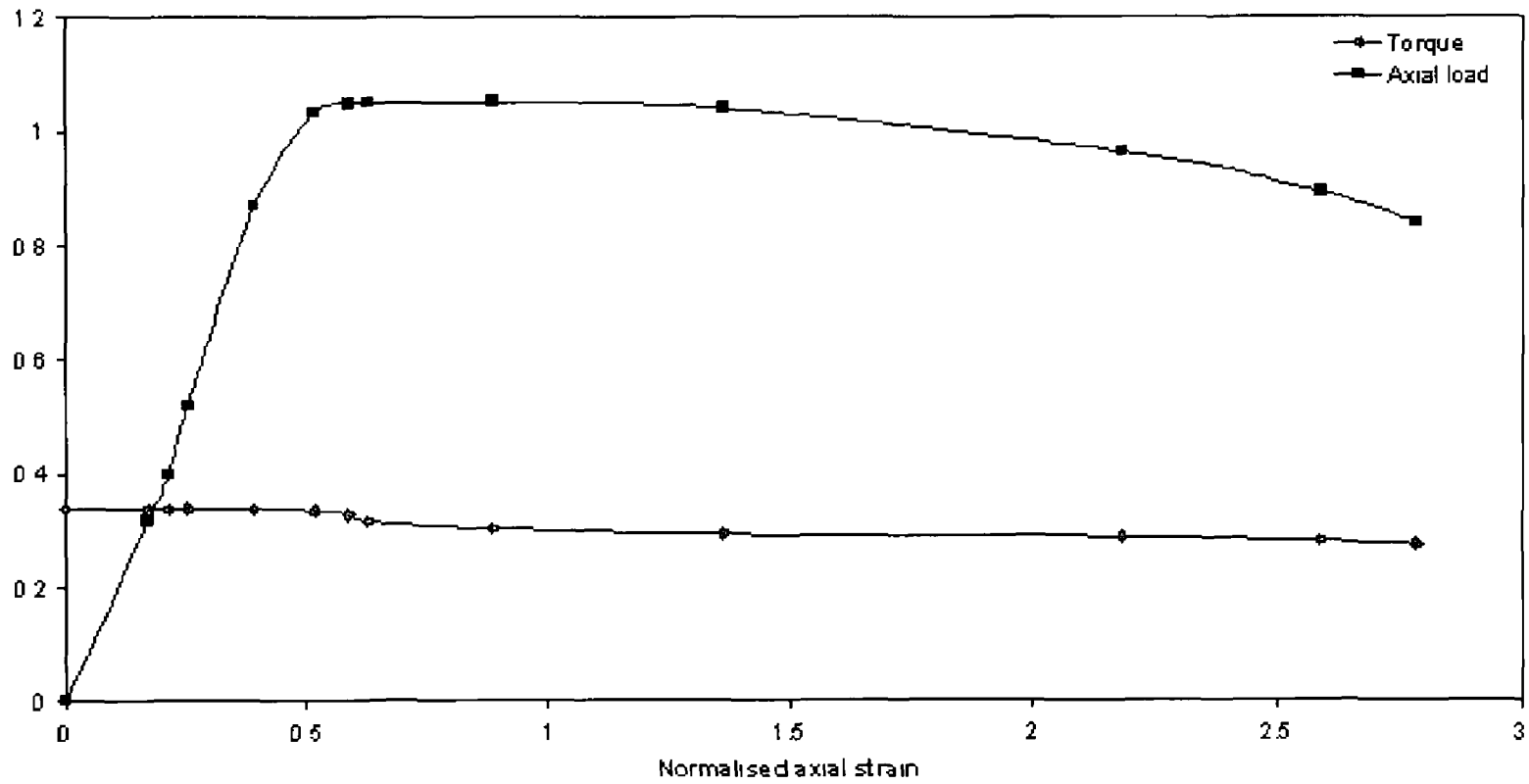


Figure 4.15 Normalised axial strain versus normalised torque and load curve ($T = 25\%Y_T$)

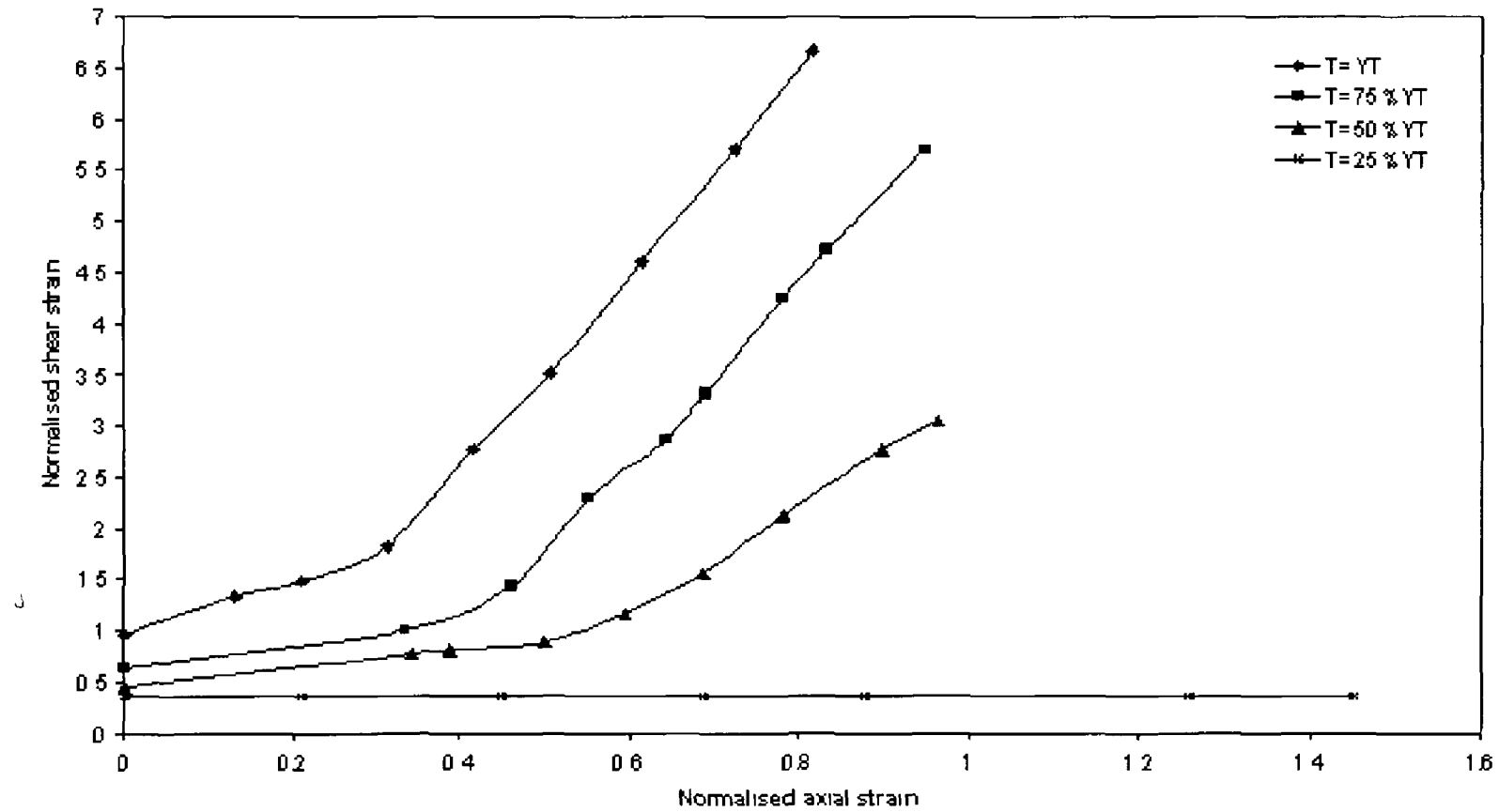


Figure 4 16 Normalised axial strain versus normalised shear strain (torque maintained constant)

strain increases, the outer layer begins to yield and as the torque carrying ability reduces to maintain the initially applied torque constant, the shear strain begins to increase rapidly

4 3 3 DETERMINATION OF YIELD POINTS

The magnitude of the combined stresses when the material yielded due to combined loading were determined for two types of the loading paths. In the first loading path, where the axial displacement maintained constant, the experimental results shown in figure 4 4 are replotted in terms of axial and shear stresses and are shown in figure 4 17. The shear stress, from the corresponding torque reading, was calculated according to the following procedure. When a rod is subjected to pure torsion it becomes plastic initially at the outermost fibre. Further application of the stress increases the size of the plastic annulus and moves towards the axis of the rod. Theoretically, at any time of the torsion testing, there exists an elastic core until failure of the rod. The using of the shear stress formula when the rod is twisted beyond yield point becomes irrelevant due to the presence of the elastic and plastic sections. In this research work the shear stress values beyond the yield point was computed by graphical interpolation method. The shear stress-shear strain curve is initially plotted using elastic formula. A few points on the curve are picked at regular intervals. A graph is drawn to represent half the rod specimen. The x-axis is taken as the radius of the rod and ordinates as shear stress. The yield stress and shear stress corresponding to the first point are plotted at the outer radius of the rod. The deviation in the stress-strain curve between yield point and first point in the graph is exactly traced on the rod graph. The intersection of this curve and the outer fibre of the rod will give the actual shear stress in the rod. The reduction in the elastic-plastic shear stress compared to the elastic stress will be less in the first point and increases with every other point. The slope of the elastic-plastic curve, depending on the strain hardening property of the material, becomes saturated at a certain inclination.

In the second loading path, where the angle of twist is maintained constant, the experimental results shown in figure 4 10 are replotted in terms of axial and shear

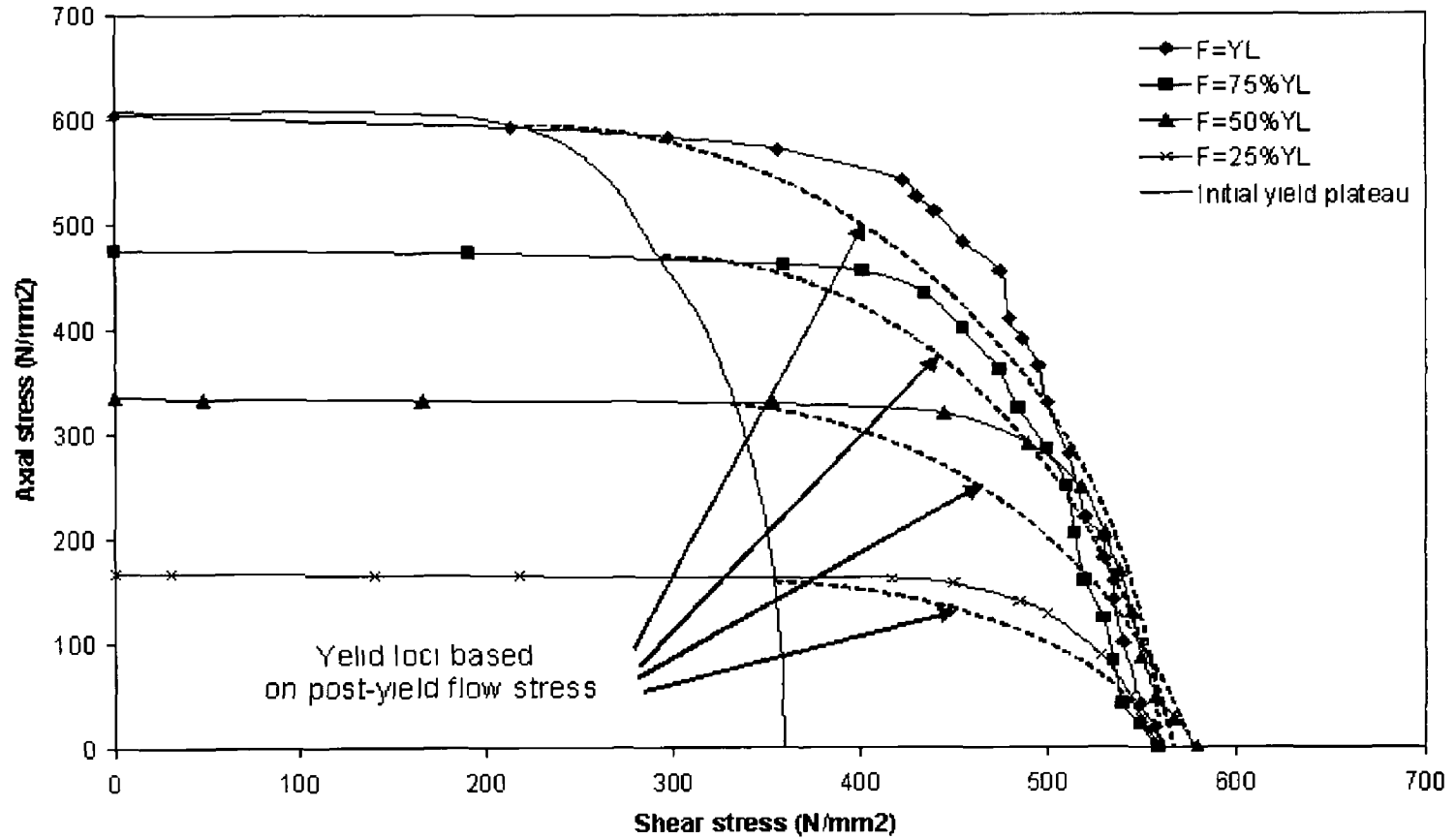


Figure 4 17 Axial stress versus shear stress (constant axial displacement)

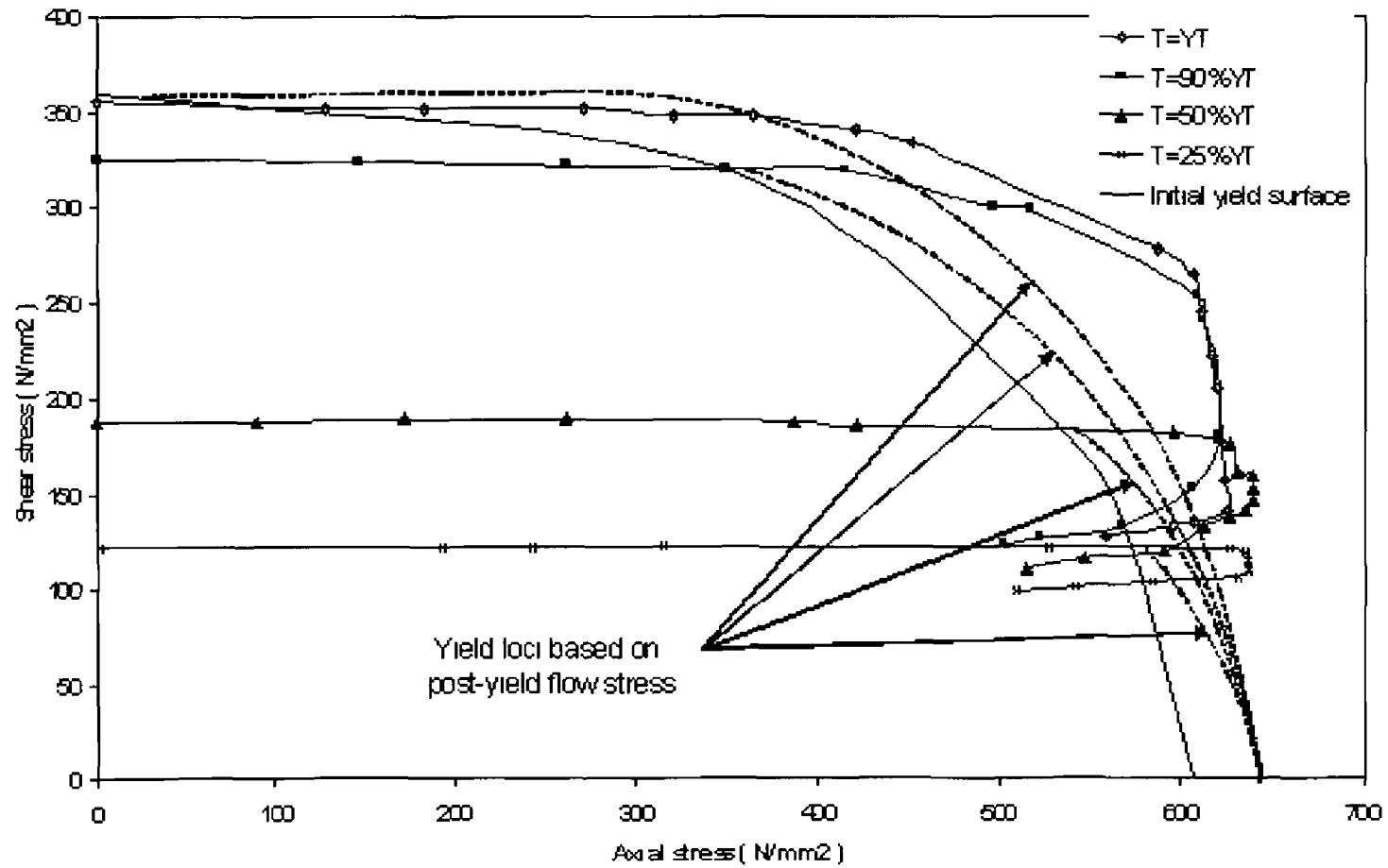


Figure 4.18 Axial stress versus shear stress (constant angle of twist)

stresses and are shown in figure 4 18 The shear stress was calculated similarly as mentioned in the first loading path

The three dashed lines are the Mises yield loci based on the post yield flow stress of the steel rod specimen while the solid line is the initial yield locus based on the proof stress as shown in figures 4 17 and 4 18 It can be seen from these figures that most of the experimental points of the combined loading are in the domain of these yield loci which are based on the post yield flow stress It can be also seen that few points remain outside these domains which may be due to the fact that von Mises yield criteria is not in its own the governing factor of the material response in the plastic region, as the behaviour of the material is strongly dependent on the loading path in the plastic region The figures also reveal that most of the experimental points are lying beyond the initial yield locus due to the strain hardening of the material

The following procedure was adopted to determine the combined stress of the steel rod specimen when yielding started In figure 4 18 the initially applied shear stress remains unchanged until the axial stress reaches a certain value when plastic yielding starts, hence the axial stresses, which correspond to the initiation of the decrease of the shear stresses, were determined from the figure These axial stresses and the initial value of the shear stresses were normalised and plotted as shown in figure 4 19 The upper solid line in figure 4 19 is von Mises' criteria while the lower one is Tresca's criteria The von Mises' and Tresca's curves were drawn according to the equations $\sigma^2 + 3\tau^2 = Y^2$ and $\sigma^2 + 4\tau^2 = Y^2$ respectively It is observed from this figure that most of the experimental points inclined towards the Mises' ellipse Therefore it can be concluded that the results confirm the general thought that the Mises' yield criteria is best yield criteria for metals

4 4 COMBINED LOADING OF THIN-WALLED TUBES

4.4.1 TORSION FOLLOWED BY TENSION

Angle of Twist Maintained Constant

The uniaxial tensile and pure torsion tests were carried out on thin-walled tube specimens Two tension tests were carried out on virgin specimens under the same

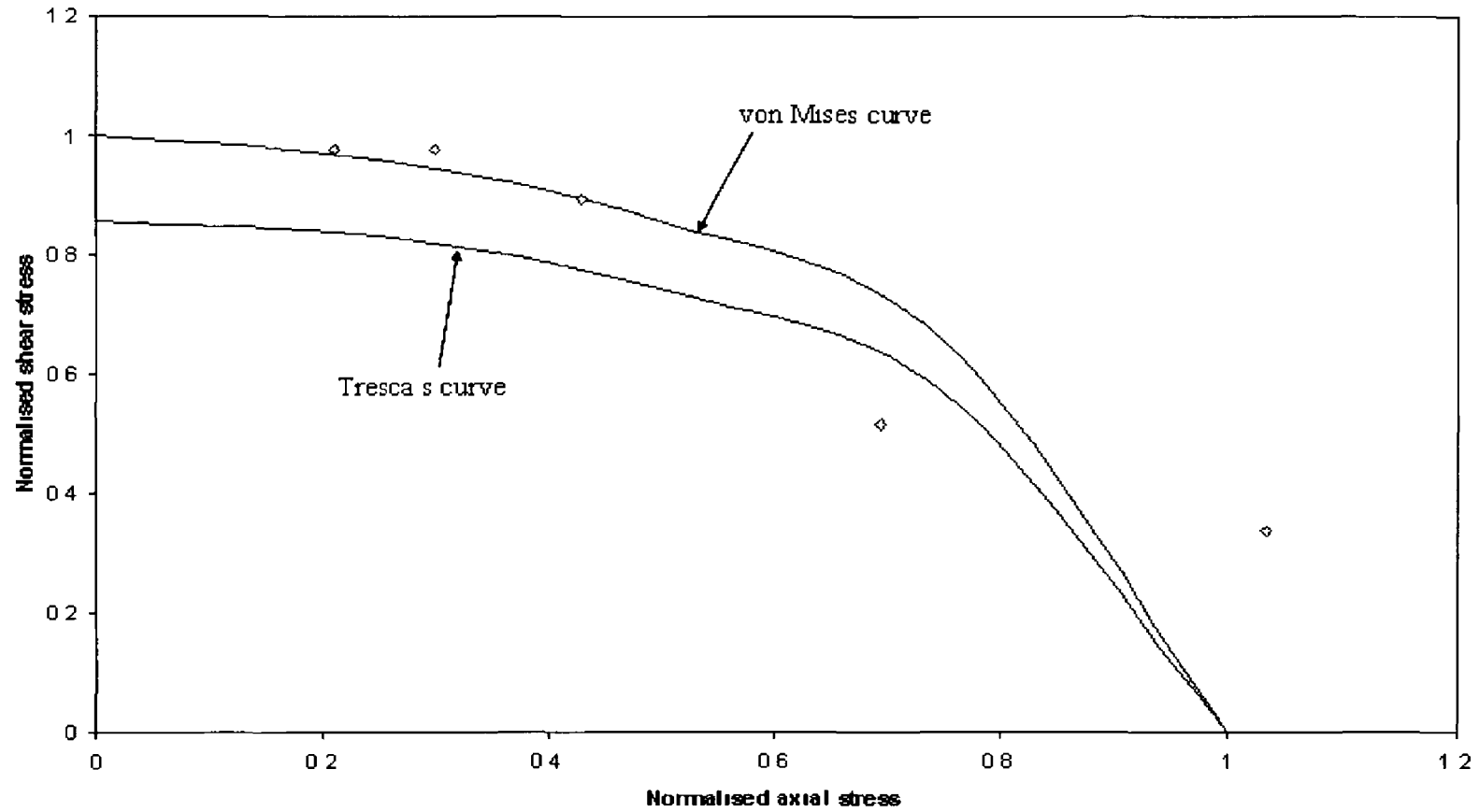


Figure 4.19 Comparison of experimentally obtained yield stresses with those of Mises' and Tresca's

loading conditions and the proof axial stress at 0.2 percent offset. The uniaxial tensile load versus the axial strain curve of the thin-walled tube is shown in figure 4.20. The corresponding axial yield load was averaged to be 5.2 kN. Two pure torsion tests were carried out on virgin specimens under the same loading conditions and the proof yield torque was averaged to be 8.8 Nm, figure 4.21 shows the torque-shear strain curve for the thin-wall tube used in this investigation. The mechanical properties of the thin-walled tubes are given in table 4.2.

Table 4.2 Mechanical properties of the thin-walled tube

Modulus of elasticity (GPa)	Modulus of rigidity (GPa)	Tensile yield load (kN)	Yield torque (Nm)	Tensile yield stress (MPa)	Shear yield stress (MPa)
210	73	5.2	8.8	311.7	201.4

In this loading mode the tube was subjected to an initial torque and then, holding its corresponding angle of twist constant, the axial load was gradually increased beyond the uniaxial tensile load of the tube. This procedure was repeated for four different initial torques equal to 1.0, 0.75, 0.50, and 0.25 of the yield torque.

Figure 4.22 shows the variation of the initially applied normalised torque with the subsequent application of the normalised axial load, for different levels of initially applied torque. The figure reveals that the magnitude of the initially applied torque remains constant until the gradually applied axial load reaches a specific value which when combined with the torque causes the material to yield. As the axial load increases the torque begins to decrease rapidly and reaches to almost nil and the axial load reaches to about 1.01 times the yield axial load. Thereafter any increase in the axial load causes the onset of plastic instability and necking of the specimen. The experimental results are plotted in terms of shear stress and axial stress as depicted in figure 4.23. It appears from the figure that the specimen subjected to high initial

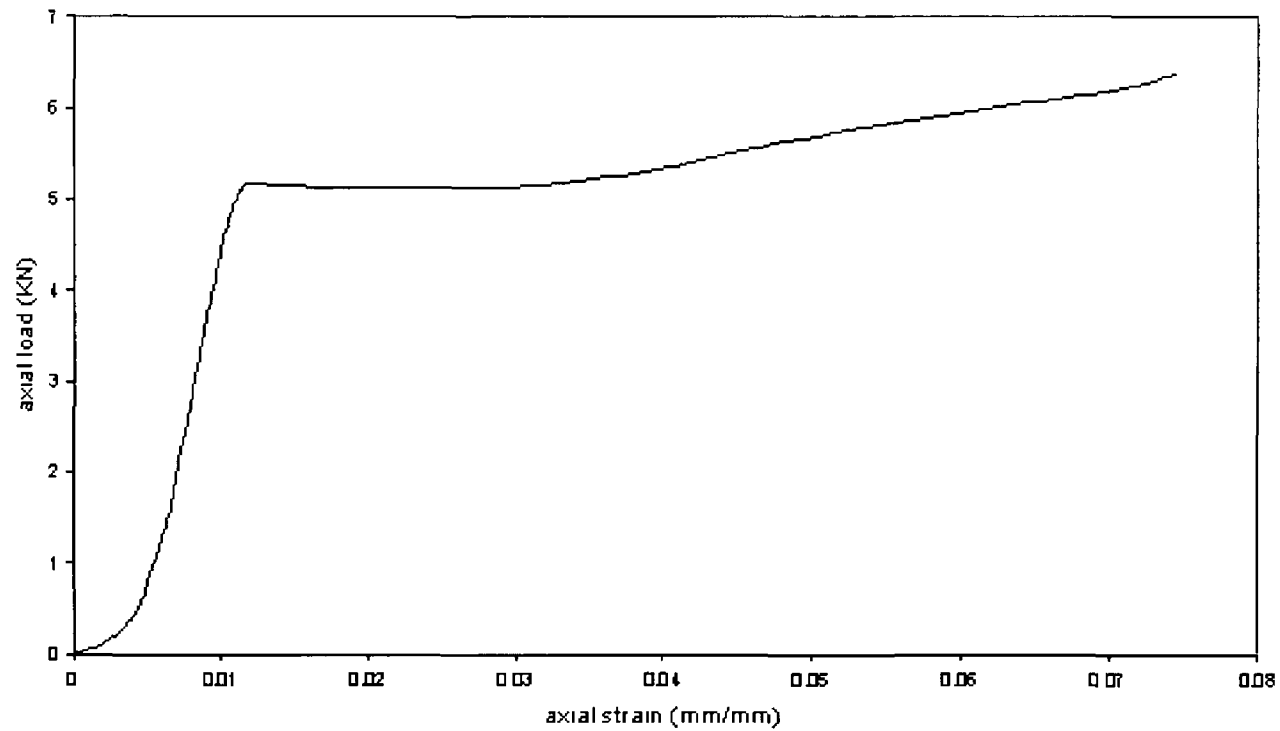


Figure 4 20 The uniaxial tensile load versus the axial strain curve of the thin-walled tube

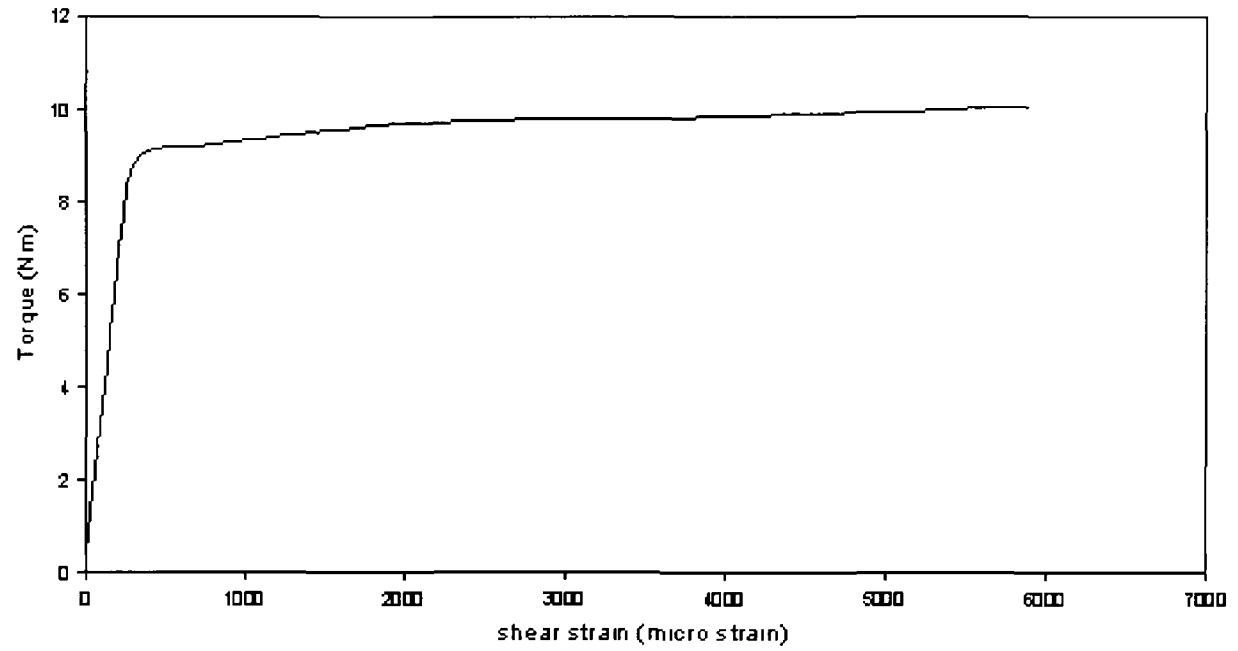


Figure 4 21 torque versus shear strain curve of thin-walled tube

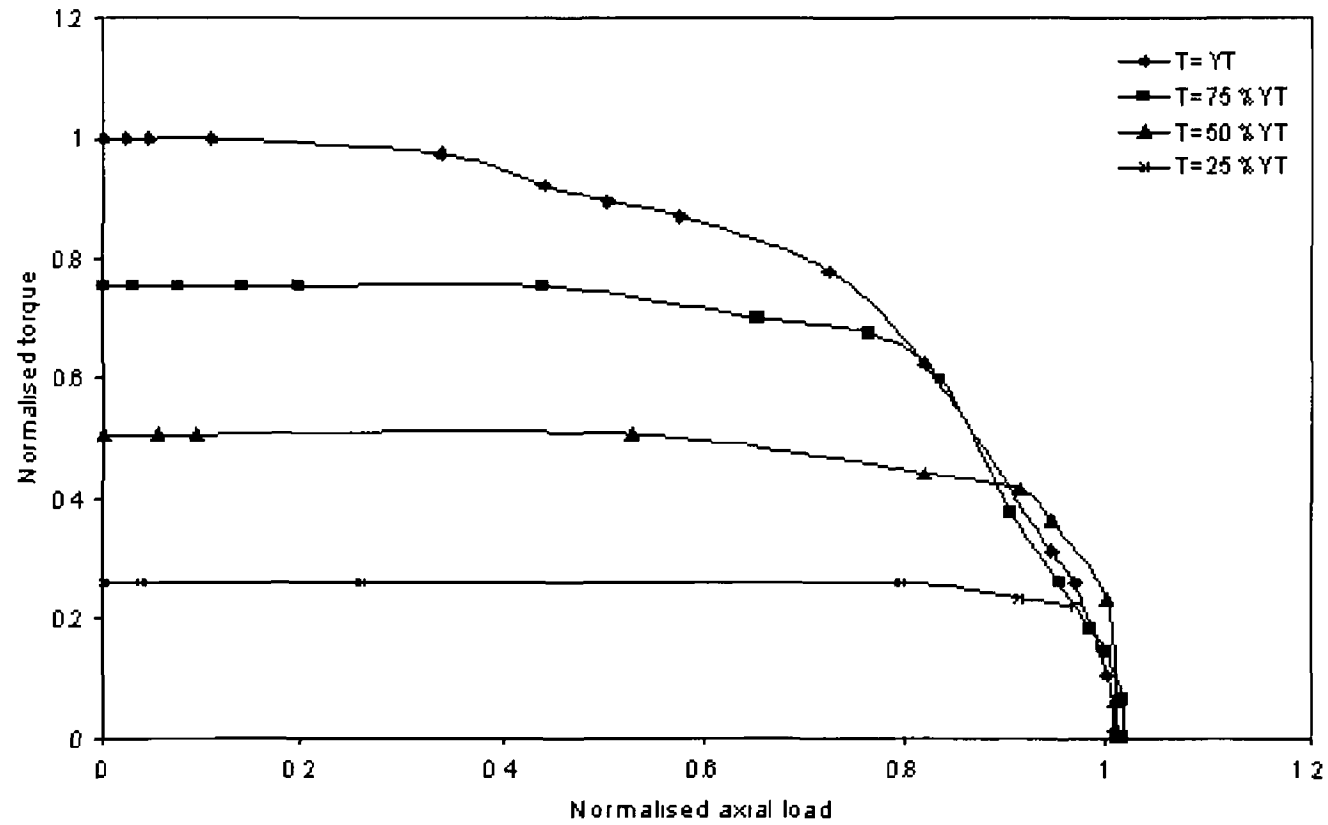


Figure 4.22 Normalised torque versus normalised axial load curve (angle of twist constant)

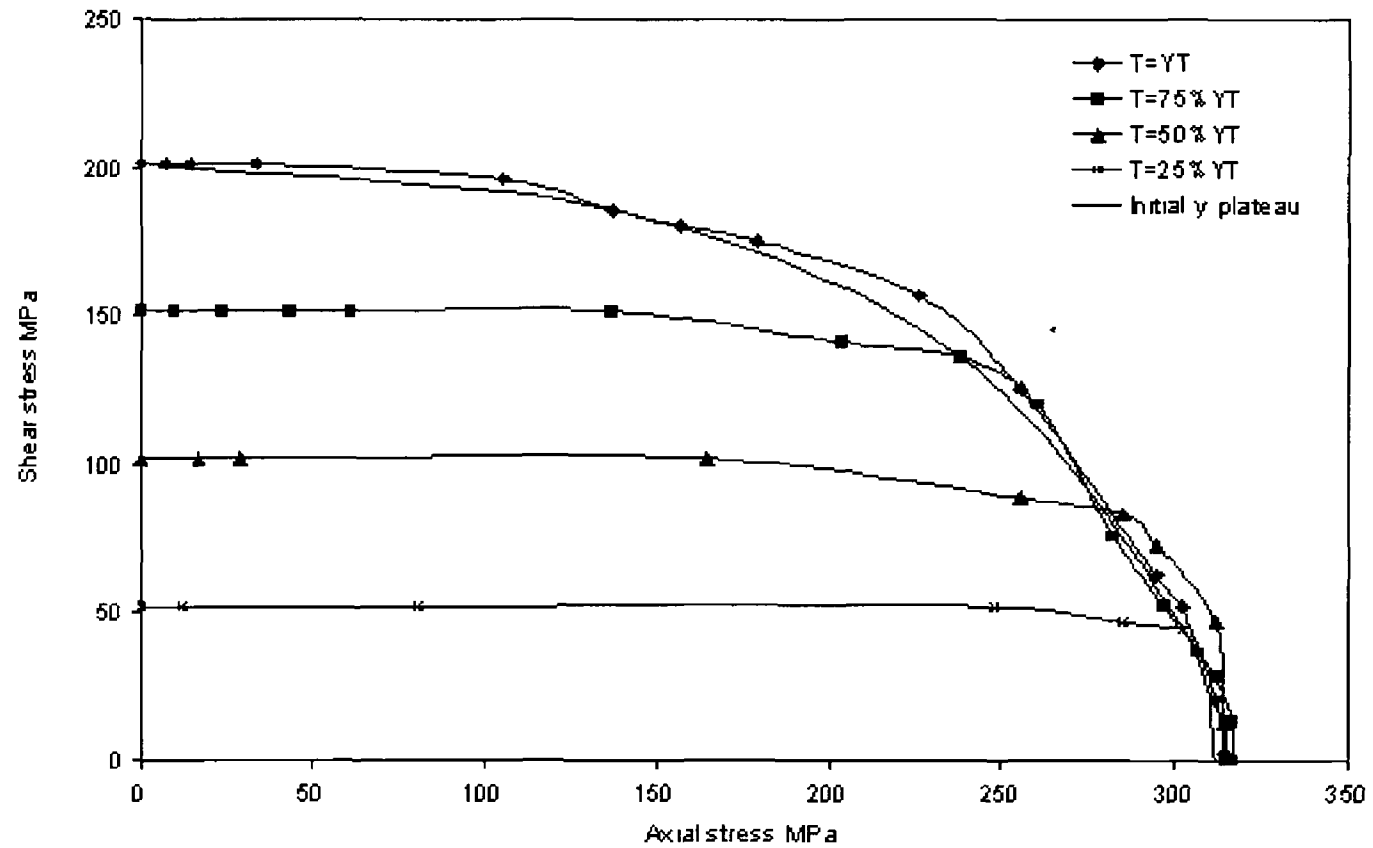


Figure 4.23 Axial stress versus shear stress (constant angle of twist)

torque followed by application of the axial load yields plastically at an early stage than the specimen subjected to lower initial torque, this is due to the fact that the combined stress level meets the von Mises yield plateau at an early stage. Furthermore, it is also observed from the figure that most of the experimental points lie beyond the initial yield locus due to the strain hardening of the material.

The comparison of the thin-walled tube's result with the solid rod result for this type of loading is shown in figure 4.25. It can be seen from the figure that the rate of decrease of the torque with the increase in the axial strain is much faster in the thin-walled tube than the solid rod, because the distribution of the shear stress in the tube is linear and is non-linear in the solid rod. The figure reveals that, in the thin-walled tube, the residual torque left within the tube is much less than the solid rod. It can be concluded that for a thin-walled tube, the sustainability of the initially applied torque will be reduced to almost nil due to the subsequent application of the axial load.

4.4.2 TENSION FOLLOWED BY TORSION

Axial Displacement Held Constant

In the second loading path, the tube was subjected to an initial axial load and then, holding its corresponding axial displacement constant, the torque was gradually increased quasi-statically beyond the yield torque. This procedure was repeated for three different initial axial loads equal to 50, 75 and 100 percent of the yield axial load. The experimental points for this type of loading have been plotted in terms of normalised axial load and normalised torque for different levels of initially applied axial loads and are presented in figure 4.24. It can be seen from the figure that as the torque increased gradually, the initially applied axial load remains unchanged for a certain level of torque and then it starts to decrease slowly until the von Mises yield condition produced by the combined axial load and torque. After that the axial load in the specimen decreases rapidly as the load carrying capability is drastically reduced. When the specimen is subjected to a higher initial axial load and then the torque is applied gradually, the initially applied axial load begins to decrease at a greater rate at the initial stage of loading and tends to drop rapidly at 0.65 times the yield torque. When the initial axial load is smaller, the subsequent holding capacity of the

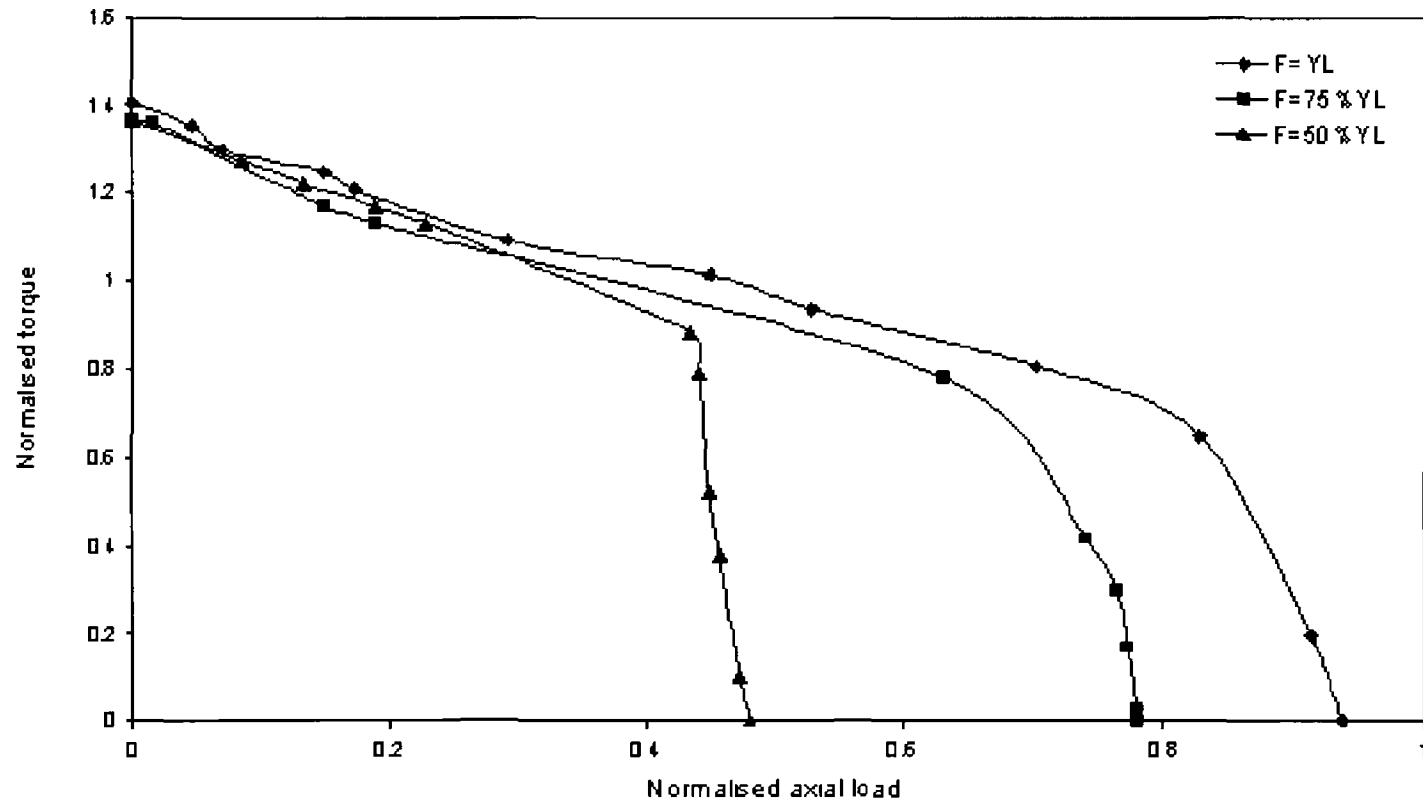


Figure 4 24 Normalised torque versus normalised axial load (axial displacement constant)

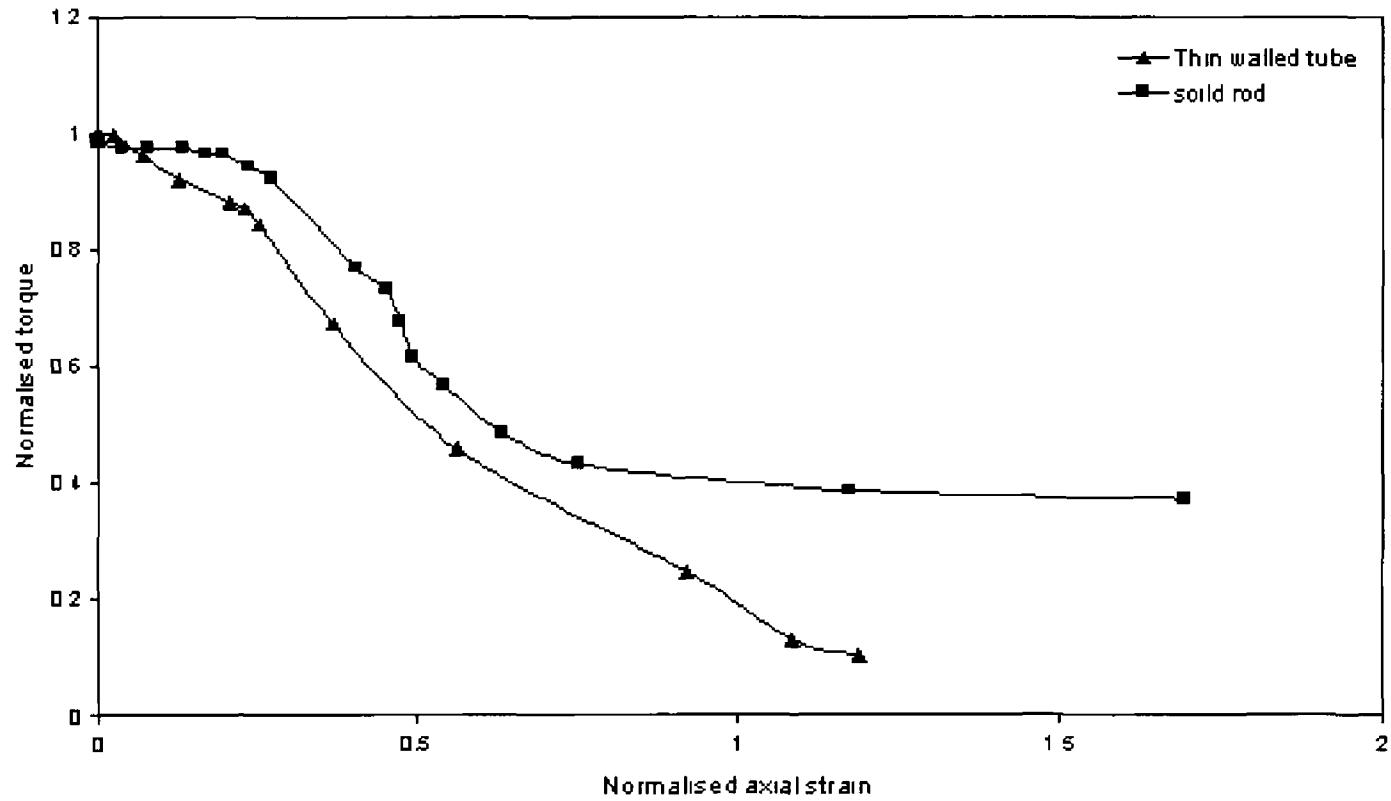


Figure 4.25 Comparison of thin-walled tube's results with solid rod (angle of twist constant)

specimen is extended to 0.88 times the yield torque after which yielding occurs rapidly. All the curves have exceeded the yield torque and moved towards the maximum torque the specimen can carry.

The comparison of the thin-walled tube and solid rod results are depicted in figure 4.26. The figure shows the reduction in the sustainability of the normalised axial load with the increase in the applied normalised shear strain. It is observed from the figure that the axial load decreases very rapidly with the shear strain in the thin-walled tube compared to the solid rod.

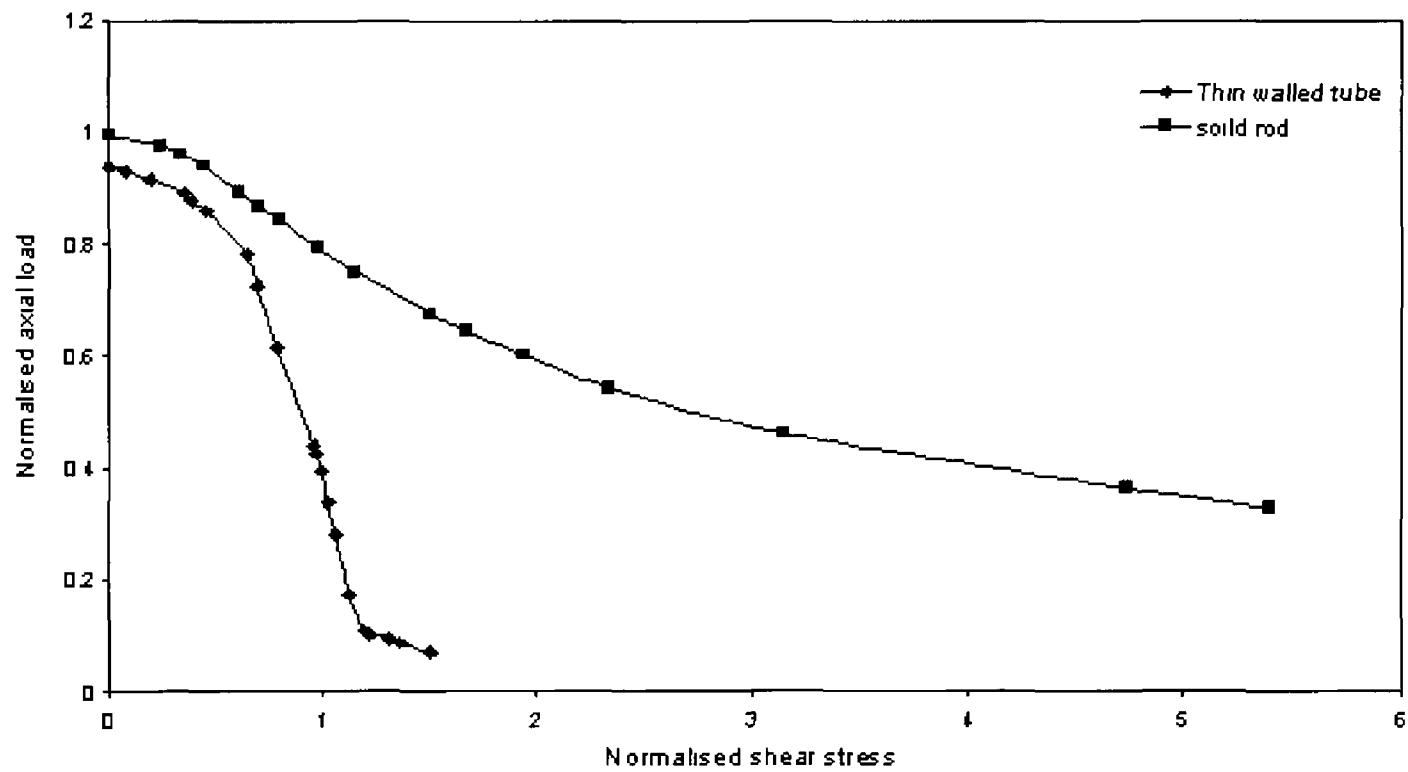


Figure 4.26 Comparison of thin-walled tube's results with solid rod (axial displacement constant)

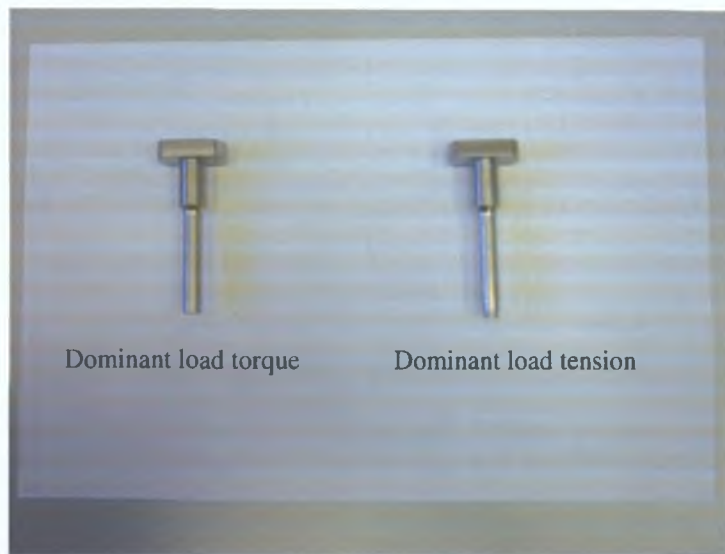


Plate 4.1-Fracture mode of the solid rod specimen

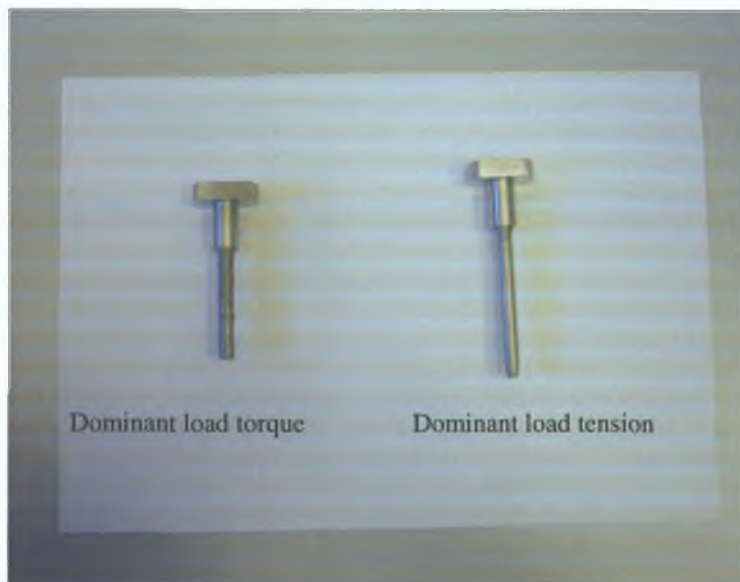


Plate 4.2-Fracture mode of the tube specimen

CHAPTER FIVE

FINITE ELEMENT ANALYSIS

5.1 INTRODUCTION

This chapter is divided into two sections. First section is devoted to the basic theoretical outline of the numerical methods used to solve the combined tension-torsion loading of steel rods. The second section details the modelling, loading and boundary conditions used to simulate the problem. The results from the simulations are presented and analysed.

5.2 The Finite Element Method

The finite element method (FEM) is a numerical procedure that can be applied to obtain solutions to a variety of problems in engineering, steady transient, linear or non-linear problems in stress analysis, heat transfer, fluid flow and electromagnetics problems. A basic theoretical outline of the method presented in this section is drawing mostly from reference [75]. In any finite element analysis, the basic steps consist of the following:

- i) **Discretization** The problem is divided into a number of finite subdomains each of simple geometry. Each subdomain called element has a number of nodal points, the locations in space of which are given in co-ordinates relative to a set of global axes. The shape of each element is defined in terms of these co-ordinates by interpolation or shape function.
- ii) **Assume a variation of unknown** An interpolation function is proposed for the variation of the unknown (i.e. displacement, temperature etc. depending on the analysis) inside each element in terms of values at the nodes. These interpolation functions in many cases are the same as the shape functions used to describe the element shape.

- iii) Finite element response matrices For each element, coefficient matrices which describe the response characteristics of the element are determined
- iv) Assemble the element matrices The stiffness matrices of the individual elements are combined to determine the stiffness matrix for the entire problem domain This forms a matrix equation defining the behaviour of the entire solution domain
- v) Application of boundary conditions Some of the nodal unknowns must be restrained in order to solve the problem
- vi) Solve the system of equations The primary nodal unknowns are determined by solving a set of equations In most problems the number of equations is very large, thus special solution techniques are employed After solution the values of the dependant variables at all the nodes of the domain are unknown
- vii) Determine other variables Using the nodal values and interpolation functions, other parameters such as stresses and strains are determined

5 2 1 General Theory

There are many methods available for determining the governing equations of equilibrium for finite element method One of these methods is the use of the principle virtual displacements (which is also called the principle of virtual work) to express the equilibrium of the body This principle states that the equilibrium of the body requires that for any compatible, small virtual displacements which satisfy the essential boundary conditions imposed on the body, the total internal virtual work is equal to the total external virtual work For a three dimensional body with body forces f^B , surface traction f^S , and concentrated forces F^I resulting in virtual displacement U , virtual stress σ and virtual strain ϵ , the principle can be stated as

$$\int_V \{\bar{\epsilon}\}^T \{\sigma\} dv = \int_V \{\bar{v}\}^T \{f^B\} dv + \int_S \{\bar{U}\}^T \{f^S\} ds + \int_I \{\bar{U}\}^T F^I \quad (1)$$

where,

$$\{\bar{\epsilon}\}^T = [\bar{\epsilon}_{xx} \quad \bar{\epsilon}_{yy} \quad \bar{\epsilon}_{zz} \quad \bar{\gamma}_{xx} \quad \bar{\gamma}_{yy} \quad \bar{\gamma}_{zz}]$$

$$\{\bar{U}\}^T = [U \quad V \quad W] \quad \bar{U}, \bar{V} \text{ and } \bar{W} \text{ are displacements in global directions}$$

$$\{f^B\}^T = [f_x^B \quad f_y^B \quad f_z^B] \quad \text{superscript B indicates body}$$

$$\{f^S\}^T = [f_x^S \quad f_y^S \quad f_z^S] \quad \text{superscript S indicates surface}$$

$$\{F^I\}^T = [F_x^I \quad F_y^I \quad F_z^I] \quad \text{superscript I indicates points}$$

In the finite element analysis the problem domain is approximated as an assemblage of discrete finite elements with the elements being interconnected at nodal points on the element boundaries. The displacements measured within each element are assumed to be a function of the displacements at the nodal points. Therefore, for element m ,

$$U^{(m)}(X,Y,Z) = H^{(m)}(X,Y,Z) \hat{U} \quad (2)$$

where $H^{(m)}$ is the displacement interpolation matrix or shape function for element m and \hat{U} is a vector of the three global displacements U_i, V_i and W_i at all nodal points, including those at the supports of the element assemblage, i.e., \hat{U} is a vector of dimension $3N$.

Using the assumption on the displacements within each finite element, as expressed in equation (2), equilibrium equations that correspond to the nodal point displacements of the assembly of finite elements can be derived from equations (1) and (2)

$$\sum_m \int_{V^{(m)}} \epsilon^{(m)T} \sigma^{(m)} dV^{(m)} = \sum_m \int_{V^{(m)}} \bar{U}^{(m)T} f^{B(m)} dV^{(m)} + \sum_m \int_{S^{(m)}} \bar{U}^{S(m)T} f^{S(m)} dS^{(m)} + \sum_m \bar{U}^{iT} F^I \quad (3)$$

within the assumption on the displacements in equation (2) the corresponding element strains can be evaluated as

$$\boldsymbol{\varepsilon}^{(m)} (X,Y,Z) = \mathbf{B}^{(m)} (X,Y,Z) \quad (4)$$

where

$\mathbf{B}^{(m)}$ is the strain-displacement matrix for element m. The rows of $\mathbf{B}^{(m)}$ are obtained by appropriately differentiating and combining rows of matrix $\mathbf{H}^{(m)}$

The stress within a finite element are related to the element strains and the element initial stresses by

$$\boldsymbol{\sigma}^{(m)} = \mathbf{D}^{(m)} \boldsymbol{\varepsilon}^{(m)} + \boldsymbol{\sigma}^{I(m)} \quad (5)$$

where

$\mathbf{C}^{(m)}$ is the matrix relating strain to stress of element m and $\boldsymbol{\sigma}^{I(m)}$ is the element initial stresses. $\mathbf{C}^{(m)}$ is essentially a matrix which contains the material behaviour of the element and can vary from element to element, substituting equations (2),(5) in to equation (3) for the element displacements, strains and stresses,

$$\bar{\mathbf{U}}^T \left[\sum_m \int_{V(m)} \mathbf{B}^{(m)T} \mathbf{D}^{(m)} \mathbf{B}^{(m)} dV^{(m)} \right] \hat{\mathbf{U}} = \hat{\mathbf{U}}^T \left[\begin{array}{l} \left\{ \sum_m \int_{V(m)} \mathbf{H}^{(m)T} \mathbf{f}^{B(m)} dV^{(m)} \right\} + \\ \left\{ \sum_m \int_{S(m)} \mathbf{H}^{S(m)T} \mathbf{f}^{S(m)} dS^{(m)} \right\} - \\ \left\{ \sum_m \int_{V(m)} \mathbf{B}^{(m)T} \boldsymbol{\sigma}^{Im} dV^{(m)} \right\} + \mathbf{F} \end{array} \right] \quad (6)$$

where $\mathbf{H}^{S(m)}$ is the surface displacement interpolation matrix for element m, and is obtained from the volume displacement interpolation matrix $\mathbf{H}^{(m)}$, in equation (2) by substituting the element surface coordinates and \mathbf{F} is a vector of the externally applied forces to the nodes of the finite element assembly. It may be noted that i^{th} component in \mathbf{F} is the concentrated nodal force, which corresponds to i^{th}

displacement component in \hat{U} . In equation (6) the nodal point displacement vector, \hat{U} , is outside the summation sign as it is independent of the element considered. To obtain the equations for the unknown nodal point displacements from equation (6), virtual displacement theorem can be used by imposing unit virtual displacements in turn at all displacement components. This leads to $\hat{U}^T = I$ (where I is identity matrix) and denoting nodal point displacement by U , the equilibrium equation of the element assemblage corresponding to the nodal point displacements are

$$KU = R \quad (7)$$

The global stiffness matrix K is given by

$$K = \sum_m \int_{V^{(m)}} H^{(m)T} f^{B(m)} dV^{(m)} \quad (8)$$

The load vector $R = R_B + R_S - R_I + R_C$

Where R_B is the effect of the element body forces,

$$R_B = \sum_m \int_{V^{(m)}} H^{(m)T} f^{B(m)} dV^{(m)} \quad (9)$$

R_S is the effect of the element surface forces,

$$R_S = \sum_m \int_{S^{(m)}} H^{S(m)T} f^{S(m)} dS^{(m)} \quad (10)$$

R_I is the effect of the element initial stresses,

$$R_I = \sum_m \int_{V^{(m)}} B^{(m)T} \sigma^{I(m)} dV^{(m)} \quad (11)$$

and $R_C = F$ (i e the concentrated loads)

It can be noted that the summation of the element volume integrals in equation (8) expresses the direct addition of the element stiffness matrices $K^{(m)}$ to obtain the stiffness matrix of the total element assemblage. In the same way, the assemblage body force vector R_B is calculated by directly adding the element body force vectors $R_B^{(m)}$, R_S , R_I and R_C are similarly obtained. Equation (7) is a statement of the static equilibrium of the finite element mesh. In equilibrium consideration, applied forces may vary with time, in which case the displacements also vary with time and equation (7) is a statement of equilibrium for any specific point in time. However, if in actuality the loads are applied rapidly, inertia forces need to be considered, i e, a truly dynamic problem needs to be solved. Using d'Alembert's principle, the element

inertia forces may be included as part of the body forces. In such case equation (9) becomes

$$R_B = \sum_m \int_{V^{(m)}} H^{(m)T} [f^{B(m)} - \rho^{(m)} H^{(m)} U] dV^{(m)} \quad (12)$$

where f^B no longer includes inertia forces, U lists the nodal point accelerations and $\rho^{(m)}$ is the mass density of element m . In this case, the equilibrium equations are

$$MU + KU = R \quad (13)$$

where R and U are time independent. The matrix M is the mass matrix of the structure and is given by

$$M = \sum_m \int_{V^{(m)}} \rho^{(m)} H^{(m)T} H^{(m)} dV^{(m)} \quad (14)$$

In actually measured dynamic response of structures it is observed that energy is dissipated during vibration, which in vibration analysis is usually taken account of by introducing velocity-dependent damping forces as additional contributions to the body forces, equation (12) becomes as follows

$$R_B = \sum_m \int_{V^{(m)}} H^{(m)T} [f^{B(m)} - \rho^{(m)} H^{(m)} U - K^{(m)} H^{(m)} U] dV^{(m)} \quad (15)$$

where U is a vector of the nodal point velocities and $K^{(m)}$ is the damping property parameter of element m . In this case, the equilibrium equations are

$$MU + CU + KU = R \quad (16)$$

where C is the damping matrix of the structure and can be written as

$$C = \sum_m \int_{V^{(m)}} K^{(m)} H^{(m)T} dV^{(m)} \quad (17)$$

In the above formulation it is assumed that the displacements of the finite element assemblage are small that the material is linearly elastic and that the boundary conditions remains unchanged during the application of loads. The above assumptions have entered the equilibrium equation in the following forms

- (i) the fact that the displacements must be small have entered into the evaluation of the stiffness matrix K and load vector R , because all integrations have been performed over the original volume of the finite elements
- (ii) The strain-displacement matrix B of each element was assumed to be constant and independent of element displacements

- (iii) The assumption of a linear elastic material is implied in the use of a constant stress-strain matrix D
- (iv) The unchanged boundary conditions is implied by keeping constant constraint relations for the complete response

The above observations point to the different types of non-linearity that may arise in finite element analysis

- Non-linearity due to large displacements, large rotations, but small strains
- Non-linearity due to large displacements, large rotations and large strains
- Material non-linearity

5.2.2 Solution Methodology

The basic problem in a general non-linear analysis is to find the state of equilibrium of a body corresponding to the applied loads. Assuming that the externally applied loads are described as a function of time, the equilibrium conditions of a system of finite elements representing the body under consideration can be expressed as

$${}^tR - {}^tF = 0 \quad (18)$$

where tR lists the externally applied nodal point forces in the configuration at time t and the vector tF lists the nodal point forces that correspond to the element stresses in this configuration. Hence tR and tF can be expressed respectively as

$${}^tR = {}^tR_B + {}^tR_S + {}^tR_C \quad (19)$$

and

$${}^tF = \sum_m \int_{V^{(m)}} {}^tB^{(m)T} {}^t\sigma^{(m)} dV^{(m)} \quad (20)$$

where in general large deformation analysis the stresses as well as the volume of the body at time t are unknown

The equation (18) must express the equilibrium of the system in the current deformed geometry taking due account of all non-linearities. Considering the solution of the non-linearity response, it is recognised that the equilibrium equation (18) must be satisfied throughout the complete history of load application

There are three basic choices which must be made for the solution of the large deformation problems,

- (i) the type of mesh
- (ii) how the deformation is measured, and how the stresses are measured

When these choices are made the solution process is effectively carried out using step by step incremental analysis. The basic approach in an incremental step by step solution is to assume that the solution for the discrete time t is known and that the solution for discrete time $t + \Delta t$ is required, where Δt is a suitably chosen time increment. Therefore, considering equation (18) at time $t + \Delta t$, it can be written as

$${}^{t+\Delta t}R - {}^{t+\Delta t}F = 0 \quad (21)$$

since the solution is known at time $t + \Delta t$, then

$${}^{t+\Delta t}F = {}^tF + F \quad (22)$$

where F is the increment in nodal point forces corresponding to the increment of element displacements and stresses from time t to time $t + \Delta t$. This vector can be approximated using a tangent stiffness matrix tK which corresponds to the geometric and material conditions at time t

$$F \cong {}^tKU \quad (23)$$

where U is a vector of incremental nodal point displacements. Substituting equations (23) and (22) into equation (21),

$${}^tKU = {}^{t+\Delta t}R - {}^tF \quad (24)$$

and solving for U , an approximation to the displacements at time $t + \Delta t$ can be calculated,

$${}^{t+\Delta t}U \cong {}^tU + U \quad (25)$$

The exact displacement at time $t + \Delta t$ are those that correspond to the applied loads ${}^{t+\Delta t}R$. Only an approximation to these displacements is calculated by equation (24). Having evaluated an approximation to the displacements corresponding to time $t + \Delta t$, an approximation to the stresses and corresponding nodal point forces at time $t + \Delta t$ can be obtained, and then proceeded to the next time increment calculations. However, because of the assumption in equation (24), such a solution may be subjected to very significant errors and, depending on the time or load step

sizes used, may indeed be unstable. In practice, it is therefore necessary to iterate until the solution of equation (21) is obtained to sufficient accuracy. A different solution procedure is adopted for the solution of equation (24), depending on the type of the problem. The Newton-Raphson iterative procedure along with Gauss elimination method or other suitable method for the solution of the system of equations are employed for the static non-linear problems.

5.3 The Finite Element Analysis Package ANSYS

ANSYS is a general purpose finite element analysis package. It can simulate problems in area of structural mechanics, electromagnetic, heat transfer, fluid dynamics, acoustics and coupled problems. In structural analysis it has the capacity to analyse static or dynamic linear and non-linear problems. The simulations carried out in this research work are non-linear.

5.3.1 Solution Procedures

This section will outline the theoretical methods for the analysis drawing particularly from reference [77]. The Newton-Raphson method is a numerical method used by Ansys for iterative solution of the equilibrium equations presented in 5.2. Wave front solver or conjugate gradient solvers are used for the solution of the system of equations at each iteration. In this method an iterative solution is sought for equation (21) by defining the out of balance load vector $\Delta R_{(t+1)}$ as,

$$\Delta R_{(t+1)} = \{F^a\} - \{F^{nr}\} \quad (26)$$

where $\{F^a\}$ is applied load vector and $\{F^{nr}\}$ is the restoring load vector corresponding to the element internal loads.

$\Delta R_{(t+1)}$ by the virtual displacement principle is related as

$$[K_t^T] \{\Delta u_t\} = \Delta R_{(t+1)} = \{F^a\} - \{F_t^{nr}\} \quad (27)$$

and

$$\{u_{t+1}\} = \{u_t\} + \{\Delta u_t\} \quad (28)$$

$[K_i^T]$ and $\{F_i^{nr}\}$ are both evaluated based on the values given by $\{u_i\}$. The subscripts in the above equations refer to the iteration number. The restoring load vector $\{F_i^{nr}\}$ would be equal to the applied load vector $\{F^a\}$ or be within a small tolerance, that is the final converged solution would be in equilibrium. In non-linear analysis, the solution process requires the load applied in increments and performing the Newton-Raphson iteration at each load increment. The incremental time is automatically determined by number of factors such as number of equilibrium iteration needed, time point at which element will have a change of status, allowable plastic strain increment etc. Convergence is attained when vector norm

$$\|\{R\}\| < \epsilon_R R_{ref} \quad (29)$$

where $\{R\}$ is the residual vector and

$$\{R\} = \{F^a\} - \{F^{nr}\} \quad (30)$$

ϵ_R is tolerance (default = 0.001) and R_{ref} is reference values which is $\|\{F^a\}\|$ by default. The vector norm used in the analysis is the square root of the sum of the squares (SRSS) value of the terms expressed as,

$$\|\{R\}\| = (\sum R_i^2)^{1/2} \quad (31)$$

5.3.2 Large Strain Theory

The theory of large strain of ansys is used for elastic-plastic elements. Let the position vector of a body in the deformed and undeformed state are represented by $\{X\}$ and $\{x\}$ respectively, then the displacement vector $\{u\}$ is computed by

$$\{u\} = \{x\} - \{\bar{X}\} \quad (32)$$

The deformation gradient is defined as $[F] = \frac{d\{x\}}{d\{X\}}$ applied to equation (18) would

give

$$[F] = [I] + \frac{d\{u\}}{d\{X\}} \quad (33)$$

where $[I]$ is the identity matrix

The deformation gradient $[F]$ includes the volume change, the rotation and the shape change of the deforming body $[F]$ can be separated into a rotation and the shape change matrix using the right polar decomposition theorem

$$[F] = [R] [U] \quad (34)$$

where $[R]$ = rotation matrix and $[U]$ = right stretch (shape change) matrix

Once $[U]$ is known, a logarithmic strain measure can be obtained as

$$[F] = \text{In} [U] \quad (35)$$

Computationally, the evaluation of equation (35) is performed by one of the two methods using incremental approximation

$$[\mathcal{E}] = \int d[\mathcal{E}] \approx \sum [\Delta \mathcal{E}_n] \quad (36)$$

with

$$[\Delta \mathcal{E}_n] = \text{In} [\Delta U_n] \quad (37)$$

where $[\Delta U_n]$ is the increment of the stretch matrix computed from the incremental deformation gradient,

$$[\Delta F_n] = [\Delta R_n] [\Delta U_n] \quad (38)$$

where $[\Delta F_n]$ is

$$[\Delta F_n] = [F_n] [F_{n-1}]^{-1} \quad (39)$$

where $[F_n]$ is the deformation gradient at the current time step and $[F_{n-1}]$ is at the previous time step

Two methods are employed for evaluating equation (37), method 1 is

$$[\Delta \mathcal{E}_n] = \sum_{i=1}^3 \text{In}(\lambda_i) \{\rho_i\} \{\rho_i\}^T \quad (40)$$

where λ_i and $\{\rho_i\}$ are the eigen value and eigen vector for the i_{th} principle stretch increment of the incremental stretch matrix $[\Delta U_n]$

This method is employed by large strain solid elements. For standard solid and shell elements an approximate method is used by evaluating the deformation gradient at the midpoint configuration

$$[\Delta \mathcal{E}_n] = [R_{1/2}]^T [\Delta \bar{\mathcal{E}}_n] [R_{1/2}] \quad (41)$$

and

$$[\Delta \bar{\epsilon}_n] = [B_{1/2}] \{\Delta u_n\} \quad (42)$$

where, $[\Delta u_n]$ is the displacement increment over the time step and $[B_{1/2}]$ is the strain displacement matrix evaluated at the midpoint geometry

The computed strain increment can be then added to the previous strain $\{\Delta \epsilon_{n-1}\}$ to obtain the current total logarithmic strain

$$[\Delta \epsilon_n] = \{\epsilon_{n-1}\} + \{\Delta \epsilon_n\} \quad (43)$$

The strain is then used in the stress updating procedure in the stress-strain relationship matrix. The element matrices and load vectors are derived using an update Lagrangian formulation. The equilibrium equation of this form is

$$[K_i] \Delta u_i = \{F^{app}\} - \{F_i^{nr}\} \quad (44)$$

where $\{F^{app}\}$ is the applied force vector and $\{F_i^{nr}\}$ is the force obtained from Newton-Raphson current trial solution

The target matrix $[K_i]$ has the form

$$[K_i] = \int [B_i]^T [D_i] [B_i] dV \quad (45)$$

integrated over the element volume. $[B_i]$ is the strain displacement matrix in terms of current geometry and $[D_i]$ is the current stress-strain matrix. The Newton-Raphson restoring force,

$$F_i^{nr} = \int [B_i]^T \{\sigma_i\} dV \quad (46)$$

where $\{\sigma_i\}$ is the current Cauchy stress

In this work, only the isotropic hardening model was used. This model uses von Mises yield criteria and associated flow rule. The equivalent stress is given by

$$\sigma_e = \left[\frac{3}{2} \{S\}^T \{S\} \right]^{1/2} \quad (47)$$

where $\{S\}$ is the deviatoric stress. When σ_e is equal to the current stress σ_z , then the material is assumed to yield. The yield criterion is,

$$F = \left[\frac{3}{2} \{S\}^T \{S\} \right]^{1/2} - \sigma_z = 0 \quad (48)$$

For work hardening, σ_z is a function of the amount of plastic work done. For isotropic hardening σ_z is the equivalent stress corresponding to equivalent plastic strain in uni-axial stress-strain curve.

5.3.3 Elasto-Plastic Behaviour

Material non-linearities occur when the stress is a non-linear function of the strain. The relationship is also path dependent, that is, the stress depends on the strain history as well as the strain itself. The general theory for elasto-plastic analysis provides the user with three main elements: the yield criterion, the flow rule and the hardening rule. The yield criterion determines the stress level at which yielding is initiated. The flow rule determines the direction of plastic straining (i.e. which direction the plastic strain flows) relative to x, y, z axes. Finally, the hardening rule describes the changes the yield surface undergoes with progressive yielding, so that the various states of stress for subsequent yielding can be established. For an assumed perfectly plastic material the yield surface does not change during plastic deformation and therefore the initial yield condition remains the same. However, for a material experiencing strain hardening, plastic deformation is generally accompanied by changes in the yield surface. Two hardening rules are available and these are isotropic (work) hardening and kinematic hardening.

5.3.4 Material Model

ANSYS has an extensive library of material models available to the user [84]. In this research work a bilinear isotropic hardening plasticity model was used for all simulations.

5.4 Modelling

5.4.1 Solid Steel Rod

In any finite element simulation, the most important step is the idealisation and modelling of the deforming body. Good modelling of the deforming body is of most

importance to obtain an accurate solution. Simulations were carried out for a solid steel rod of 8.0mm diameter and 60.0mm length. The geometry of the rod was

Table 5.1 Material data used for material model (Solid Rod)

Young's Modulus, E	210 GPa
Tangent Modulus, E_{tan}	1.785 GPa
Poisson's Ratio, ν	0.30
Yield Strength, σ_Y	0.607 GPa

modelled to be consistent with the specimen used in the experiment. The elements used in the model are three dimensional, 20-node structural solid elements (solid95). A three dimensional structural surface effect element (surf154) is used to apply the torsion loading to the model. Figure 5.1 shows the finite element model of the rod used in the analysis. The model consists of 576 elements and the total amount of nodes in the model is 2777. The material properties used for the model were obtained from the experimental results and are shown in table 5.1.

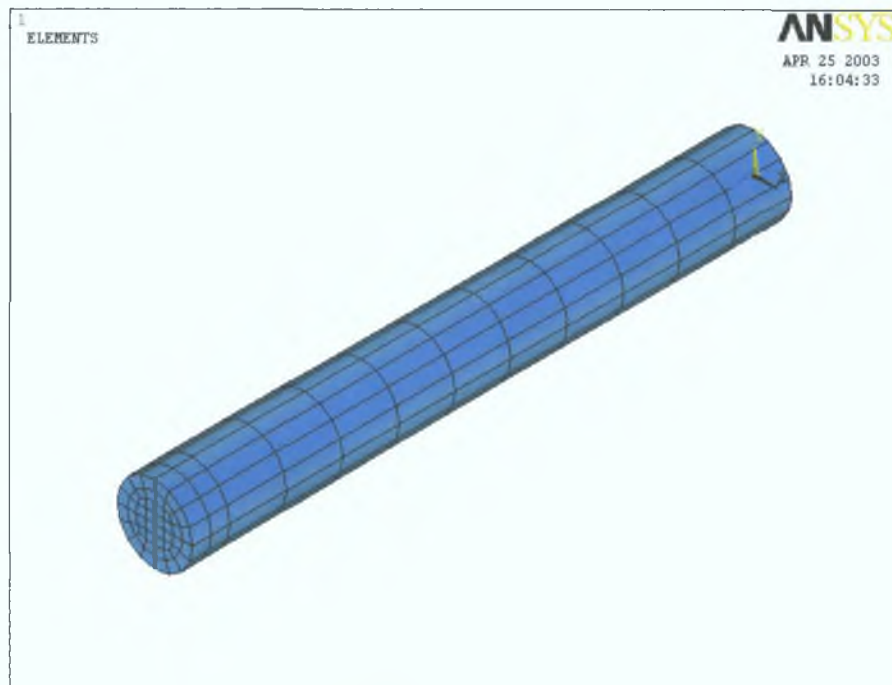


Figure 5.1 Finite Element Model (Solid Rod)

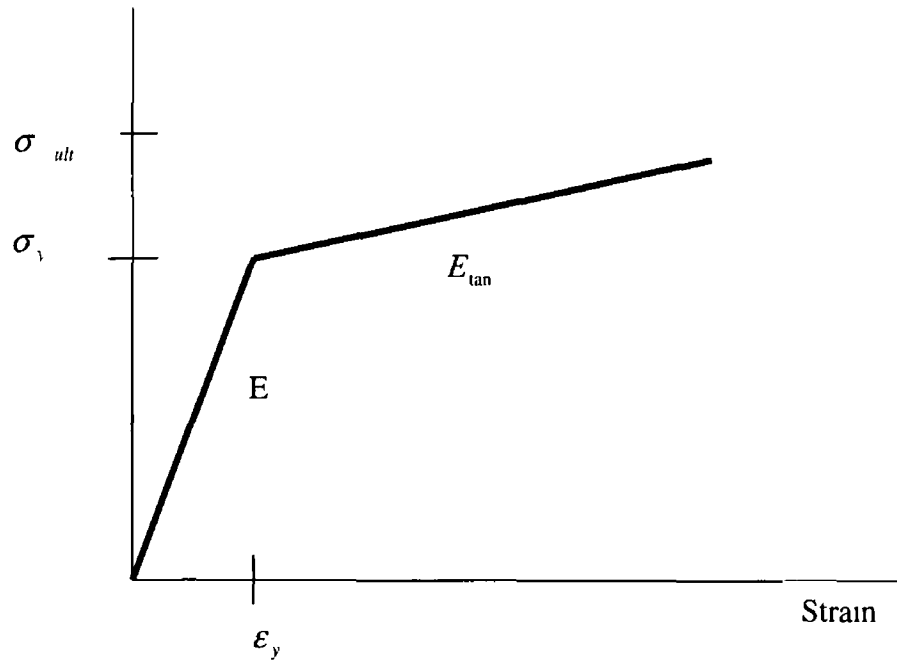


Figure 5.2 Material model used for the rod

A bi-linear elsto-plastic material model was used for the steel rod, as illustrated in figure 5.2. The summary of the theories involved in a material with bi-linear isotropic hardening behaviour are shown in table 5.2. The basic steps characterises a non-linear elasto-plastic analysis are shown in a brief flow chart in figure 5.5

Table 5.2 Summary of the theories involved in a material with bi-linear isotropic Hardening behaviour

Material option	Yield criteria	Flow rule	Hardening rule	Material response
Bi-linear isotropic hardening	von Mises	Associative (Prandtl-Reuss equs)	Isotropic	Bi-linear

5.4.2 Thin-Walled Tube

Simulations were carried out for a steel thin-walled tube of 6.80mm outer diameter, 5.0mm inner diameter and 60.0mm length. The geometry of the thin-walled tube was modelled to be consistent with the specimen used in the experiments. The elements used in the model are three dimensional, 20-node structural solid elements (Solid95). A 3-dimensional structure surface effect element (Surf154) is used to apply the torsion loading to the model. The finite element model of the thin-walled tube is shown in figure 5.3. The model consists of 432 elements and the total amount of nodes in the model is 2340. The material properties used for the model are obtained from experimental results and are shown in table 5.3. A bi-linear elasto-plastic material model was used for the thin-walled tube, as illustrated in figure 5.4.

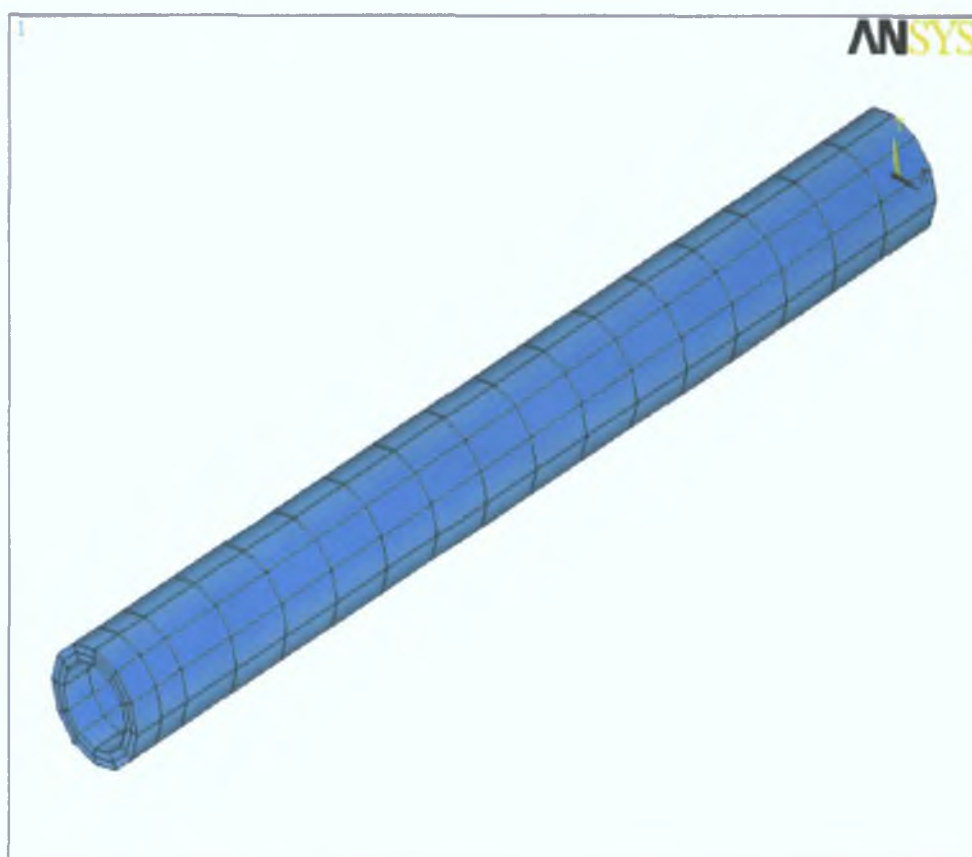


Figure 5.3 Finite element model (Thin-walled Tube)

Table 5 3 Material used for material model (thin-walled tube)

Young's Modulus, E	210 GPa
Tangent Modulus, E_T	2 1106 GPa
Poisson's Ratio, ν	0 30
Yield Strength, σ_y	0 3117 GPa

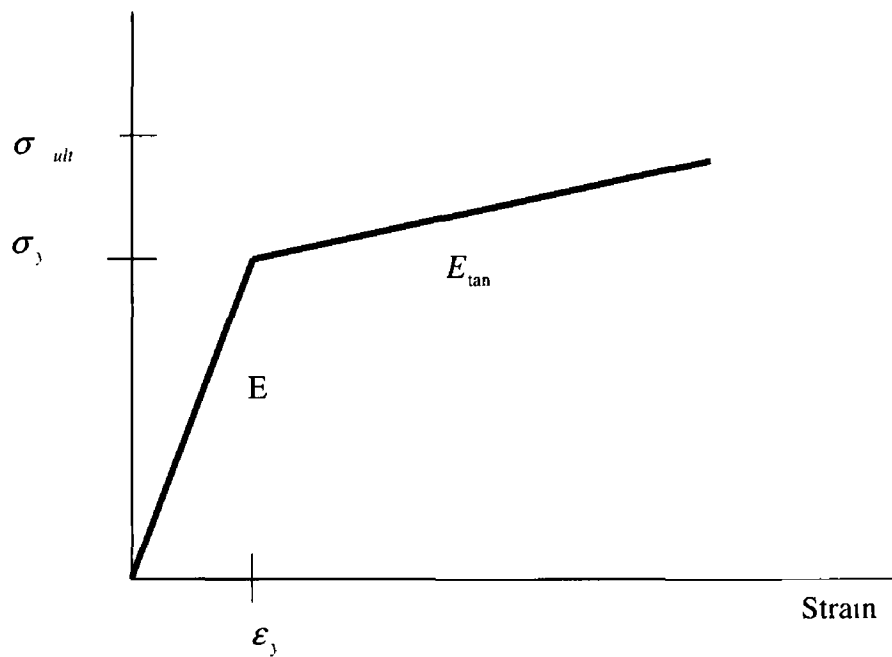


Figure 5 4 Material model used for tube

5.5 Boundary Conditions, Loading and Solution

The boundary condition was modelled by constraining all the degrees of freedom of the nodes at one end of the model and the load was applied at the other end. The

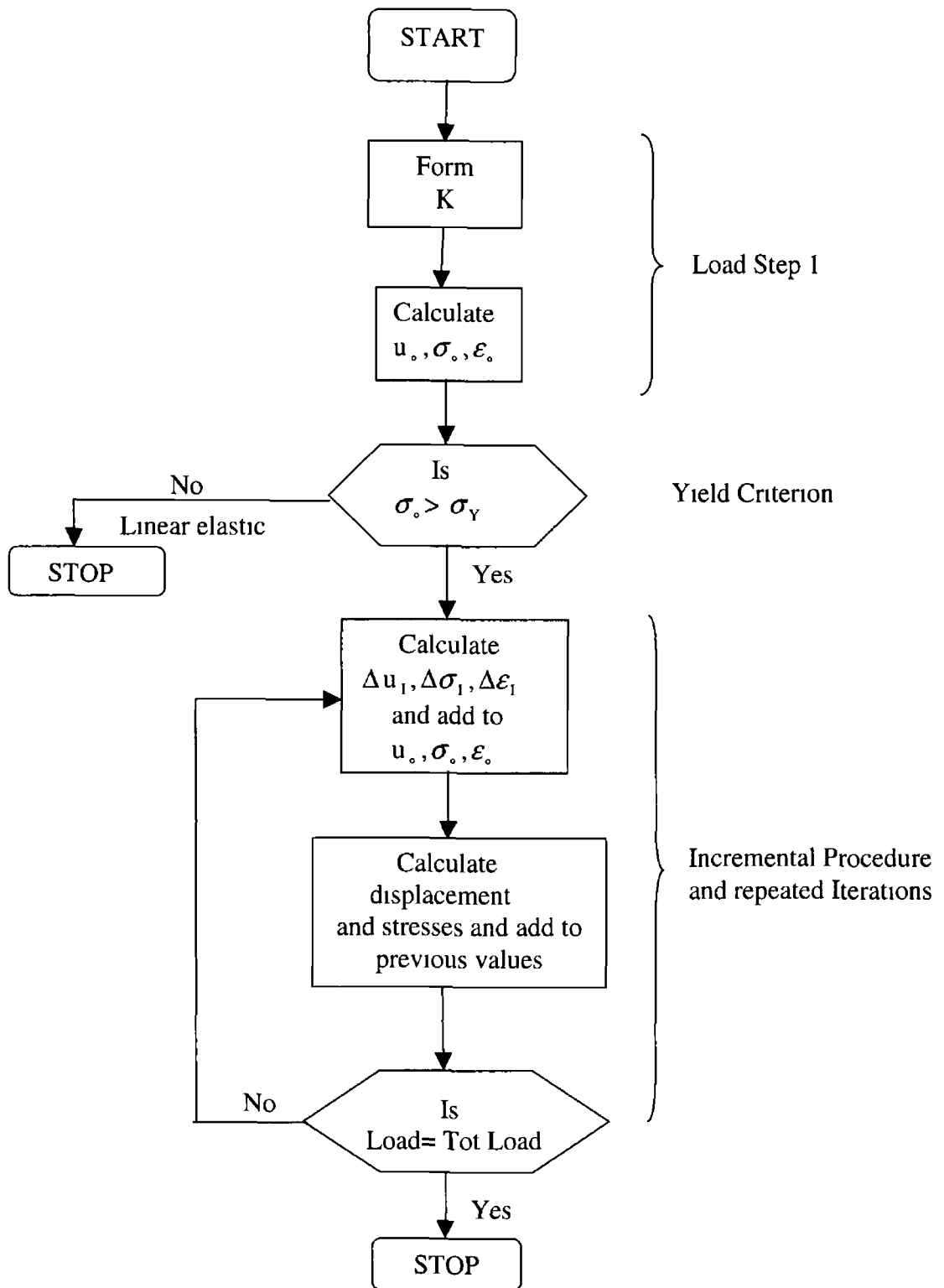


Figure 5 5 The basic steps of a non-linear , elasto-plastic analysis

loading method used in the finite element analysis was identical to that used in the experiments. The model (solid rod) was subjected to combined tension-torsion loading in four different loading paths. In the first loading path, the model was subjected to initial elastic torque of different values corresponding to 25, 50, 75, and 100 percent of the yield torque, followed by the application of the axial load, beyond the yield load, keeping the corresponding angle of twist constant. In the second loading path, the same procedure was repeated except the torque, rather than the angle of twist, was maintained constant. An initial elastic axial load was applied to the model, followed by application of the torque, beyond the yield torque, keeping the corresponding axial displacement constant in the third loading path. This procedure was repeated for different initial axial load corresponding to 25, 50, 75, and 100 percent of the yield axial load. In the fourth loading path, the same procedure was repeated as in the third loading path except the axial load, rather than axial displacement, was maintained constant. The finite element analysis for each loading path was performed in two load steps. In the first load step, an initial axial load or initial torque was applied to the end of the model. The second load step consists of applying the torque beyond the yield torque or applying the axial load beyond the yield load.

In the case of the thin-walled tube, the model was subjected to combined tension and torsion in two different loading paths. The model, in the first loading path, was subjected to initial elastic torque and then, keeping the angle of twist constant, followed by application of the axial load beyond the yield load. In the second loading path, the model was subjected to initial axial load and then, holding the axial displacement constant, followed by application of the torque beyond the yield torque. The same procedure for the two loading paths was repeated for different initial values of axial load and torque corresponding to 25, 50, 75 and 100 percent of the yield axial load and torque. All analyses were performed using the commercial finite element code ANSYS (version 5.7).

5.6 Results and Analysis

5.6.1 Torsion followed by Tension, Solid Rod

Angle of Twist Held Constant

In this loading path, an initial torque was applied to the model as the first load step and then, holding the corresponding angle of twist constant, the axial load was applied in the subsequent load steps. The axial load was applied to the model in increments, therefore, the total axial load was applied gradually. This procedure was repeated for four different levels of initial elastic torque corresponding to 31%, 50%, 75% and 100% of the yield torque. The results plotted in terms of axial stress and shear stress at the outer surface is depicted in figure 5.6. It can be seen from this figure that for loading of the model under investigation the value of the initially applied torque remains constant until the combined stress state reaches a specific value. As the axial load increases, the outer layer of the model starts to yield and the torque begins to decrease in a specific manner which is governed by the yield criterion. The figure indicates that the higher initial torque applied to the model followed by increasing axial load, the model yields at an earlier stage than the model subjected to a lower initial torque. It also can be seen from the figure that, the higher the magnitudes of the initially applied torque, the greater is the rate of decrease in the torque carrying ability with the gradually applied axial load.

Figures 5.7 to 5.10 show the angular displacement and the distribution of shear stress in the deformed solid rod at 25%, 50%, 75% and 100% of the yield torque after applying the axial load.

Torque held Constant

In this type of loading, the model was subjected to an initial torque as the first load step and then the axial load was applied in the subsequent load steps. The axial load was applied to the model in increments, therefore, the total axial load was applied gradually. This procedure was repeated for four different levels of initial elastic torque corresponding to 25 percent, 50 percent, 75 percent and 100 percent of the yield torque. Figure 5.11 shows the plot of axial strain versus shear strain for

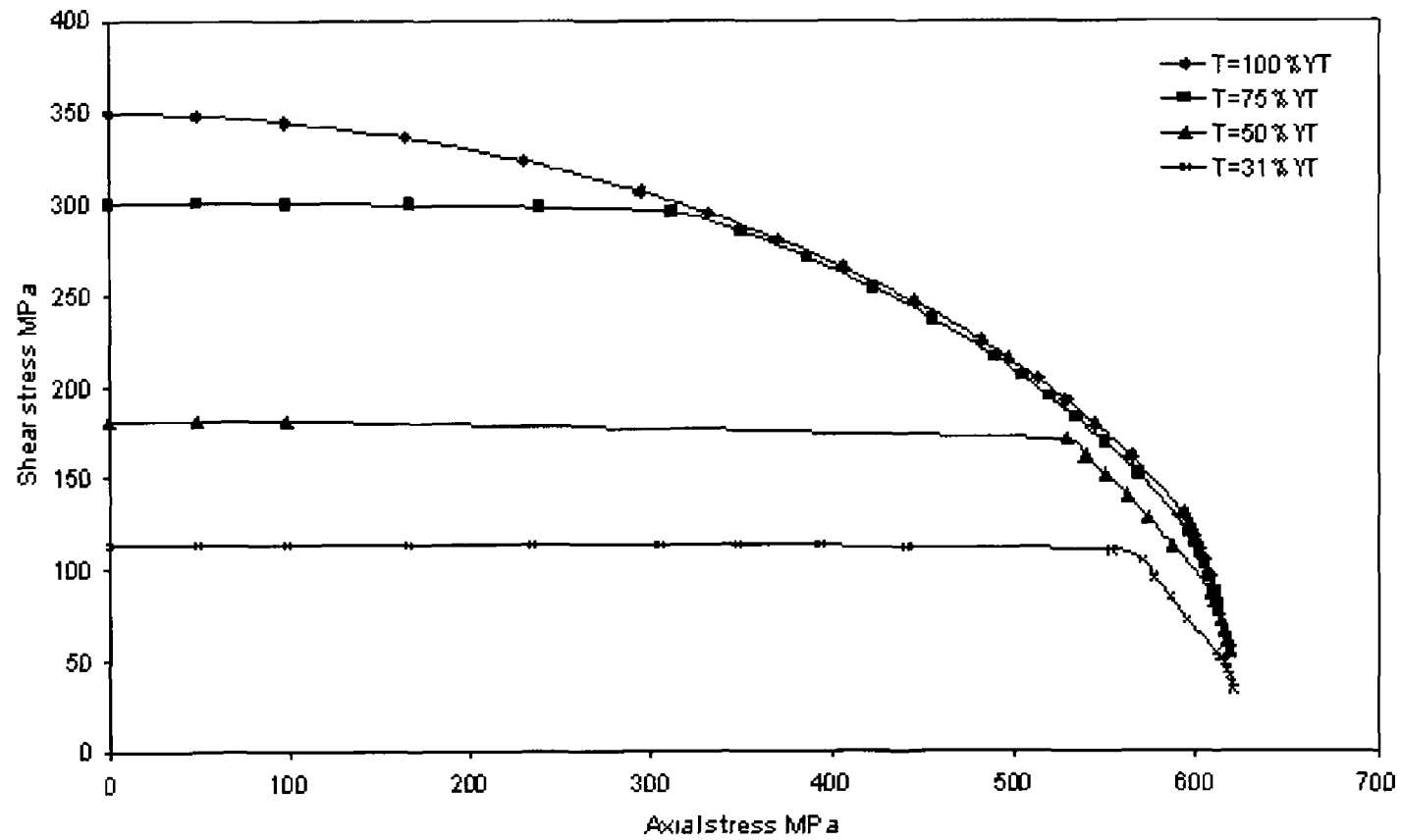
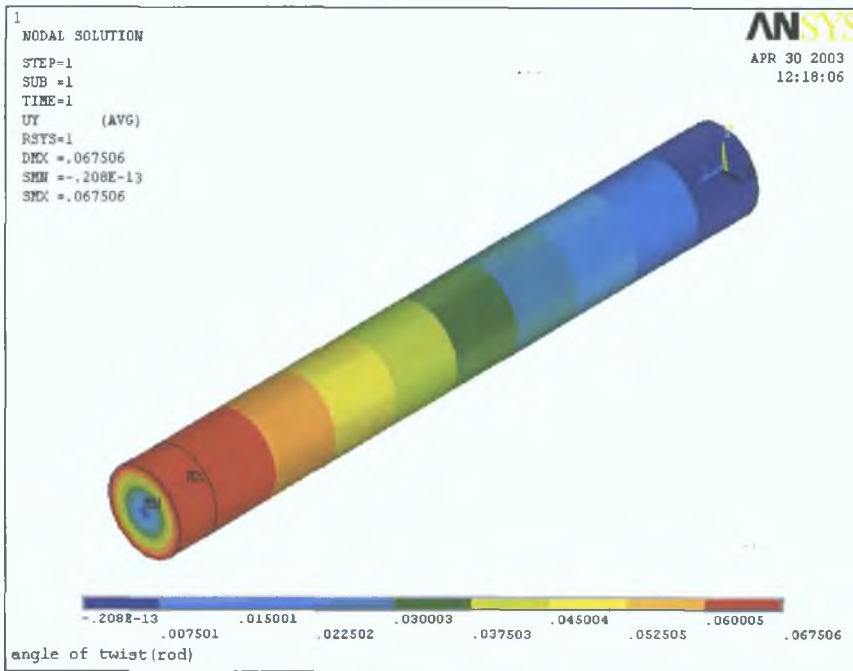
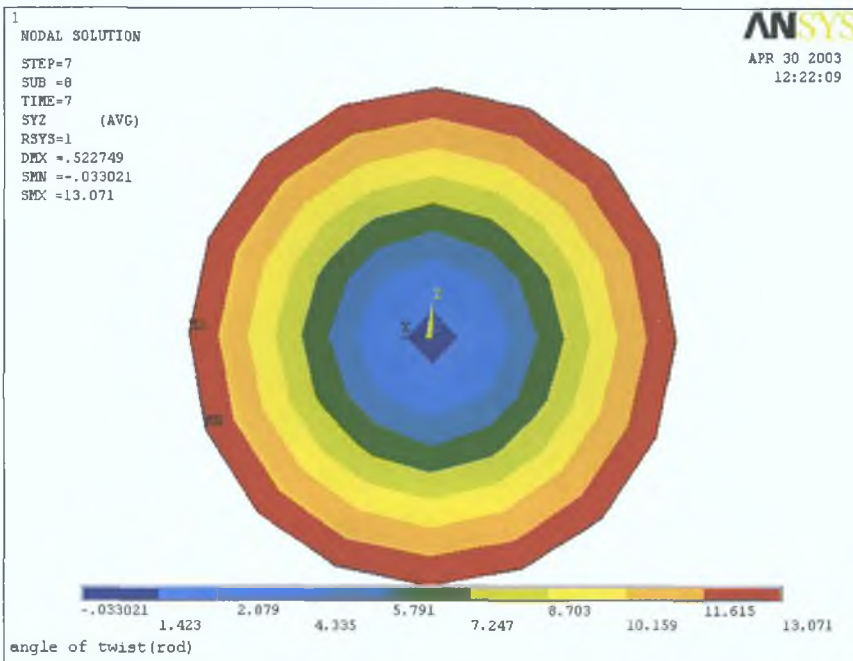


Figure 5.6 Axial stress versus shear stress (angle of twist constant) (solid rod)

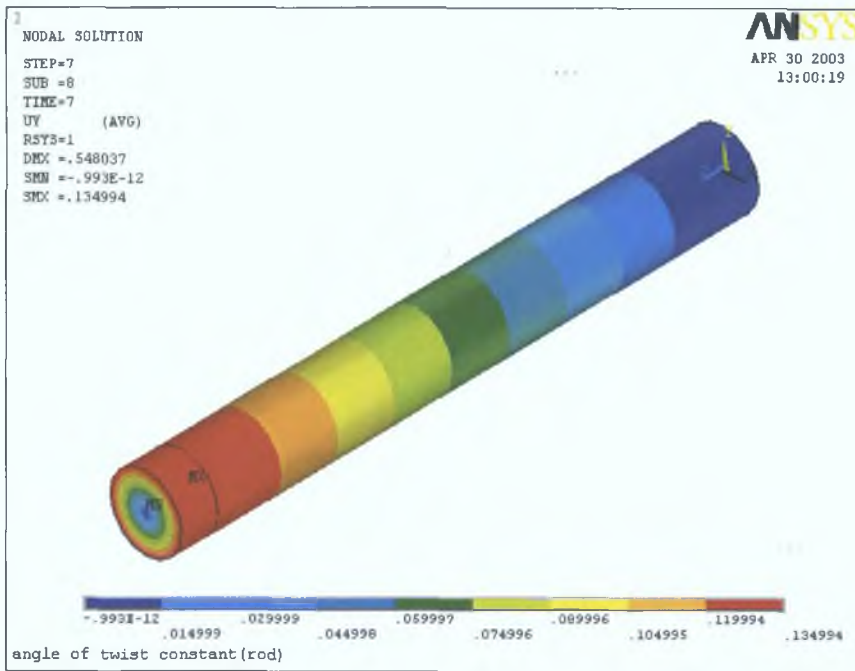


Angular Displacement

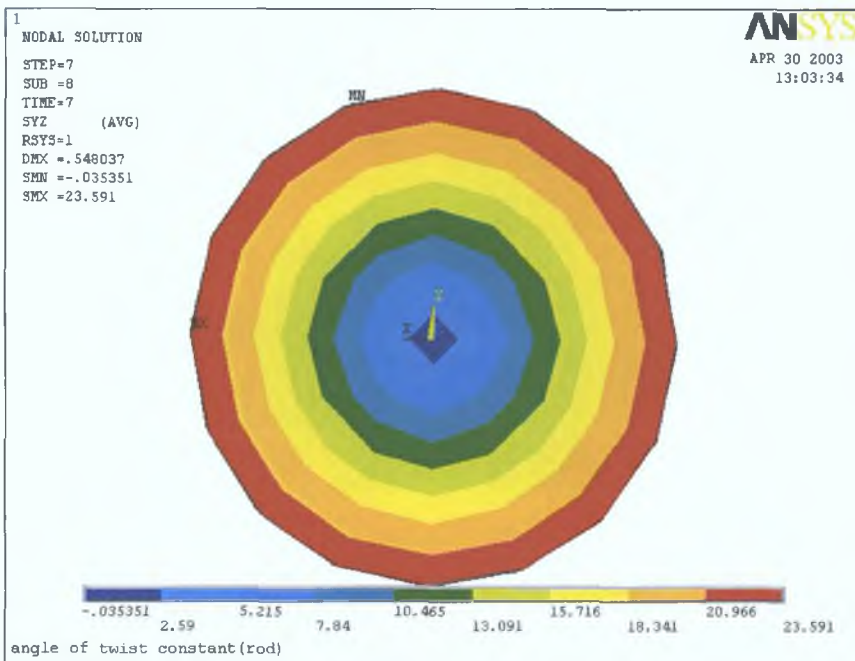


Distribution of shear stress

Figure 5.7 Deformation of the Rod after applying axial load (constant angle of twist) ($T= 25\%YT$)

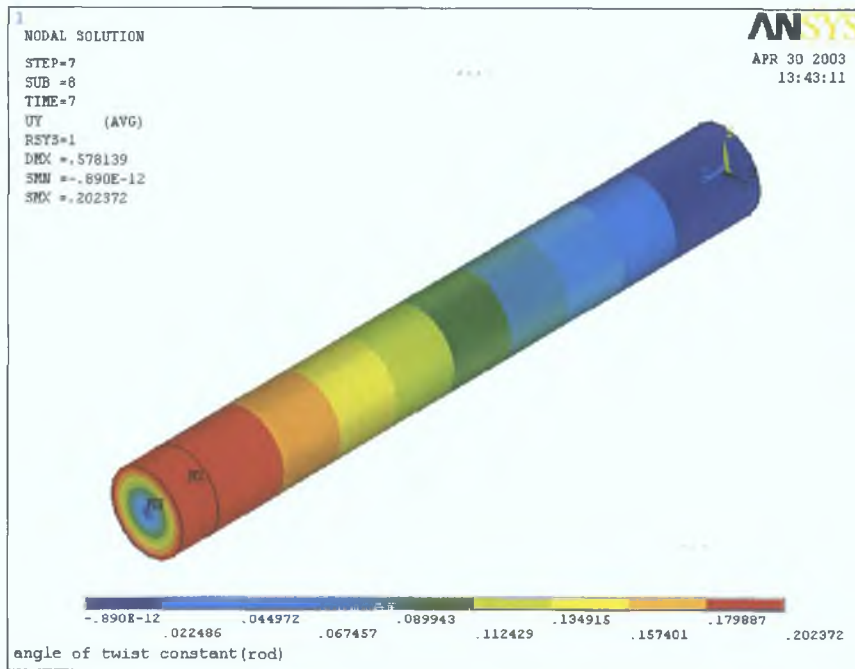


Angular Displacement

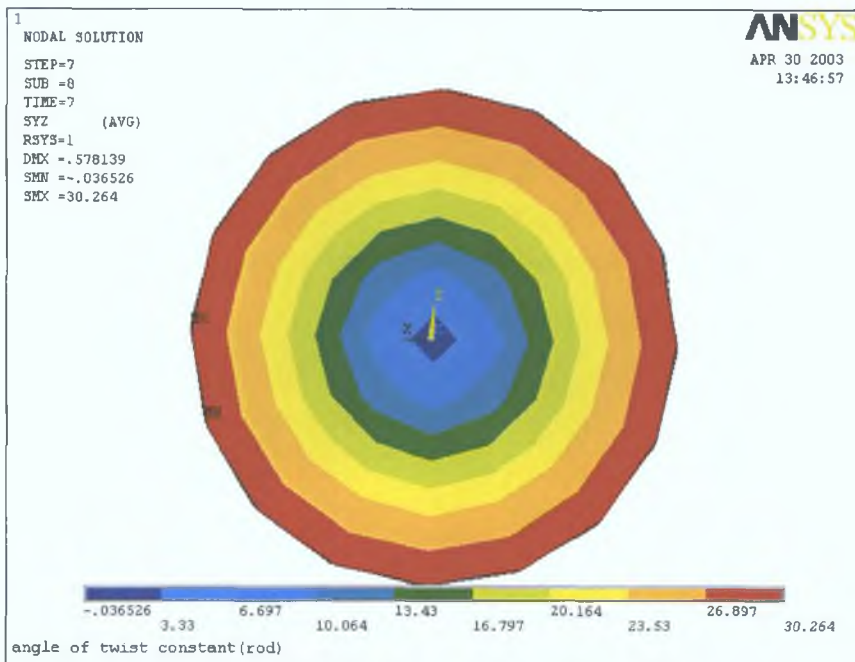


Distribution of shear stress

Figure 5.8 Deformation of the Rod after applying axial load (constant angle of twist) ($T=50\%YT$)

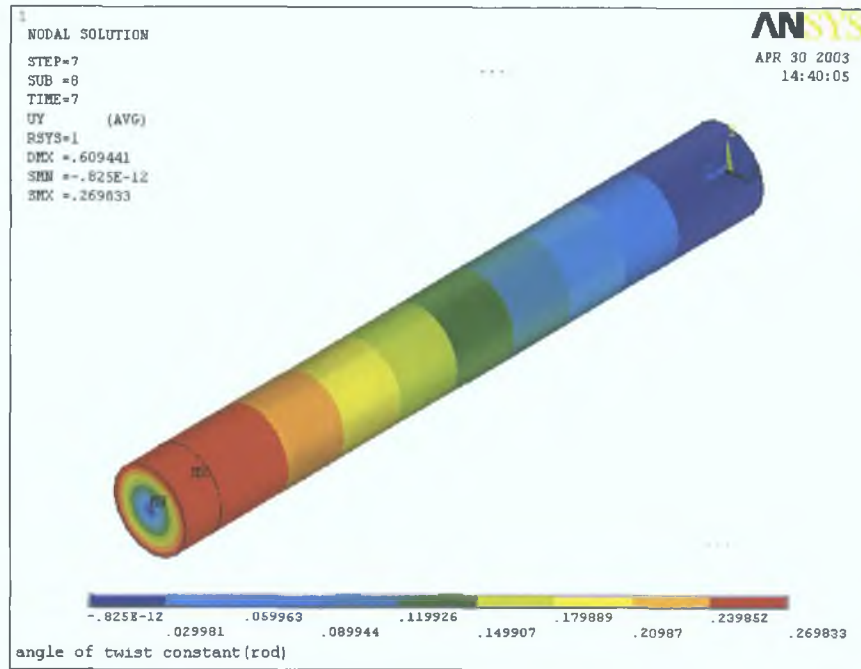


Angular Displacement

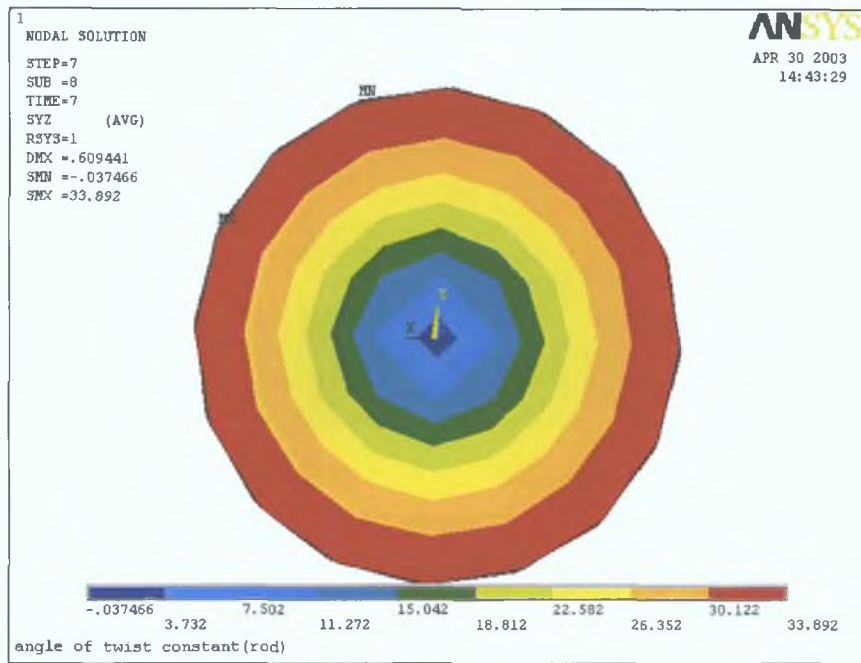


Distribution of shear stress

Figure 5.9 Deformation of the Rod after applying axial load (constant angle of twist)
($T = 75\% Y_T$)



Angular Displacement



Distribution of shear stress

Figure5.10 Deformation of the Rod after applying axial load (constant angle of twist) (T= 100%YT)

different initial torques. The figure reveals that, initially the shear strain remains constant for a given torque. The axial strain increases due to increase in the axial load. When the combined axial stress and shear stress reaches the yield stress, the outer layer begins to yield and to maintain the initially applied torque constant, the shear strain begins to increase.

The results plotted in terms of the axial stress and shear stress in figure 5.12 show that the magnitude of the shear stress remains unchanged until the combined stress state reaches a specific value. As the axial stress increases, beyond the von Mises yield locus the shear stress begins to decrease in a specific manner, which is governed by the yield criterion. Beyond the von Mises yield locus the model undergoes strain hardening and when the combined stress state reaches the maximum yield plateau the model of the rod starts to show an unstable deformation pattern.

Figures 5.13 to 5.16 show the angular displacement and the distribution of shear stress in the deformed solid rod at 29%, 57%, 75% and 92% of the yield torque after the application of the axial load.

5.6.2 Tension followed by Torsion, Solid Rod

Axial Displacement Held Constant

For this type of loading, an initial axial load was applied to the model as the first load step and then, holding the corresponding axial displacement constant, a torque was applied in the subsequent load steps. The torque was applied to the model in increments, therefore, the total torque was applied gradually. This procedure was repeated for four different initial axial loads, $P/P_y = 1.0, 0.75, 0.50$ and 0.25 . The axial stress versus the shear stress at the outer surface was plotted and presented in figure 5.17. It was observed from the figure that as the shear stress increases due to the increase in the torque, the axial stress initially remains unchanged as long as the combined stress does not reach a critical value. When the combined stress in the model reaches the von Mises yield stress, the axial stress decreases and the combined stresses follow the yield plateau as shown in figure 5.17. It was also observed from

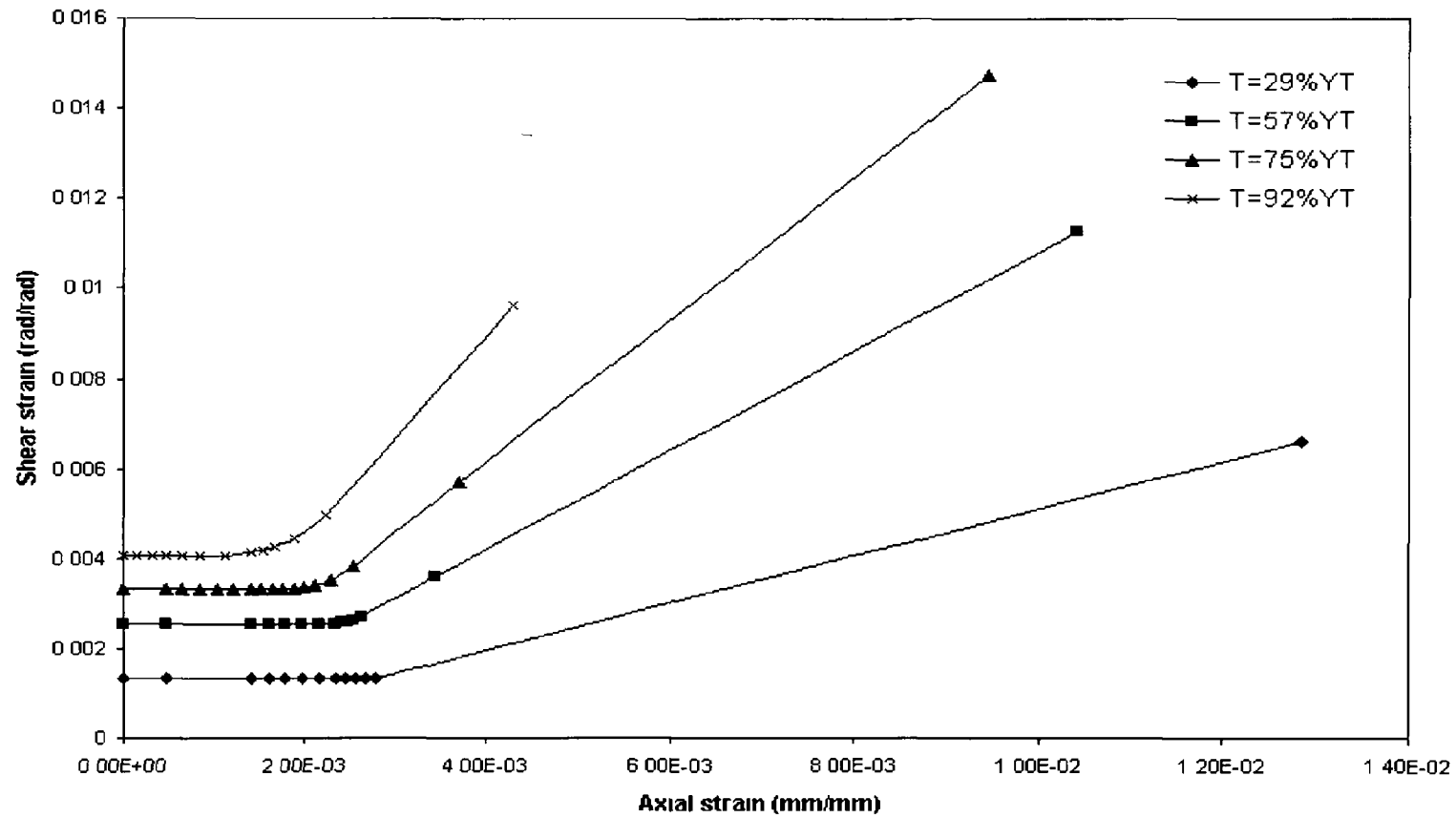


Figure 5 11 Axial strain versus shear strain (constant torque)
(solid rod)

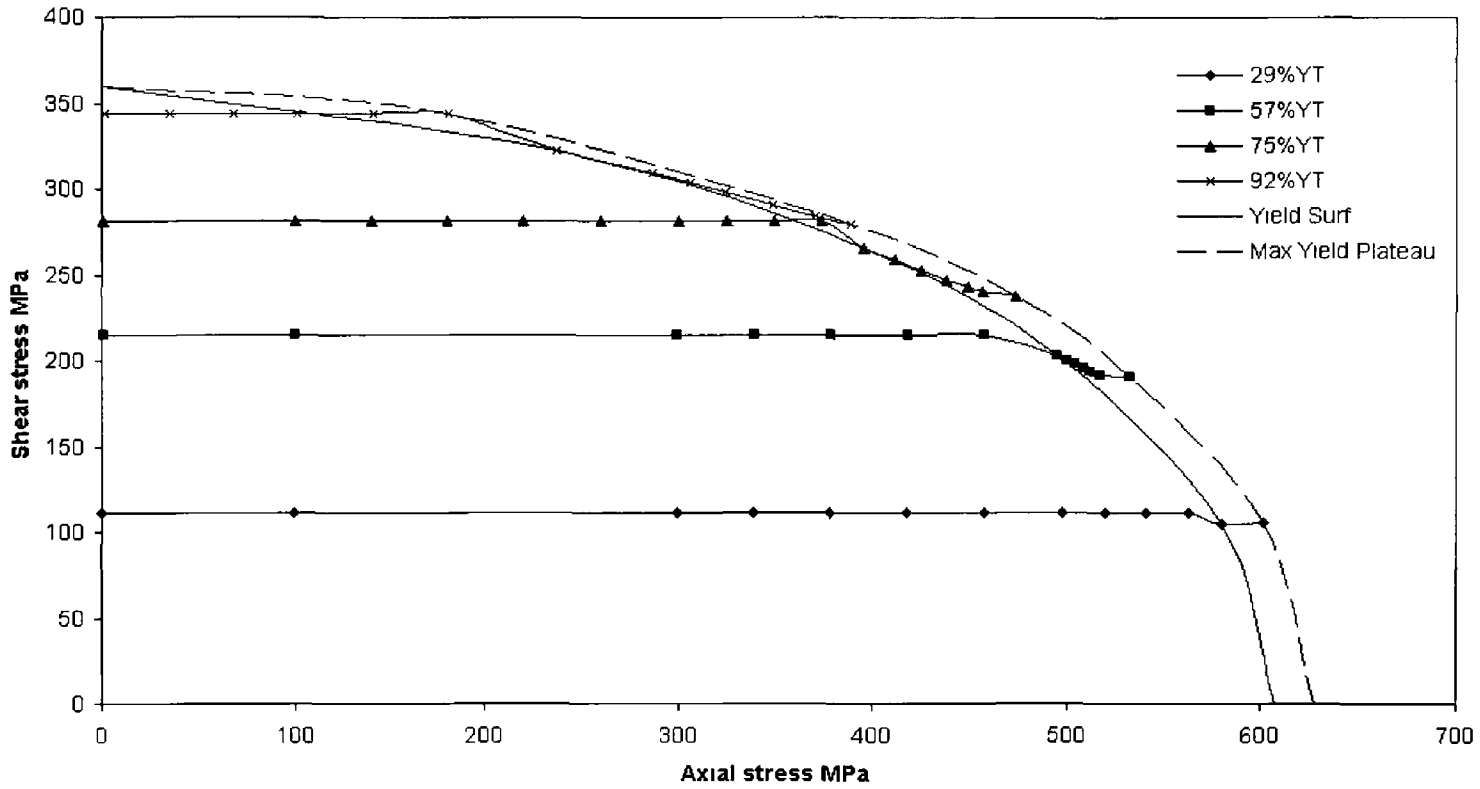
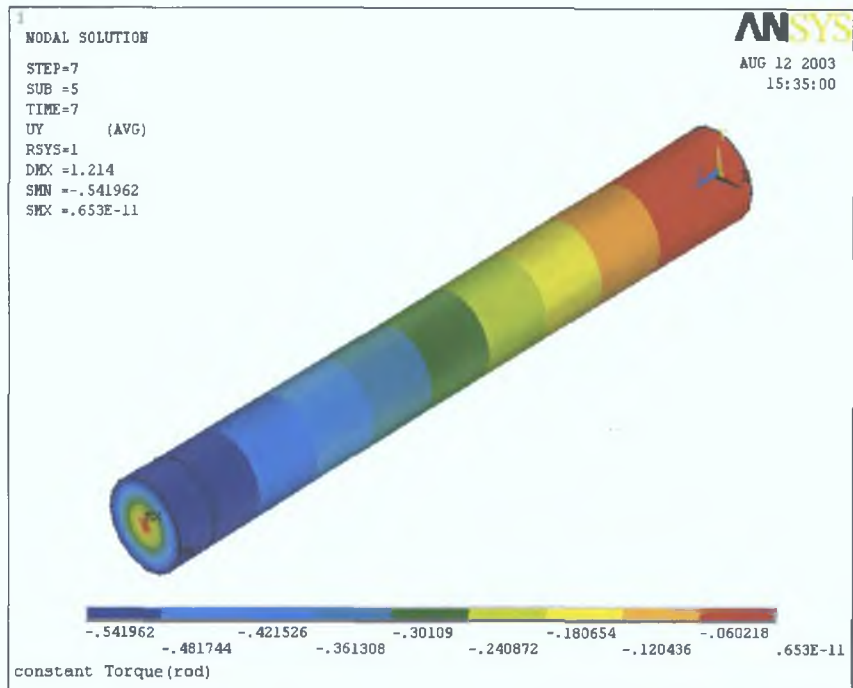
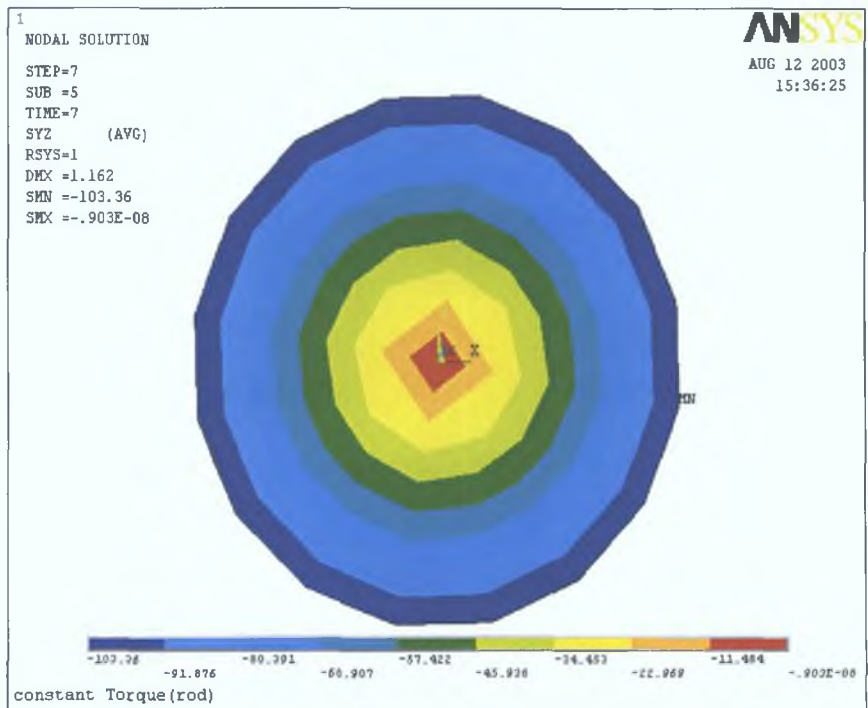


Figure 5 12 Axial stress versus shear stress (constant torque)
(solid rod)

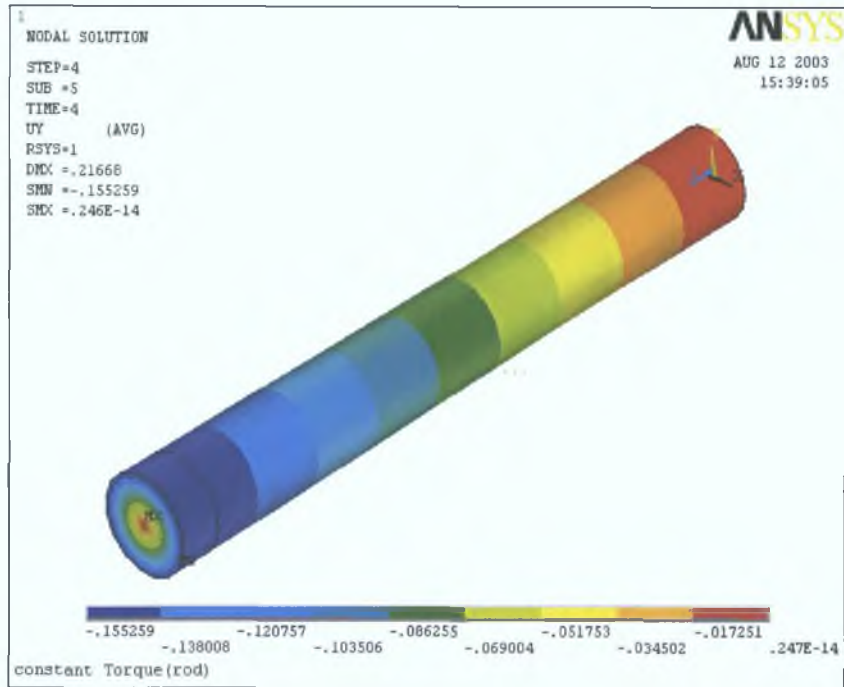


Angular Displacement

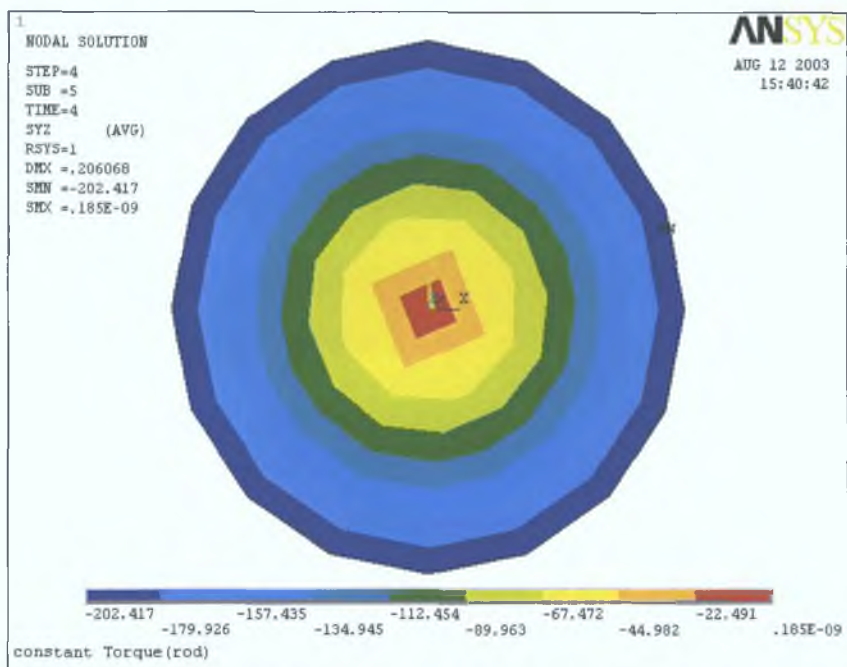


Distribution of shear stress

Figure 5.13 Deformation of the Rod after applying axial load (constant torque) ($T= 29\%YT$)

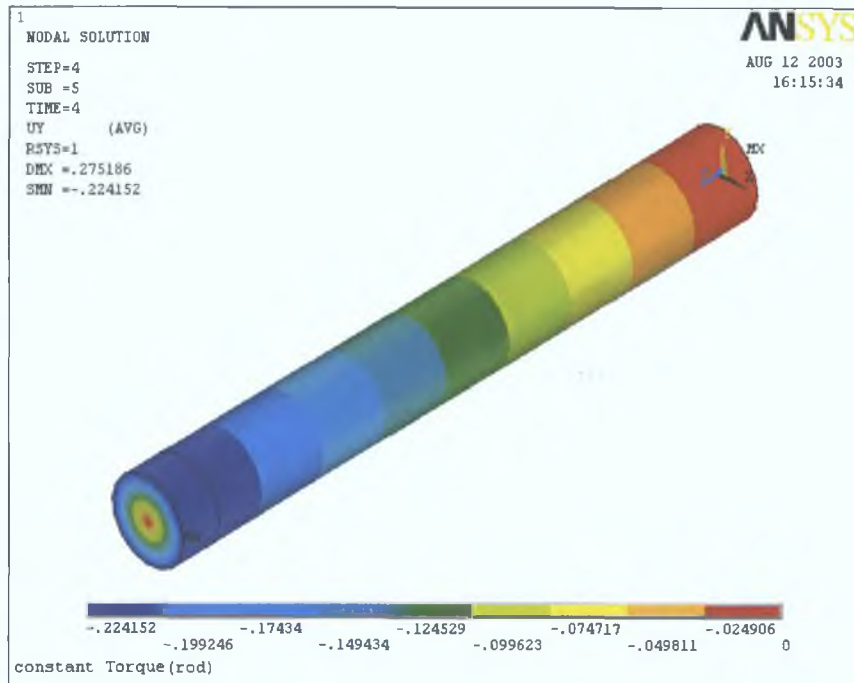


Angular Displacement

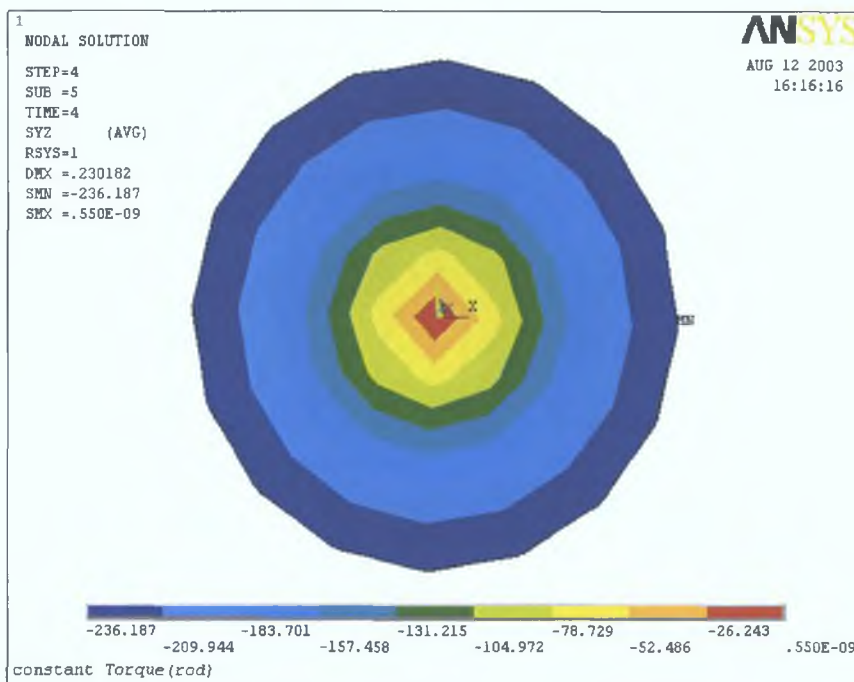


Distribution of shear stress

Figure 5.14 Deformation of the Rod after applying axial load (constant torque) ($T = 57\% Y_T$)

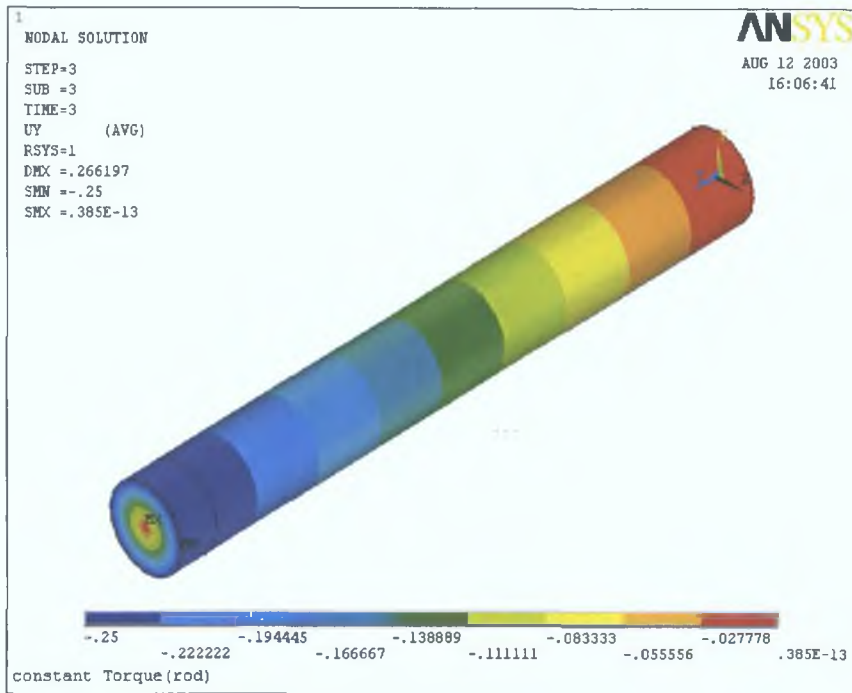


Angular Displacement

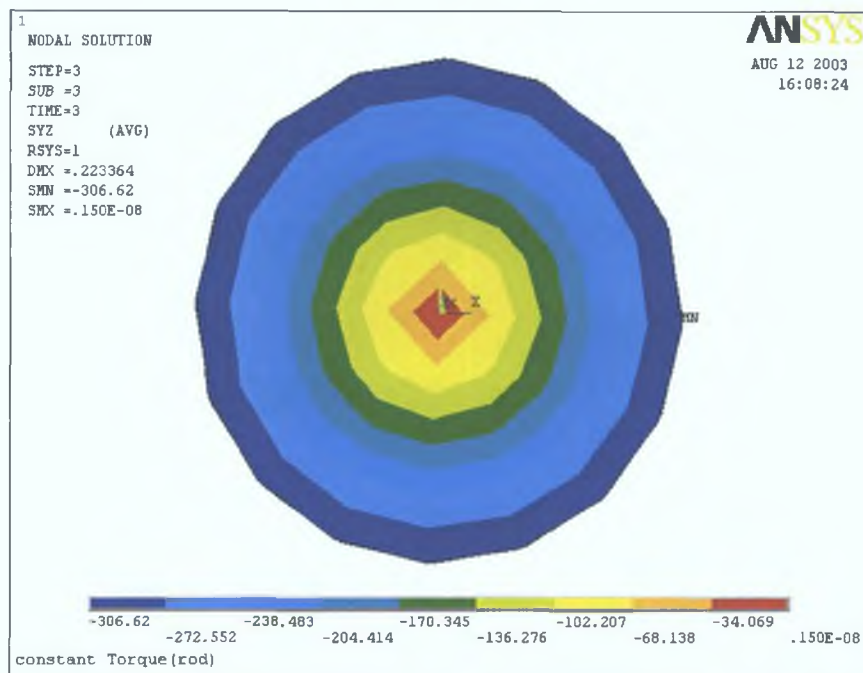


Distribution of shear stress

Figure 5.15 Deformation of the Rod after applying axial load (constant torque)
($T = 75\%YT$)



Angular Displacement



Distribution of shear stress

Figure 5.16 Deformation of the Rod after applying axial load (constant torque)
 (T=92%)

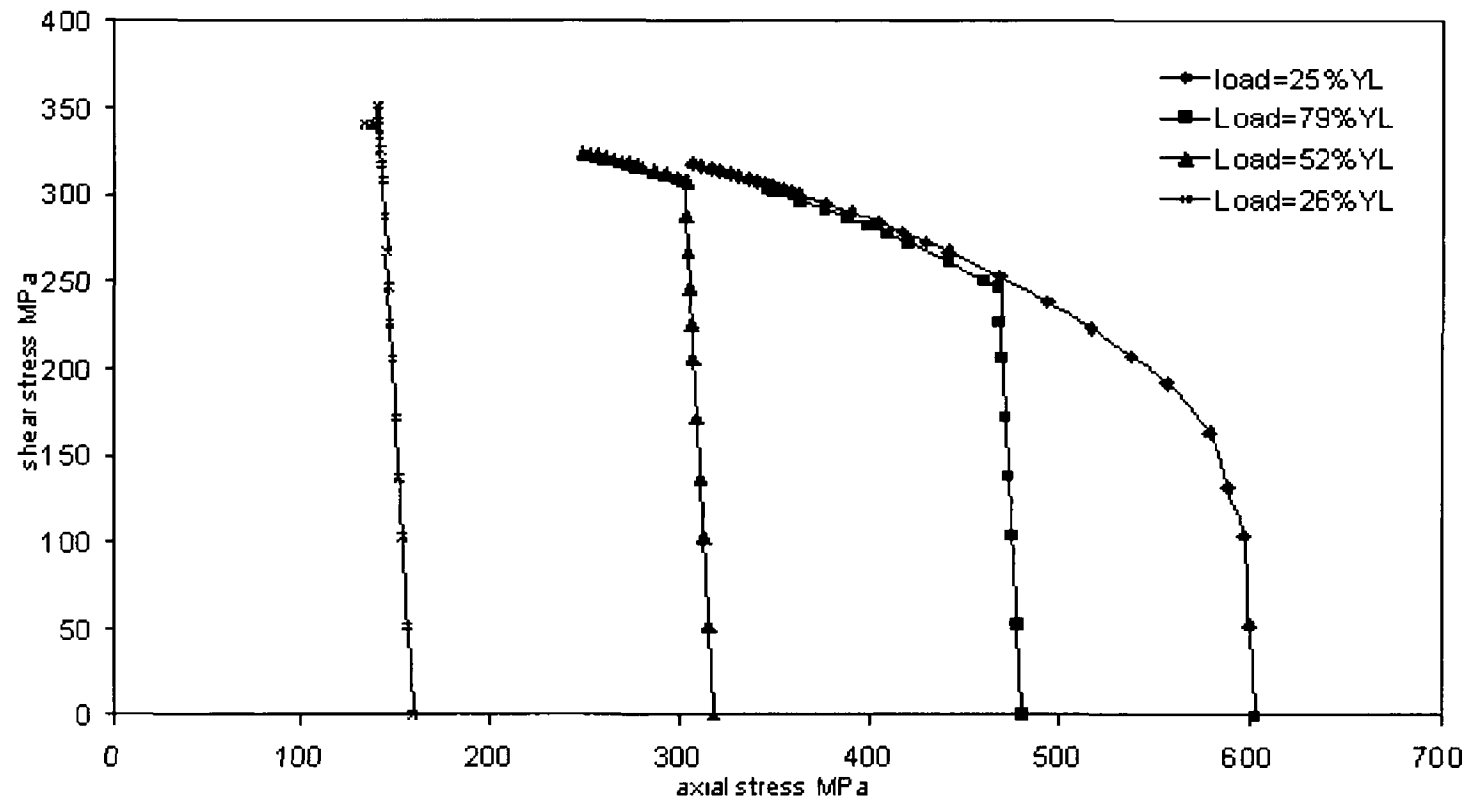


Figure 5 17 Axial stress versus shear stress (axial displacement constant)
(solid rod)

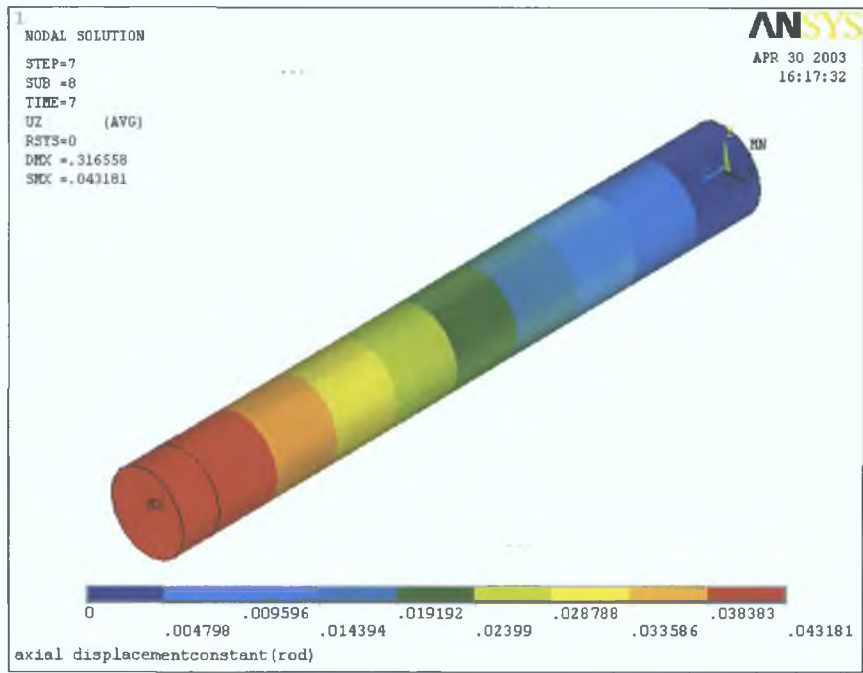
the figure that when the model was subjected to higher initial axial load, the axial stress starts to decrease at greater rate at the initial stage of loading and tends to drop rapidly

Figure 5 18 to 5 21 show the axial displacement and the distribution of axial stress of the deformed solid rod at 25%, 50%, 75% and 100% of the yield load after the application of the torque

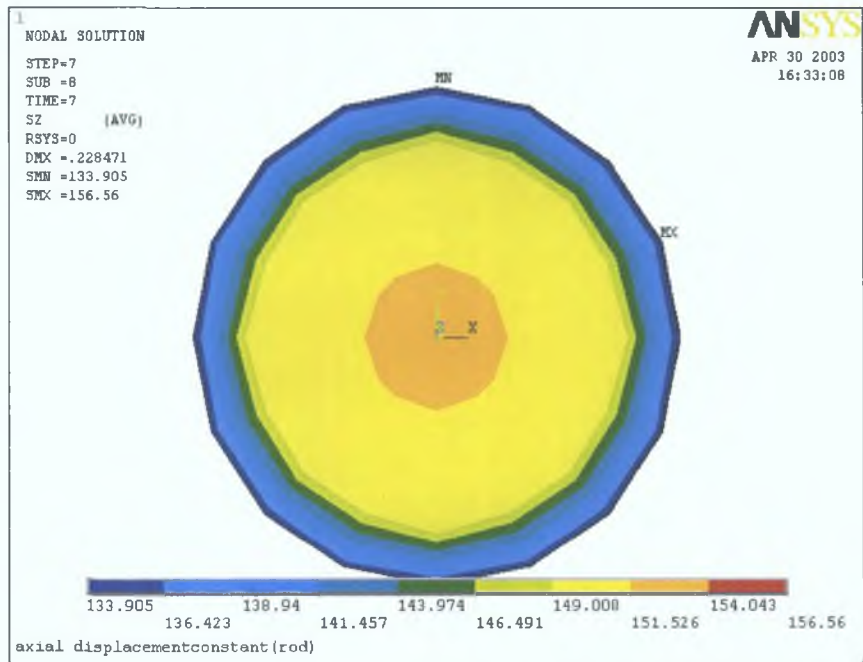
Axial Load Maintained Constant

In the fourth loading case where an initial axial load was applied to the model as first load step, and then a torque was applied in the subsequent load steps. The torque was applied in increments, therefore, the total torque was applied gradually. The shear strain versus the axial strain was plotted as shown in figure 5 22. It was observed from this figure that the axial strain remains unchanged for a given axial load up to the combined yield stress. As the shear strain increases due to increase in the torque beyond the combined yield stress, the axial strain starts to increase as the model reaches a plastic state on the outer layer the initially applied axial load is carried by the inner elastic core and the outer layer which reached plastic instability, this causes an increase in the axial strain. The rate of increase in the axial strain is significantly higher for the higher initial axial load. This procedure was repeated for four different levels of initial elastic axial load, as illustrated in figure 5 22. The results shown in 5 23 shows that as the shear stress increases due to the increase in the torque, the axial stress initially remains constant for a certain level of torque. When the combined axial stress and shear stress reaches von Mises stress, the axial stress decrease and the combined stresses increase in the strain hardening range. As the combined stresses reach a critical value the combined stresses follow the maximum yield plateau as shown in figure 5 23

Figures 5 24 to 5 27 show the axial displacement and the distribution of axial stress in the deformed solid rod at 25%, 50%, 75% and 90% of the yield load after the application of the torque

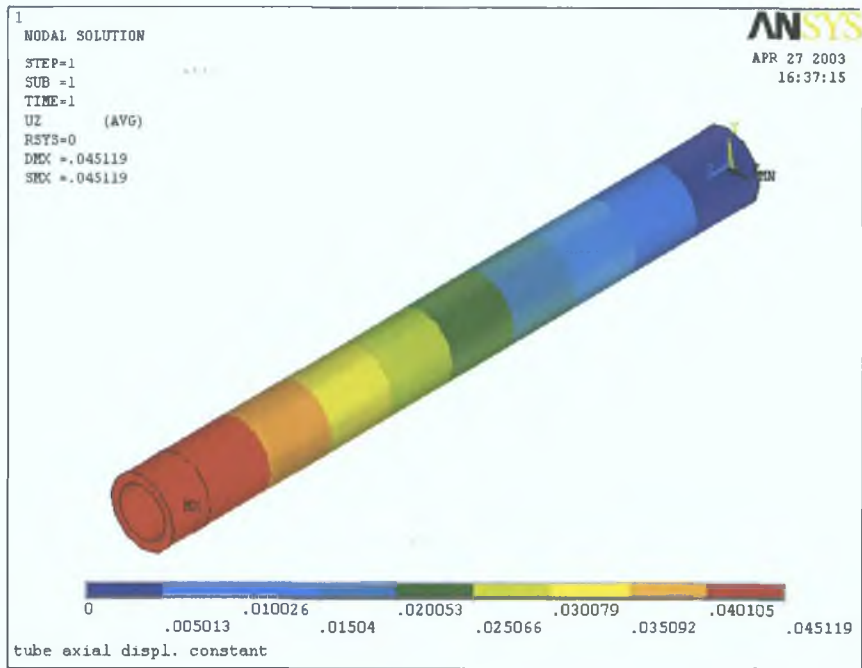


Axial Displacement

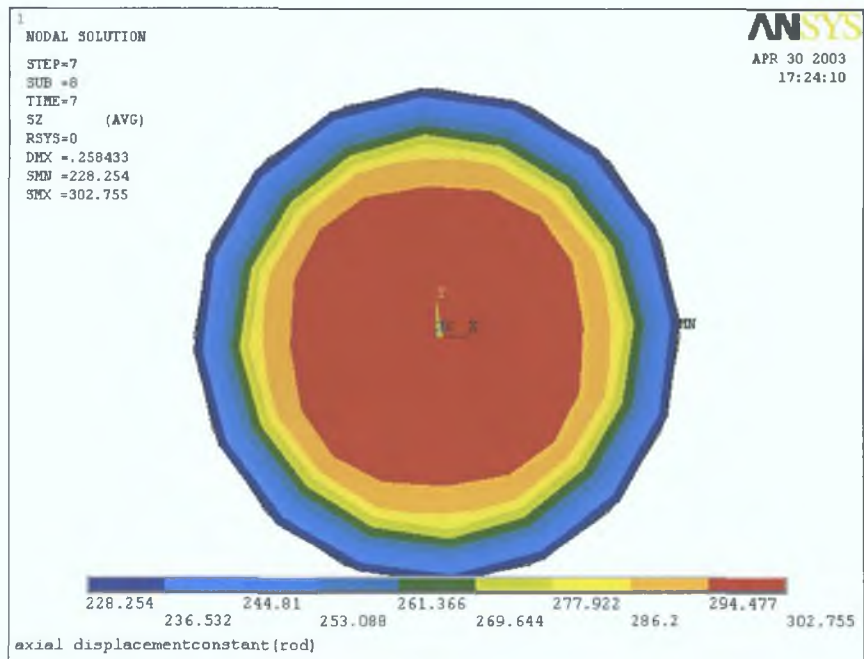


Distribution of axial stress

Figure 5.18 Deformation of the Rod after applying torque (constant axial displacement) (F= 25%YL)

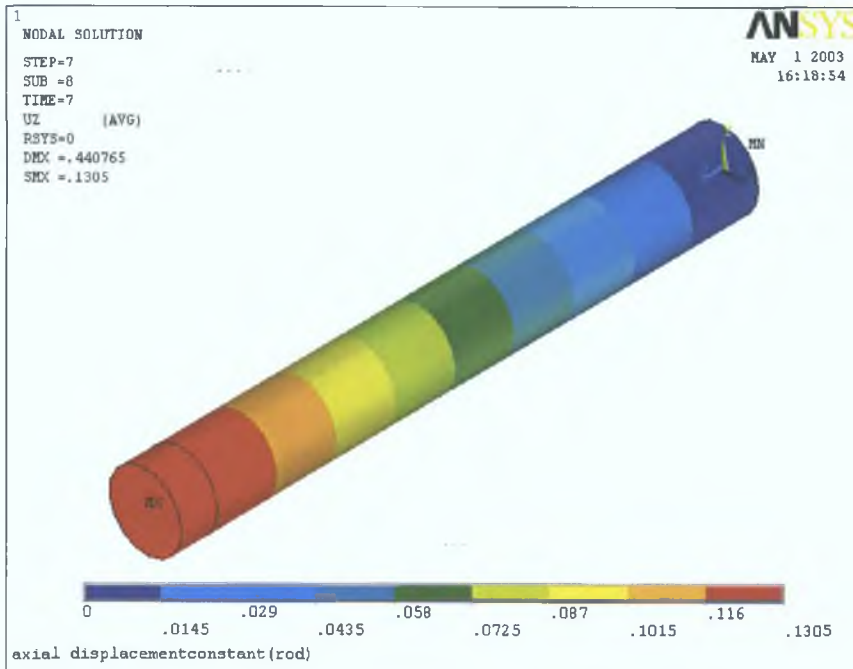


Axial Displacement

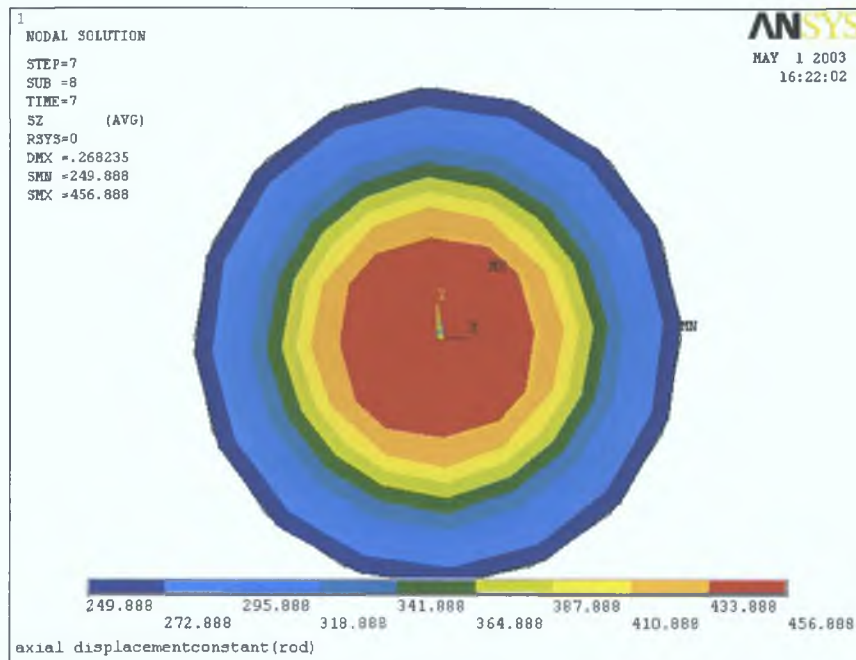


Distribution of axial load

Figure 5.19 Deformation of the Rod after applying torque (constant axial displacement) (F= 50%YL)

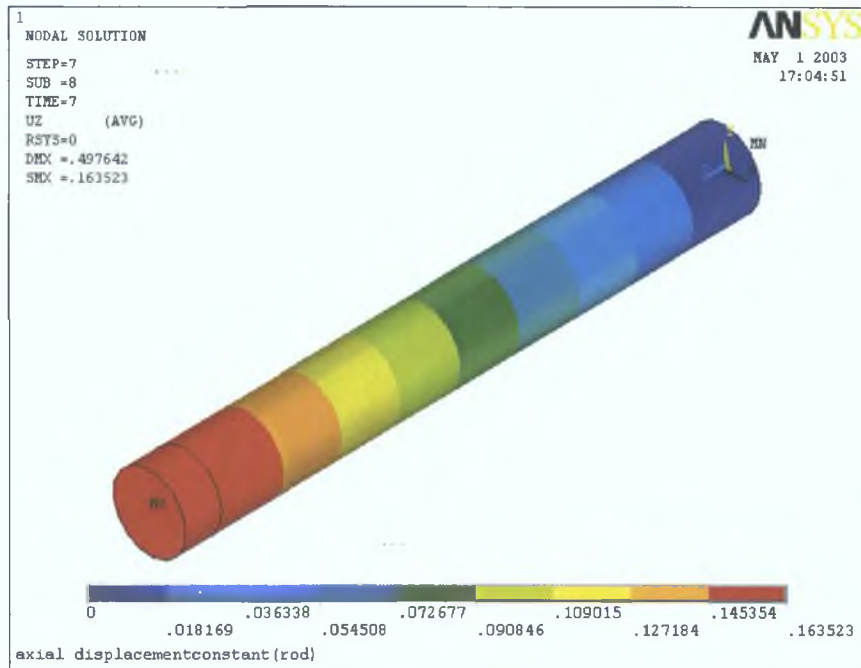


Axial Displacement

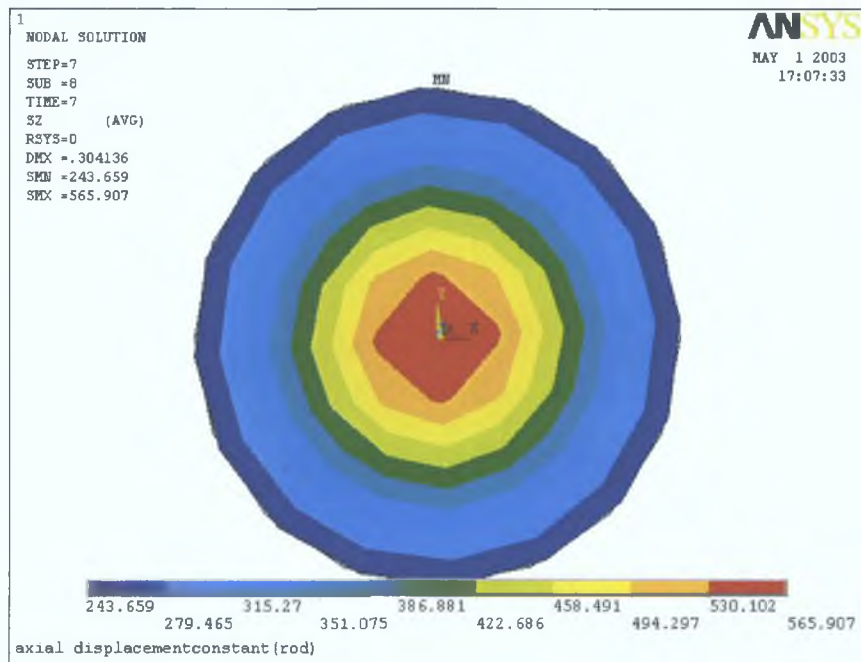


Distribution of axial load

Figure 5.20 Deformation of the Rod after applying torque (constant axial displacement) (F= 75%YL)



Axial Displacement



Distribution of axial stress

Figure 5.21 Deformation of the Rod after applying torque (constant axial displacement) (F= 100%YL)

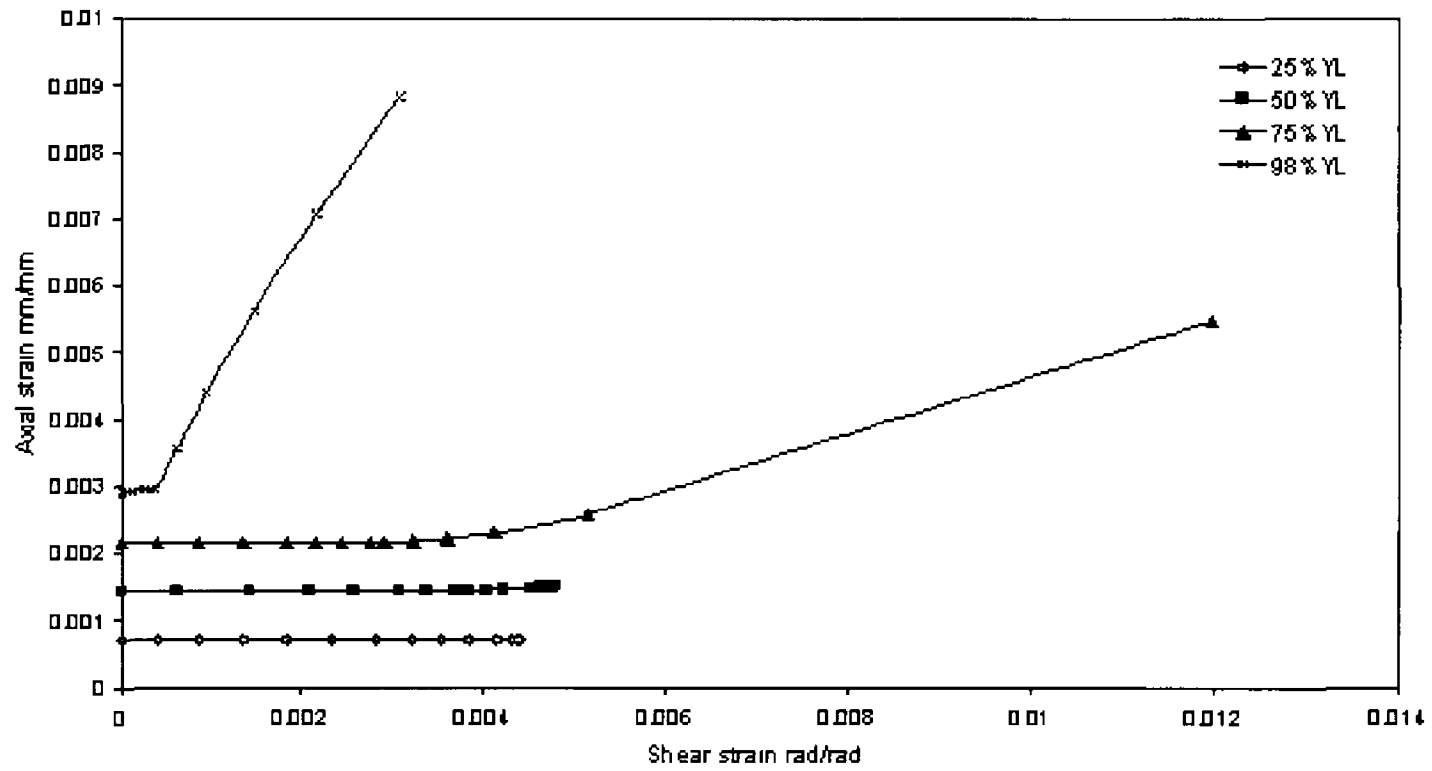


Figure 5.22 Shear strain versus axial strain (constant load)
(solid rod)

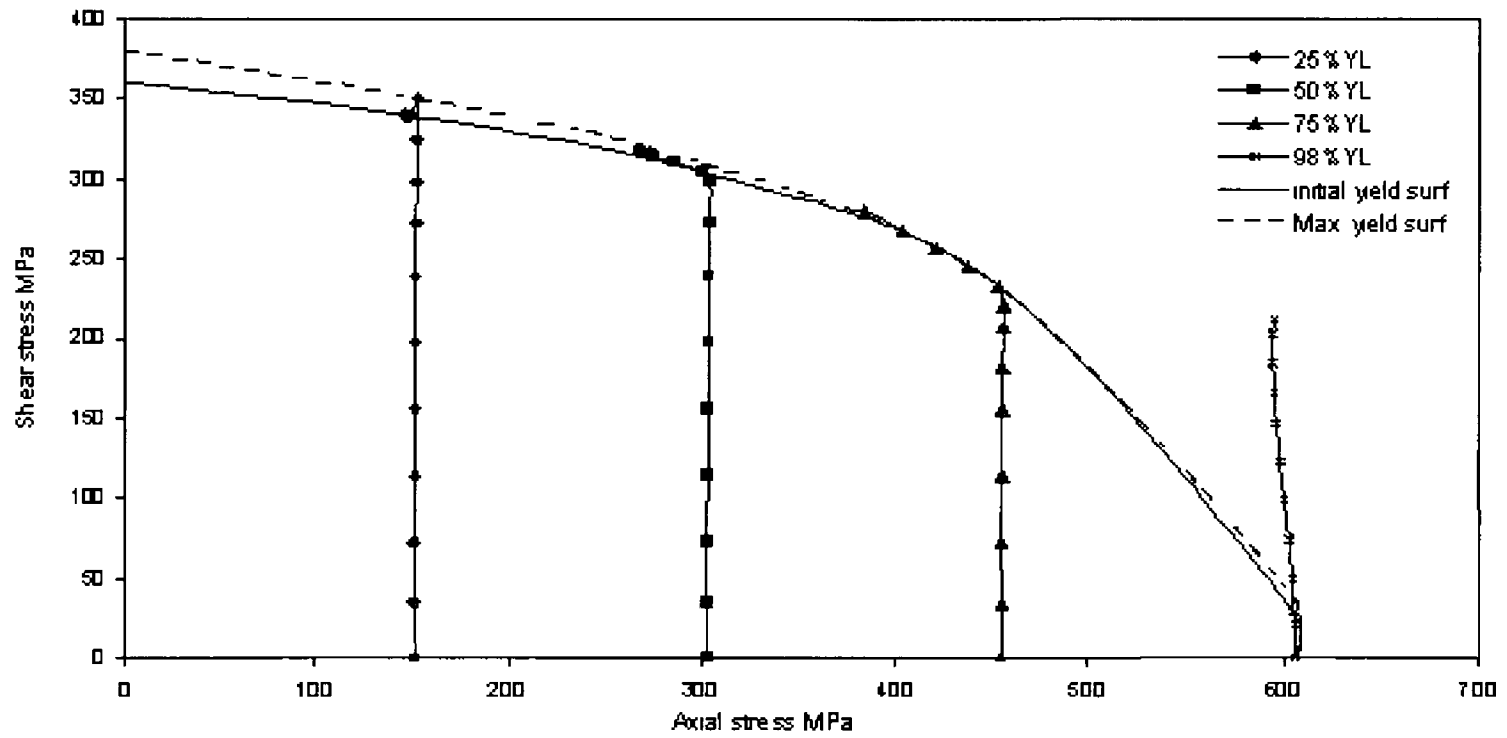
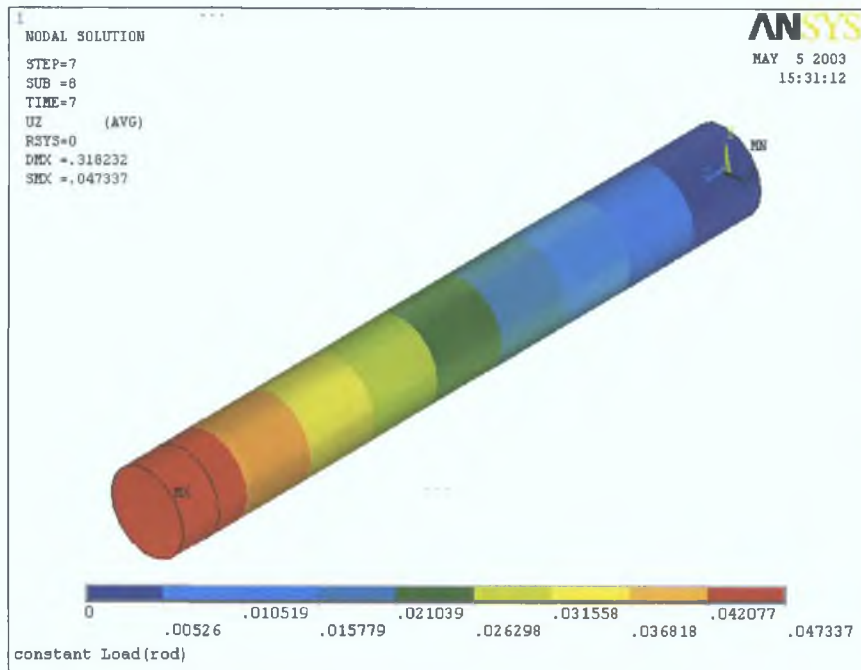
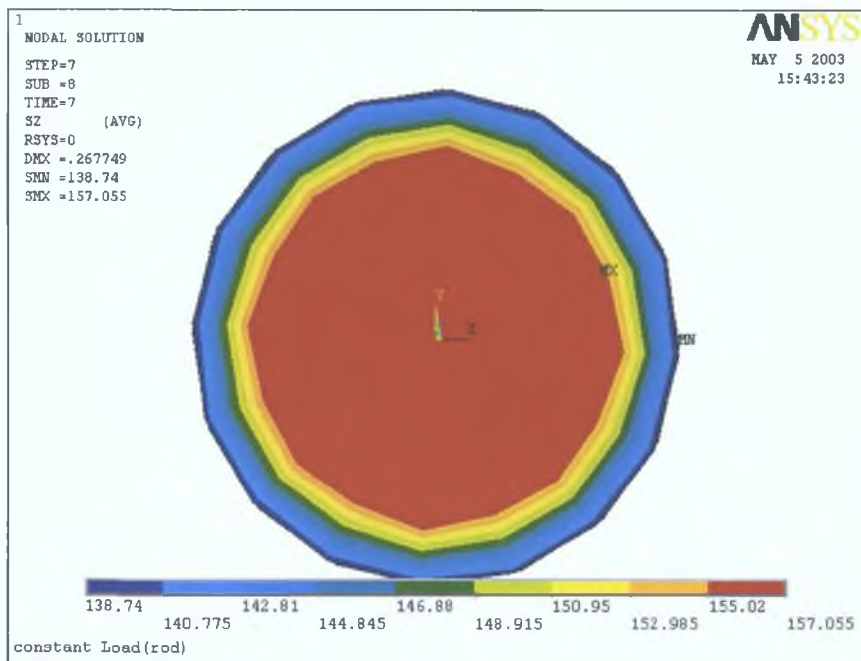


Figure 5.23 Axial stress versus shear stress (Constant load)
(solid rod)

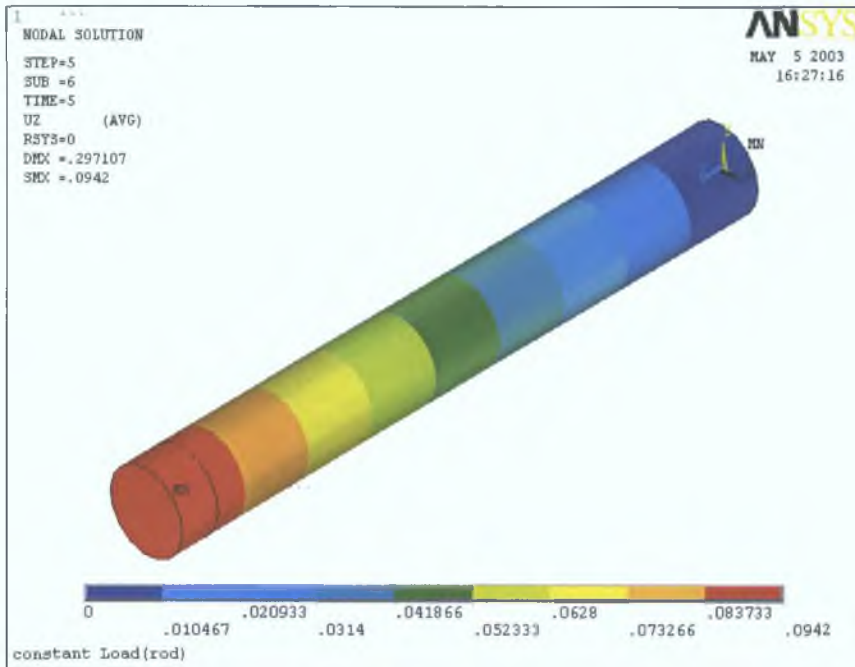


Axial Displacement

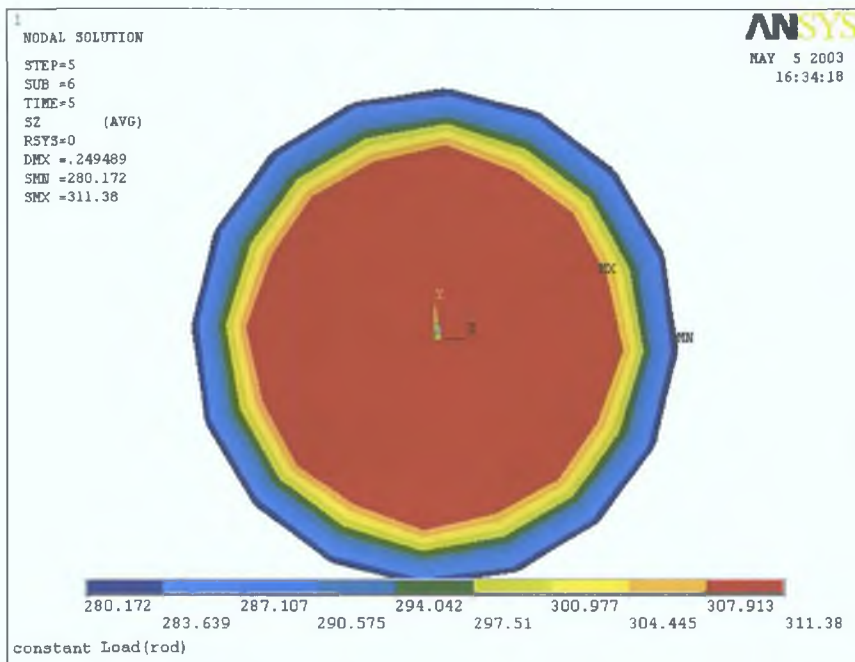


Distribution of axial stress

Figure 5.24 Deformation of the Rod after applying torque (constant load) (F= 25%YL)

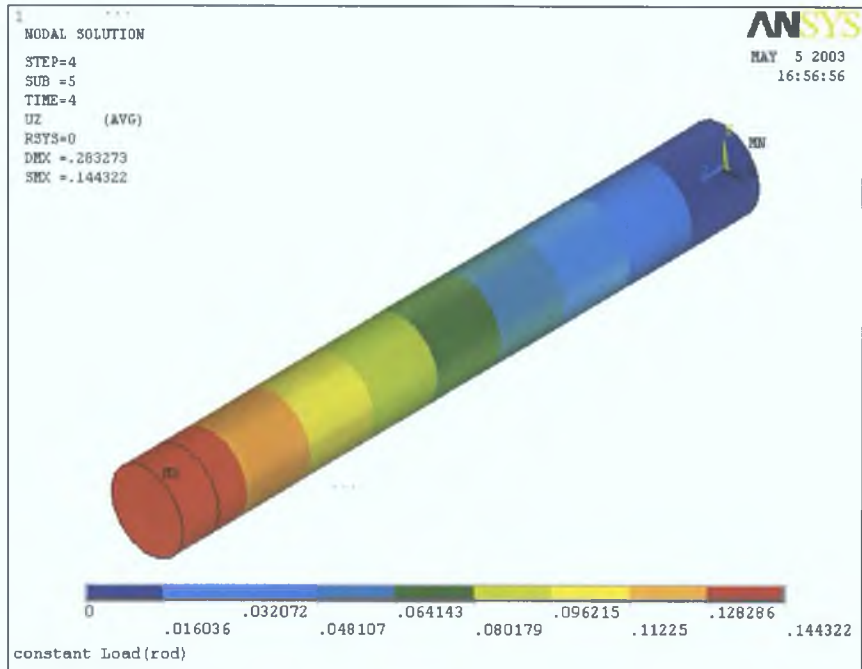


Axial Displacement

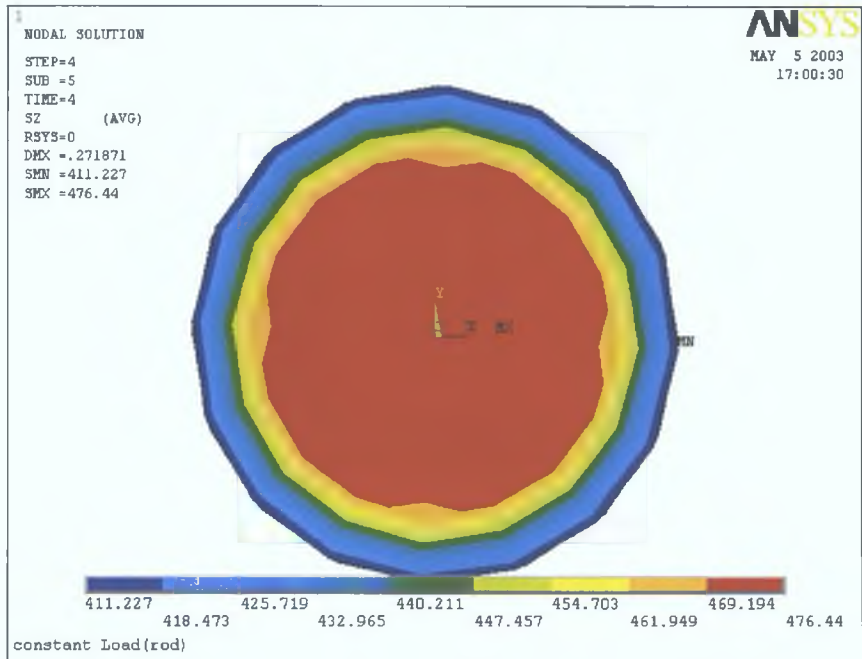


Distribution of axial stress

Figure 5.25 Deformation of the Rod after applying torque (constant load) (F= 50%YL)

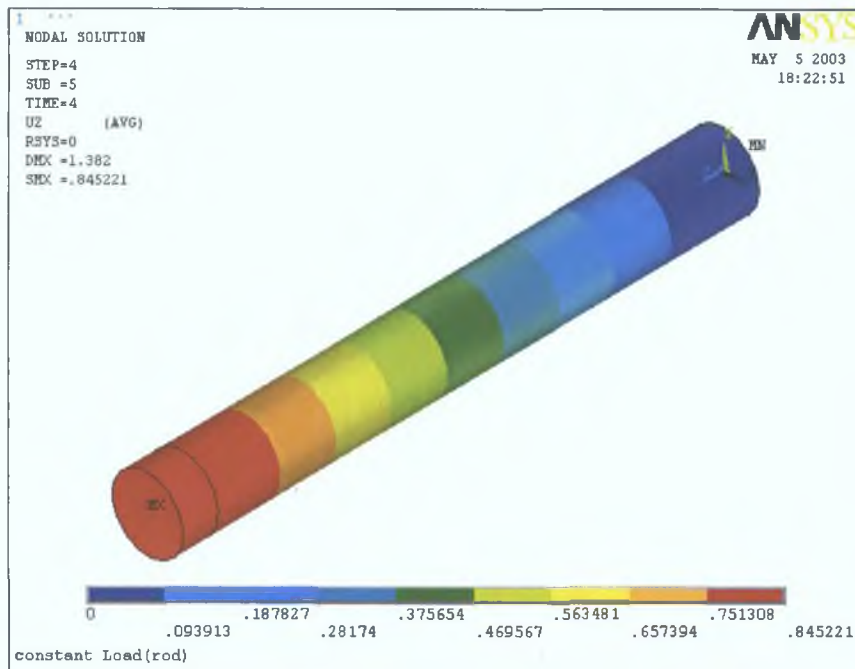


Axial Displacement

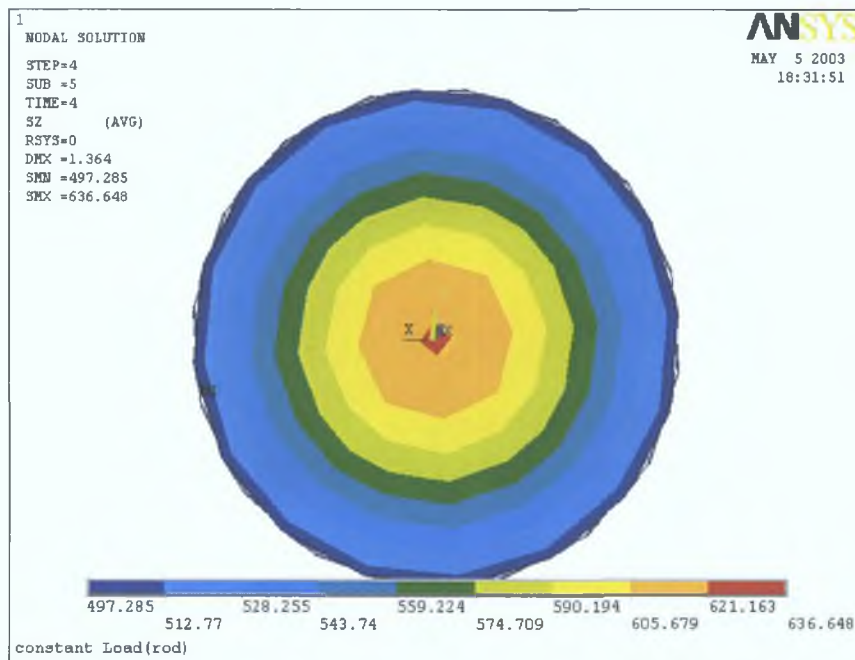


Distribution of axial stress

Figure 5.26 Deformation of the Rod after applying torque (constant load) (F= 75%YL)



Axial Displacement



Distribution of axial stress

Figure 5.27 Deformation of the Rod after applying torque (constant load) (F=90%YL)

5.6.3 Torsion followed by Tension, Tube

Angle of Twist Constant

In the first type of loading, the model was subjected to an initial torque as the first load step and then, holding its corresponding angle of twist constant, the axial load was applied in the subsequent load steps. However the axial load was applied to the model in increments, therefore the total axial load was applied gradually. Figure 5.28 shows that the magnitude of the initially applied torque remains constant until the combined stress reaches a critical value. As the axial stress increases due to the increase in the axial load the shear stress starts to decrease in a specific manner which is governed by the yield criteria. It is seen from figure 5.28 that when the initially applied torque is nearly close to the yield torque, the torque and hence the shear stress begins to decrease as soon as the axial load is applied. The shear stress initially decreases at slower rate and as the axial stress increases further due to the increase in the axial load the shear stress decreases at faster rate. When the axial load reaches nearly the yield load the torque and hence the shear stress decreases and reduces to almost zero.

Figures 5.29 to 5.31 show the angular displacement and the distribution of shear stress in the deformed tube at 25%, 50% and 75% of the yield torque after the application of the axial load.

5.6.4 Tension followed by Torsion, Tube

Axial Displacement constant

For the second type of loading, an initial axial load was applied to the model as first load step and then, keeping its corresponding axial displacement constant, the torque was applied to the model in subsequent load steps. The torque was applied to the model in increments, therefore, the total torque was applied gradually. This procedure was repeated for four different initial axial loads, $F = 0.94, 0.77, 0.48$ and 0.24 . The axial stress versus the shear stress for different levels of initially applied axial load was plotted and presented in figure 5.32. This figure shows that there is no reduction in the initially applied axial load and hence no reduction in the

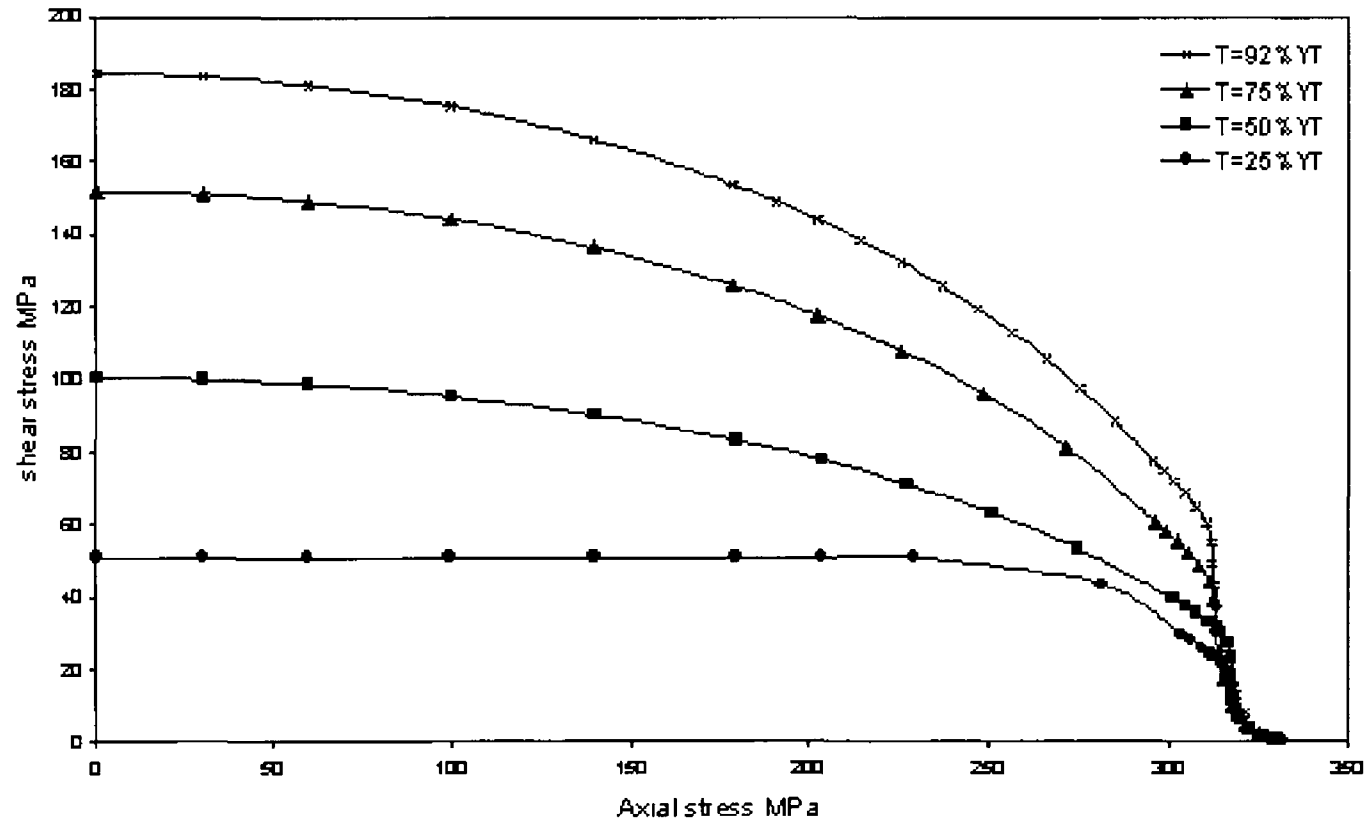
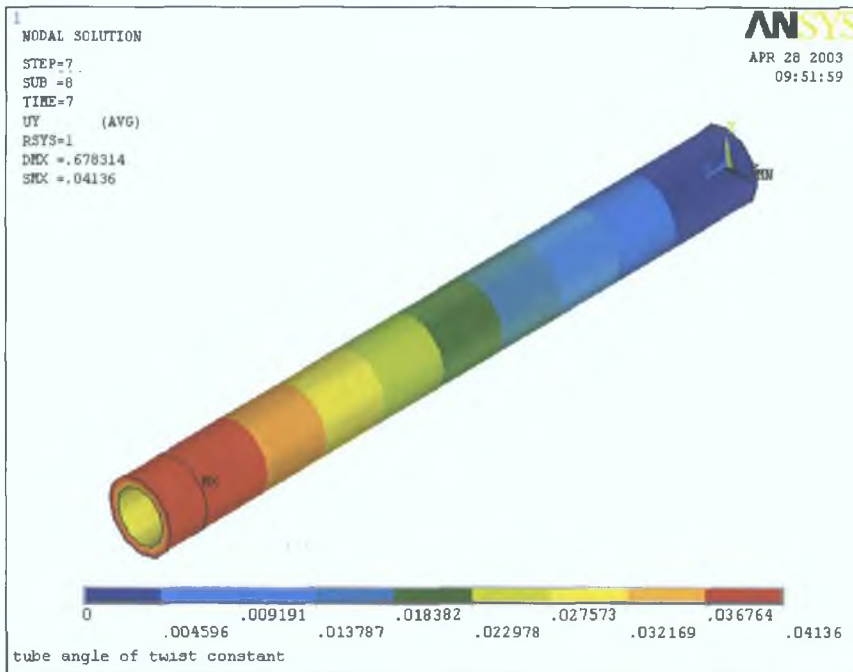
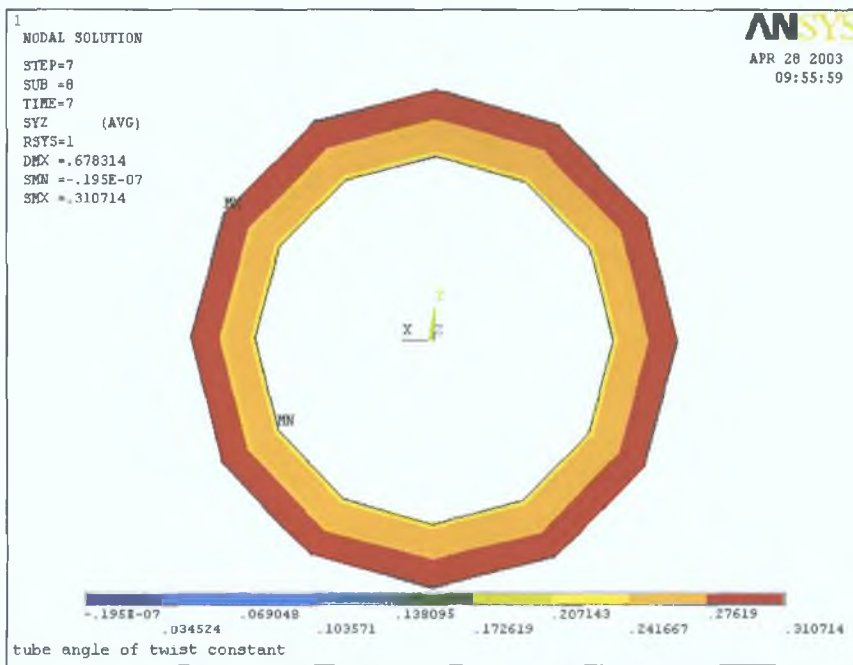


Figure 5.28 Axial stress versus shear stress (constant angle of twist)
(Thin-walled tube)

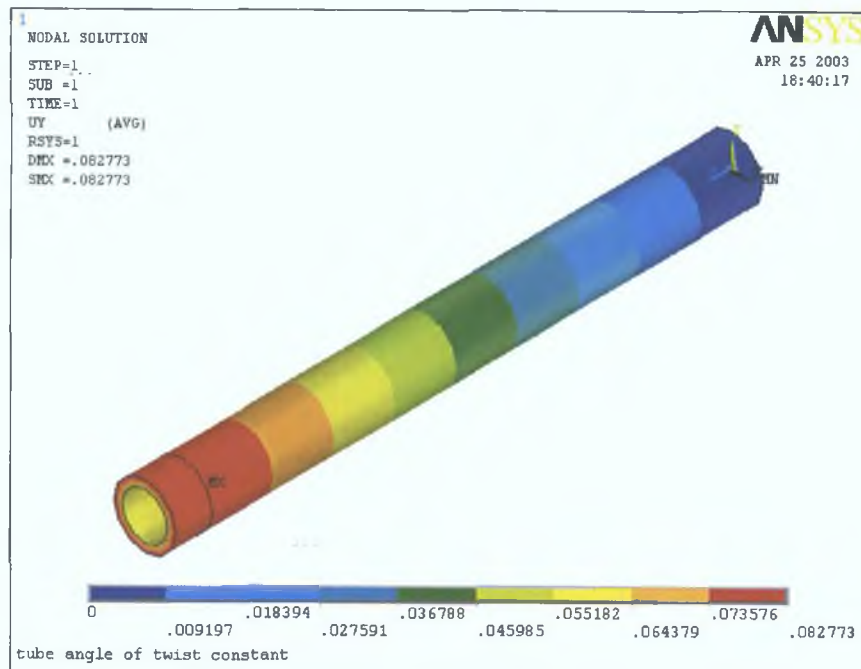


Angular Displacement

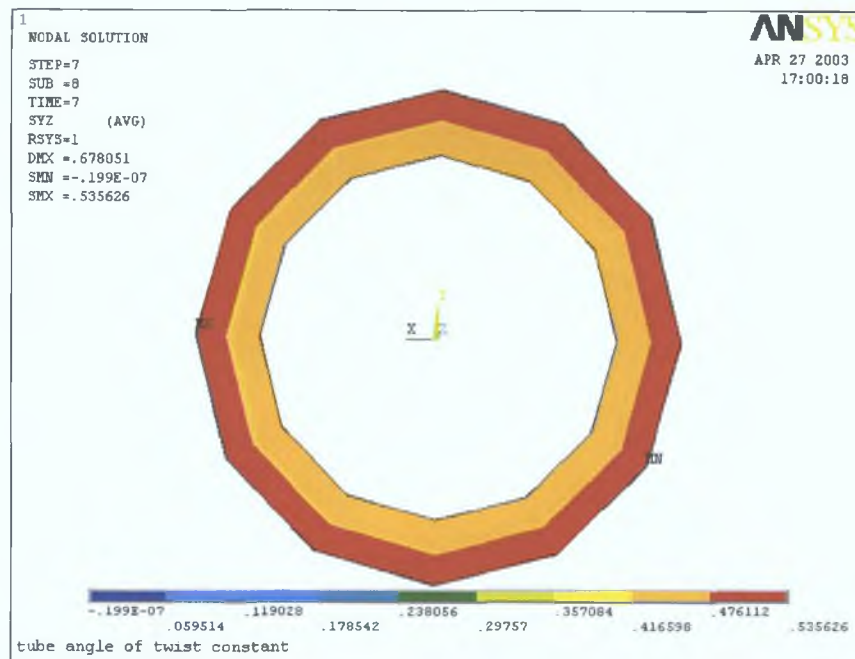


Distribution of shear stress

Figure 5.29 Deformation of the Tube after applying axial load (constant angle of twist)
($T = 25\% Y_T$)

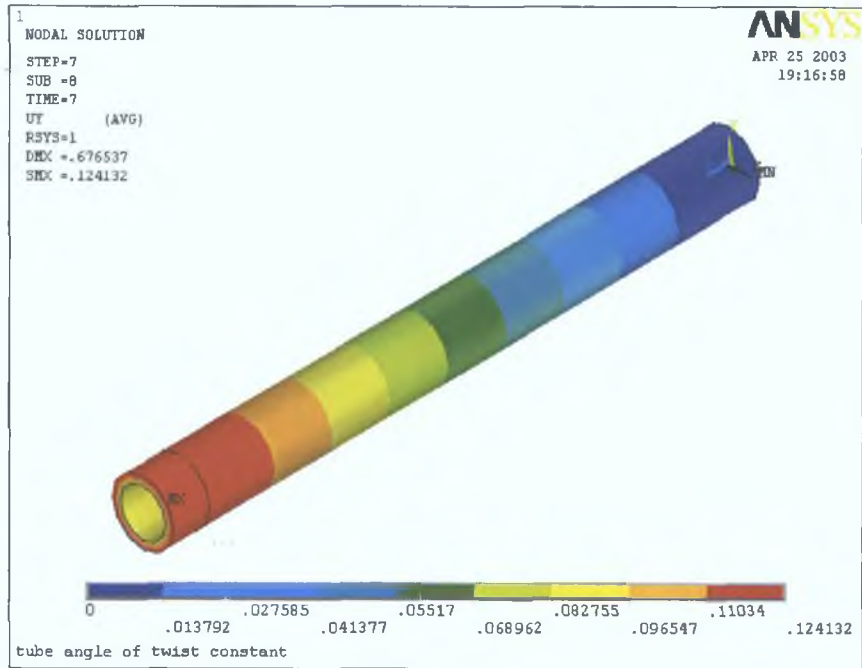


Angular Displacement

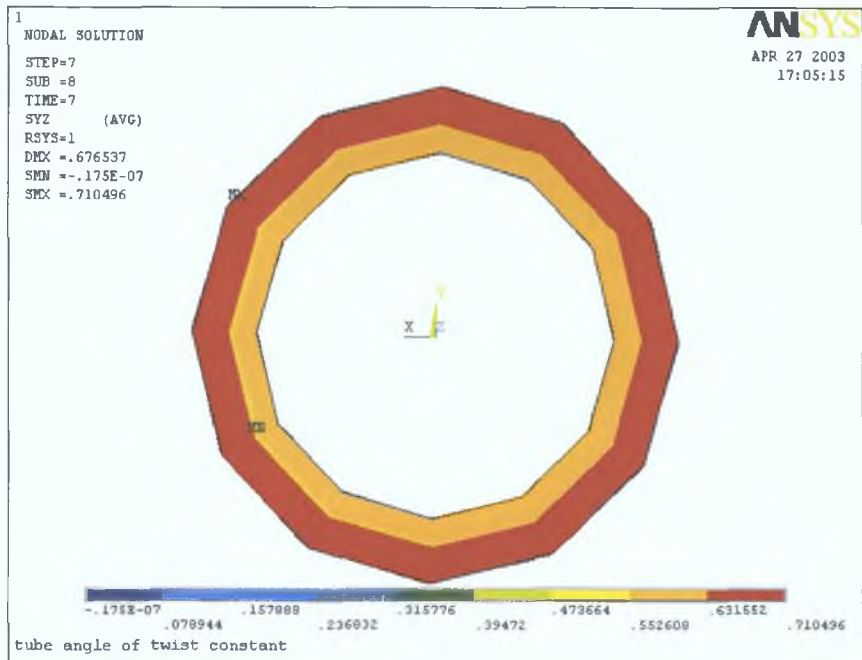


Distribution of shear stress

Figure 5.30 Deformation of the Tube after applying axial load (constant angle of twist) (T= 50%YT)



Angular Displacement



Distribution of shear stress

Figure 5.31 Deformation of the Tube after applying axial load (constant angle of twist)
($T = 75\%YT$)

corresponding axial stress as long as the combined stress does not reach a critical value. The axial stress starts to decrease due to the decrease in the axial load when the combined stress in the model becomes equal to a specific value, as dictated by the yield criteria, and the material exhibits a reduced ability to sustain the initially applied axial load with the subsequently applied torque. It also can be seen from the figure that when the initially applied axial load is nearly equal to its yield load (about 94% of the yield load) the axial load and hence the axial stress begins to decrease rapidly with the increase of torque.

Figures 5.33 to 5.36 show the axial displacement and the distribution of axial stress in the deformed tube at 25%, 50%, 75% and 100% of the yield load after the application of the torque.

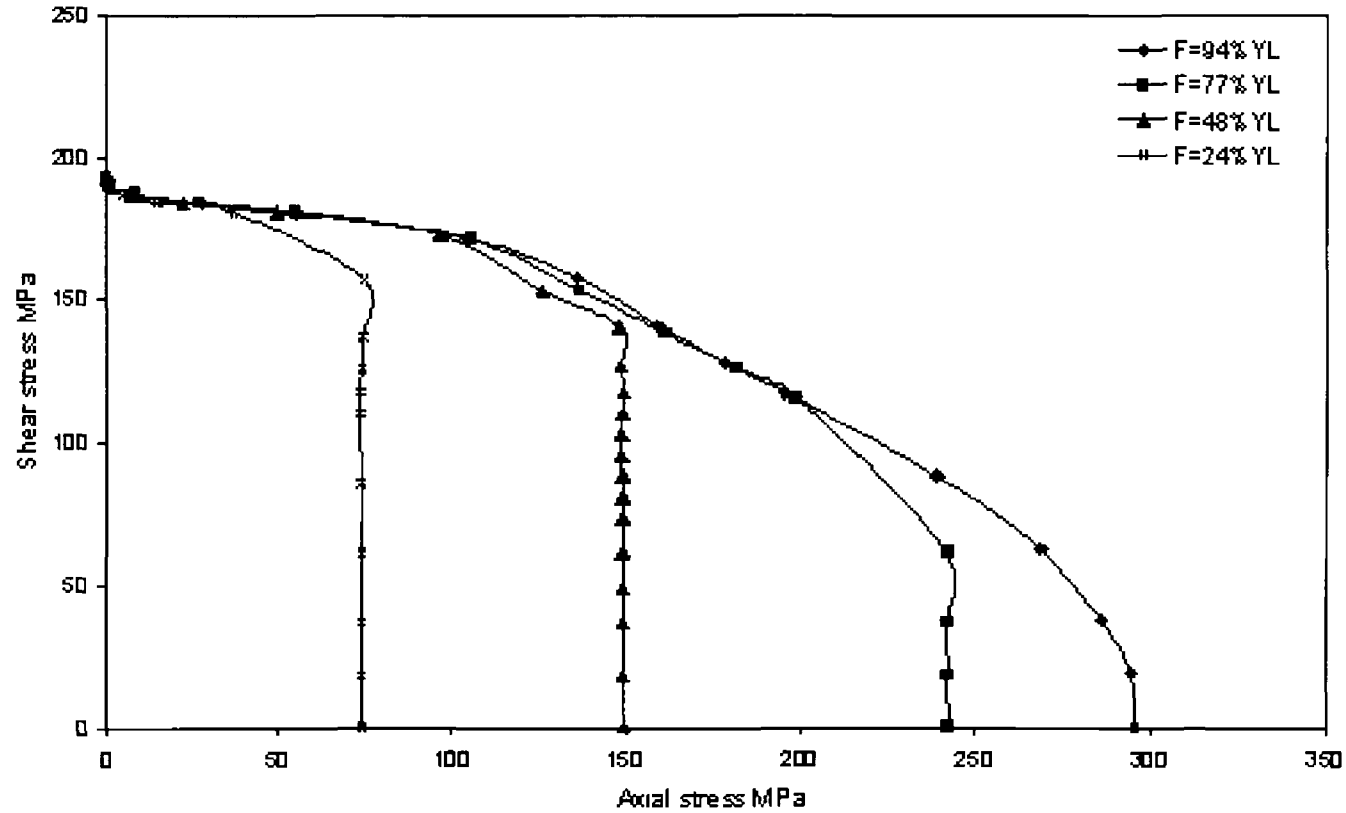
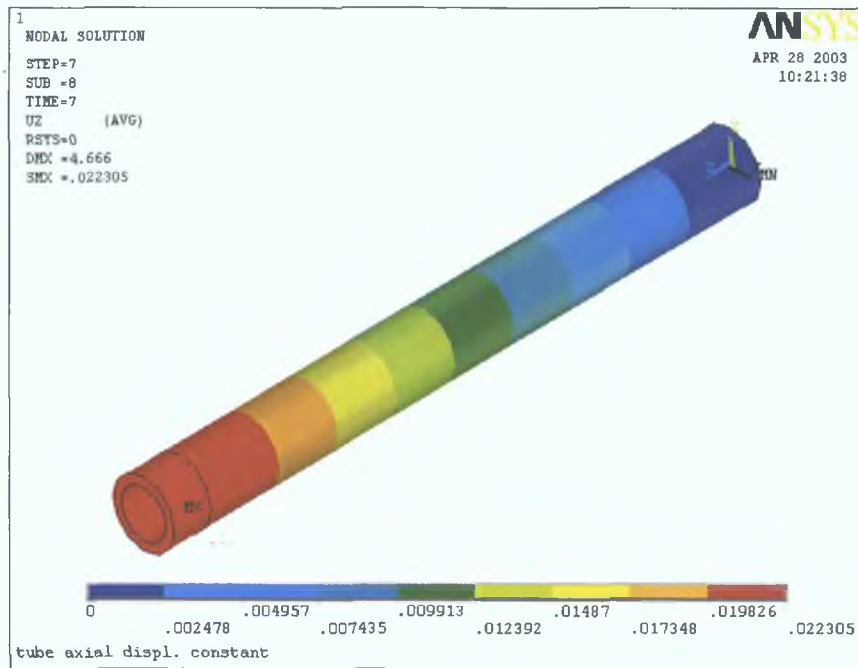
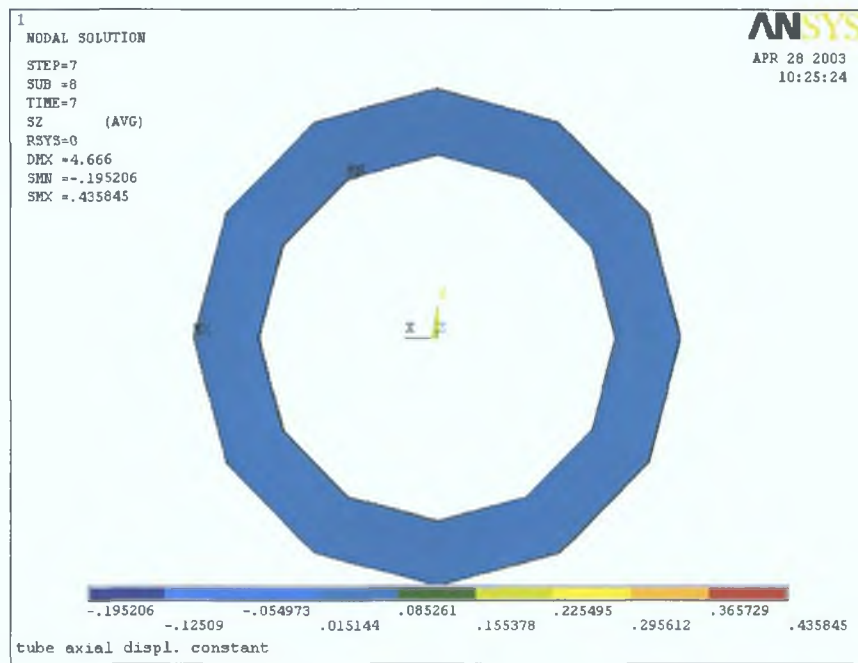


Figure 5.32 Axial stress versus shear stress (axial displacement constant)
(Thin-walled tube)

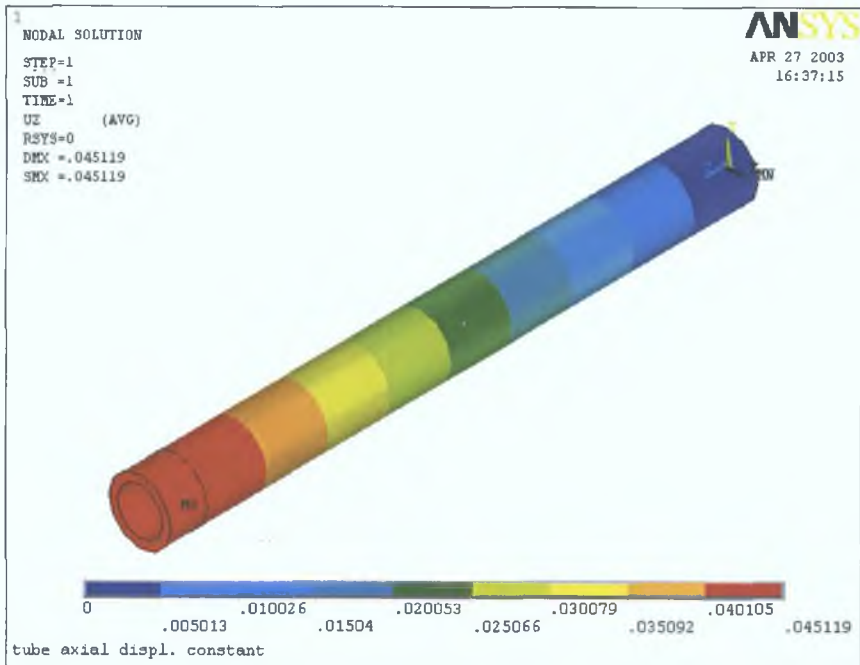


Axial displacement

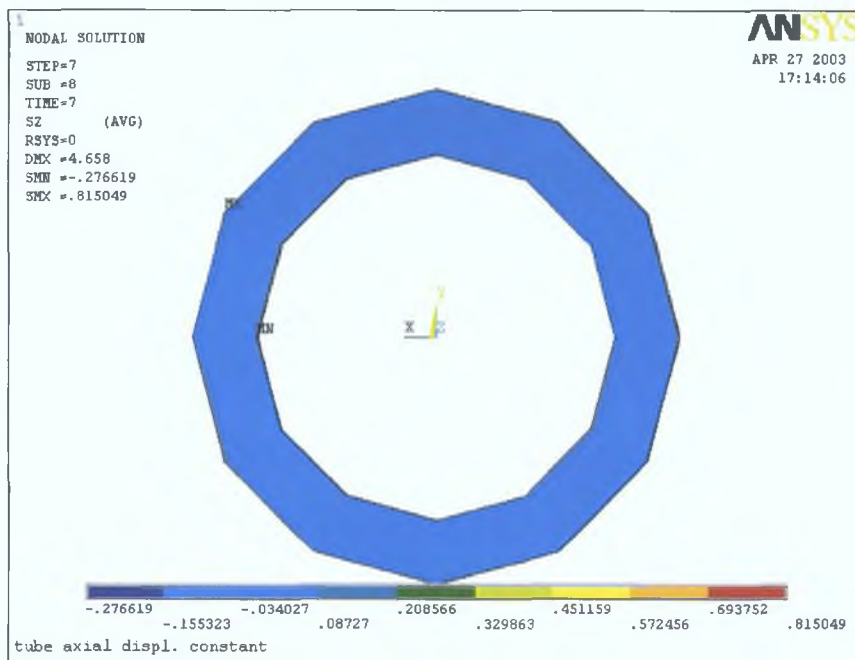


Distribution of axial stress

Figure 5.33 Deformation of the Tube after applying torque (constant axial displacement) (F= 25%YL)

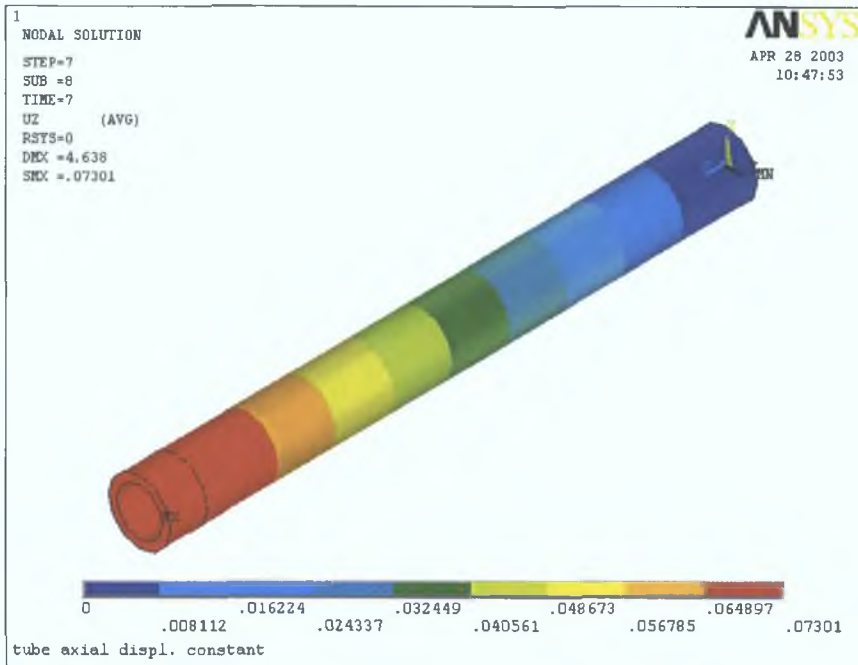


Axial Displacement

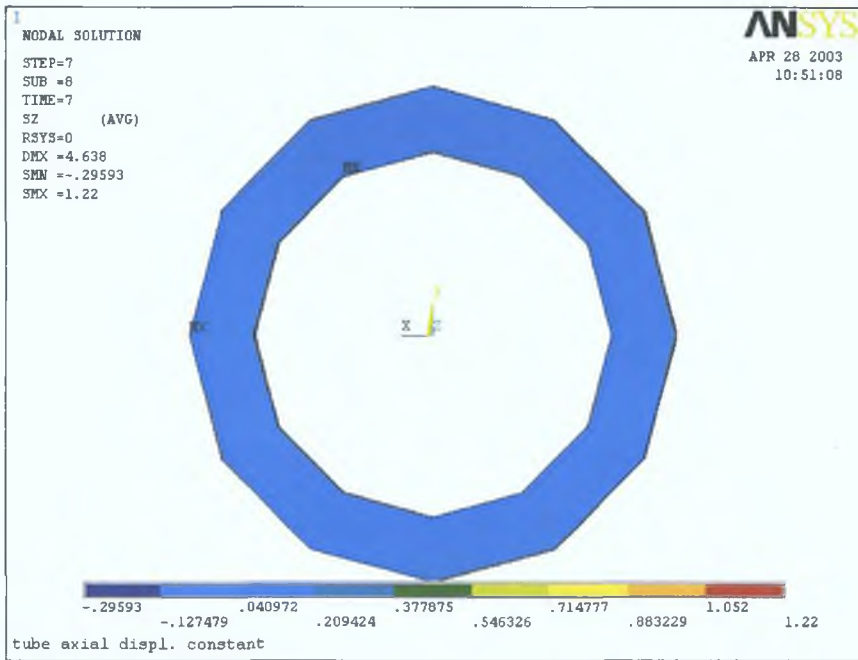


Distribution of axial stress

Figure 34 Deformation of the Tube after applying torque (constant axial displacement)
 (F= 50%YL)

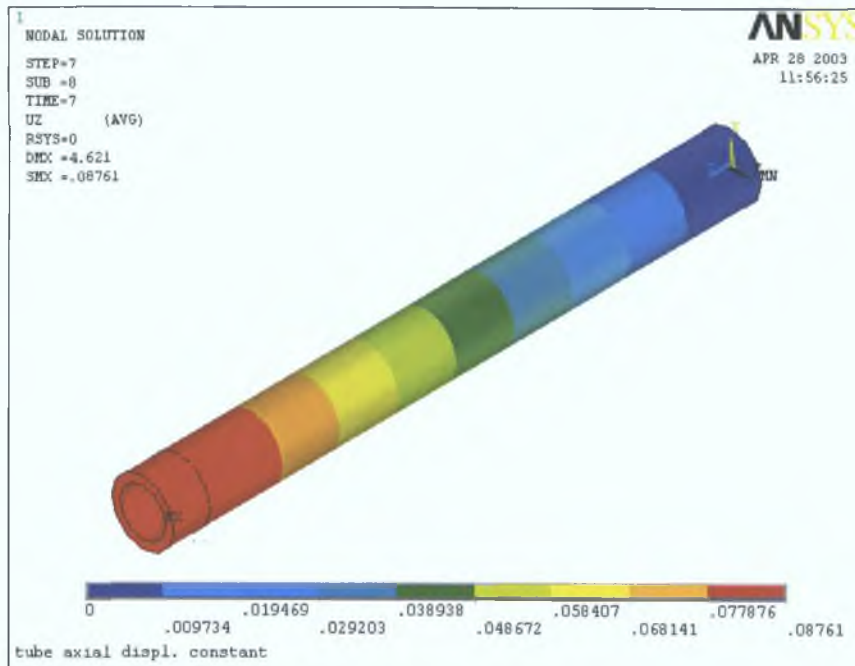


Axial Displacement

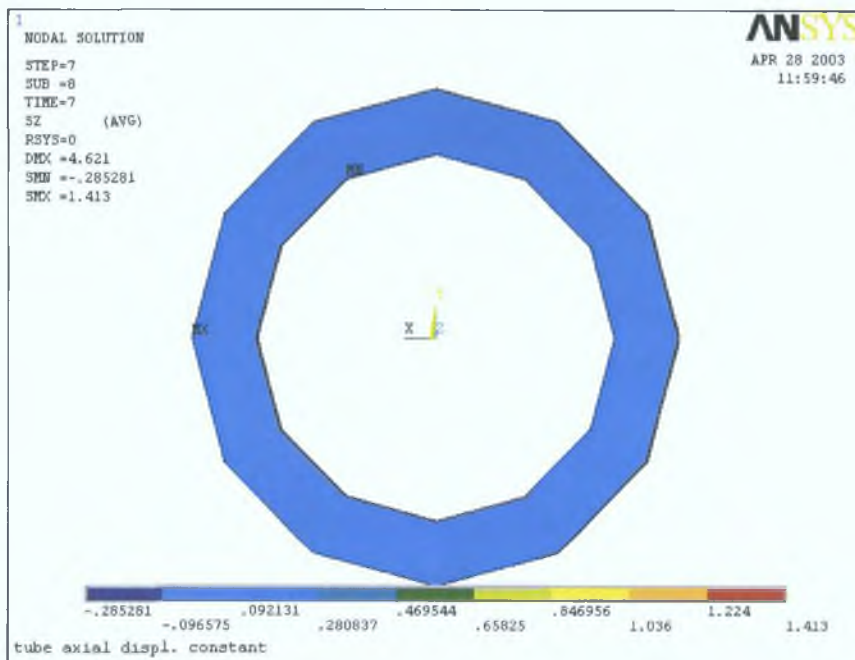


Distribution of axial stress

Figure 5.35 Deformation of the Tube after applying torque (constant axial displacement) (F= 75%YL)



Axial Displacement



Distribution of axial stress

Figure 5.36 Deformation of the Tube after applying torque (constant axial displacement) (F= 100%YL)

CHAPTER SIX

VERIFICATION OF FINITE ELEMENT RESULTS

6.1 INTRODUCTION

Finite element analysis (FEA) of structures plays an increasingly important role in engineering practice, as it is relatively inexpensive and time efficient compared with physical experiments. Therefore, finite element analysis is more economical than physical experiments, provided that the finite element model (FEM) is accurate. Hence, it is necessary to verify the finite element with experimental results. This chapter details the comparison of experimental results with the finite element analysis results.

6.2 VERIFICATION OF FEA PREDICTION

6.2.1 Tension followed by Torsion, Solid Rod

Axial Displacement Maintained Constant

In the first type of loading, where the model was subjected to initial axial load and then the torque was applied gradually keeping the initial axial displacement constant, the experimental and the finite element analysis results have been plotted in terms of shear and axial stresses and are presented in figure 6.1. The solid lines shown in the figure represent the plots of the finite element analysis results for the above-mentioned type of loading. It is apparent from the figure that, the finite element simulation results agree well with the experimental results up to a value just over the combined yield curve. Thereafter the finite element results show drops in the combined axial and shear stresses. The differences between the finite element and experimental results is due to the inability of the existing elastic-plastic material model used in Ansys to describe the mechanical behaviour of the material used in the experimental investigations.

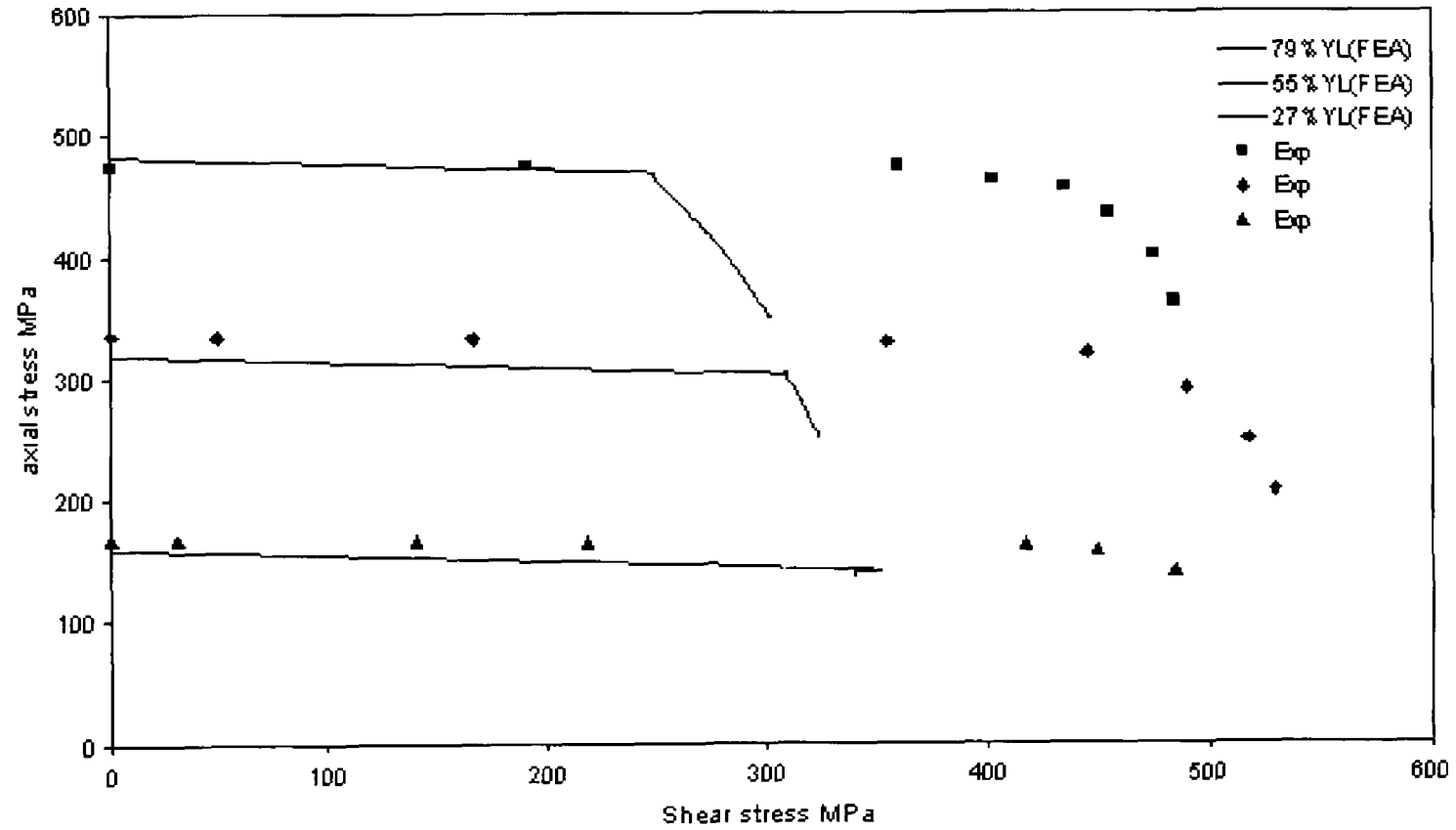


Figure 6 1 Comparison of experimental and FEA results of the Solid Rod
(axial displacement constant)

Axial Load Constant

The experimental points for this type of loading have been replotted in terms of axial stress and shear stress and are presented in figure 6.2. The solid lines shown in the figure present the finite element analysis. The figure reveals that the finite element simulation results agree well with the experimental results up to a value just over the combined yield curve. Thereafter the finite element results show a drop in the combined axial stress and shear stress. The differences between the finite element and experimental results is due to the inability of the existing elastic-plastic material model used in Ansys to describe the mechanical behaviour of the material used in the experimental investigations.

6.2.2 Torsion followed by Tension, Solid Rod

Angle of Twist Held Constant

The experimental and the finite element analysis results for this type of loading have been plotted in terms of the axial stress and the shear stress and are presented in figure 6.3. The solid lines shown in the figure represent the plots of the finite element analysis results for the above mentioned type of loading. The figure reveals that the finite element analysis results are reasonably in good agreement with the experimental results. It is observed from the figure that, when the initial torque is equal to 31% and 50% of the yield torque the finite element analysis results lie reasonably close to experimental results. It is also observed from the figure that for higher initial torque the rate of decrease of shear stress in the finite element analysis is relatively high compared to the experimental results. This is due to inability of the existing elastic-plastic material model used in Ansys to describe the mechanical behaviour of the material used in the experimental investigations.

Torque Held Constant

The experimental results are plotted alongside those from the finite element analysis for this type of combined loading in terms of the axial stress and shear stress and are

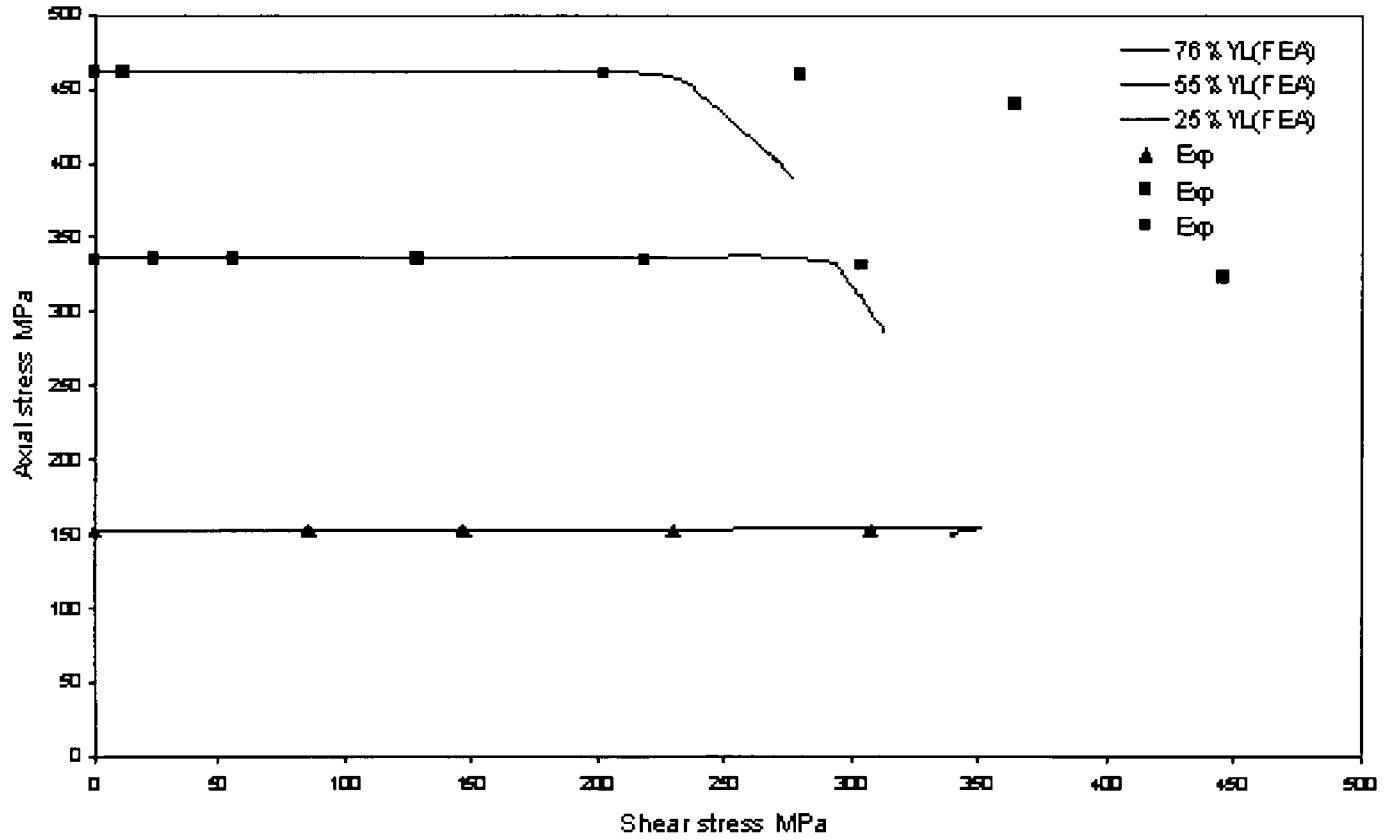


**Figure 6 2 Comparison of expermental and FEA results of the solid Rod
(constant axial load)**

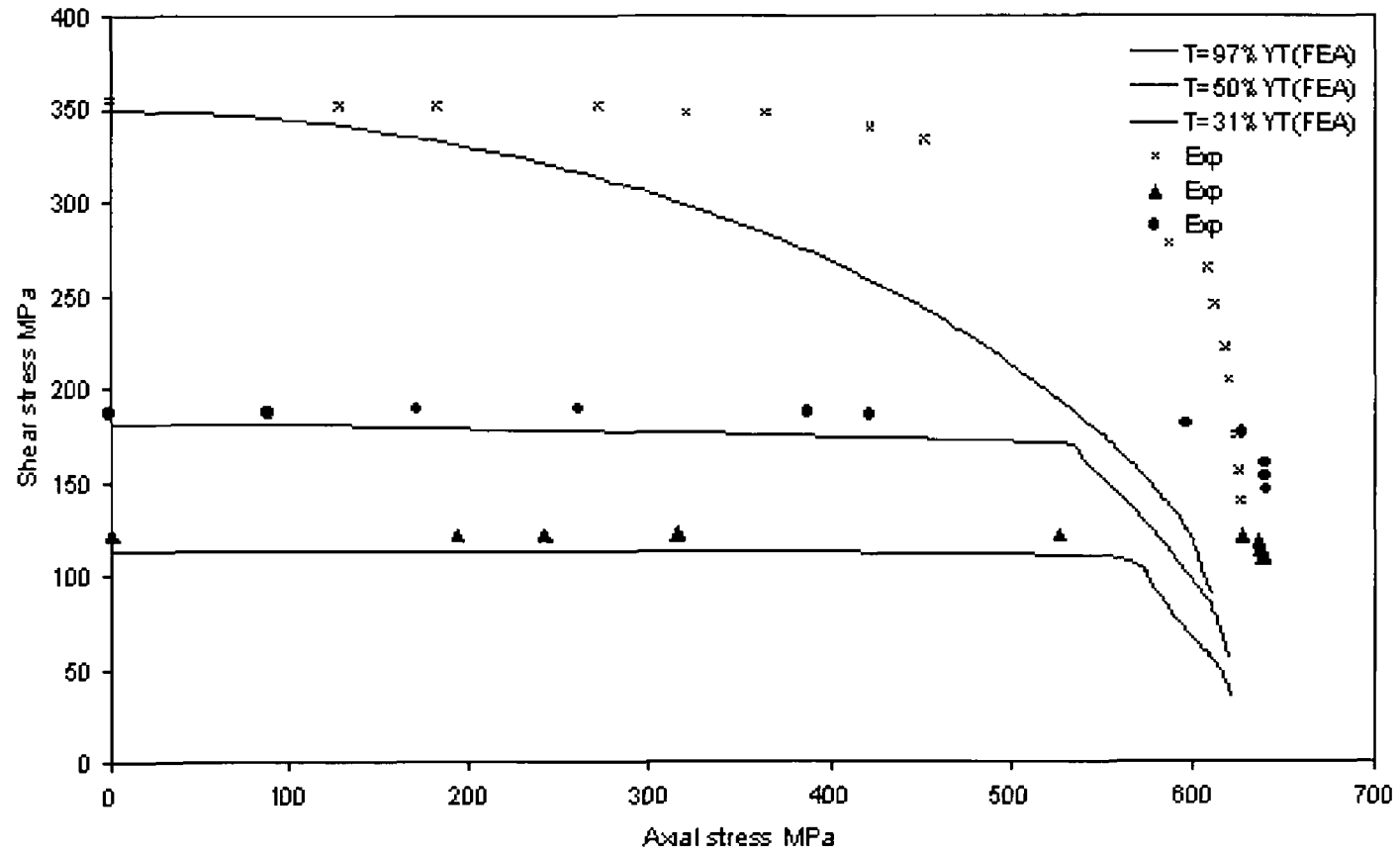


Figure 6.3 Comparison of experimental and FEA results of the solid Rod (constant angle of twist)

presented in figure 6.4. The solid lines shown in the figure present the plots of the finite element analysis results. It can be seen from the figure that the finite element results are in good agreement with the experimental results up to a value just over the combined yield curve. After that the finite element results show a drop in the combined axial and shear stresses. This difference is due to the inability of the existing elastic-plastic material model used in Ansys to describe the mechanical behaviour of the material used in the experimental investigations.

6.2.3 Tension followed by Torsion, Tube

Axial Displacement Constant

In this type of loading, the experimental and the finite element analysis results have been plotted in terms of the axial stress and shear stress and are presented in figure 6.5. The solid lines shown in the figure represent the plots of the finite element analysis results. It is apparent from the figure that, the finite element analysis results are reasonably in good agreement with the experimental results up to a value just over the combined yield curve. The figure reveals that the experimental points decrease relatively slowly, when the combined stress state reaches the plastic yield stress compared to the finite element analysis results. This is due to the inability of the existing elastic-plastic material model used in Ansys to describe the mechanical behaviour of the material used in the experimental investigations.

6.2.4 Torsion followed by Tension, Tube

Angle of Twist Constant

The experimental and the finite element analysis results, for this type of loading, have been plotted in terms of the axial stress and shear stress and are presented in figure 6.6. The solid lines shown in the figure present the finite element analysis results for the above mentioned type of loading. The figure reveals that the finite element analysis results are in good agreement with the experimental results up to a value just over the combined yield curve. There after the finite element results show a drop in the combined axial and shear stresses. The difference between the experimental and finite element analysis results is due to the inability of the existing

elastic-plastic material model used in Ansys to describe the mechanical behaviour of the material used in the experimental investigations

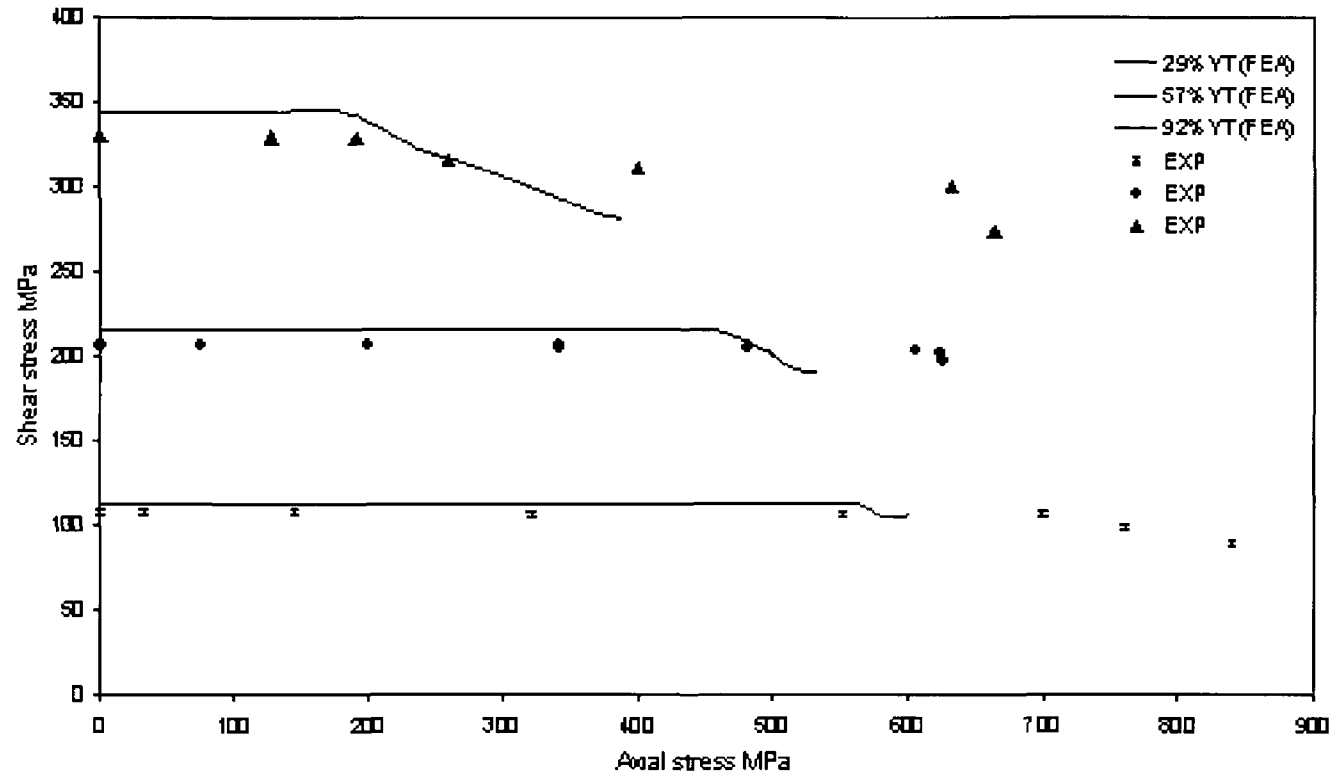


Figure 6.4 Comparison of Experimental and FEA results of the Solid Rod (constant torque)

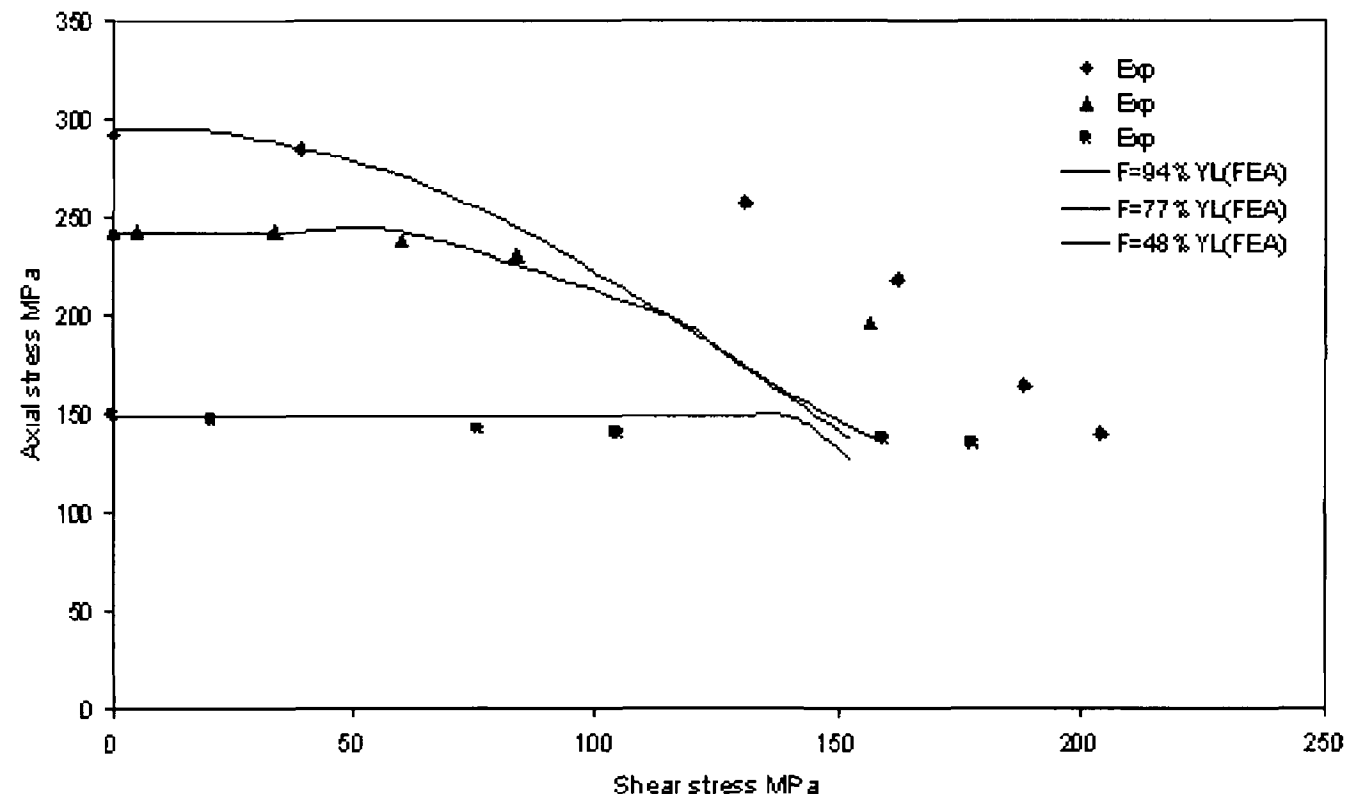


Figure 6.5 Comparison of experimental and FEA results of the Tube (axial displacement constant)

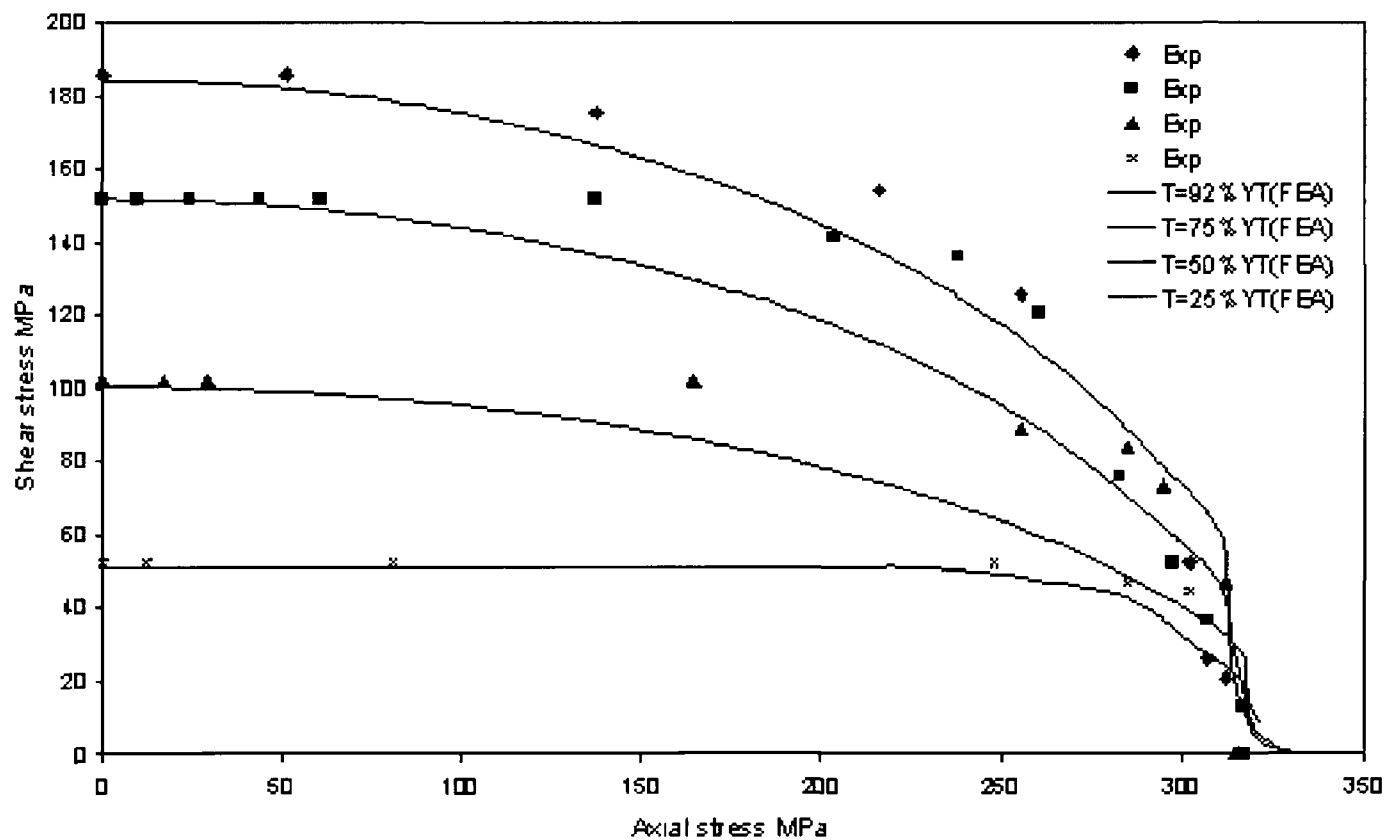


Figure 6.6 Comparison of experimental and FE A results of the Tube (constant angle of twist)

CHAPTER SEVEN

CONCLUSIONS

7.1 INTRODUCTION

This chapter gives a brief summary of the concluding remarks arising from the present research work. It also highlights the contribution arising from this thesis and the recommendations for further work.

7.2 GENERAL CONCLUSIONS

The main conclusions resulting from the experimental investigation and the finite element analysis are summarised below.

7.2.1 Experimental Investigation

- In the first type of loading, where the axial displacement is held constant, the initially applied axial load begins to decrease with the subsequently applied torque when the combined stress reaches a critical value which is governed by the yield criteria. With the increase in the torque, the axial load carrying capacity is reduced without in any way compromising its torque carrying ability.
- Similarly, in the second type of loading, where the angle of twist is held constant, the torque carrying capacity of the specimen drops rapidly once the yield load is reached. When the initially applied torque is closer to the yield torque, the maximum axial load that can be applied to the specimen decreases significantly. After the specimen becomes fully plastic, even without any increase in the axial load, the axial stress and the shear stress increase rapidly as necking commences and the specimen fails rapidly.

- In the case of the thin-walled tube, where the initial angle of twist kept constant, the rate of decrease of the torque is much faster than those of the solid rods. The residual torque left within the tube is much less than the solid rod and the sustainability of the initially applied torque is reduced to almost zero due to subsequent application of the axial load.
- In the second loading path, where the tube was subjected to an initial axial load and then, holding its corresponding axial displacement constant, the torque was gradually increased until the specimen failed. The rate of decrease in the initially applied axial load was much faster than those of the solid rods.

7.2.2 Finite Element Analysis

- In this case, where the model was initially subjected to a torque and then, keeping the corresponding angle of twist constant, the axial load applied in the subsequent load steps. The initially applied torque decreases as the axial load increases according to the yield criteria. The higher the magnitude of the initially applied torque, the greater is the rate of decrease in the torque carrying ability with the gradually applied axial load.
- For this case, where an initial axial load was applied to the model as the first load step and then, keeping its initial axial displacement constant, the torque was applied in the subsequent load steps. The axial load carrying ability of the model drops rapidly once the yield load is reached. When the model was subjected to high initial axial load, the axial stress starts to decrease at a greater rate.
- When the thin-walled tube model was subjected to an initial torque as the first load step and then, keeping the angle of twist constant, the axial load was applied in the subsequent load steps. The ability of the model, when yielding starts, to sustain the initially applied torque decreased with the subsequently applied axial load without affecting its axial load carrying ability.

- Similarly, when the tube was subjected to an initial axial load as the first load step and then, keeping its initial axial displacement constant, the torque was applied in the subsequent load steps, when yielding starts, the axial load carrying ability of the tube decreased with the subsequently applied torque

7 2 3 Comparison of Experimental Results with the FEA Results

- For the combined loading of the solid rod, the finite element analysis results are reasonably in good agreement with the experimental results for the four types of loading used. Similarly, for the combined loading of the thin-walled tubes the results of the finite element analysis agree well with experimental results

7 3 THESIS CONTRIBUTION

In the course of this research, it is believed that the following contributions have been made in the general area of the research topic

- Development of a novel adaptive control system for the Tension-Torque machine
- The specimen can sustain combined axial and torsion loads well beyond the von Mises yield curve
- The subsequent loading of the specimen becomes dominant to describe the elasto-plastic behaviour of the specimen
- Development of finite element methodology for predicting the effect of the combined tension and torsion loading conditions on the failure loads of the experimental specimens

7 4 RECOMMENDATION FOR FURTHER WORK

- The non-proportional combined loading tests carried out in this research work can be conducted after annealing the specimen and at different strain rates

- The non-proportional combined loading tests can be conducted on threaded rod
- In a similar manner the proportional combined loading tests can be conducted and compared with finite element analysis code
- The micro-structure of the fractured specimens can be observed and studied
- Mild steel (En8) was used for all experimental investigations and simulations in this work. Different materials including composite material can be used

References

- 1 Mendelson, A , "Plasticity Theory and Application", Book, the Macmillan Company, New York, 1968, Library of Congress Catalog Card no 68-12718
- 2 Snyder, R D and Byars, E F , "Engineering Mechanics", McGraw-Hill, Inc , 1973, ISBN-0-07-059530-5
- 3 Bickford, J H , "An introduction to the design and behaviour of bolted joints", Marcel Dekker Inc , New York (third edition), 1995
- 4 Reddy, J N , "Introduction to finite element method", Published by McGraw-Hill, 1993, ISBN 0070513554
- 5 ANSYS Inc ANSYS user Manual for release 5.7 Cannonsburg Pennsylvania ANSYS, Inc
- 6 Nadai, A , "Theory of flow and fracture of solids", Book, McGraw-Hill Company, Inc , Vol 1, Second edition, 1950
- 7 Lode, W , "Versuche ueber den Einfluss der mittleren Hauptspannung auf das Fließen der Metalle Eisen Kupfer und Nickel ", Z Physik, 36, 1926, pp 913-939
- 8 Hill, R , "The mathematical theory of plasticity ", Book, Oxford University Press, London, 1950
- 9 Hohenemser, K , Proceeding of 3rd Int Cong App Mech , Stockholm, Vol 2, 1930
- 10 Taylor, G I and Quinney, H , "The plastic deformation of metals", Phil Trans Roy Soc , London, A230, 1931, pp 323-362
- 11 Morrison, J L M and Shepherd, W M , "An experimental investigation of plastic stress-strain relations", Proc Instn Mech Engrs , 163, 1950
- 12 Hill, R and Siebel, M P L , "On the plastic distortion of solid bars by combined bending and twisting", J of Mechanics and physics of solids, Vol 1, 1953, pp 207-214
- 13 Meguid, S A and Campell, J D , "Elastic-plastic tension-torsion in a circular bar of rate-sensitive material", J of applied math (Trans Of the ASME, Ser E) Vol 46 (2), 1979, pp 311-16
- 14 Meguid, S A and Klair, M S , "Theoretical and experimental results of the plastic and strain hardening behaviour of En8 at a controlled rate", Int J of Mech Sci , Vol 26, No 11/12, 1984, pp 607-616

- 15 Naghdi, P M and Roeley, J C , “An experimental study of biaxial stress-strain relations in plasticity”, *J of the Mechanics and Physics of Solids*, Vol 3, 1954, pp 63-80
- 16 Prager, W and Hodge, P G , “Theory of perfectly plastic solids”, Book, Wiley, New York, 1951
- 17 Gaydon, F A , “On the combined torsion and tension of a partly plastic circular cylinder”, *Quart J Mech And Applied Math* , Vol 5, 1952, pp 29-41
- 18 Sved, G and Brooks, D S , “Elasto-plastic behaviour of a round bar subjected to axial force and torque”, *Acta Techn Hung* , Vol 50, 1965
- 19 Brooks, D S , “The elasto-plastic behaviour of a circular bar loaded by axial force and torque in the strain hardening range”, *Int J Mech Sci* , Pergman Press, Vol 11, 1969, pp 75-85
- 20 Ali, A R M and Hashmi, M S J , “Theoretical and experimental results of the elastic-plastic response of a circular rod subjected to non-proportional combined torque and tension loadings”, *Proc Instn Mech Engrs* , Vol 213, Part c, 1999, pp 251-261
- 21 Tsangarakis, N , Pelletier, G P and Pepi, M S , “Response of an Alumina Fiber-reinforced Aluminium Composite to combined tension-torsion”, *Experimental Mechanics*, 1992, pp 49-53
- 22 Rees, D W A , “deformation and fracture of metal matrix particulate composites under combined loadings”, *composites Part A* 29A, 1998, pp 171-182
- 23 Maguide, S A , “Plastic flow of mild steel (En8) at different strain rates under abruptly changing deformation paths”, *J Mech Phys Solids*, Vol 29, No 5/6, 1981, pp 375-395
- 24 McMeeking, R M , “The finite strain tension-torsion test of a thin-walled tube of elastic-plastic material”, *Int J solids structures*, Vol 18, No 3, 1982, pp 199-204
- 25 Narayanaswamy, O S , Samanta, S K and Ghosh, A K “Plastic deformation and spring back of rectangular bars subjected to combined torsion and tension”, *J Mech Phys Solids*, Vol 30, No 6, 1982, pp 427-445
- 26 Correa, E C S , Aguilar, M T P and Cetlin, P R , “The effect of tension/torsion strain path changes on the work hardening of Cu-Zn brass”, *J Materials Processing Technology*, Vol 124, 2002, pp 348-388

- 27 Correa, E C S , Aguilar, M T P , Monteiro, W A and Cetlin, P R , “Work hardening behaviour of prestrained steel in tensile and torsion tests”, *J Mater Sci Lett* , Vol 19, 2000, pp 779-781
- 28 Jiang, W , “The elastic-plastic response of thin-walled tubes under combined axial and torsional loads part I- monotonic loading”, *J of Pressure Vessel technology* (Transaction of the ASME), Vol 115, Aug 1993, pp 283-290
- 29 Jiang, W , “The elastic-plastic response of thin-walled tubes under combined axial and torsional loads Part II-Variable loading”, *J pressure Vessel Technology* (Transaction of the ASME), Vol 115, Aug 1993, pp 291-296
- 30 Jiang, W and Wu, K , “Thin-walled tubes subjected to combined internal pressure and axial load”, *AIAA Journal*, Vol 31, No 2, Feb 1993, pp 377-387
- 31 Khan, A S and Liang, R , “Behaviour of three BCC metals during non-proportional multi-axial loadings experiments and modelling”, *J of Int plasticity*, Vol 16, 2000, pp 1443-1458
- 32 Danish, G H and Hawk yard, J B , “A tension-torsion machine for testing yield criteria and stress-strain relationships at $T=78^{\circ}k$ ”, *Int J of Mech Sci* , Vol 18, pp 57-62, Pergamon Press 1976
- 33 Meguid, S A , Malvern, L E and Campbell, J D , “Plastic flow of mild steel under proportional and non-proportional straining at a controlled rate”, *J of Engineering Materials and Technology*, Vol 101, July1979, pp 248-253
- 34 Phillips, A , Tang, J L and Ricciuti, M , “Some new observations on yield surfaces”, *Acta Mech* , 20, 1974, pp 23-29
- 35 Phillips, A and Weng, G J , “An analytical study of an experimentally verified hardening law”, *Trans ASME, J Applied Mech* , Vol 42, 1975, pp 375-378
- 36 Phillips, A and Kasper, R , “On the foundation of thermo-plasticity-an experimental investigation”, *J Appl Mech* , Vol 40, 1973, pp 891-896
- 37 Phillips, A and Tang, J L , “The effect of loading path on the yield surface at elevated temperature”, *Int J of solids and structures*, Vol 8, 1972, pp 463-474
- 38 Phillips, A , Liu, C S and Justusson, J W , “An experimental investigation of yield surface at elevated temperature”, *Acta Mech* , 14, 1972, pp 119-146
- 39 Naghdi, P M Essenburg, F and Koff, W , “An experimental study of initial and subsequent yield surface in plasticity”, *J of Appl Mech* , Vol 201, No 25, 1958, pp 201-209

40. Mair, W. M. and Pugh, H. L. D., "Effect of prestrain on yield surfaces in copper", *J. Mech. Engng. Sci.*, 6, 1964.
41. Moreton, D. N., Moffat, D. G. and Parkinson, D. B., "The yield surface behaviour of pressure vessel steels", *J. of Strain Analysis*, Vol.16, No.2, 1981, pp. 127-136.
42. Han, C. W and Yeh, W. C., "On the experimental determination of yield surfaces and some results of annealed 304 stainless steel", *Int. J. of plasticity*. Vol.7, 1991, pp. 803-826.
43. Daneshi, G. H. and Hawkyard, J. B., "An investigation into yield surfaces and plastic flow laws for F.C.C metals at room temperature and a low temperature ($T=78^{\circ} \text{ K}$)", *Int. J. Mech. Sci.*, Vol.18, 1976, pp. 195-200.
44. Phillips, A. and Lu, W. Y., "an experimental investigation of yield surfaces and loading surfaces of pure aluminium with stress-controlled and strain-controlled paths of loading", *J. of Eng. Mat. And Tech.*, Vol.106, 1984, pp349-354.
45. Ohashi, Y., Kawashima, K. and Mori, N., "On proportional combined loading tests of an aluminium alloy and its analytical formulation", *J. of Engineering materials and Technology*, Vol.98, 1976, pp. 282-288.
46. Ohashi, Y. and Tokuda, M., "Precise measurement of plastic behaviour of mild steel tubular specimens subjected to combined torsion and axial force", *J. Mech. Phys. Solids*, Vol.21, 1973, pp.241-261
47. Ikegami, K. and Niitsu, Y., "Effects of complex loadings on plastic deformation of stainless steel (SUS 304) at high temperature", *Nuclear Engineering and Design* 114, 1989, pp. 355-364.
48. Niitsu, Y., Horigushi, A. and Ikegami, K., "Effect of temperature variation on plastic behaviour of S25C Mild steel", *Int. J. Pres. Ves.& piping* 53, 1993, pp.511-523.
49. Khan, A. S. and Wang, X., "On non-proportional infinitesimal plastic deformation after finite plastic prestraining and partial unloading", *J. Mech. Phys. Solids*, Vol.36, No.5, 1988, pp.519-535.
50. Khan, A. S. and Parikh, Y., "Large deformation in polycrystalline copper under combined tension-torsion, loading, unloading and reloading or reverse loading: a study of two incremental theories of plasticity", *Int. J. of plasticity*, Vol.2, 1986, pp. 379-392.
51. Krempl, E. and Bordonaro, C. M., "Non-proportional loading of nylon 66 at room temperature", *Int. J. of plasticity*, Vol.14, Nos. 1-3, 1998, pp. 245-258.

52. Maruyama, K. and Nakagawa, M., "Proposal of new torque control method and new design system in bolted joint", *Bull. Res. Lab. Precis. Mach. Electron.*, Tokyo Instron, Tokyo Inst. Technol., Vol.55, March 1985, pp. 25-29.
53. Gardiner, W. A., "Torque-tension relationships- what they are, why they are important", SME technical paper, No.- AD75-771, 1975.
54. Hariri, B. T., "Establishment of design criteria for tightening bolted joints", M. Eng. Thesis, Dublin City University, Dec. 1990.
55. Tsuji, H. and Maruyama, K., "Behaviour of bolted joints tightened in plastic region-Estimation of yield point load at threaded portion", *Journal of the Japan Soc. of Precis. Eng.*, Vol.57 (9), 1991, pp. 1627-1632
56. Tsuji, H. and Maruyama, K. "Behaviour of bolted joints tightened in plastic region-Equivalent diameter of threaded portion to estimate yield clamping force", *Journal of the Japan Soc. of Precise. Eng.*, Vol. 58(7), 1992, pp. 1227-1231.
57. Chapman, I., Newnham, J. and Wallace, P., "The tightening of bolts to yield and their performance under load", *J. Vibration, Acoustics, Stress, and Reliability in Design*, Vol.108, 1986, pp. 213-221.
58. Menezes, L. F., Fernandes, J. V. and Rodrigues, D. M., "Numerical simulation of tensile tests of prestrained sheets", *J. of Material Science and Engineering A264*, 1999, pp. 130-138.
59. Tsukahara, H. and Iung, T. "Finite element simulation of the Piobert-Luders behaviour in an uniaxial tensile test", *J. of Materials and Engineering A248*, 1998, pp. 304-308.
60. Dumoulin, S., Tabourot, L., Chappuis, C., Vacher, P. and Arrieux, R., "determination of the equivalent stress-equivalent strain relationship of a copper sample under tensile loading", *J. of Materials Processing Technology 5803*, 2002, pp. 1-5.
61. Pietrzyk, M., "Finite -element simulation of large plastic deformation", *J. of Materials Processing Technology 106*, 2000, pp.223-229.
62. Kim, H. S., "Finite element analysis of torsional deformation", *J. of Materials Science and Engineering A299*, 2001, pp. 305-308.
63. Kim, H. S., "Finite element analysis of high pressure torsion processing", *J. of Materials Processing Technology 113*, 2001, pp. 617-621.
64. Kim, H. S., Hong, I. S., Lee, Y. S., Dubravina, A. A., and Alexandrov, I. V., "Deformation behaviour of copper during a high pressure torsion process", *J. of Material processing Technology*, 2003.

65. Savaidis, A., Savaidis, G. and Zhang, Ch., "elastic-plastic analysis of a notched shaft under multiaxial non-proportional synchronous cyclic loading", *Theoretical and Applied Fracture Mechanics* 36, 2001, pp. 87-97.
66. Savaidis, A., Savaidis, G. and Zhang, Ch., "FE fatigue analysis of notched elastic-plastic shaft under multiaxial loading consisting of constant and cyclic components", *Int. J. of Fatigue*, Vol.23, 2001, pp. 303-315.
67. Pidaparti, R. M., Jayanti, S., Henkle, J. and El-Mounayri, H., "Design simulation of twisted cord-rubber structure using ProE/ ANSYS", *J. of Composite Structure*, Vol. 52, 2001, pp. 287-294.
68. Abu Rayhan Md. Ali, "Plastic Yielding characteristics of a rod under successively applied torsion and tension loadings", Ph.D. Thesis, Dublin City University, 1995.
69. <http://www.natinst.com>
70. Moore, J. H., "artificial intelligence programming with LabView: genetic algorithms for instrumentation control and optimization", *Computer Methods and Programs in Biomedicine* 47, 1995, pp. 73-79.
71. Cautero, G., Paolucci, G., Brena, B., Agostino, R. G., tommasini, R., Comelli, G. and Rosei, R., "A LabView-based control system for a surface Science experimental station", *Meas. Sci. Technol.*, Vol.5, 1994, pp. 1002-1011.
72. Kraub, A., Weimar, U. and Gopel, W., "LabView for sensor data acquisition", *trends in analytical chemistry*, Vol.18, No.5, 1999, pp. 312-318.
73. Morse, D. H., Antolak, A. J., Bench, G. S. and Roberts, M. L., "A flexible LabView-based data acquisition and analysis system for scanning microscopy", *Nuclear Instruments and Methods in Physics research B158*, 1999, pp.146-152.
74. "LabView Function and VI Reference Manual", National Instruments Corporation, USA, January 1998 Edition.
75. Path, K. J., "Finite element procedures", Prentice Hall, 1996.
76. Zienkiewicz, O. C., Taylor, R. L., "The finite element method", Vol. 1-2, 4th Edition, McGraw-Hill, New York, 1994.
77. Beer, G. and Watson, J. O., "Introduction to finite element and boundary elements methods for engineers", John Wiley and Sons, 1992.

- 78 Belytschko, T , Kam Liu, W and Moran, B , “Non-linear finite elements for continua and structures”, Published by John Wiley and Sons, 2000, ISBN 0471987735
- 79 Chandrupatla, T R and Belegundu, A D , “Introduction to finite elements in engineering”, published by prentice Hall, 2001, ISBN 0130615919
- 80 Szabı, B and Babuska, I, “Finite element analysis”, Published by John Wiley and Sons, 1991, ISBN 0471502731
- 81 Crisfield, M A , “Non-linear finite elements analysis of solids and structures”, Published by John Wiley and Sons, 1997, ISBN 04717059X
- 82 Introduction to ANSYS, Release 5.3, 2nd ed , July 1996
- 83 P khonke (ed), “ANSYS User’s Manual”, Rev 5.1, Vol 4, theory, Swanson Analysis System Inc , Houston, 1994
- 84 ANSYS, Structural non-Linearities, Training Manual, 2nd ed , Vol 1, Rev 5.5, 1999
- 85 Saeed Moaveni, “Finite element analysis theory and application with ANSYS”, Book, NJ Prentice Hall, 1999
- 86 Kachanov, L M , “Fundamental theory of plasticity”, Book, MIR Publisher, 1974
- 87 Chakrabarty, J , “Theory of Plasticity”, Book, McGraw-Hill Book Company, 1987, ISBN-0-07-010392-5
- 88 Kachanov, L M , “Foundations of the theory of plasticity”, North Holland Publishing Company, 1971
- 89 Johnson, W and Mellor, P B , “Engineering plasticity”, Ellis Horwood Limited, 1983, ISBN-0-85312-346-2
- 90 Benham, P P and Warnock, F V , “Mechanics of Solids and Structures”, Pitman, 1973
- 91 Herrm, E J , “Mechanics of materials”, Book, Pergamon Press ltd , UK, Vol 1, 1980
- 92 Herrm, E J , “Mechanics of materials”, Book, Pergamon Press ltd , UK, Vol 2, 1980
- 93 Błazynski, T Z , “applied elasto-plasticity of solids”, published by MacMillan press ltd , London, 1983, ISBN 0333345452

APPENDIX 1

1 1 Theory of Plasticity

The theory of plasticity is the branch of mechanics that deals with the calculation of stresses and strains in a body permanently deformed by a set of applied forces. The theory is based on certain materials experimental observations on the macroscopic behaviour of metals in uniform stress of combined stresses. The observed results are then idealised into a mathematical formulation to describe the behaviour of metals under complex stresses. Unlike elastic solids, in which the state of strain depends only on the final state of stress, the deformation that occurs in a plastic solid is determined by the complete history of the loading. The plasticity theory is, therefore, essentially incremental in nature, the final distortion of the solid being obtained as the sum total of the incremental distortion following the strain path. Theory of plasticity is concerned with the prediction of the maximum load that can be applied to the body without causing any excessive yielding. Situations in which elastic and plastic strains are comparable in magnitude arise in a number of important structural problems when the loading is continued beyond the elastic limit. Structural designs based on the estimation of collapse loads are more economical than elastic design, since the plastic method takes full advantage of the available ductility of the material. The following assumptions are made regarding the behaviour of plastic solids in the theory

- i The material is assumed to be isotropic and remains so throughout the deformation
- ii The theory assumes that the onset of plastic yield takes place sharply, either from zero strain (rigid plastic material) or from an elastic strain (elastic-plastic material), that is because of the complex nature of the stress-strain curve
- iii It is assumed that the yield stress is independent of the direction of straining, that is there is no Bauschinger effect and the current yield stress depends only up on the total strain up to the point considered

- iv The plastic stress-strain relations are used only when all of the material has reached to yield Localised yielding or gradual transition from elastic to plastic behaviour may lead to plastic theory being adopted while most of the material remains elastic
- v The period of time for which the load is applied can be ignored as long as the rate of straining is not considered to affect the yield stress characteristics
- vi The laws of plasticity are such that the strains occurring at any point are related to the current stresses at that point Logarithmic or natural strains are considered in the plasticity theory The logarithmic and conventional strains are almost equal for small strains but diverge for large strains

1 2 Theories of Yielding

The problem of designing a pressure vessel, rotating disc or some component containing a two or three principal stress system so that the material remains elastic, i.e. no yielding, when under full load is rather more complex One could adopt a trial and error method of building a component and testing it to find when the deformations were no longer proportional to the applied load, but this obviously be very uneconomical It is therefore essential to find some criterion based on stresses, or strains, or perhaps strain energy in the complex system which can be related to the simple axial conditions If a theoretical criterion can be established which agrees with complex material behaviour, it is then only necessary to establish experimentally the yield point in a simple tension or compression test

A number of theoretical criteria for yielding have been proposed over the past century, each seeking to obtain adequate correlation between estimated component life and that actually achieved under service load conditions for both brittle and ductile material applications The five main theories are

- The maximum principal stress theory, often attributed to Rankine, states that yielding will occur in a material under complex stress when σ_1 attains a value equal to the yield stress σ_y , in a simple tension test on the same material It gives good prediction for brittle materials

- The maximum principal strain theory, accredited to saint-Venant, postulated that yielding commenced when the maximum principal strain (tensile), ϵ_1 , was equivalent to the strain corresponding to the yield stress in simple tension. This theory fits experimental data on brittle materials better than those on ductile materials.
- The maximum shear stress theory is usually coupled with the names of Guest and Tresca. The assumption in this theory is that yielding is dependent on the maximum shear stress in the material reaching a critical value. It is suitable for ductile materials.
- The total strain energy, as proposed by Beltrami, and also attributed to Haigh, is based on critical value of the total strain energy stored in the material, and this is a product of stress and strain. This theory gives fairly good results for ductile materials but is seldom used in preference to the theory below.
- The shear or distortion strain energy theory has received considerable verification in practice and is widely regarded as the most reliable basis for design, particularly when dealing with ductile material. This theory was also independently established by Maxwell, von Mises and Hencky, and is nowadays generally referred to as the Mises criterion. This theory states that failure occurs when the maximum shear strain energy component in the complex stress system is equal to that at the yield point in the tensile test,

i.e.
$$\frac{1}{12G} [(\sigma_1 - \sigma_2)^2 + (\sigma_2 - \sigma_3)^2 + (\sigma_3 - \sigma_1)^2] = \frac{Y^2}{6G}$$

or
$$\sigma_1^2 + \sigma_2^2 + \sigma_3^2 - (\sigma_1\sigma_2 + \sigma_2\sigma_3 + \sigma_3\sigma_1) = Y^2$$

where Y is the yield stress in tension. For biaxial case, it becomes

$$\sigma_1^2 - \sigma_1\sigma_2 + \sigma_2^2 = Y^2$$

For two dimensional normal and shear stresses it becomes

$$\sigma_x^2 + \sigma_y^2 - \sigma_x\sigma_y + 3\tau_{xy}^2 = Y^2$$

If an element is subjected to tensile load and torque (i.e. when $\sigma_y = 0$), the above

equation reduces to
$$Y = \sqrt{\sigma_x^2 + 3\tau_{xy}^2} \quad (1)$$

In the above theories it has been assumed that the properties of the material in tension and compression are similar. For the same type of loading Tresca's criteria provides the following relation

$$Y = \sqrt{\sigma_x^2 + 4\tau_{xy}^2} \quad (2)$$

1.3 Elastic-Plastic Stress-Strain Relations

1.3.1 The Elastic Stress-Strain Relations

The complete stress-strain relations describe the elastic and plastic deformation of a material. The basic stress-strain relations in the elastic range are described below where the effects of time and temperature are not considered. It is assumed that the material is isotropic and the Bauschinger effect is negligible. It should be noted that the shearing strains, $\gamma_{xy}, \gamma_{yz}, \gamma_{zx}$ are the shear components of the strain tensor and therefore have values equal to half the corresponding values of engineering shear strain. For an isotropic material, the elastic stress-strain relations are usually written in the form

$$\begin{aligned} E\varepsilon_x &= \sigma_x - \nu(\sigma_y + \sigma_z) \\ E\varepsilon_y &= \sigma_y - \nu(\sigma_z + \sigma_x) \\ E\varepsilon_z &= \sigma_z - \nu(\sigma_x + \sigma_y) \\ 2G\gamma_{xy} &= \tau_{xy} \\ 2G\gamma_{yz} &= \tau_{yz} \\ 2G\gamma_{zx} &= \tau_{zx} \end{aligned} \quad (3)$$

where E is Young's modulus, ν Poisson's ratio and G the modulus of rigidity.

If σ_m is the hydrostatic stress and ε_m the corresponding volumetric strain, then the above mentioned equations can be written in the form

$$\begin{aligned} \varepsilon_x &= \frac{1}{2G}(\sigma_x - \sigma_m) + \frac{(1-2\nu)}{E}\sigma_m \\ \varepsilon_y &= \frac{1}{2G}(\sigma_y - \sigma_m) + \frac{(1-2\nu)}{E}\sigma_m \\ \varepsilon_z &= \frac{1}{2G}(\sigma_z - \sigma_m) + \frac{(1-2\nu)}{E}\sigma_m \end{aligned} \quad (4)$$

$$\gamma_{xy} = \frac{\tau_{xy}}{2G}$$

$$\gamma_{yz} = \frac{\tau_{yz}}{2G}$$

$$\gamma_{zx} = \frac{\tau_{zx}}{2G}$$

where $3\sigma_m = \sigma_x + \sigma_y + \sigma_z$. The terms $(\sigma_x - \sigma_m)$, $(\sigma_y - \sigma_m)$ and $(\sigma_z - \sigma_m)$ are reduced or deviatoric components and are generally written in the form σ_{ij} . The complete elastic stress-strain relations may therefore be written, when using an obvious double suffix notation, as

$$\begin{aligned} \epsilon_{ij} &= \frac{\sigma_{ij}}{2G} + \frac{(1-2\nu)}{E} \delta_{ij} \sigma_m \\ \sigma_m &= \frac{1}{3} \sigma_{ii} \end{aligned} \quad (5)$$

the delta symbol, δ_{ij} , is equal to unity when $i = j$ and to zero when $i \neq j$

1.3.2 Plastic Stress-Strain Relations

When a metal is deformed under continuously increasing stress, it is first strained elastically, the stress-strain relationship under combined stress being expressed by the equations of theory of elasticity. With increasing stress, the material yields and permanent plastic flow occurs. The total strain under load is then a combination of an elastic and a plastic component. When the stress is released the elastic component disappears and the material is left with the permanent plastic strain. Unless previous working has been severe the microscopic elastic behaviour of a metal can only slightly be affected by distortion of lattice. During unloading, elastic recovery is limited by the plastic yielding of favourably oriented grains.

In the elastic range the strains are uniquely determined by the stresses, that is to say for a given set of stresses the strains can be computed directly using Hook's law without any regard to as to how this stress state was attained whereas in the plastic range the strains are in general not uniquely determined by the stresses but depend on the whole history of loading or how the stress state was reached. Plastic stress-strain relations are considered to be governed by the "incremental" or "flow" type of

theory, as opposed to the “total” or “instant” type of theory which is sufficient to describe the elastic stress-strain

If a circular steel specimen is strained in uniaxial tension beyond the initial yield to some point C as shown in figure1, where CDE defines the subsequent yield curve,

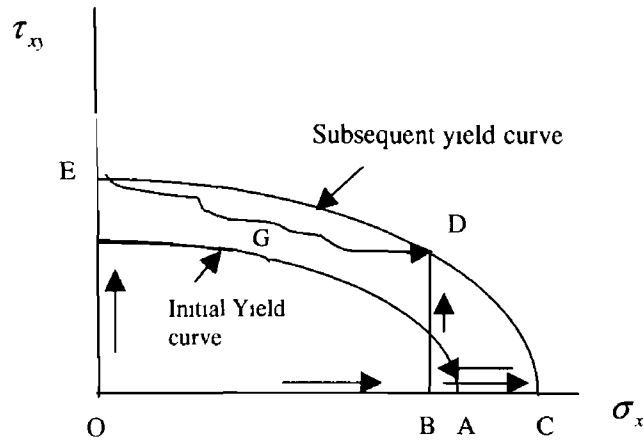


Figure1 Effect of loading path on plastic strains

then the plastic strains are

$$\epsilon_x^p = \epsilon^p$$

$$\epsilon_y^p = \epsilon_z^p = -\frac{1}{2}\epsilon^p$$

$$\epsilon_{xy}^p = \epsilon_{yz}^p = \epsilon_{zx}^p = 0$$

If the specimen is now unloaded to the point B and then a shear stress is applied increasing from B to D on the new yield locus, the plastic strains will still be as given above. Now if the specimen is first stressed in shear to the point E on the new yield locus and then, by any other path inside EDC, such as EGD, is stressed to the point D, the plastic strains would be

$$\epsilon_{xy}^p = \gamma^p \quad \text{and} \quad \epsilon_x^p = \epsilon_y^p = \epsilon_z^p = \epsilon_{xz}^p = \epsilon_{yz}^p = 0$$

which is obviously completely unrelated to the previous strain state. Thus even though the same stress state at D exist for both loading paths, and therefore the elastic strain states are the same, the plastic strain states are different. Because of the above mentioned dependence of the plastic strains on the loading path, the differentials or increments of plastic strain throughout the loading history is computed and then the total strain is obtained by integration or summation

1 4 Elastic-Plastic Torsion

When a gradually increasing torque T is applied to a circular shaft of uniform diameter D , the strain is entirely elastic until the shear stress at the outer surface reaches the yield stress in shear. The shear stress and strain vary linearly with radius in the elastic regime so that, as the outermost fibres take on a permanent set, the rest of the cross-section will still be elastic. As the torque continues to increase more and more the cross-section becomes plastic, the elastic-plastic interface being a concentric circle of decreasing diameter.

The elastic stress distribution across the prismatic bar of circular cross-section is expressed by

$$\tau_{z\theta} = \frac{Gr\theta}{L} \quad (6)$$

and the value of the maximum shear stress is given by

$$\tau_{z\theta \max} = \frac{Ga\theta}{L} \quad (7)$$

The stress distribution for a non-strain-hardening a strain-hardening material are shown schematically in figure2. The total torque transmitted by a non-strain-hardening bar is given by

$$T = \int_{r=0}^{r=c} \tau_{z\theta} 2\pi r^2 dr + \int_{r=c}^{r=a} \tau_y 2\pi r^2 dr \quad (8)$$

The first term on the right side of the above equation is the torque transmitted by the elastic core, where the shear stress varies linearly with r the second term is the torque transmitted by the plastic annulus, where the shear stress is constant and independent of r . The elastic-plastic boundary occurs at $r = c$. Integration of equation (8) provides

$$T = \frac{\pi c^4 G \theta}{2L} + \frac{2\pi a^3 \tau_y}{3} + \frac{2\pi c^3 \tau_y}{3} \quad (9)$$

Compatibility at the elastic-plastic boundary requires that

$$\tau_y = \frac{G\theta c}{L} \quad (10)$$

Combining equation (4) and (5) and rearranging gives

$$T = \frac{2\pi a^3 \tau_y}{3} \left\{ 1 - \frac{1}{4} \left(\frac{c}{a} \right)^3 \right\} \quad (11)$$

Thus when the entire section becomes plastic $c=0$ and the above equation is converted to

$$T_p = \frac{2\pi a^3 \tau_y}{3} \quad (12)$$

where T_p is the torque required to make the bar fully plastic. In the elastic-plastic and fully plastic regimes, the shear stress at the surface of the bar is τ_y . The shear strain at the surface of the bar is $\gamma = a\theta/L$ for all regimes.

For a strain-hardening material, the torque according to Nadai [] is given by

$$T = \int_0^a \tau 2\pi r^2 dr \quad (13)$$

Where the subscripts on the shear stress are dropped. Changing the variable from r to γ gives

$$T = \int_0^{\gamma_a} \frac{\tau 2\pi \gamma^2 d\gamma}{\theta_1^3} \quad (14)$$

Differentiating the above equation with respect to θ_1 gives

$$d(T\theta_1^3) = 2\pi f(\gamma_a) \gamma_a^2 d\gamma_a \quad (15)$$

At the specimen surface $\tau_a = f(\gamma_a)$ and $\gamma_a = a\theta_1$. Thus substituting these values into equation (15)

$$d(T\theta_1^3) = 2\pi \tau_a a^3 \theta_1^2 d\theta_1$$

or

$$\frac{d(T\theta_1^3)}{d\theta_1} = 2\pi \tau_a \theta_1^2 a^3 \quad (16)$$

Expanding the above equation gives

$$\frac{dT}{d\theta} \theta_1^3 + 3T\theta_1^2 = 2\pi \tau_a a^3 \theta_1^2$$

or

$$\tau_a = \frac{1}{2\pi a^3} \left[3T + \theta_1 \frac{dT}{d\theta_1} \right] \quad (17)$$

the first term on the right side of equation (17) is the torque due to the maximum yield shear stress of τ_a in a fully plastic non-strain-hardening material, whereas the second term is a correction for strain hardening. These terms can be readily derived from the torque-twist curve as shown in figure 3, where

$$\frac{dT}{d\theta_1} = \frac{BC}{CD}$$

$$\theta_1 = CD$$

$$\theta_1 \frac{dT}{d\theta_1} = BC$$

so that
$$\tau_a = \frac{1}{2\pi a^3} \{3BA + BC\} \quad (18)$$

The shear strain at the surface is given by $\gamma_a = a\theta_1$. Thus, the shear stress versus shear strain curve can be deduced by drawing tangents to the torque versus the angle of twist per unit length curve

1.5 The Levy-Mises and Prandtl-Reuss Equations

The general three-dimensional equations relating the increments of total strain to the stress deviations were given independently by Levy and von Mises. These equations are

$$\frac{d\varepsilon_x}{\sigma_x} = \frac{d\varepsilon_y}{\sigma_y} = \frac{d\varepsilon_z}{\sigma_z} = \frac{d\gamma_{yz}}{\tau_{yz}} = \frac{d\gamma_{zx}}{\tau_{zx}} = \frac{d\gamma_{xy}}{\tau_{xy}} = d\lambda \quad (19)$$

The proportionality factor is written as $d\lambda$ to indicate that incremental strains are being related to finite stresses. $d\lambda$ is an instantaneous non-negative constant of proportionality which may vary throughout a straining programme. In these equations the total strain increments are assumed to be equal to the plastic strain increments, the elastic strains being ignored. These equations can be applied to problems of large plastic flow and can not be used in the elastic-plastic range.

The generalised equations to include both elastic and plastic components of strain are due to Prandtl and Reuss, and known as Prandtl-Reuss equations. Reuss assumed that the plastic strain increment at any instant of loading is proportional to the instantaneous stress deviation and the shear stresses, that is

$$\frac{d\varepsilon_x^p}{\sigma_x} = \frac{d\varepsilon_y^p}{\sigma_y} = \frac{d\varepsilon_z^p}{\sigma_z} = \frac{d\gamma_{yz}^p}{\tau_{yz}} = \frac{d\gamma_{zx}^p}{\tau_{zx}} = \frac{d\gamma_{xy}^p}{\tau_{xy}} = d\lambda \quad (20)$$

or
$$d\varepsilon_y^p = \sigma_y d\lambda \quad (21)$$

The total strain increment is the sum of the elastic and plastic strain increment Thus,

$$d\epsilon_y = d\epsilon_y^p + d\epsilon_y^e$$

From equations (5) and (21)

$$d\epsilon_y = \sigma_y d\lambda + \frac{d\sigma_y}{2G} + \frac{(1-2\nu)}{E} \delta_y d\sigma_m \quad (22)$$

Since plastic straining causes no changes of plastic volume, the condition of incompressibility, in terms of the principal or normal strains can be written as

$$d\epsilon_1^p + d\epsilon_2^p + d\epsilon_3^p = d\epsilon_x^p + d\epsilon_y^p + d\epsilon_z^p = 0 \quad (23)$$

If the principal stress directions are considered, equation (20) gives,

$$\frac{d\epsilon_1^p - d\epsilon_2^p}{\sigma_1 - \sigma_2} = \frac{d\epsilon_2^p - d\epsilon_3^p}{\sigma_2 - \sigma_3} = \frac{d\sigma_3^p - d\sigma_1^p}{\sigma_3 - \sigma_1} = d\lambda$$

With the help of equation (23), equation (20) can be rewritten in terms of the actual stresses as

$$d\epsilon_x^p = \frac{2}{3} d\lambda \left[\sigma_x - \frac{1}{2}(\sigma_y + \sigma_z) \right]$$

$$d\epsilon_y^p = \frac{2}{3} d\lambda \left[\sigma_y - \frac{1}{2}(\sigma_z + \sigma_x) \right]$$

$$d\epsilon_z^p = \frac{2}{3} d\lambda \left[\sigma_z - \frac{1}{2}(\sigma_x + \sigma_y) \right]$$

$$d\gamma_{xy}^p = d\lambda \tau_{xy}$$

$$d\gamma_{yz}^p = d\lambda \tau_{yz}$$

$$d\gamma_{zx}^p = d\lambda \tau_{zx}$$

Thus equation (22) consists of three equations of the type

$$d\epsilon_x = \frac{2}{3} d\lambda \left[\sigma_x - \frac{1}{2}(\sigma_y + \sigma_z) \right] + [d\sigma_x - \nu(d\sigma_y + d\sigma_z)] / E \quad (24)$$

and three of the type

$$d\gamma_{xy} = \tau_{xy} d\lambda + d\tau_{xy} / 2G \quad (25)$$

Finally, it is seen from equation (22) that the volumetric and deviatoric strain increments can be separated for the total strain increment Thus equation (22) can be rewritten as

$$d\epsilon_y = \sigma_y d\lambda + d\sigma_y / 2G \quad (26)$$

$$d\varepsilon_y = \frac{1-2\nu}{E} d\sigma_u \quad (27)$$

How ever Hill [] has shown that for a material which strain hardens isotropically, $d\lambda$ of equation (26) can be replaced by $3d\bar{\sigma}/2\bar{\sigma}H$, where $\bar{\sigma}$ is the equivalent stress and H is the slope of equivalent stress equivalent strain curve Thus equation (26) becomes

$$d\varepsilon_y = 3\sigma_y d\bar{\sigma}/2\bar{\sigma}H + d\sigma_y/2G \quad (28)$$

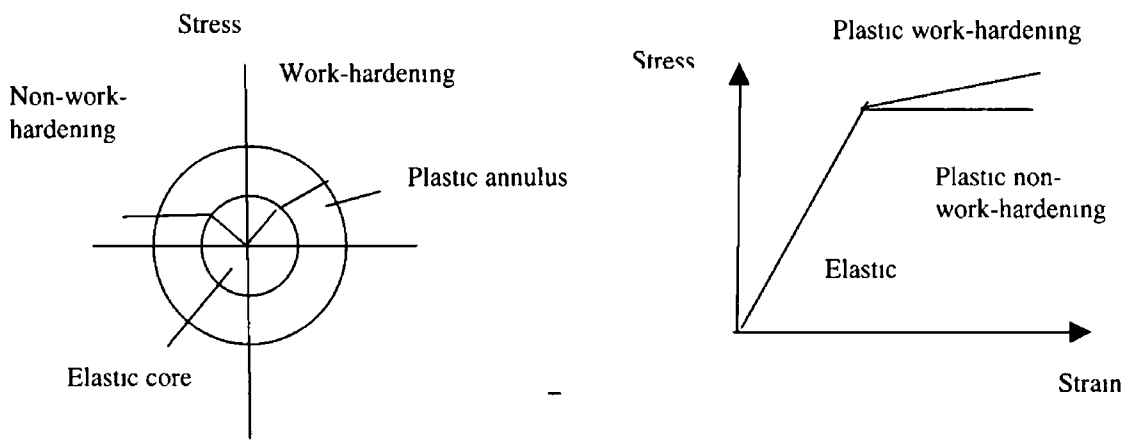


Figure 2 Stress distributions for a non-strain-hardening and a strain-hardening material

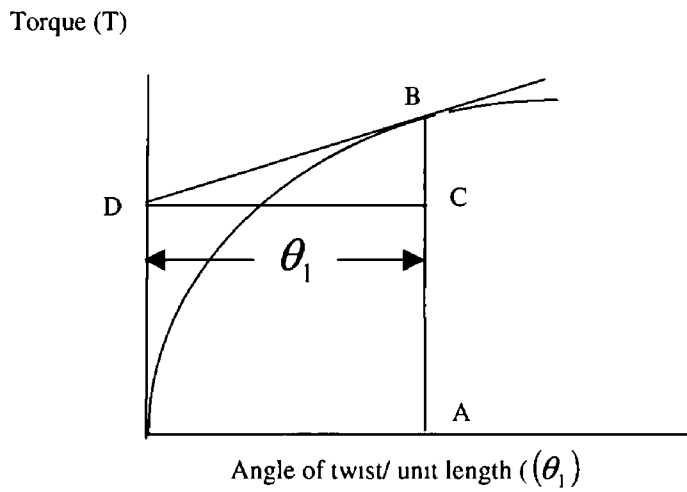


Figure 3 Torque versus angle of twist/unit length curve

LIST OF PUBLICATIONS

- [1] N M Zarroug, Padmanabhan, R , Macdonald, B J , Young, P and M S J Hashmi, “Elastic-plastic behaviour of mild steel (En8) rod under combined tension-torsion loading”, Proceeding of the international conference on advanced material and processing technologies, 2001, Vol 1, Madrid, pp 47-55
- [2] N M Zarroug, R Padmanabhan, B J MacDonald, P Young, M S J hashmi, “Mild steel (En8) rod tests under combined tension-torsion loading”, J of Material Processing Technology, 2003
- [3] Nuri M Zarroug and M S J Hashmi, “Elastic-plastic finite element analysis of a mild steel rod (En8) under combined tension-torsion loading comparison with experimental results”, Proc IMC-19, Queens University, Belfast, 2002
- [4] Nuri M Zarroug, A G Olabi and M S J hashmi, “Mild steel (En8) thin-walled tube subjected to combined tension-torsion loading”, Proceeding of the international conference on advanced material and processing technologies, 2003, Vol 1, Dublin, pp 603-606
- [5] Nuri M zarroug, A G Olabi and M S J Hashmi, “ Finite element simulation of the deformation behaviour of mild steel rod subjected to combined torque and tension loading”, accepted for publication in the proceeding of IMC-20, Cork Institute of Technology, Cork, 2003
- [6] R Padmanabhan, N M Zarroug, B J MacDonald, and M S J Hashmi, “A Novel Adaptive control system for a custom-built tension-torsion machine” (submitted to the proceeding of IMECHE, design and application)